Improving reconstructions of digital holograms

by

Jonathan Maycock, BSc.

NUI MAYNOOTH

Ollscoil na hÉireann Má Nuad

Dissertation submitted in partial fulfillment of the requirements for candidate for the degree of Doctor of Philosophy

Department of Computer Science,
National University of Ireland, Maynooth, Co. Kildare, Ireland.

Supervisors: Dr. Bryan M. Hennelly and John B. McDonald

December 2012

Abstract

Digital holography is a two step process of recording a hologram on an electronic sensor and reconstructing it numerically. This thesis makes a number of contributions to the second step of this process. These can be split into two distinct parts: A) speckle reduction in reconstructions of digital holograms (DHs), and B) modeling and overcoming partial occlusion effects in reconstructions of DHs, and using occlusions to reduce the effects of the twin image in reconstructions of DHs. Part A represents the major part of this thesis. Speckle reduction forms an important step in many digital holographic applications and we have developed a number of techniques that can be used to reduce its corruptive effect in reconstructions of DHs. These techniques range from 3D filtering of DH reconstructions to a technique that filters in the Fourier domain of the reconstructed DH. We have also investigated the most commonly used industrial speckle reduction technique - wavelet filters. In Part B, we investigate the nature of opaque and non-opaque partial occlusions. We motivate this work by trying to find a subset of pixels that overcome the effects of a partial occlusion, thus revealing otherwise hidden features on an object captured using digital holography. Finally, we have used an occlusion at the twin image plane to completely remove the corrupting effect of the out-of-focus twin image on reconstructions of DHs.

Acknowledgments

Firstly, I would like to thank my supervisors Bryan Hennelly and John McDonald. For your patience in explaining difficult concepts and for your original insights and intellect, I will be forever in your debt Bryan. For your tenacity, guidance and for always being there when times got tough, I will forever be in your debt John (aka Kofi).

I would like to thank Enrique Tajahuerce and Braham Javidi for the use of two of their digital holograms until we got our own lab up and running.

I would like to acknowledge financial support of Science Foundation Ireland, Enterprise Ireland, and the Embark Initiative of the Irish Research Council for Science, Engineering, and Technology for the financial support I received over the course of my Ph.D.

For a tough, but fair Viva Voce exam and for their helpful suggestions that improved the final version of my thesis I thank Prof. John Sheridan and Prof. John Ringwood.

Thanks to the following people for keeping me sane during my time in Maynooth: Des, Jonathan, Alison, Stuart, Wally, Sujana, Aidan and Sue. A special thanks to Conor who walked with me step by step on our journey of discovery through the field(s) of digital holography.

Thanks must also be extended to Prof. Dr. Helge Ritter who hired me as a post-doc four years ago, but never pressured me to finish my Ph.D. And to my friends Christof and Slobodan for making working life as a post-doc so much fun.

For their love and support, I can't thank my family enough. Especially Mam, who is always there to listen and advise. I would be lost without you. Thanks

to my sister, Emily, and brother, Carl, for always keeping it real. And it was a privilege to have my brother, Keith, the dreamer, in the lab with me as he (more quickly than I) also worked towards his Ph.D.

Finally, I want to thank my wife, Sonja, for all her support during this long process. Especially in the final months, you were so great, allowing me to concentrate on my thesis while you took the lion's share of the family responsibilities. But I do not only want to thank you for that - I want to thank you for this wonderful life we are building together. Just look at our amazing daughter Licia! And in a couple of weeks we will meet her little brother...

Declarations

I confirm this is my own work and the use of all material from other sources has been properly cited and fully acknowledged. Part of the work in this thesis has been presented in publications listed in Chapter 1.2

National University of Ireland Maynooth — Jonathan Maycock

December 2012

For Dad. I wish you were still with us.

Contents

Page

1 Introduction **1**

1.1 Background 3

1.1.1 Holography and digital holography 3

1.1.2 Speckle reduction in reconstructions of digital holograms . . 10

1.1.3 Occlusions in digital holography 19

1.2 Publications 25

1.3 Outline of the thesis 27

2 Theory and background **29**

2.1 Holography 29

2.2 Digital holography 33

2.2.1 Digital hologram recording and sampling 34

2.2.2 Digital holography setups 37

2.2.3 Numerical reconstruction of digital holograms 46

2.3 Speckle 52

2.3.1 First-order statistical properties of speckle 54

2.3.2 Second-order statistical properties of speckle 60

2.3.3 Speckle in digital holography 62

2.3.4 Addition of independent speckle patterns 65

2.4 Wigner distribution function 67
2.5 Summary 75

3 Discrete Fourier filter for speckle reduction 76
3.1 Introduction 76
3.2 Analysis 77
3.3 Metrics 84
3.4 Results and discussion 87
3.5 Summary 95

4 Speckle reduction using wavelets 97
4.1 Introduction 97
4.2 Analysis 98
4.3 Metrics 101
4.4 Results and discussion 104
4.5 Summary 121

5 Speckle reduction using three dimensional filtering 123
5.1 Introduction 123
5.2 Analysis 126
5.2.1 Convolution and filtering 126
5.2.2 Numerical computation of the 3D intensity field 129
5.2.3 Speckle size and independent speckle patterns 133
5.2.4 Gaussian filtering and our model 139
5.3 Metrics 142
5.4 Experimental results 146
5.4.1 1D filtering 149
5.4.2 2D filtering 153
5.4.3 3D filtering 155

5.4.4 Comparison with other techniques 164
5.5 Summary 166

6 Occlusions in digital holography **171**
6.1 Introduction 171
6.2 Wigner distribution function 173
6.2.1 The WDF and Digital Holography 173
6.2.2 The WDF and occlusions 175
6.3 Results and discussion 180
6.4 Summary 184

7 Occluding the twin image **186**
7.1 Introduction 186
7.2 Analysis of the technique 187
7.3 Results and discussion 193
7.4 Summary 197

8 Conclusion **198**
8.1 General discussion 198
8.2 Future work 202
8.2.1 Discrete Fresnel filter 202
8.2.2 Extension of the Discrete Fourier filter 203
8.2.3 Speckle reduction by simulation of other optical methods . . 203
8.2.4 Object recognition of partially occluded objects in reconstructions of DHs 204
8.3 Outlook 204

9 Appendix A **207**

10 Appendix B **209**

11 Appendix C **211**

12 Appendix D **214**

13 Appendix E **225**

14 Appendix F **229**

References **238**

Abbreviations used in thesis

CCD	charged-coupled device
CCM	corner coordinate matrix
DH	digital hologram
DHM	digital holographic microscope
DFF	discrete Fourier filter
DFT	discrete Fourier transform
DFST	discrete Fresnel transform
DLCT	discrete linear canonical transform
DSP	digital signal processing
EFI	extended focus image
FFT	fast Fourier transform
FT	Fourier transform
FST	Fresnel transform
HDPE	high density polyethylene
IFT	inverse Fourier transform
JPEG	joint photographic experts group
MLA	microlens array
NOISE	noninvasive optical imaging by speckle ensemble
OCT	optical coherent tomography
PTFE	polytetrafluoroethylene
PSI	phase-shift interferometry
SAR	synthetic aperture radar
WDF	Wigner distribution function
2D	two-dimensional
3D	three-dimensional

Nomenclature used in thesis

$h(x, y)$	complex amplitude of the interference pattern on the face of the camera
$R(x, y)$	complex amplitude of the reference wavefield on the face of the camera
$O(x, y)$	complex amplitude of the object wavefield on the face of the camera
$O^*(x, y)$	complex conjugate of the object wavefield on the face of the camera
$I(x, y)$	intensity of the object and reference wavefields on the face of the camera
exp	the exponential function
j	the imaginary unit, where $j^2 = -1$
θ	an angle
λ	wavelength of the light
W_{CCDx}	aperture size of the digital camera in x
W_{CCDy}	aperture size of the digital camera in y
$\Delta\xi$	pixel size in the x direction
$\Delta\eta$	pixel size in the y direction
$\Delta\xi_d$	pixel size in the x direction at reconstruction plane d
$\Delta\eta_d$	pixel size in the y direction at reconstruction plane d
N_x	number of pixels on the sensor in the x direction
N_y	number of pixels on the sensor in the y direction
T_x	sampling interval in x direction
T_y	sampling interval in y direction
W_x	physical size of the object to be captured in x
W_y	physical size of the object to be captured in y
d	distance the object is placed from the camera
$A(x, y)$	amplitude derived from four PSI interferograms
$\phi(x, y)$	phase derived from four PSI interferograms

FT	the Fourier transform operator
FT^{-1}	the inverse Fourier transform operator
DFT	the discrete Fourier transform operator
DFT^{-1}	the inverse discrete Fourier transform operator
$recon(m_{x'}T_{x'}, m_{y'}T_{y'})$	is the numerical representation of a complex optical wavefield
$Image(m_{x'}T_{x'}, m_{y'}T_{y'})$	intensity image calculated from $recon(m_{x'}T_{x'}, m_{y'}T_{y'})$
$\phi(m_{x'}T_{x'}, m_{y'}T_{y'})$	phase calculated from $recon(m_{x'}T_{x'}, m_{y'}T_{y'})$
E	the mean, or expectation, operator
R_e	the real part of random phasor sum
I_m	the imaginary part of random phasor sum
$\parallel J \parallel$	the Jacobian of the transformation between two sets of variables
σ	the standard deviation
σ^2	the variance
$\langle\rangle$	is an ensemble average
$C_I(x, y)$	normalized autocovariance function of intensity signal $I(x, y)$
S_x	the speckle size in the x direction
S_y	the speckle size in the y direction
S_z	the speckle size in the z direction
$f(x)$	a function or signal (x = spatial domain)
$F(u)$	the Fourier transform of $f(x)$, (u = spatial frequency domain)
$\psi\{f(x)\}(x, u)$	represents the Wigner distribution function of a signal $f(x)$
W	spatial extent of a signal
B	frequency extent of a signal
$f(\mathbf{r})$	a plane immediately in front of a diffuse non-uniform object
$d(\mathbf{r})$	a uniform diffuser
$t(\mathbf{r})$	a transparency that modulates a diffuser

α	the speckle index
β	the edge preservation metric
R	the resolution
$P_{\mathrm{x}}(x)$	the probability density function for X having a value of x
$h(\mathbf{r})$	the impulse response of the system
WT	the wavelet transform operator
$\Psi(x, y)$	the mother wavelet
ω	an overall metric for the quality of images
$G(x, y, z)$	a 3D Gaussian distribution
occlusion(x)	a 1D occlusion
$\psi\{\text{occlusion}(x)\}(x, u)$	the WDF of the occlusion

Chapter 1

Introduction

Digital holography [BL66, GL67, YM80a, BHG+74, SJ94, YZ97] has been researched since its inception in 1966 [BL66], but it is only recently that its true potential is beginning to be realised. This is due to the advent of low-cost, high resolution, and high dynamic range electronic sensors. Like holography, it involves a two step process of recording and reconstructing wavefronts, albeit in a very different way. For the recording step, digital holography uses an electronic sensor instead of photographic material, and for the reconstruction step it uses a computer to simulate optical reconstruction instead of physically reconstructing the wavefront. This thesis makes a number of contributions to the second step of this process, digital hologram reconstruction.

The contributions of the thesis are split into two distinct parts: A) speckle reduction in reconstructions of digital holograms (DHs), and B) modeling and overcoming partial occlusion effects in reconstructions of DHs, and using occlusions to reduce the effects of the twin image in reconstructions of DHs. Part A, comprising chapters 3, 4, 5 is concerned with speckle reduction in DH reconstructions and represents the major part of this thesis. Speckle is an artifact of all coherent imaging systems, including ultrasound and synthetic aperture radar (SAR) imaging.

Since digital holography is essentially a coherent imaging process, the reconstructions display speckle. Denis Gabor, the father of holography [Gab48], stated in an early paper on speckle reduction [Gab70] that speckle noise was the number one enemy of holography. We note that there are applications that make use of speckle, such as speckle photography and speckle interferometry [Goo06]. However, for the purpose of this thesis, speckle is considered a noise and we investigate a number of ways to reduce it. We are motivated by the fact that some digital holographic applications require some level of speckle reduction in order to perform well. To this end, we have developed a number of techniques that can be used to reduce the corruptive effect of speckle in reconstructions of DHs.

All of our techniques require only a single DH to reduce the speckle effect. This means that they can reduce the speckle content in reconstructions of DHs of captured dynamic scenes. The first technique follows Dainty and Welford [DW71], who optically reduced speckle in image plane hologram reconstructions by employing a rotating aperture in the Fourier plane of the hologram. Based on this idea we have reduced speckle by filtering the discrete Fourier transform (DFT) of reconstructed DHs. We have named this digital signal process the discrete Fourier filter (DFF) [MHM+07] and we have used it successfully on DH reconstructions from a number of different digital holographic architectures. In the following chapter we offer a comprehensive analysis of applying wavelets to the problem of speckle reduction in reconstructions of DHs [MMM+08]. Finally, we have developed is a 3D filtering technique that successfully reduces speckle using a convolution based framework and Gaussian filtering on DH 3D intensity fields [MHM13].

In Part B, we have investigated the nature of different types of opaque occlusions and the effect of reconstructing only certain parts of the DH. Part B comprises of Chapters 6 and 7. Our analysis is based on the Wigner chart [Wig32, Bas97]. The motivation of this research is to reconstruct a subset of the DH in order

to reveal hidden features on a partially occluded object [EMM+05, MEH+06b, MEH+06a]. By hidden features we mean features that are not visible at certain reconstructive perspectives or that are not visible due to out-of-focus noise from the occluding object. Finally, we have used an occlusion at the twin image plane to completely remove the corrupting effect of the out-of-focus twin image on reconstructions of DHs. This work is motivated by the need to increase the quality of single capture DHs such that they can be used in the retrieval of three-dimensional (3D) data from dynamic scenes.

1.1 Background

In this section, we review the literature relevant to this thesis. We begin with the invention of holography in 1948, and then discuss a modification to Gabor's original setup, namely the off-axis hologram, which was the catalyst for holography to become the popular field it is today. Digital holography is covered in some detail, from the early work of Brown and Lohmann [BL66] through to and beyond the seminal paper of Schnars and Jüptner [SJ94], which described the principle of recording holograms directly on a CCD target and numerically reconstructing them. This ushered in the era of digital holography as we know it today. This is followed by a brief preview of the thesis.

1.1.1 Holography and digital holography

Denis Gabor published a paper in 1948 [Gab48], in which he proposed a novel two step imaging process known as holography. In this work, which earned him the Nobel prize for physics in 1971, Gabor realised that when a coherent reference wave is present, together with the light diffracted from a rough object (or diffuse light transmitted through a transparent object) then information about the full

complex wavefield of the object can be recorded. This is in spite of the fact that the recording material only responds to the intensity of the light [Goo05]. Gabor used an in-line (or on-axis) setup and thus his holograms were corrupted by the DC terms and the twin image [see Section 2.1]. In those days it was also not possible to produce good quality coherent light, which is essential to create high quality holograms, and therefore holography only first received mild interest in the area of electron microscopy.

However, with the advent of the laser, which is capable of producing powerful coherent light, holography began to see an increase in interest. Leith and Upatnieks [LU62] introduced a modification of Gabor's original recording setup in 1962 that solved the twin image problem, and thus extended the applicability of holography. While Gabor had been restricted to using an in-line setup, Leith and Upatnieks were able to offset the reference wave at an angle thus producing hologram reconstructions that were free of the DC terms and twin image. The off-axis technique was demonstrated by Leith and Upatnieks in the early 1960's [LU62, LU63, LU64]. Around the same time Denisyuk [Den62] succeeded in producing white light reflective holograms. This enabled the viewing of a hologram using an incandescent light bulb. It was the work of Leith and Upatnieks, and that of Denisyuk, that accelerated the interest in holography in the 1960's.

Holography has had many applications since its discovery. Many of them stem from Stetson's work in 1965 on holographic interferometry [PS65, SP65]. This technique allows for measuring the change of the phase of a wavefield and thus changes to any physical quantity that effects this change. This area is sometimes called holographic nondestructive testing, and some of its applications are: measurement of vibration modes [PS65, SP65], deformation measurement [BHW65], contour measurement [HH66] and the determination of refractive index changes [SV73].

Digital holography [BL66, GL67, YM80a, BHG$^+$74, SJ94, PZT95b, PZT95a,

YZ97, JT00] differs from holography in that an electronic sensor, rather than photographic material, is used to capture the hologram during the recording step. In addition the reconstructions are performed numerically on a computer instead of physically reconstructing the hologram. They have advantages over traditional holograms in that no chemicals or physical development is necessary and the use of an electronic sensor allows video rates of capture [SJ94]. Of course, there are some exceptions to this description when the recording step is modified and a photographically captured hologram is scanned into a computer [MLJ04], or when the reconstruction step is performed physically using a spatial light modulator [KSO06]. Many of the contributions outlined in this thesis may be applied to alternative types of DHs. Digital holography has received increased attention over the last decade due to the continuing advances in electronic sensors with high spatial resolution and high dynamic range.

The first significant steps towards digital holography began when Brown and Lohmann [BL66] used a computer-guided plotter to draw a hologram in 1966. Brown and Lohmann reconstructed their holograms optically and used them for the purpose of pattern recognition. They found that their binary holograms yielded reconstructions of similar quality to optical holograms of comparable dimensions. The following year, Goodman and Lawrence [GL67] recorded a hologram on a vidicon camera with the lens removed. They then used a digital PDP-6 computer to reconstruct it.

In 1971 Huang [Hua71] published a paper on computer generated holography and computerized reconstruction of holograms. He discussed Fourier and Fresnel hologram reconstructions as well as digitization and quantization effects. This work was followed by Kronrod *et al.* [KMY72] in 1972 and Demtrakopoulos and Mittra [DM74] in 1974 who considered numerical reconstruction of holograms that were recorded at acoustic or microwave frequencies. Also in 1974, Bruning *et*

al. [BHG$^+$74] used a 1024 photodiode array and a PDP-8 computer to measure the phase in the interference pattern to an accuracy of $\frac{\lambda}{100}$ (where λ is the wavelength of the light used). While trying to detect defects in the optical surfaces and lenses, they were able to reduce error in the system by averaging the captured wavefronts many times.

By 1980, the area of computer generated holography and numerical reconstruction of holograms had matured. A complete description can be found in Yaroslavskii and Merzlyakov's [YM80b] book on digital holography. Kreis [Kre05] points out that digital holography experienced a long period of stagnation in the 1980's and that it was not until 1994 that interest in the field was revived. In that year, Schnars and Jüptner [SJ94] successfully captured and numerically reconstructed holograms using a CCD sensor. It was the first time that the numerical reconstruction of Fresnel holograms recorded with a CCD camera was achieved. They highlighted the fact that the method was limited to small objects at large distances from the target because of the low spatial resolution of the CCD relative to photosensitive materials. This limitation has become less of an issue with the recent advances in CCD technology.

Soon after this paper was published, interest in digital holography increased substantially. For the case of digital holograhy this was due to the fact that now the phase could be easily reconstructed numerically. We note that the phase had been calculated previously within the field of electronic speckle pattern interferometry [Løk84, PPT93, PT94]. However, after the initial paper by Schnars [Sch94] in which he described the procedure for determining the phase in a DH, work in the area of digital holographic metrology quickly followed [PZT95b, PZT95a]. In these papers, Pedrini *et al.* investigated vibration analysis of surfaces using digital double-pulsed holography [PZT95b] and compared two reflecting surfaces using digital holographic interferometry [PZT95a]. Shortly after this, completely new

applications including microscopy and pattern recognition were found for DHs.

In 1997, Yamaguchi and Zhang [YZ97] introduced a new technique of DH recording, known as phase-shifted interferometry (PSI). In order to maximise the detector capacity the angle between the object and the reference waves was reduced to zero. This meant that, like Gabor's first hologram, the resultant reconstruction was affected by that of the twin image and DC terms. To overcome this, they captured four separate interferograms and used them to compute the complex wavefield of the scene. The mathematical extraction of the complex field, meant that the dc-component and out-of-focus twin image were no longer present. This technique has been used to capture many of the DHs used in this thesis. A description of it is given in Section 2.2. Unfortunately, PSI is limited to the capture of static objects.

The following year, Zhang and Yamaguchi [ZY98] performed 3D microscopy with their new PSI setup. Classical optical microscopy has the limitation that if one wants to investigate samples that are thicker than the depth of focus of the system, then one must perform mechanical scanning along the optical axis. Digital holographic reconstruction is an efficient tool for investigating samples in depth without the need for moving optical equipment. In 1999 Cuche *et al.* [CMD99] investigated the numerical reconstruction in both amplitude and phase of off-axis Fresnel microscopic DHs. By introducing a microscope objective they demonstrated that digital holographic microscopy allows one to reconstruct the optical topography of specimens with nanometric resolution. In fact the resolution is equal to the diffraction limit of the imaging system as is true for classical optical microscopy. Image focusing, phase reconstruction, and correction of the phase aberrations were all performed digitally. An in-line digital holographic microscope (DHM) system that uses a long distance microscope was proposed by Yu *et al.* [XPMA01] in 2001. The in-line configuration of the system meant its resolution

was greatly increased. The following year Pedrini and Tiziani [PT02] developed a short-coherence DHM using a lensless system. The short-coherence of the laser meant that a DH was only captured if the path lengths of the reference and the object beam were exactly equal. A sequence of holograms were recorded and each of these holograms were then reconstructed numerically. The advantages of the system were a high spatial resolution and the ability to detect of the 3D shape. Ferraro *et al.* [FGA+05] used the fact that post-capture various slices of 3D object can be numerically reconstructed and focused at different depths using a DHM system. These different slices can then be stitched together and an extended focus image (EFI) can be created in which the entire object under consideration is in focus. Ferraro *et al.* [FGA+05] created EFIs of silicon microelectromechanical system objects using a DHM. In 2005 Marquet *et al.* [MRM+05] produced DHM images of living cells in a culture for the first time. Reconstructing the phase allowed them to measure the captured cells with subwavelength accuracy. DHM is an area of digital holography that shows great promise for the future, as the inherent 3D nature of holograms allow biologists to study organisms in a more complete manner than was previously possible.

In 2000, Javidi and Tajahuerce [JT00] performed 3D pattern recognition by use of in-line digital holography. Using information about the 3D objects shape, location, and orientation allowed them to perform 3D pattern recognition techniques with high discrimination and to measure 3D orientation changes. In the following year, Frauel *et al.* [FTCJ01] performed distortion-tolerant 3D pattern recognition. The distortion tolerance is achieved by a nonlinear composite correlation filter. Both of these techniques used PSI to capture the DHs. Recently 3D pattern recognition [JK05] and distortion tolerance 3D pattern recognition [KJ04] have been achieved using single exposure in-line digital holography. This technique has the benefit of being viable for dynamic scenes as only a single capture

is required and the out-of-focus twin image is tolerated.

The potential of in-line holography to analyse flow in liquid or gas by means of tracking particles has been known since as early as 1965 [Tho65]. Holography enabled the determination of the size and distribution of moving particles in air or liquids without significant disturbance of the sample volume. Conventional optical reconstruction of the particle field involves reconstructing the hologram with the same reference beam and then manually evaluating the resulting image as a screen is moved through the image volume [LS87]. In more recent times, digital holography has been used to analyse particles for flow field measurement [AKJ97, OZ00, MY00]. The advantage of using DHs over optical holograms is twofold: the tedious manual procedure of moving an imaging plane through the image volume is eliminated and it is also possible to use numerical methods to suppress the effects of the unwanted twin image [LS87]. In 2003, Pan and Meng [PM03] described a technique that significantly improves particle axial-location accuracy by exploring the reconstructed complex amplitude information. Soulez *et al.* [SDF$^+$07] proposed an inverse-problem approach in 2007, which yields the optimal particle set that best models the observed hologram image. This was a departure from the usual method of reconstructing using the Fresnel transform, which can present several problems such as twin-image noise and border effects.

One of the advantages of using digital holography over traditional holography is that the resultant hologram can be easily stored on a computer, and later transmitted. Digital holograms encode multiple perspectives of a captured scene simultaneously, and effectively store this data in a distributed fashion. However, the resultant data files can be quite large (approximately 64 MBs for a PSI hologram captured on a 2048×2048 CCD). This has meant that compression of digital holograms has received some interest recently [NFJT02, MNF$^+$02, NMJ03, NJ04]. In 2006, Shortt *et al.* studied the compression of DHs using wavelets [SNJ06b] and nonuni-

form quantization [SNJ06a]. In the same year Darakis and Soraghan [DS06a] investigated the compression of PSI DHs using standard baseline JPEG. They found that these standard compression methods worked well when applied to the separate interferograms rather than the DH itself. Darakis and Soraghan have also used Fresnelets [DS06b], which were introduced by Liebling *et al.* [LBU03], to compress DHs. Issues involving security of data have been researched by encrypting digital holograms [TJ00], and the compression of encrypted DHs has also recently been achieved [NJ04, SNJ06c].

In the following sections, we continue our literature review with an emphasis on the two central topics of this thesis.

1.1.2 Speckle reduction in reconstructions of digital holograms

The presence of speckle is due to the interference of coherent light scattered from many points on a rough surface [Goo06]. If the illumination is incoherent this interference has the same effect, however the integration of the many different wavelengths produces a smooth speckle free image [Yam03]. Since digital holography is essentially a coherent imaging system, the reconstructed images suffer from the effect of speckle. It degrades the quality of the resulting images and makes it difficult or impossible to resolve fine detail. All coherent imaging systems suffer from speckle and when we consider the viewing of reconstruction of DHs this speckle is an unwanted noise [Kre05]. We note however that there are a number of fields in which speckle is used to determine the properties of the surface of an object, whether that be strain, stress or vibration analysis. Goodman provides a comprehensive treatment of these fields in his recent book [Goo06] on speckle phenomena in optics, but they are beyond the scope of this thesis. See Section. 2.3 for a more thorough description of speckle and some of its statistical properties.

The presence of speckle hinders the application of image processing techniques to digital holographic data. The reduction of speckle is therefore an important topic whenever reconstructions of DHs are to be used. Indeed a degree of speckle reduction in reconstructions of DHs is important for certain digital holographic applications. One such area which benefits from speckle reduction is the extraction of 3D shape information from DHs. Existing focus measures [EMN+05, MLJ04, LU04, GK89] are hampered by the speckled appearance of the reconstructions, and results are improved when a pre-processing speckle reduction step is used. Another area that benefits from speckle reduced DH reconstructions is that of pattern recognition [JT00, FTCJ01, JK05, KJ04]. Speckle noise also impedes pattern recognition algorithms and therefore a speckle reduction step is usually performed first. The analysis of particles for flow field measurement using reconstructions of DHs has also benefitted from speckle reduction [DRM+04]. However, some of these digital holographic applications use standard noise reduction techniques that have not been developed and optimised to address the underlying properties of speckle in DHs. The techniques presented in this thesis have been developed specifically for speckle reduction and hence are more suitable for digital holographic applications. For example, one of the speckle reduction algorithms developed during the course of this work, the DFF [MHM+07] [see Chapter 3], has been used as a pre-processing step in the segmentation of 3D objects encoded in DHs [EMF+07], and for the reduction of speckle in digital holographic displays [KMP+10]. In his recent book on holographic interferometry, Kreis [Kre05] notes that there is a lot of scope for more research to be carried out in the field of speckle reduction in DHs. This thesis makes a number of contributions to this area. Speckle is present in all coherent imaging systems and speckle reduction in ultra sound imaging [GCS05], SAR imaging [USB03] and optical coherent tomography (OCT) imaging [AKF04] is still being actively researched. The possibility of using some or all of our speckle

reduction techniques in these and other areas could be investigated in the future [see Chapter 8]. This is due to the fact that our techniques are designed to reduce the effects of a fully developed speckle pattern such as is found in many other imaging domains.

Some of the techniques in this thesis are numerical models of established optical methods for reducing speckle. Therefore, we now present a chronological review of some of the most important works in optical speckle reduction. Iwai and Asakura [IA96] classified the principles of speckle reduction into five categories: 1) control of spatial coherence, 2) control of temporal coherence, 3) temporal averaging based on spatial sampling, 4) spatial integration at the detector, and 5) digital image processing. The speckle reduction techniques developed in this thesis fall into the fifth category of digital image processing, or digital signal processing (DSP) techniques. It is important to emphasise that speckle reduction has been studied extensively within the fields of echography (i.e., ultrasound imaging) and SAR imaging. However, here we restrict our review to important optical methods as it is these that have inspired some of the techniques in this thesis.

In category 1, a reduction in spatial coherence is usually achieved through an averaging process in which independent speckle patterns are added together on an intensity basis. One way to produce a reduction of spatial coherence effect is to use a rotating diffuser (i.e., ground glass) in the path of the capturing laser beam. This randomly modulates the laser beam ensuring that the path length from a point on the wavefront arriving at the diffuser to the detector changes over the integration time of the detector. It means that the light arriving at the sensor is only partially coherent in the spatial sense. In fact the differing path lengths also introduce a time delay, which produces a reduction the temporal coherence of the light. Therefore, light produced in such a setup can be described as a partially coherent. In 1967, Martienssen and Spiller [MS67] showed that light produced

from placing a moving diffuser in the path of a laser behaves like light produced from a quasi-monochromatic light source. They were able to reconstruct holograms showing reduced speckle. This work was extended in the early 1970's by Arsenault and Lowenthal [AL70] and Schröder [Sch71]. In 1978, Il and Baxter [IB75] used random spatial phase modulation with two diffusers to reduce the coherence of the source and thus reduce the speckle content. In 1986 Ambar *et al.* [AATA85] studied the reduction of speckle in laser-microscope images when the object was illuminated by a laser through a rotating multimode optical fiber. Once again the principle of their speckle reduction technique is based on independent addition of microscope images on an intensity basis. In 2002, Trisnadi [Tri02] used a diffuser to produce independent speckle patterns and thus reduce the speckle contrast in a laser projection display. Völker *et al.* [VZW$^+$05] built on Ambar et al's. [AATA85] work in 2005 by reducing speckle in laser speckle imaging by illuminating the object surface through a diffuser. Slow rotation of the diffuser leads to statistically independent surface speckles on time scales that can be selected by the rotation speed. Another way to produce a partially coherent source is by changing the illumination of the angle of the laser during hologram recording or reconstructing. In 1973, van Ligten [vL73] illuminated an object with a number of wavefronts, ensuring that each wavefront was coherent with the reference beam at the detector. Then, in the Fourier plane he created a filter that was designed to only allow light from a single wavefront through at a given time. This filter was then moved in the Fourier plane and the resultant intensities were summed at the detector simulating a reduction in spatial coherence and thus a reduction in speckle. In 1973, Leger *et al.* [LMP75] showed that changing the angle of illumination between two successive captures of a speckle pattern, while depending on the surface roughness, will produce a decorrelation between the two patterns. They showed that the correlation between the two speckle patterns decreases as the difference in angle increases. In

that same year, Gama [Gam75] produced this change of angle by using a vibrating source and showed that the resulting holographic reconstructions displayed a reduced speckle contrast pattern. He further showed that for certain classes of objects, resolution was not affected. We have investigated this phenomenon and developed a technique partly based on this principle [see Chapter 5].

In category 2, a reduction of temporal coherence is usually achieved using a spectrum of wavelengths. In practice it is very difficult to physically construct a laser multimode source with a high degree of spatial coherence over a wide range of wavelengths. This means that there have been limited works that use a reduction of temporal coherence in order to reduce speckle [IA96]. However, if such a source is used, during reconstruction the speckle is reduced by temporally averaging a number of independent speckle patterns. In 1973, George and Jain [GJ73] derived an expression to find the wavelength spacing required to decouple the speckle patterns arising from two different wavelengths in an imaging system and backed up their theory with experimental verification. In 1990, Saloma *et al.* [SKM90] reduced speckle using combined techniques from categories 1 and 2. They used both a multi-wavelength laser ensuring a decrease in temporal coherence, and a secondary light source that was virtually extended on a time integrated basis producing a decrease in spatial coherence. In 1993, Dingel and Kawata [DK93] used a laser diode to illuminate a conventional microscope with a continuously changing speckle pattern. The decorrelated speckle patterns were averaged on an intensity basis by a video detector in order to reduce the speckle. In 2001, Kinell and Sjödahl reduced speckle in a temporal phase unwrapping system used for shape measurement. A reduced spatial and temporal coherence effect was achieved by projecting a set of fringes with varying fringe spacings and phase shifts onto the object and each generated image was added on an intensity basis reducing the speckle. In 2004, Kim *et al.* [KLT$^+$04] used coherent backscattering

spectroscopy of rat colon tissues for detection of early precancer. By reducing both the spatial coherence (by adjusting the width of an aperture in the system) and the temporal coherence (by using a broad spectrum of light, $\lambda = 520 - 650$ nm), they were able to dramatically reduce the speckle content. This required the capture and summation of over a 1000 independent speckle patterns. Once again we have investigated this phenomenon and developed a technique partly based on this principle in Chapter 5.

The works in categories 3 and 4 can be viewed together as spatial integration at the detector is a common aspect of both. Dainty and Welford [DW71] optically reduced speckle in image plane hologram reconstructions in 1971, by rotating a circular aperture in the Fourier plane of the image. This produced n decorrelated speckle patterns and when these were summed the speckle was smoothed with some loss in resolution. Three years later Hariharan and Hegedus [HH74] gave a full analysis of the effect of sampling in the Fourier plane. They then proceeded to experimentally reduce speckle by superimposing the exposures from band passed filtered images of a diffuse object. In 1973, Yu and Wang [YW73] used a movable random mask instead of a rotating aperture. Ensuring that each speckle image is uncorrelated they achieve reduced speckle by averaging the reconstructions on an intensity basis. In a number of papers in 1974 and then 1975, McKechnie investigated both theoretically and experimentally the speckle reduction of time-averaged speckle patterns produced by a rotating circular aperture [McK74a, McK74b, McK74c]. McKenhnie's work was further extended in 1982 by Kawagoe *et al.* [YKA82]. In 1977, Östlund and Biedermann [ÖB77] investigated using a moving aperture and a moving random mask for speckle reduction in recording images of diffuse objects with coherent light. They conclude that these methods are equivalent to recording the image with the full aperture in coherent light and re-imaging and recording this speckled image in incoherent light with a smaller aperture or random mask

in a fixed position. In 1981 Iwai *et al.* [TIA81] investigated the autocorrelation function of the time-varying speckle intensity fluctuations at the detector. In 1998 speckle was reduced in a laser projection system by the introduction of moving diffractive optic elements [LWP98]. The diffractive optic element splits the laser beam into a number of independent beamlets with random phase distributions. The n different speckle patterns produced by these beamlets are rotated and the speckle in averaged by the observers eyes. The work of Dainty and Welford [DW71] and Hariharan and Hegedus [HH74] was used as the basis for our development of a digital speckle reduction technique called DFF [MHM$^+$07] [see Chapter 3].

Image noise removal is traditionally achieved by linear processing techniques such as mean, Wiener, low-pass, high-pass or band-pass filtering [GW02]. The median filter is a classical nonlinear technique which has been used successfully in the removal of salt and pepper noise. Some of these techniques such as the mean [MNF$^+$02, NJ04, JFH$^+$05, YYMY06, SNJ06c, DS06a, DS06b] and median filter [FTCJ01, NFJT02, NOK$^+$05] have been used to reduce speckle in DHs. However, these techniques have not been developed specifically for the reduction of speckle. There have been numerous DSP techniques developed since the 1980's that fall into category 5 in Iwai and Asakura's scheme. In 1981, Lee [Lee81] proposed a local minimum mean-square-error type filter to explicitly account for the multiplicative nature of the speckle. Lee investigated reducing the speckle content in SAR images and extended this work in [Lee83, Lee86]. In 1985 Crimmins [Cri85] introduced a nonlinear iterative algorithm called a geometric filter. In tests performed on SAR images he showed that it compared favorably against the median filter. Following Lee, Kuan *et al.* [KSSC85, KSSC87] proposed a local minimum mean-square-error type filter. However, they observed that unlike multiplicative noise or Poisson noise, speckle noise is not only signal-dependent but is also spatially correlated. In Kuan's model the correlation of speckle was taken into account

to improve reduction.

We now look at some of the recent contributions to the area of speckle reduction in DH reconstructions. In 2004, Dubois *et al.* [DRM$^+$04] used a spatially partially coherent source during recording to reduce the effects of speckle in a digital holographic microscopy system. In order to create the spatially partially coherent source a rotating diffuser was placed in the path of the coherent light source. This technique was also used by Kim [Kim04] in 2004 to reduce speckle in holographic 3D displays and by Sucerquia *et al.* [GSRC06] two years later who introduced static (but different) diffusers during the recording stage of capturing DHs and then added together the resulting reconstructions. Also in 2006, Baumbach *et al.* [BKKJ06] added together reconstructions from laterally shifted holograms of an object to reduce the speckle content. Nomura *et al.* [NONN08] proposed reducing speckle in reconstructions of DHs by superposing reconstructed DHs recorded at different wavelengths. Using a wavelength-tunable laser, they added together reconstructions from each of the captured DHs on an intensity basis, thus reducing the speckle content. Pen *et al.* [PXL$^+$11] and Xiao *et al.* [XZR$^+$11] recently introduced methods that reduce coherent noise in digital holographic phase contrast microscopy and off-axis DHs either shifting the specimen under investigation or by slightly shifting the specimen under investigation or by rotating the linear polarization state of both illumination and reference beams simultaneously. In each case they capture multiple DHs and add their reconstructions together on an intensity basis to reduce speckle. The implementation of a synthetic aperture for digital holography has been realised recently [CGC01, Mas02, BCL02, KAJ02, HNM07, MLJ08]. It is achieved by moving either the CCD or the sample, capturing multiple DHs between successive moves, and then stitching together the resulting DHs to form a larger DH. The primary purpose of a synthetic aperture is to increase the resolution of the resulting images.

However, increasing the aperture size also causes the average speckle size to reduce [see Chapture. 2.3.3.] All of these techniques required a change to the setup (i.e., the introduction of diffusers) and/or multiple captures of holograms to achieve a reduction in speckle. This is in contrast to the techniques developed in this thesis, which require no modification to the setup and only a single capture is required for processing. This implies that our techniques can be directly applied to all existing recorded DHs.

There have also been contributions to speckle reduction in which only a single DH was used. To lessen the effects of speckle noise, while investigating compression and Internet transmission of DHs, Naughton *et al.* [NMJ03] applied a subsampling (spatial integration) operation. They applied this to the intensity in the reconstruction plane and the operation integrates nonoverlapping blocks of $n \times n$ pixels to a single value. Garcia-Sucerquia *et al.* [GSRP05] also used a subsampling operation to reduce the effects of speckle in reconstructions of DHs. Furthermore, they suggested the merging of the subsampling operation with that of the median filter, although no quantative results are given in terms of the effects on resolution or edge preservation. In 2004, Bertaux *et al.* [BFRJ04], put forward an approach for the removal of speckle, which was based on the maximum-likelihood technique and used a general model for image reflectivity. The image was further improved by applying a constraint on isoline gray levels, which results in smoothness without blurring of the edges of the objects in the image. Finally, in 2006 Charrière *et al.* [CPC+06] convolved reconstructions with a Gaussian filter to reduce noise in images of cells captured by a DHM system. However as the focus of their paper was not on speckle reduction, but on living specimen tomography, details of the filtering process is not given.

In Chapter 4 we present a comprehensive analysis of applying standard wavelets to the problem of speckle reduction in reconstructions of DHs. In our investigation

of wavelet based speckle reduction of DH reconstructions we use both soft and hard thresholding combined with four different thresholding schemes. Wavelets have been used extensively to reduce the speckle content of ultrasound [ABT01], computer generated television holography fringes [KG96], optical coherence tomography [AKF04] images and synthetic aperture radar [FH98]. Many different wavelet techniques have been developed for the suppression of speckle noise [see references in [PWV+06]].

1.1.3 Occlusions in digital holography

In this section, we review some of the relevant literature related to the second contribution of this thesis, namely occlusions in digital holography. In preparation for our contribution to this area in Chapter 6, we first review the literature related to overcoming partial occlusion effects and then review the literature related to overcoming the problem of the out-of-focus twin image in holography. This is in preparation of our contribution to the removal of the out-of-focus twin image in reconstructions of DH [see Chapter 7].

One of the more remarkable qualities of human vision is its ability to compensate for missing visual information [RE98]. Although we have a blind spot, our visual system appears to fill in this spot with the colors, textures, and forms appropriate to that part of the visual input [Ram88]. Some computer vision systems try to mimic this ability using complicated algorithms [EZ96]. However, these are computationally expensive and at best provide an estimate of the occluded area. Digital holography provides an alternative modality by using the information inherent in a DH to allow us overcome problems of partial occlusion. In Chapter 6 we present, to the best of our knowledge, the first investigation on overcoming the effects of partial occlusions in reconstructions of DHs. To this end we employ the Wigner distribution function (WDF), or more specifically the Wigner chart,

a 2D graphical representation of the WDF [MEH+06b]. Recently, Nakatsuji and Matsushima [NM08] also studied occlusions in the context of digital holography. They explored the possibility of using digital holography to capture free-viewpoint images of scenes with occlusions. In particular, they created a synthetic aperture in order to increase the effective sensor size and therefore enlarge the field of view. Exploiting the 3D propterties of DHs allowed them to reconstruct the scene from different perspectives thus overcoming occlusions. Occlusions in other forms have seen some limited research in digital holography, and the study of occlusions similar to the situation we have studied have been actively researched in other fields [HJ05, JPDH06, HHJ07].

In 2003, Kishk and Javidi [KJ03] studied the effects of occlusions in DHs that had been watermarked by a hidden 3D object. One of their findings was that the effect of occluding some of the DH pixels results in additive noise and reduction in the energy of the reconstructed 3D objects. Kim and Lee [KL05] and Okman and Akar [OA07] have also studied the effects of occlusions in digital hologram watermarks. Like Kishk and Javidi [KJ03], they considered occlusions to be an attack that occurs in the hologram plane.

There has been a recent resurgence in another field of 3D imaging called integral imaging in which the effects of occlusions have been studied. Integral imaging is based on ray optics and uses a microlens array to create different perspective views of the captured scene. In 2005, Hong and Javidi [HJ05] used the 3D properties of integral imaging to overcome foreground occlusions in a scene. The following year Javidi *et al.* [JPDH06] proposed a method to recognize partially occluded 3D objects by using 3D volumetric reconstruction integral imaging. The correlation results of occluded 3D images for volumetric reconstruction show substantial improvements compared with those for conventional 2D imaging of occluded images. In 2007, working in the same group, Hwang *et al.* [HHJ07] extended this work

in integral imaging and investigated two different algorithms for overcoming the effects of partially occluded objects.

We have also investigated the use of occlusions for twin image removal in in-line digital holography [see Chapter 7] and we now provide a literature review of previous methods that have sought to reduce the effects of the out-of-focus twin image in holography. In 1951, soon after Gabor's invention, Bragg and Rogers developed an innovative solution to the twin image problem [BR51, Rog94]. They realised that the disturbance caused by the unwanted twin image on the wanted image plane is, in fact, its own hologram. If a second hologram is taken of the original object, which accurately reproduces the disturbance that is due to the unwanted twin image at the wanted image plane, the first reconstruction can be corrected by subtraction. This method fell into obscurity until later advances in digital technology allowed for a simplified subtraction process [Rog94]. A similar subtraction based technique was reported by Kirkpatrick and El-Sum [KES56] in 1956, where two holograms must be recorded and the object must be repositioned for the second recording enabling a canceling of the twin image term. In 1998, Xiao *et al.* [XXZ+98] showed how the Bragg and Rogers method could be applied in x-ray holography in real time by recording two holograms while taking advantage of the penetration property of x-ray radiation.

In 1963, Leith and Upatnieks proposed [LU63] an off-line optical architecture that enables the complete separation of the twin image term and the DC terms from the wanted image [see Section 2.1]. However, the increased bandwidth needed for this set-up poses a problem for digital holography. In digital holography, the pixelated recording cameras have resolutions an order of magnitude less than commercially available photo materials. Thus, in relation to holography, the bandwidth is already severely limited and the use of an off-line architecture only serves to limit it further. Nevertheless, Cuche *et al.* [CMD00] proposed and experimentally val-

idated the off-line technique for real time digital holographic recording making it possible to digitally spatially filter the DH in order to completely remove the DC terms and the twin image.

In 1966, another twin reduction method was proposed by effectively recording in the far field of the object [DJT66]. When replayed in the far field the image of the object comes to a focus, but the twin image is so spread out that it appears as a DC term and can be easily removed. This method was later successfully applied to particle analysis [TWZ67, TT76]. In 2006, Garcia *et al.* [JGSJK$^+$06] extensively reviewed lensless in-line holographic microscopy and showed that the twin image is of no consequence in the reconstructions. They comment that this is because of the diverging reference beam. While the reconstruction of the object image converges upon reconstruction, the out-of-focus twin image continues to diverge and effectively forms the Fraunhofer case where it is a constant DC term in the far-field.

Twin removal has been successfully accomplished with both deterministic phase retrieval and iterative phase retrieval. Deterministic phase retrieval algorithms are based on analysing the propagation of an intensity diffraction pattern. Iterative methods on the other hand rely on recursive ping-pong algorithms that converge over time based on some constraints that are imposed in every iteration of the algorithm. In 2000, Tiller et al. [TBPN00] used deterministic phase retrieval in combination with numerical simulations of light propagation to solve the twin image problem. Earlier, Liu and Scott [LS85, LS87] performed the first investigation of iterative phase retrieval for removing the twin image. They found that the retrieval of phase allowed for the separation of the twin image and the wanted image. However, their algorithm is limited to purely absorbing objects and cannot recover phase shifts caused by transmissive objects. Liu continued to improve upon these algorithms by incorporating into them a noise constraint based on a model of ad-

ditive noise [Liu90]. Koren *et al.* [KJP91, KPJ93] developed a new constraint for these iterative twin removal algorithms. They used the fact that the out-of-focus image was considerably larger in area than it is in its focused counterpart to form their constraint. Their algorithm worked for complex objects as well as absorbing objects. These phase retrieval twin removal algorithms were soon successfully applied to in-line x-ray holography [LHJK93, KYO$^+$96]. In 1972 Gerchberg [Ger72] demonstrated how phase retrieval could be used with electron microscopy to recover the phase of the wavefield. The iterative phase retrieval algorithm was later extended for the case of multiple recordings of different in-line holograms by Zhang *et al.* [ZPOT03]. Recently [LF07] improvements have been made on the iterative technique by using an improved model of the object. This improved method works well for phase objects as well as for pure absorbing objects.

Marie *et al.* [MBA79] introduced the first DSP technique for the removal of the twin image in 1979. Improved DSP based algorithms were developed some years later by Onural and Scott [OS85, Onu85, OS87]. They described linear filtering operations to decode the information contained in the holograms. However, their work did not allow for phase objects. In 1990, Nugent [Nug90] made further advances in linear filtering for twin image reduction that did allow for phase objects in some cases. Yang *et al.* [YXZJ99] have developed an algorithm that is quite similar to the previous work of Bragg and Rogers [BR51]. They devised a DSP method that relies on multiple reconstructions and subtractions. A similar method was developed by Zhang and Zhang [ZZ03], however their algorithm requires two in-line holograms to be captured.

As discussed in Section 1.1.1, Yamaguchi and Zhang [YZ97] developed a new method for recording DHs without the twin image in 1997. This is known as phase shifting digital holography and is discussed in more detail in Section 2.2.2.3. Recently, Chen *et al.* [CLY$^+$07] presented a method that allows for the phase-

shifting technique to be applied with an arbitrary phase shift and just two captures. In 1966, Gabor and Goss [GG66] also implemented an early technique based on phase shifting in which two holograms were captured with a quarter wave phase shift was used between captures. Reconstruction was optical and required the use of a quadrature prism to combine the previous captures and remove the virtual image. A number of these phase modulation twin image removal methods are reviewed by Takaki *et al.* [TKO99]. In the case of optical scanning holography, techniques have been proposed [DPW$^+$96, SX04, PKI$^+$00, DPI96] to remove the twin image that involved simultaneous acquisition of sine and cosine Fresnel zone-lens plate coded images and adding together the resulting two holograms.

A number of techniques have appeared in the literature relating to twin image removal in in-line electron holography [TLH91, Bar91, LC86]. One of the most successful methods for twin image reduction in electron holography is by recording multiple holograms of the same objects with different wavelengths and then superimposing the intensities of the reconstruction. The out-of-focus twin image will change for each wavelength and average out. A similar technique has also been developed based on distance instead of wavelength [LC86]. By recording a series of holograms of the same objects, but at different distances, implies that the out of focus images will be different in each reconstruction and will integrate to approximate a constant value. This technique has the added benefit of reduced speckle.

In relation to the work presented in this thesis for the removal of the out-of-focus twin image, the most relevant two references are by Pedrini *et al.* [PFFT98] and Denis *et al.* [DFFD05]. Pedrini *et al.* [PFFT98] proposed the first instance of spatially filtering the reconstruction planes of DHs. This involves cutting out the wanted digitally reconstructed image from its surrounding pixels. However, this area still contained considerable noise from the unwanted twin image. Denis *et*

al. [DFFD05] also proposed spatially filtering the DH reconstruction domain and it is their method that we have built on in Chapter 7. They showed that by removing the reconstructed focused unwanted twin image and returning to the plane of the wanted image by numerical propagation, the affect of the out-of-focus twin image could be removed. We propose the use of a similar technique for macroscopic objects. We also discuss for the first time the relative spreading of the unwanted twin image and the wanted image and how to manage this spreading using the Wigner chart [see Chapter 7.]

1.2 Publications

Part of the work in this thesis has been presented in the publications listed in this section.

Journal publications

J. Maycock, C. P. McElhinney, B. M. Hennelly, T. J. Naughton, J. B. Mc Donald, and B. Javidi. "Reconstruction of partially occluded objects encoded in three-dimensional scenes by using digital holograms", *Applied Optics*, **45**, pp. 2975-2985, May, 2006.

J. Maycock, B. M. Hennelly, J. B. Mc Donald, T. J. Naughton, Y. Frauel, A. Castro, and B. Javidi. "Reduction of speckle in digital holography by discrete Fourier filtering", *J. Opt. Soc. Am. A*, **24**, pp. 1617–1622, June, 2007.

Accepted journal paper

J. Maycock, B. M. Hennelly and J. B. Mc Donald. "Speckle reduction of reconstructions of digital holograms using three dimensional filtering", *accepted for publication in Optics Communications*, 2013.

Invited conference paper

J. Maycock, C. P. Mc Elhinney, A. E. Shortt, T. J. Naughton, J. B. McDonald, B. M. Hennelly, U. Gopinathan, D. S. Monaghan, J. T. Sheridan, and B. Javidi. "Holographic image processing of three-dimensional objects",*Proc. SPIE Optics East, Boston*, **6016**, pp. 60160K, Oct., 2005.

Conference papers

K. M. Molony, J. Maycock, J. B. McDonald, B. M. Hennelly, and Thomas J. Naughton. "A comparison of wavelet analysis techniques in digital holograms",*Proc. SPIE Strasbourg*, **6994**, pp. 699412, Apr., 2008.

J. Maycock, B. M. Hennelly, J. B. Mc Donald, T. J. Naughton, Y. Frauel, A. Castro, and B. Javidi. "Speckle reduction using the discrete Fourier filter technique", *IMVIP, National University of Ireland, Maynooth*, pp. 201, Sept., 2007.

B. M. Hennelly, D. P. Kelly, J. Maycock, T. J. Naughton, and J. B. McDonald. "Speckle reduction from digital holograms by simulating temporal incoherence", *Proc. SPIE, San Diego* **6696**, pp. 66961I, Aug., 2007.

B. M. Hennelly, J. Maycock, C. P. Mc Elhinney, J. B. McDonald, T. J. Naughton, and B. Javidi. "Analysis of partially occluded objects encoded in digital holograms using the Wigner distribution function", *Proc. SPIE, San Diego* **6311**, pp. 63110M, Aug., 2006.

J. Maycock, C. P. Mc Elhinney, B. M. Hennelly, J. B. McDonald, T. J. Naughton, and B. Javidi. "Reconstruction of partially occluded objects using digital holograms", *Proc. SPIE, Strasbourg* **6187**, pp. 61870V, Apr., 2006.

C. P. Mc Elhinney, J. Maycock, J. B. McDonald, T. J. Naughton, and B. Javidi. "Three-dimensional scene reconstruction using digital holograms", *Proc. SPIE – Opto-Ireland: Imaging and Vision*, **5823**, pp. 48-57, Jun., 2005.

1.3 Outline of the thesis

In Chapter 2 we review some of the basic theory behind holography, digital holography and speckle. The setups for capturing in-line, off-line, and PSI DHs are discussed. We review the first and second-order statistics of speckle, and the effect of adding together independent speckle patterns on an intensity basis. There then follows a number of chapters that describe new techniques for reducing the effects of speckle in reconstructions of DHs. Chapter 3 presents a technique called the DFF, which involves filtering reconstructions of DHs in the Fourier domain in an effort to reduce the speckle content. Chapter 4 presents a comprehensive analysis of applying wavelets to the problem of speckle reduction in reconstructions of DHs. We have used hard and soft thresholding and a number of thresholding schemes to reduce the speckle content. In Chapter 5 we report on new DSP techniques

that reduce speckle by filtering using a convolution framework. We investigate 1D filtering in the x,y and z directions, 2D filtering in the x and y directions and full 3D filtering. We rely on the fact that the adding together of different independent speckle images on an intensity basis reduces the speckle content. Overcoming the effects of partial occlusions in reconstruction of DHs is investigated in Chapter 6. The analysis is done using the Wigner chart, and simulations are carried out to verify our theoretical hypotheses. In Chapter 7, we present our contribution to the removal of the out-of-focus twin image from reconstructions of in-line DHs. Once again, our analysis is carried out using the Wigner chart. Finally, in Chapter 8 we summarise the contributions that this thesis makes to the field of digital holography and suggest future directions that could be pursued.

Chapter 2

Theory and background

In this chapter we take a closer look at holography, including both the original Gabor [Gab48] in-line hologram and the off-axis holograms of Leith and Upatnieks [LU62]. We proceed to review in-line and off-axis DHs [SJ94] and PSI DHs [BHG$^+$74, YZ97]. DH reconstructions suffer from a noise phenomenon known as speckle. A large part of this thesis is concerned with the reduction of this noise and therefore we review the properties of speckle here. A general explanation of the speckle phenomena is given, including a review of its first and second order statistics, and the effect of aperture size and propagation distance on speckle size in DHs. We then investigate how to reduce the speckle content by adding together independent speckle patterns. Finally, the Wigner distribution function, used to analyse occlusions in DHs in Chapters 6 and 7, is is described.

2.1 Holography

Holograms have fascinated people since their invention. The fact that holograms encode information about the phase of the wavefield means that different perspectives of a 3D object can be recreated when they are reconstructed. This is not

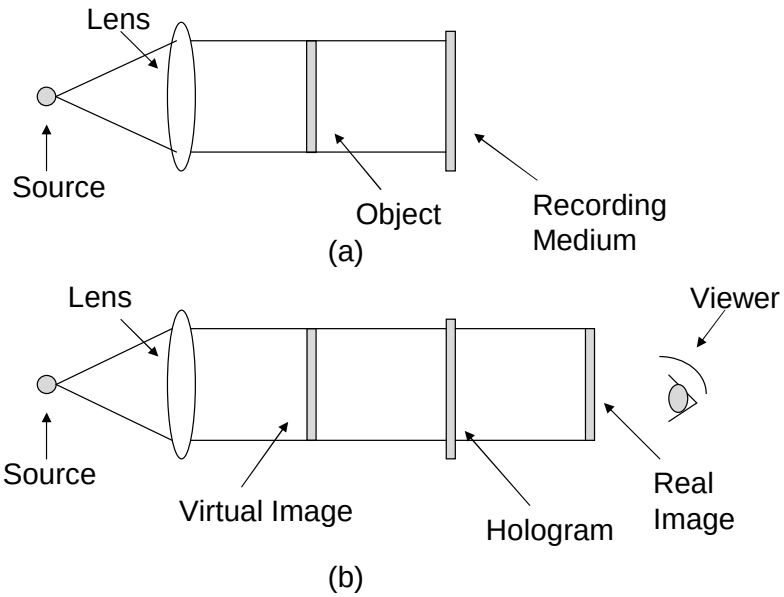

Figure 2.1: The capture (a) and reconstruction (b) of a Gabor hologram.

possible with conventional photography and thus has engaged minds for the last 60 years.

Gabor [Gab48] invented holography in 1948. He realized that when a coherent reference wave is present with the light diffracted from a rough object then information about the amplitude and the phase of the object wavefield can be recorded. Figure 2.1 shows the two step process of recording and reconstructing a Gabor hologram. We note that in Gabor's original set up no lens was present and a diverging wave illuminated the object. In order for this setup to work the object should be highly transmissive. This type of hologram is known as an in-line or on-axis hologram as the reference wavefield travels in the same direction as the object wavefield, although it should be noted that in-line DHs generally employ a separate object independent reference wave field, which is generated using beam splitters; A Mach-Zehnder interferometer or a Michelson interferometer are two such architectures. Figure 2.1 (a) shows a point source of coherent light illuminating an object. As light passes through the object, the parts of the beam that

are diffracted constitute the object wave, and the parts of the beam that pass unobstructed through the object constitute the reference wave. The intensity of the light incident on the recording medium can be written as the sum of two wavefields

$$h(x,y) = R(x,y) + O(x,y), \tag{2.1}$$

where $R(x,y)$ is the amplitude of the reference wavefield, $O(x,y)$ is the amplitude of the object wavefield. The real-valued intensity $|h(x,y)|^2$ is recorded and may be written as

$$I(x,y) = |h(x,y)|^2 = |R(x,y)|^2 + |O(x,y)|^2 + R^*(x,y)O(x,y) + R(x,y)O^*(x,y), \tag{2.2}$$

where $I(x,y)$ is the intensity, * denotes the complex conjugate, $R^*(x,y)O(x,y)$ and $R(x,y)O^*(x,y)$ are the virtual and real image terms, and $|R(x,y)|^2$ and $|O(x,y)|^2$ are the DC terms. As the third term, $R^*(x,y)O(x,y)$, is proportional to the object wavefield, $O(x,y)$, it produces a virtual image of the object. Consequentially the fourth term, $R(x,y)O^*(x,y)$, which is proportional to the conjugate of the object wavefield, produces a real image [Goo05].

Figure 2.1 (b) shows the reconstruction of a Gabor hologram. Assuming the hologram is illuminated by the same reference wave that was used to capture the hologram, then the resulting reconstruction produces a virtual image in the location where the object once stood, a real image at the same distance, but on the opposite side of the hologram, and a bright spot, caused by the reference wave intensity. A serious limitation of the Gabor hologram is that when the real image is brought to focus it contaminated by the out-of-focus virtual image. Similarly, when the virtual image is viewed by an observer, the out-of-focus version of the real corrupts this image [Goo05].

Leith and Upatnieks [LU62] introduced a modification of Gabor's original

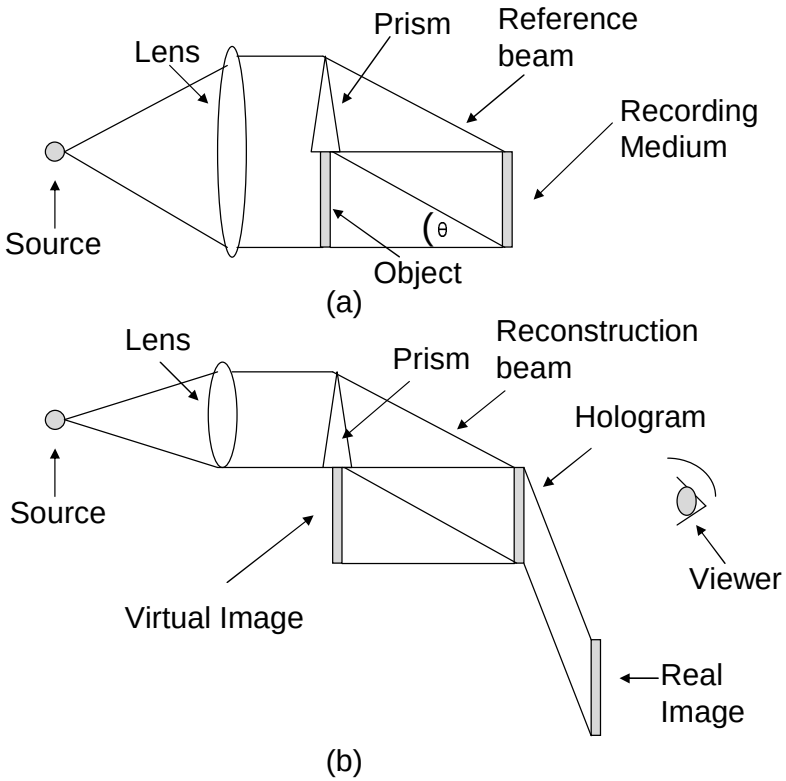

Figure 2.2: The capture (a) and reconstruction (b) of a Leith and Upatnieks' hologram.

recording setup in 1962 that solved the problem of the overlapping out-of-focus images and thus extended the application of holography. The major difference in their technique was the introduction of a second separate reference wave, which they offset at an angle to the object wave. The resultant hologram is known as an off-axis hologram. Figure 2.2 illustrates one possible setup for capturing and reconstructing the off-axis hologram. At the recording plane we observe the sum of two mutually coherent waves, one representing the object wave and the other a reference wave. The amplitude distribution at the recording plane is

$$h(x, y) = R(x, y) \exp[-j2\pi uy] + O(x, y), \tag{2.3}$$

where exp is the exponential function, j is the imaginary unit (with $j^2 = -1$), and

the spatial frequency, u, of the reference wave is given by

$$u = \frac{\sin\theta}{\lambda}, \tag{2.4}$$

and λ is the wavelength of the light used, and θ the angle between the reference and object waves. The captured intensity at the recording plane becomes

$$\begin{aligned} |h(x,y)|^2 &= |R(x,y)|^2 + |O(x,y)|^2 \\ &+ R^*(x,y)O(x,y)\exp[j2\pi uy] \\ &+ R(x,y)O^*(x,y)\exp[-j2\pi uy]. \end{aligned} \tag{2.5}$$

When reconstructed the third term, $R^*(x,y)O(x,y)\exp[j2\pi uy]$, produces a virtual image that is deflected away from the reference beam axis at an angle θ [see Figure 2.2 (b)]. Likewise, the fourth term, $R(x,y)O^*(x,y)\exp[-j2\pi uy]$, produces a real image that is deflected away from the reference beam axis at and angle $-\theta$ [see Figure 2.2 (b)]. As long as the angle, θ, between the object and reference waves is made large enough, the observer can obtain an unobstructed view of the virtual image.

We have limited our discussion to transmissive Fresnel holograms, but there are of course numerous other types of holograms. These include Fraunhofer, Fourier, reflection, rainbow and multiplex holograms. For an excellent description of these holograms consult Goodman [Goo05]. We now turn our attention to DHs.

2.2 Digital holography

Digital holography [BL66, GL67, YM80a, BHG$^+$74, SJ94, YZ97] is a 3D imaging technology that involves the capture of the complex wavefield emanating from real world objects by a CCD and their numerical reconstruction of the image using a

computer. In the early days of digital holography, the holograms were not recorded directly, but rather captured on film and then scanned and digitized [Hua71]. Advances continue in the storage capacity and speed of processing of computers and the spatial resolutions of electronic recording devices (e.g. CCDs). These advances have made it possible to record holograms electronically and to reconstruct them using computer simulation of light propagation. This means that the analysis of wavefronts can be performed without physical reconstruction [Ras01].

In digital holography, the real-valued intensity $|h(x, y)|^2$ (see Equation 2.1) is recorded on a two-dimensional array of sensors ($M \times N$ cells) of dimension $\Delta\xi \times \Delta\eta$. We now write the intensity recorded on the CCD as $|h(m\Delta\xi, n\Delta\eta)|^2$, where m and n are integer numbers. The corrupting effect of the DC terms can be far noisier than that of unwanted out-of-focus-twin image. However, a number of successful methods have been developed in the literature eliminate this negative effect. These methods are based on high pass filtering of the DH [KJ97], subtracting stochastically different holograms [DMS03], phase-shifting [ZLG04] and by subtracting the numerical generated intensity of the object and reference waves from the DH [GLCC07].

2.2.1 Digital hologram recording and sampling

The sampling requirements for the capture of DHs have been a subject of active research over the past decade. In this section we give a brief overview of how the physical parameters in recording digital holograms control the resolution in the final image as well as the distance at which an object of a given size must be placed from the camera. A detailed derivation of these properties may be found in [KHP+09]. The various physical parameters that affect the image quality and image formation in a reconstructed digital hologram are:

1. The aperture size of the digital camera in both dimensions, W_{CCDx} and

W_{CCDy}

2. The sampling interval of the camera in both dimensions, T_x and T_y
3. The size of the pixels in both dimensions, $\Delta\xi$ in x and $\Delta\eta$ in y
4. The wavelength of the light, λ
5. The physical size of the object in both dimensions, W_x and W_y
6. The distance the object is placed from the camera, d

These six different parameters contribute in different ways in terms of image resolution, sampling requirements and object placement (from the camera). For the sake of brevity we will consider only the parameters in the x dimension and the results can be easily generalized to the y dimension.

2.2.1.1 Image Resolution

The camera aperture controls the resolution of the reconstructed complex image. The camera aperture size determines the point spread function of the imaging system and it therefore controls the maximum spatial frequency recordable in the imaging system which is equal to $W_{CCDx}/\lambda d$. We can also see that the wavelength of the laser and the object camera distance also control the bandwidth of the reconstructed image. We note that the averaging effect that occurs within the pixel results in an averaging of the complex wavefield. This also effect the bandwidth of the reconstructed image but the limiting effect is usually determined by the camera aperture. We do not discuss the theoretical image resolution any further as it is somewhat outside the scope of this thesis. We note that the resolution in DH is also limited by image quality degradation caused by speckle. Speckle is discussed later in this chapter.

2.2.1.2 Sampling and object distance

The pixel pitch or sampling interval determines the distance between overlapping copies of the reconstructed image that are caused by sampling. They are separated by integer multiples of $\lambda d/T_x$. This forces a limit on the maximum object size that we can record without adjacent copies of the image overlapping each other (aliasing). Thus we can conclude that the maximum object size is given by

$$W_x = \lambda d T_x \tag{2.6}$$

We can see that the smaller the pixel pitch, the greater the separation of the copies, and therefore the larger the object size we can record for a given distance. For a given object and a given CCD pixel size we can determine the minimum distance at which we should place the object from the camera

$$d = W_x T_x \lambda \tag{2.7}$$

Apart from repeating this result from [KHP+09] we do not give any further investigation to the effects of sampling in this thesis.

2.2.1.3 Quantization

In recording of a digital hologram the pixel values are quantized in accordance with the bit-depth of the memory registers in the detection system. The bit-depth in modern cameras is typically 8 to 12 bits per pixel. The effect of quantization is to degrade the image quality of the reconstructed image. This is discussed in detail in [PH11]. For the bit depth of the cameras used in this thesis the effect of quantization is insignificant when compared with other sources of noise, such as speckle noise.

2.2.2 Digital holography setups

In this section, we review three setups for capturing DHs. The first setup, in-line digital holography, is based on Gabor's original optical in-line setup, except that here we have separated the laser by amplitude division and are using a reflection object rather than a transparent object. The second setup, off-axis digital holography, is based on Leith and Upatnieks [LU62] original off-axis optical setup. Finally, we review the PSI setup introduced by Yamaguchi and Zhang [YZ97] in 1997.

2.2.2.1 In-line digital holography

In-line digital holography, like its optical counterpart, refers to an experimental setup in which the reference wavefield travels in the same direction as the object wavefield [see Figure. 2.3 (a)]. Both wavefields are incident on an electronic sensor (e.g. CCD) with no angle difference between the wavefields. The DHs that are used in this thesis were recorded with an optical system [JT00, FTCJ01] based on a Mach-Zehnder interferometer. A linearly polarized laser beam is expanded and collimated, and divided into object and reference beams. The reference beam combines with the light diffracted from the object and forms an interference pattern in the plane of the camera, thus forming a DH.

As in the optical case, this method suffers from poor reconstructed image quality due to the presence of the DC terms (the intensity of the reference and object beams) and the out-of-focus twin image. We have already suggested a number of ways to remove the DC terms from the resultant DHs [see Section 2.2]. In this thesis, we employ the method of spatial filtering of the hologram given by Kreis and Jüptner [KJ97]. This method involves computing the Fourier transform (FT) of the DH, using a Fast Fourier Transform (FFT), algorithm and removing the lower (center) frequencies before applying an inverse FFT to return to the DH plane.

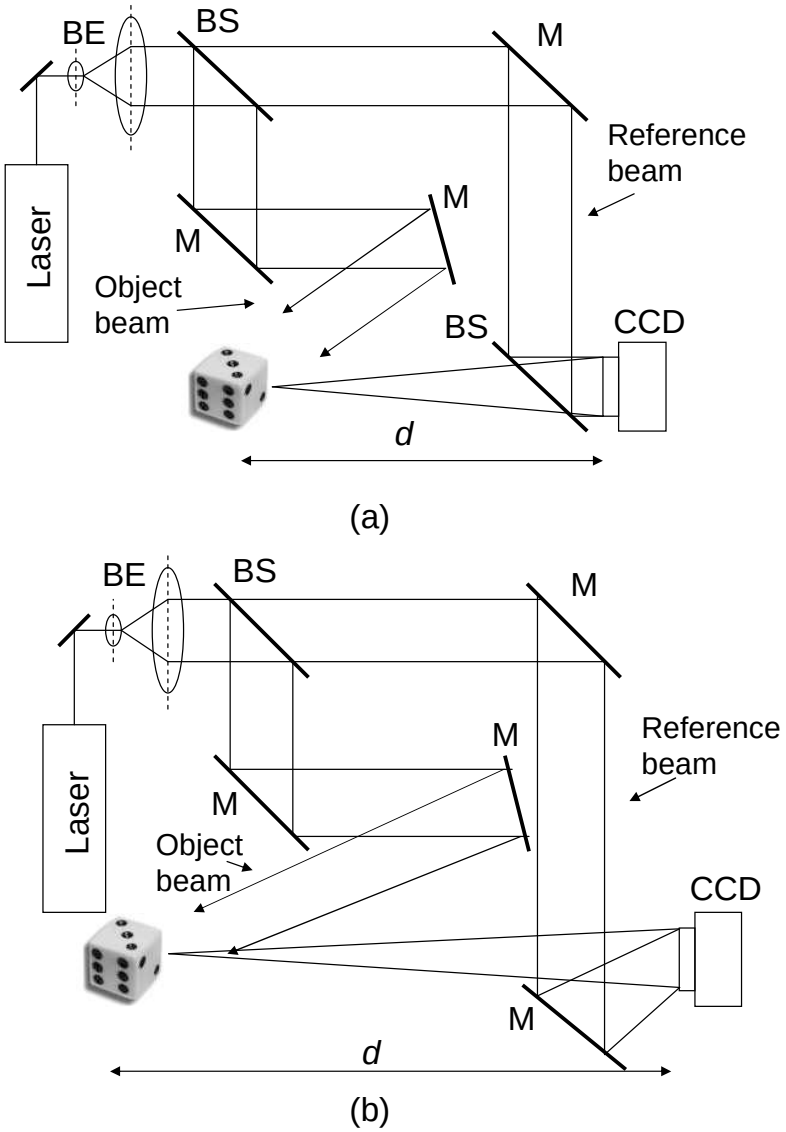

Figure 2.3: Experimental setup for (a) In-line digital holography and (b) off-axis digital holography. BE, beam expander; BS, beam splitter; M, mirror; CCD, charged-coupled device; d, distance from the object to the camera.

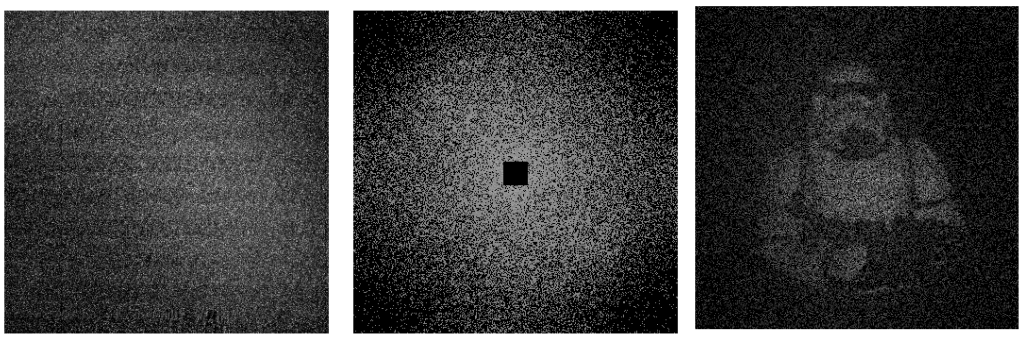

Figure 2.4: In-line setup with (a) the recorded intensity on the CCD, (b) the amplitude of the Fourier Transform of the DH with the lower frequencies set to zero, and (c) the reconstructed real image of the object.

This will effectively reduce the impact of the two intensity terms (DC terms) appearing on the left hand side of Equation 2.2 [Kre05]. However, the problem of removing the out-of-focus twin image remains a difficult one. We have found two methods in the literature [PFFT98, DFFD05] for the removal of the twin image in digital holography [see Section 1.1.3]. In Chapter 7 we offer another contribution to removing its effects.

Figure 2.4 (a) shows the recorded intensity of a DH taken of a stormtrooper figure using an in-line setup. In order to eliminate the effects of the DC terms we apply an FFT algorithm to this intensity DH and removed the lower frequencies [see Figure. 2.4 (b)]. After removal of the DC terms an inverse FFT is applied. Figure 2.4 (c) shows the real image of the object after application of the discrete Fresnel transform. We note the corruptive influence of both the out-of-focus twin image and speckle on the image.

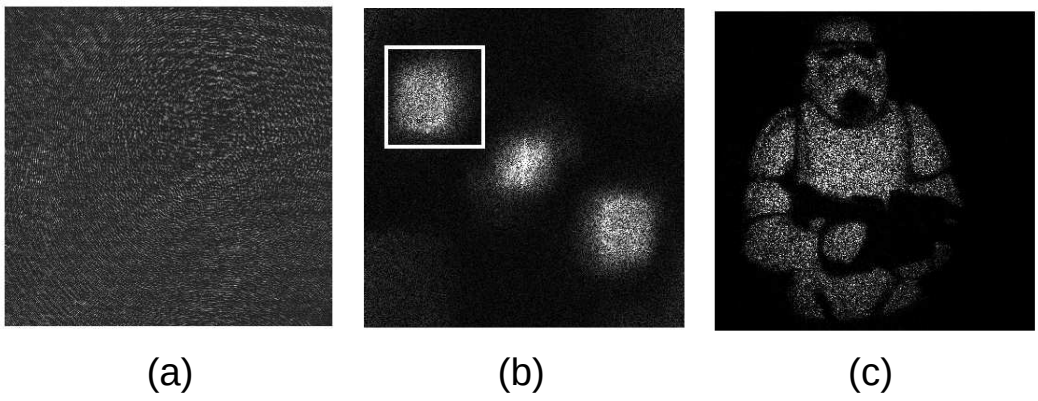

Figure 2.5: off-axis setup with (a) the recorded intensity on the CCD, (b) the amplitude of the Fourier Transform of the DH (real image energy highlighted by box), and (c) the reconstructed real image of the object.

2.2.2.2 Off-axis digital holography

Isolation of the real image may be achieved using an off-axis recording setup equivalent to that used by Leith and Upatnieks [LU62] and illustrated in Figure. 2.3 (b). The difference between this setup and the in-line setup in Figure. 2.3 (a) is that the reference beam and the object beam are incident on the CCD at different angles. Figure 2.5 (a) shows the recorded intensity of a DH taken of a stormtrooper figure using an off-axis setup. Elimination of the twin image is trivial when this configuration is used, as the real image, DC terms and the out of focus twin image are separated in space in the spatial frequency domain. The FT of the DH can be spatially filtered [CMD00], thus allowing extraction of the real image [see Figure. 2.5 (b)]. Figure 2.5 (c) shows the real image of the object after numerical recontruction.

It would seem that the off-axis setup should be used in place of the in-line setup, as it ensures easy removal of the twin image. However, increasing the angle between the reference and the object wavefields increases the spatial resolution requirements of the setup and forces us to place the object at a much greater

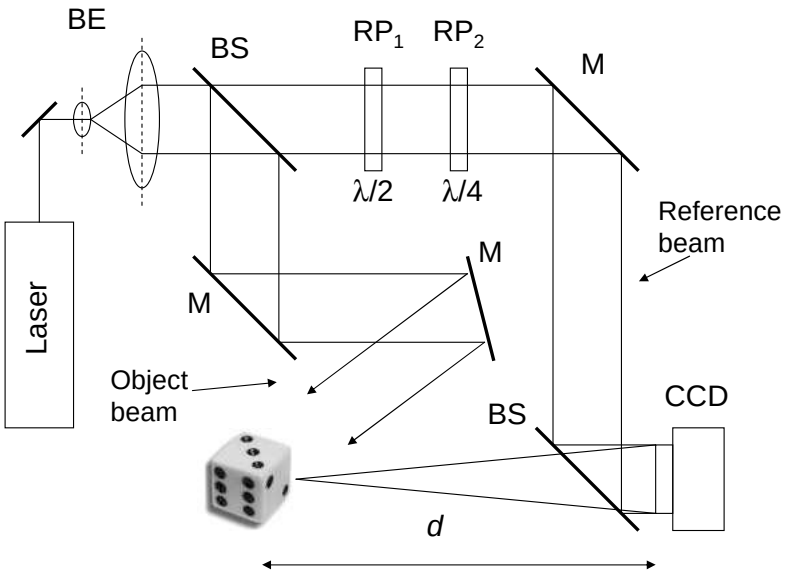

Figure 2.6: Experimental setup for PSI: BE, beam expander; BS, beam splitter; RP, retardation plate; M, mirror, CCD, charged-coupled device; d, distance from the object to the camera.

distance from the CCD. The greater distance is needed to ensure that smaller angular plane waves reach the CCD. In effect we are losing a large portion of the bandwidth available to us and this is highly undesirable when one considers the already limited resolution of CCDs. Therefore, if we want to maximize the resolution of the CCD, an in-line setup should be used. In 1997, Yamaguchi and Zhang [YZ97] used PSI to capture DHs using an in-line setup. In the next section, we discuss how PSI overcomes the problem of the out-of-focus twin image.

2.2.2.3 Phase-shift interferometry

The PSI setup used in this thesis is shown in Figure. 2.6. The only difference between this setup and the in-line setup introduced in Section 2.2.2.1 is the the addition of two wave retardation plates. The linearly polarized reference beam passes through half-wave plate RP_1 and quarter-wave plate RP_2. By rotating the plates we can achieve four phase shift permutations of 0, $\frac{\pi}{2}$, π, and $\frac{3\pi}{2}$. Once

again the reference beam combines with the light diffracted from the object and forms an interference pattern in the plane of the camera. For each of the four phase shifts we record an interferogram, or in-line DH. The intensity of each of the four interferograms is described by Equation 2.2, and the amplitude, $A(x, y)$, and phase, $\phi(x, y)$, of the object field can be calculated by

$$A(x,y) = \frac{\sqrt{(I(x,y;\frac{3\pi}{2}) - I(x,y;\frac{\pi}{2}))^2 + (I(x,y;0) - I(x,y;\pi))^2}}{4} \tag{2.8}$$

and

$$\phi(x,y) = \tan^{-1}\frac{I(x,y;\frac{3\pi}{2}) - I(x,y;\frac{\pi}{2})}{I(x,y;0) - I(x,y;\pi)} \tag{2.9}$$

respectively. Therefore we use these four real-valued images (interferograms) to compute the camera-plane complex field $h(x, y)$ [BHG+74, YZ97],

$$h(x,y) = A(x,y)\exp[-j\phi(x,y)] \tag{2.10}$$

Figure 2.7 (a) shows the intensity of the complex field $h(x, y)$. There is no need to do any extra processing to remove either the DC terms or the out-of-focus twin image as they are not present. Figure 2.7 (b) shows the reconstructed real image of the object after application of the discrete Fresnel transform, which we use to simulate the propagation of the object wavefield back to the object plane. We discuss the Fresnel transform in more detail in the following sections. An obvious drawback to PSI is that the object needs to be completely static in order to capture the four interferograms. Traditionally this has meant that for applications that require the tracking of moving particles or the imaging of biological tissue, the approach has not been suitable. However, recognizing this limit, researchers have developed a novel way to capture multiple interferograms in parallel [ATK+08].

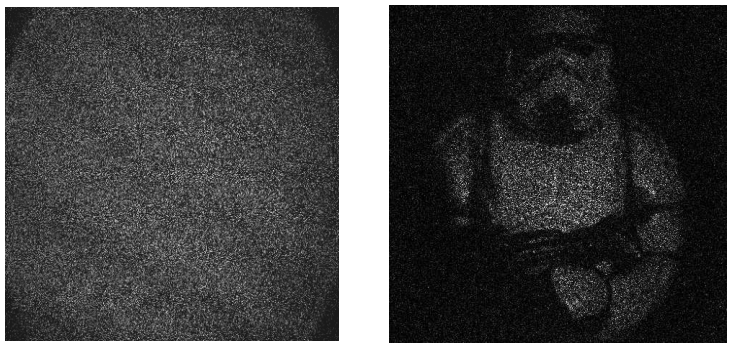

Figure 2.7: (a) The amplitude of the object wavefield in the camera plane, $A(x, y)$ for a stormtrooper object captured using an PSI setup and (b) the result of propagating the back to the object plane using the discrete Fresnel Transform gives the reconstructed real image of the object.

This method involved the addition of a phase-shifting array device located in the reference beam.

2.2.2.4 Mathematical preliminaries

The Fourier transform is the single most useful mathematical tool in the analysis of digital holograms. It allows us to describe almost any signal as the superposition of weighted (in amplitude and phase) sinusoidally varying functions in some band of frequencies. The FT calculates the weight of each component function for the signal we operate on and these are viewed as weighted delta functions in the frequency domain. Following Bracewell [Bra78] the FT of $f(x)$ is

$$F(u) = \int_{-\infty}^{\infty} f(x)\exp[-j2\pi xu]\mathrm{d}x. \tag{2.11}$$

Using this notation x is considered the spatial domain and u the spatial frequency domain. The original signal can be recovered by applying an inverse FT,

$$f(x) = \int_{-\infty}^{\infty} F(u)\exp[j2\pi xu]\mathrm{d}u. \tag{2.12}$$

Goodman [Goo05] gives the following existence conditions for the above transforms to work. (i) f must be absolutely integrable over the infinite x domain, (ii) f must have only a finite number of discontinuities and a finite number of maxima and minima in any finite rectangle, and (iii) f must have no infinite discontinuities. Bracewell [Bra78] has suggested that physical possibility is a sufficient condition for the existence of a transform, and as we are dealing with optical wavefronts we can use the FT with confidence.

The FT has a number of associated theorems [Bra78]:

1. Scaling theorem; If $f(x)$ has the FT $F(u)$, then $f(ax)$ has the FT $\frac{1}{|a|}F(\frac{u}{a})$.

2. Linearity theorem; If $f(x)$ has the FT $F(u)$ and $g(x)$ has the FT $G(u)$, then $f(x) + g(x)$ has the FT $F(u) + G(u)$

3. Shift theorem; If $f(x)$ has the FT $F(u)$, then $f(x-a)$ has the FT $\exp[-j2\pi as]$ $F(u)$. This means that if a function is shifted in position, no Fourier component is altered in amplitude, only the phase changes.

4. Convolution theorem; If $f(x)$ has the FT $F(u)$ and $g(x)$ has the FT $G(u)$, then the convolution of both functions $f(x)*g(x)$ has the FT $F(u)G(u)$. This result means that convolution of two functions is equivalent to multiplication of their transforms. In cases where convolution is computationally expensive, this becomes very useful.

5. Rayleigh's theorem; This states that the integral of the squared modulus of a function is equal to the integral of the squared modulus of its spectrum, $\int_{-\infty}^{\infty} |f(x)|^2\mathrm{d}x = \int_{-\infty}^{\infty} |F(u)|^2\mathrm{d}u$. This was first derived by Rayleigh [Ray89] and corresponds to Parseval's theorem for the Fourier series.

6. Autocorrelation theorem; If $f(x)$ has the FT $F(u)$, then its autocorrelation function $\int_{-\infty}^{\infty} f^*(s)f(s+x)\mathrm{d}s$ has the FT $|F(u)|^2$ Otherwise known as Wiener's theorem, the autocorrelation theorem can be summised as the autocorrelation function of a signal is the FT of that function's power spectrum [Wie49]. The squared term means that the autocorrelation function contains no information about the phase of the Fourier components, and therefore it is a non reversible operation.

Optical wavefronts in digital holography are usually represented in 2D, and therefore we give the 2D FT of the function $f(x, y)$ here,

$$\begin{aligned} F(u,v) &= \mathrm{FT}\{f(x,y)\} \\ &= \int_{-\infty}^{\infty}\int_{-\infty}^{\infty} f(x,y)\exp[-j2\pi(ux+vy)]\mathrm{d}x\mathrm{d}y, \end{aligned} \tag{2.13}$$

where FT is the Fourier transform operator, and u and v are spatial frequencies in the x and y directions, respectively. It follows that its inverse (using the inverse FT operator, FT^{-1}) is given by

$$\begin{aligned} f(x,y) &= \mathrm{FT}^{-1}\{F(x,y)\} \\ &= \int_{-\infty}^{\infty}\int_{-\infty}^{\infty} F(u,v)\exp[j2\pi(ux+vy)]\mathrm{d}u\mathrm{d}v. \end{aligned} \tag{2.14}$$

In this thesis, we often employ a discrete version of the FT called the discrete Fourier transform (DFT). The DFT can be thought of a string of equally spaced delta functions whose amplitude is modulated by the Fourier coefficients. The function $f_s(n_xT_x, n_yT_y)$ has the DFT,

$$F_s(m_uT_u, m_vT_v) = \mathrm{DFT}\{f_s(n_xT_x, n_yT_y)\}$$
$$= \frac{1}{N_xN_y} \sum_{n_x=\frac{N_x}{2}}^{\frac{N_x}{2}-1} \sum_{n_y=\frac{N_y}{2}}^{\frac{N_y}{2}-1} f_s(n_xT_x, n_yT_y) \exp\left[-j2\pi\left(\frac{n_xm_x}{N_x} + \frac{n_ym_y}{N_y}\right)\right], \tag{2.15}$$

where DFT is the discrete Fourier Transform operator; the sampling rate in the x and y dimensions are T_x and T_y respectively; N_x and N_y denote the number of samples in the x and y directions and (n_x, n_y) and (m_x, m_y) are integer indices in the space and spatial frequency domains respectively. The DFT is itself a sampled signal with sampling intervals of T_u and T_v in the u and v dimensions. It can be shown that $T_u = \frac{1}{N_xT_x}$ and $T_v = \frac{1}{N_yT_y}$ [Bra78]. The inverse DFT, using the inverse DFT^{-1} operator, is

$$f_s(n_xT_x, n_yT_y) = \mathrm{DFT}^{-1}\{F_s(m_uT_u, m_vT_v)\}$$
$$= \frac{1}{N_xN_y} \sum_{n_x=\frac{N_x}{2}}^{\frac{N_x}{2}-1} \sum_{n_y=\frac{N_y}{2}}^{\frac{N_y}{2}-1} F_s(m_uT_u, m_vT_v) \exp\left[j2\pi\left(\frac{n_xm_x}{N_x} + \frac{n_ym_y}{N_y}\right)\right]. \tag{2.16}$$

The DFT can be computed in $NlogN$ calculations using the FFT [CT65]. Without this optimisation it would require N^2 calculations and even modest sized data sets would run slowly on modern computers.

2.2.3 Numerical reconstruction of digital holograms

In this section we review the numerical reconstruction of a DH. We recall that $|h(x, y)|^2$ is the intensity recorded by the CCD. It is formed when the object wave $O(x, y)$, after propagation a distance d, interferes with the reference wave $R(x, y)$.

We also recall that the intensity term is made up of the sum of four terms, the object and reference DC terms and the real and virtual images. The image plane (reconstructed DH) is a distance d from the hologram (CCD) plane. It is at the image plane where the virtual image of the object will be reconstructed. This intensity is stored in a quantized and digitized form, and is first processed in order to isolate the virtual image term (in the case of PSI a series of intensities are processed to isolate the virtual image term). Numerical reconstruction produces a discretely sampled complex distribution $recon(m_{x'}T_{x'}, m_{y'}T_{y'})$ representing the reconstructed image, where $m_{x'}$ and $m_{y'}$ are integer indices and $T_{x'}$ and $T_{y'}$ are the sampling intervals in the reconstruction plane (x', y'). A number of different algorithms exist to numerically reconstruct a digital hologram, and obtain values for $recon(m_{x'}T_{x'}, m_{y'}T_{y'})$. These different algorithms have different values for $T_{x'}$ and $T_{y'}$. In this thesis we employ two methods; (i) the direct method and (ii) the spectral method.

The direct method is briefly derived as follows; We begin by applying the Fresnel Transform to the sampled signal $O(n_xT_x, n_yT_y)$ which denotes the sampled object term in the hologram (CCD) plane to obtain an equation for the continuous reconstructed image $recon(x', y')$. We assume that the object signal O has been separated from the other four terms in the intensity hologram either by spatial filtering suing the off axis method or by using the PSI approach. In the case where we have not separated the four terms we can still use the derivation below since the Fresnel Transform is linear and we can therefore consider the reconstruction to be given by the sum of the four terms individually Fresnel Transformed. The direct method is given by

$$recon(x', y') = \frac{\exp[ikd]}{j\lambda d}\exp\left[\frac{j\pi}{d\lambda}(x'^2 + y'^2)\right] \times \int\int O(n_x T_x, n_y T_y)\exp\left[\frac{j\pi}{d\lambda}(x^2 + y^2)\right] \times \exp\left[\frac{j2\pi}{\lambda d}(x' + y')\right] \mathrm{d}x\mathrm{d}y. \quad (2.17)$$

The constant $\frac{\exp[jkd]}{j\lambda d}$ does not depend on the spatial frequency coordinates or the object and so shall be omitted. We note that since the signal O exists only at discrete spatial coordinates, only these discrete values of x and y need to be considered in the above integral;

$$\begin{aligned} x &= n_x T_x \qquad & n_x &= -\frac{N_x}{2}, ..., \frac{N_x}{2} \\ y &= n_y T_y \qquad & n_y &= -\frac{N_y}{2}, ..., \frac{N_y}{2}, \end{aligned} \quad (2.18)$$

where T_x and T_y are the CCD pixel pitch in the x and y directions respectively, and where N_x and N_y are the number of pixels in the CCD camera in the x and y directions respectively. We can conclude that W_{CCDx} and W_{CCDy}, the widths of the camera in the x and y directions are given by $N_x T_x$ and $N_y T_y$ respectively.

If we sample the reconstructed complex image with sampling rate $T_{x'}$ and $T_{y'}$ in the reconstruction plane and interest ourselves only in the samples over the range of indices given by

$$\begin{aligned} x' &= m_{x'} T_{x'} \qquad & m_{x'} &= -\frac{N_x}{2}, ..., \frac{N_x}{2} - 1 \\ y' &= m_{y'} T_{y'} \qquad & m_{y'} &= -\frac{N_y}{2}, ..., \frac{N_y}{2} - 1, \end{aligned} \quad (2.19)$$

then Equation 2.17 reduces to

$$recon(m_{x'}T_{x'}, m_{y'}T_{y'}) = \exp\left[\frac{j\pi}{d\lambda}((m_{x'}T_{x'})^2 + (m_{y'}T_{y'})^2)\right] \times \sum_{n_x=\frac{N_x}{2}}^{\frac{N_x}{2}-1} \sum_{n_y=\frac{N_y}{2}}^{\frac{N_y}{2}-1} O(n_xT_x, n_xT_y)\exp\left[\frac{j\pi}{d\lambda}((n_xT_x)^2 + (n_yT_y)^2)\right] \times \exp\left[\frac{j2\pi}{\lambda d}(m_{x'}T_{x'}n_xT_x + m_{y'}T_{y'}n_yT_y)\right]. \quad (2.20)$$

If we choose the output sampling intervals to be defined as follows

$$T_{x'} = \frac{\lambda d}{N_xT_x} = \frac{\lambda d}{W_{CCDx}}$$
$$T_{y'} = \frac{\lambda d}{N_yT_y} = \frac{\lambda d}{W_{CCDy}}, \quad (2.21)$$

then Equation 2.20 above will reduce to the following;

$$recon(m_{x'}T_{x'}, m_{y'}T_{y'}) = \exp\left[\frac{j\pi}{d\lambda}((\lambda d m_{x'}T_x)^2 + (\lambda d m_{y'}T_y)^2)\right] \times \sum_{n_x=\frac{N_x}{2}}^{\frac{N_x}{2}-1} \sum_{n_y=\frac{N_y}{2}}^{\frac{N_y}{2}-1} O(n_xT_x, n_xT_y)\exp\left[\frac{j\pi}{d\lambda}((n_xT_x)^2 + (n_yT_y)^2)\right] \times \exp\left[j2\pi\frac{n_xm_{x'}}{N_x} + j2\pi\frac{n_ym_{y'}}{N_y}\right]. \quad (2.22)$$

which is in the form of a DFT as discussed in the previous section. This equation can be calculated using the very time efficient FFT algorithm. We note that the output window size in the x' and y' dimensions can be calculated to be

$$N_xT_{x'} = \frac{\lambda d}{T_x},$$
$$N_yT_{y'} = \frac{\lambda d}{T_y}. \quad (2.23)$$

It is clear that the output window size is directly proportional to the distance of propagation, d, and inversely proportional to the sampling interval T_x and T_y in both dimensions. We note that the direct method is discussed in more detail in Chapter 5.

The resultant field $recon(m_{x'}T_{x'}, m_{y'}T_{y'})$ is the numerical representation of a complex optical wavefield and from it the intensity image $Image(m_{x'}T_{x'}, m_{y'}T_{y'})$ and the phase $\phi(m_{x'}T_{x'}, m_{y'}T_{y'})$ can be determined as

$$Image(m_{x'}T_{x'}, m_{y'}T_{y'}) = |recon(m_{x'}T_{x'}, m_{y'}T_{y'})|^2, \tag{2.24}$$

and

$$\phi(m_{x'}T_{x'}, m_{y'}T_{y'}) = \tan^{-1}\left(\frac{\mathrm{Im}\{recon(m_{x'}T_{x'}, m_{y'}T_{y'})\}}{\mathrm{Re}\{recon(m_{x'}T_{x'}, m_{y'}T_{y'})\}}\right) \tag{2.25}$$

respectively, where Im{} represents the imaginary part and Re{} the real part of the resultant field $recon(m_{x'}T_{x'}, m_{y'}T_{y'})$. Schnars [Sch94] notes that a DH reconstruction has an advantage over optical reconstruction in that it has phase information. This is in contrast to the optical case where only intensity information is available (i.e., we can not capture the phase information, although it is present).

Another reconstruction method widely used throughout this thesis is known as the angular spectrum approach (spectral method) [MZK97, MGF+99]. This is based on the definition of the Fresnel transform as a chirp multiplication in the Fourier domain, i.e. $recon(x', y')$ is related to $O(x, y)$ as follows;

$$recon(x', y') = F^{-1}\{F\{O(x, y)\}\exp[j\pi\lambda d(u^2 + v^2)]\}. \tag{2.26}$$

The discrete version consists of taking the DFT of the sampled object signal, multiplying it by a sampled version of the quadratic phase version factor and then performing an inverse DFT on the result.

$$recon(m_{x'}T_{x'}, m_{y'}T_{y'}) = DFT^{-1}\left\{DFT\{O(n_xT_x, n_yT_y)\} \times \exp\left[A\right]\right\}. \qquad (2.27)$$

where $A = j\pi d\lambda\left(\left(\frac{m_x}{N_xT_x}\right)^2 + \left(\frac{m_y}{N_yT_y}\right)^2\right)$ and m_x, m_y, n_x, n_y, $m_{x'}$ and $m_{y'}$ all have the same range as previously defined. In the case of the spectral method the output sampling interval $T_{x'}$ and $T_{y'}$ are equal to the input sampling intervals, i.e. the pixel pitch, T_x and T_y. Using the spectral method for reconstruction, we transform the DH from the spatial domain into the spatial frequency domain where it is multiplied by the free space transfer function. We then use the inverse DFT to return to the spatial domain. The result is an image with the same resolution as the CCD, and thus equivalent pixel size. The direct method is often used to reconstruct far field diffraction patterns and the spectral method is usually preferable when reconstructing near field diffraction patterns, with some overlap between the two. In this thesis we have employed both methods.

As with conventional holography, a hologram encodes different views of a 3D object from a small range of angles [Goo05, Cau79]. In order to reconstruct a particular 2D perspective of the object, the appropriate windowed subset of pixels must be extracted from the hologram using the Fresnel approximation or convolution approaches described above. As the window explores the field, a different angle of view of the object is reconstructed. The range of viewing angles is determined by the ratio of the window size to the full CCD dimensions. For the experiments in Chapter 6, the Kodak Megaplus CCD has approximate dimensions of 18.5×18.5 mm and so a 1024×1024 pixel window has a maximum lateral shift of 9 mm across the face of the sensor. With an object positioned $d = 350$ mm from the camera, viewing angles in the range $\pm 0.74^\circ$ are permitted. Smaller windows will permit a larger range of viewing angles at the expense of image quality at each viewpoint. It is easily seen that if a 1024×1024 pixel window is extracted from 2048×2048 pixel DH and used to reconstruct the particular viewpoint, the

resolution of the resultant image is reduced by a quarter. We use this property of DHs to overcome the effects of partial occlusions in Chapter 6.

It now becomes important to introduce the topic of speckle in digital holography. Speckle is always present in holography, and by extension digital holography, as it uses coherent light. Speckle occurs when coherent light is diffused by an optically rough surface [Dai84]. It degrades the quality of the reconstructions and makes the accurate viewing of small details difficult. In the next sections we will discuss speckle as well as a way to reduce its effects. This will be used as a basis for some of the techniques developed in this thesis.

2.3 Speckle

A speckle pattern is observed when coherent light is either (a) reflected from an optically rough surface, or, (b) transmitted through a stationary diffuser. Most objects in the physical world are rough at the scale of the wavelength of light (an exception would be a mirror) and therefore speckle is the rule rather than the exception [Goo06]. The variations in height on the surface of diffuse reflecting objects, or the difference in thickness, absorption and changes in the index of refraction for the case of transparent diffuse objects are the causes of the speckle effect. Examples of diffuse reflecting objects include the rough surfaces of stones, wood, and unpolished metal, whereas a good example of a transparent diffuse object is ground glass [Fra79]. The reason that speckle is only apparent when using coherent light, and not incoherent light, is that in the case of incoherent light the number of fluctuations of the signal incident on the recording material (or the eye for that matter) changes so rapidly over the integration period of the detector. This means that the integral or average of these changes produces a smooth intensity image. However, for the case of coherent light, the signal does

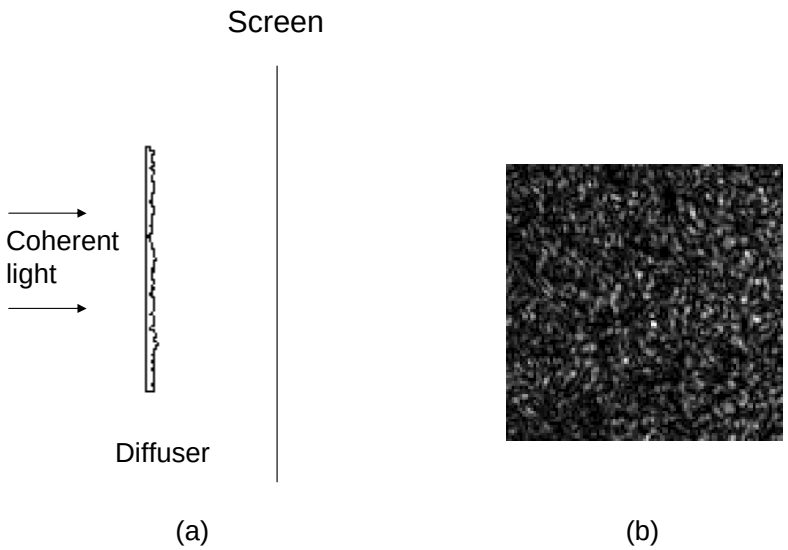

Figure 2.8: (a) a speckle pattern will be observed anywhere beyond the diffuser and (b) shows a zoomed in region of a reconstruction of a DH in which a speckle pattern is clearly seen.

not fluctuate nearly as much as in the case of incoherent light and thus a random intensity pattern is observed [Dai70].

Goodman gives a very clear intuitive explanation of the cause of speckle in his recent book [Goo06]. In it he explains that speckle occurs when a signal is composed of many independent components having both amplitude and phase. These components can have random lengths (amplitudes) and random directions (phase) or they can have known lengths and random directions. The random directions are generated by the roughness of the object or the diffuser in the system. The addition of these components results in either constructive or destructive interference at the observation plane and is known as a random walk. The square of the amplitude at the observation point is the intensity at that point. Let us now consider the production of a speckle pattern. In Figure. 2.8 (a) a coherent light source is incident on a diffuser. A screen placed anywhere beyond the diffuser will display a random intensity pattern, which is referred to as a speckle pattern.

Figure 2.8 (b) shows a zoomed in region of a reconstruction of a DH displaying such a random intensity pattern.

The contrast in a speckle pattern depends on the coherence properties of the incident light [Dai70]. As we reduce the coherence of the illumination (moving to partially coherent light), the contrast of the speckle pattern will decrease. This reduction will occur if there is a reduction in either spatial of temporal coherence. In Chapter 5 we have developed two separate speckle reduction techniques that take advantage of this fact. In the limiting case of incoherent light the contrast will reduce to zero and the speckle pattern will disappear. A speckle pattern can also be thought of as the superposition of the amplitudes of the diffraction patterns due to the different individual points on the diffuser, taking into account the phase changes introduced by the varying structure diffuser [Fra79]. This results in a large number of individual diffraction patterns that are superposed to produce a distribution that is independent of the diffuser used.

Now that we know the reasons for speckle and how speckle patterns are produced, let us turn our attention to the statistical properties of a speckle pattern.

2.3.1 First-order statistical properties of speckle

In this section, we investigate the first-order statistical properties of speckle patterns. By first-order we mean the statistical properties at a single point in space or time. The first complete analysis of the first and second order statistical properties of speckle was given by Laue [Lau14, Lau16]. Although the speckle effect was first observed as early as 1877 by Exner [Exn77], with the advent of the laser in the 1960's researchers thought that they were dealing with a new phenomenon. From this time on, interest in speckle, or sparkle as it was then known, was accelerated [Goo06]. Goodman has been credited with establishing the basic statistical properties of laser speckle in two early papers [Goo63, Goo65], but here we follow

his analysis in his most recent book [Goo06].

In order to discover the first-order statistical properties of speckle, we will first look at the statistics of the amplitude and phase of various kinds of random phasor sums. A random phasor sum can be defined as

$$A = B\exp[j\phi] = \frac{1}{\sqrt{N}} \sum_{n=1}^{N} a_n \exp[j\phi_n] \,, \tag{2.28}$$

where N represents the number of the phasor components in the random walk, A, a vector, represents the resultant complex phasor, B is the length (or magnitude) of A, ϕ represents the phase of A, a_n represents the magnitude of the nth component of the phasor sum, and ϕ_n is its phase. The scaling factor $\frac{1}{\sqrt{N}}$ is used to preserve finite second moments of the sum even as the number of component phasors approaches infinity [Goo06]. The real and imaginary parts of the resultant phasor are

$$R_e = Re\{A\} = \frac{1}{\sqrt{N}} \sum_{n=1}^{N} a_n \cos\,\phi_n \tag{2.29}$$

and

$$I_m = Im\{A\} = \frac{1}{\sqrt{N}} \sum_{n=1}^{N} a_n \sin\,\phi_n \tag{2.30}$$

respectively. We note that a number of assumptions are made about a_n and ϕ_n and these are discussed in Chapter 2 of [Goo06]. The mean, or expectation, of R_e is

$$E[R_e] = \frac{1}{\sqrt{N}} \sum_{n=1}^{N} E[a_n]E[\cos\,\phi_n] = 0 \tag{2.31}$$

and I_m is

$$E[I_m] = \frac{1}{\sqrt{N}} \sum_{n=1}^{N} E[a_n]E[\sin\,\phi_n] = 0. \tag{2.32}$$

This is obvious when we assume the statistics of ϕ are uniform, which implies that the averages of cos ϕ_n and sin ϕ_n are both zero. The variances of R_e and I_m are equal to the second moments as the means are zero. They are

$$\sigma_{R_e}^2 = E[{R_e}^2] = \frac{1}{N}\sum_{n=1}^{N}\sum_{m=1}^{N} E[a_n a_m]E[\cos\,\phi_n \cos\,\phi_n] \tag{2.33}$$

and

$$\sigma_{I_m}^2 = E[{I_m}^2] = \frac{1}{N}\sum_{n=1}^{N}\sum_{m=1}^{N} E[a_n a_m]E[\sin\,\phi_n \sin\,\phi_n] \tag{2.34}$$

respectively. It is clear that when $n \neq m$ both expressions go to zero. It is only the $n = m$ terms that remain. The variance for R_e becomes

$$\sigma_{R_e}^2 = \frac{1}{N}\sum_{n=1}^{N}\frac{E[a_n^2]}{2} \tag{2.35}$$

and similarly the variance for I becomes

$$\sigma_{I_m}^2 = \frac{1}{N}\sum_{n=1}^{N}\frac{E[a_n^2]}{2}, \tag{2.36}$$

and both derivations can be found in [Goo06].

Here we see that just like the means the variances of the real and imaginary parts of the resultant phasor are identical. It turns out the correlation between the real and imaginary parts is, like the mean, zero. We have

$$\Gamma_{R_e,I_m} = E[R_e I_m] = \frac{1}{N}\sum_{n=1}^{N} E[a_n^2]E[\cos^2\,\phi_n \sin^2\,\phi_n] = 0, \tag{2.37}$$

which indicates that there is no correlation between the real and imaginary parts of the resultant phasor. The central limit theorem can now be applied as the sum of N independent random variables is asymptotically Gaussian as $N \to \infty$ [Mid58]. The joint probability function of the real and imaginary parts of the resultant phasor becomes

$$P_{R_e,I_m}(R_e, I_m) = \frac{1}{2\pi\sigma^2} \exp\left\{-\frac{R^2 + I^2}{2\sigma^2}\right\}, \tag{2.38}$$

where $\sigma^2 = \sigma^2_{R_e} = \sigma^2_{I_m}$. The resultant complex phaser $\mathbf{A}$ is therefore said to be a circular complex Gaussian variate.

It is also important to consider the statistics of the amplitude A and phase θ of the resultant phasor. The probability density function of the amplitude and phase can be found using the rules of probability theory for the transformation of variables. We have

$$A = \sqrt{{R_e}^2 + {I_m}^2}, \qquad \theta = arctan\left\{\frac{I_m}{R_e}\right\} \tag{2.39}$$

and

$$R_e = A\cos\theta, \qquad I_m = A\sin\theta. \tag{2.40}$$

Now the joint probability function of A and θ is related to that of R_e and I_m through

$$P_{A,\theta}(A, \theta) = P_{R_e,I_m}(A\cos\theta, A\sin\theta) \parallel J \parallel, \tag{2.41}$$

where $\parallel J \parallel$ represents the Jacobian of the transformation between the two sets of variables,

$$\begin{aligned} \parallel J \parallel &= \left\| \begin{array}{cc} \frac{\partial R_e}{\partial A} & \frac{\partial R_e}{\partial \theta} \\ \frac{\partial I_m}{\partial A} & \frac{\partial I_m}{\partial \theta} \end{array} \right\| = \left\| \begin{array}{cc} \cos\theta & -A\sin\theta \\ \sin\theta & A\cos\theta \end{array} \right\| \\ &= A(\cos^2\theta + \sin^2\theta) \\ &= A. \end{aligned} \tag{2.42}$$

After multiplication, the joint probability function for the amplitude and the phase of the resultant phasor is

$$P_{A,\theta}(A,\theta) = \frac{A}{2\pi\sigma^2}\exp\left\{-\frac{A^2}{2\sigma^2}\right\}, \tag{2.43}$$

for $(A \geq 0)$ and $(-\pi \leq \theta < \pi)$, zero otherwise. Using the joint statistics of the A and θ we can now find the probability density function for the amplitude A to be

$$P_A(A) = \int_{-\pi}^{\pi} P_{A,\theta}(A,\theta)\mathrm{d}\theta = \frac{A}{\sigma^2}\exp\left\{-\frac{A^2}{2\sigma^2}\right\}, \tag{2.44}$$

for $(A \geq 0)$. This is the well known Rayleigh density function. In order to find the probability distribution of the phase we integrate Equation 2.43 with respect to the amplitude,

$$P_\theta(\theta) = \int_0^{\infty} \frac{A}{\sigma^2}\exp\left\{-\frac{A^2}{2\sigma^2}\right\}\mathrm{d}A = \frac{1}{2\pi} \tag{2.45}$$

for $(-\pi \leq \theta < \pi)$. Goodman [Goo06] points out that the joint density function for A and θ factors into a product of $P_A(A)$ and $P_\theta(\theta)$, which means that the amplitude A and the phase θ of the resultant phasor are statistically independent random variables. We will now use a rule of probability theory that will allow us to find the probability density function for the intensity of a speckle pattern. The rule states that if a random variable v is related to a random variable u through the transformation $v = f(u)$, then the probability density function $P_v(v)$ of v can be found from the probability density function $P_u(u)$ of u through [DR58]

$$P_v(v) = P_u(u)(f^{-1}(v))\left|\frac{\mathrm{d}u}{\mathrm{d}v}\right|. \tag{2.46}$$

We let $v = I$, the intensity, $u = A$, the amplitude, and

$$I = f(A) = A^2. \tag{2.47}$$

It follows that knowing the probability density function for $P_A(A)$ we can find the probability density function for $P_I(I)$ through

$$P_I(I) = P_A(\sqrt{I}) \left| \frac{\mathrm{d}A}{\mathrm{d}I} \right| = \frac{1}{2\sqrt{I}} P_A(\sqrt{(I)}). \tag{2.48}$$

This result now allows us to write an expression for the probability density function of the intensity as we already know the probability density function for the amplitude (see Equation 2.44). We apply the transformation law of Equation 2.48 and find that the intensity is distributed according to a negative exponential probability distribution [Goo00].

$$\begin{aligned} P_I(I) &= \frac{\sqrt{I}}{\sigma^2} \exp\left(-\frac{I}{2\sigma^2}\right) \cdot \frac{1}{2\sqrt{I}} \\ &= \frac{1}{2\sigma^2} \exp\left(-\frac{I}{2\sigma^2}\right) \end{aligned} \tag{2.49}$$

for $I \geq 0$. Speckle with a negative exponential distribution such as this is known as fully developed speckle and is the speckle present in our DHs. The second moment, variance, and standard deviation of the intensity are respectively given by

$$\begin{aligned} \overline{I^2} &= 2\bar{I}^2 \\ \sigma_I^2 &= \bar{I}^2 \\ \sigma_I &= \bar{I}, \end{aligned} \tag{2.50}$$

where $\bar{I}$ is the mean intensity. An important quantity that we use extensively in this thesis is called the speckle contrast, or speckle index, and it is defined as

$$\alpha = \frac{\sigma_I}{\bar{I}}. \tag{2.51}$$

Speckle index is a measure of how strong the fluctuations of intensity are in a speckle pattern compared with the average intensity. The speckle reduction techniques we have developed endeavor to reduce the speckle index. For the case of fully developed speckle, $\alpha = 1$. Therefore fluctuations of fully developed speckle

patterns are of the same order as the average intensity. This means that this type of noise can have a very corruptive effect on images of interest [Goo06].

In summary we conclude that the real and imaginary parts of the resultant phasor have a Gaussian distribution, the amplitude has a Rayleigh distribution, the phase of the resultant is uniformly distributed on the interval $(-\pi, \pi)$ and the intensity has a negative exponential probability distribution. We also note that the speckle index of a fully developed speckle pattern is approximately 1.

2.3.2 Second-order statistical properties of speckle

We now investigate a second-order statistical property of speckle, which concerns the statistics of two points and how this relates to the speckle size in a speckle pattern. The basis of this work will be used in Chapter 5, when it becomes essential to know the speckle size in reconstructions of DHs in order to optimize a speckle reduction method that we propose. Consider the system in Figure 2.9 in which a diffuse object is illuminated by a collimated plane wave (spatially and temporally coherent light). The speckle pattern is caused by the interference in the image plane between the waves from various points on the object. It is important to point out that if we were to change the object with another diffuse object, the size of the speckles at the observation plane would be of the same order. However, there would be no correlation between the two speckle patterns produced.

We now proceed to calculate the normalized autocovariance function of the intensity speckle pattern in the observation plane [see Figure 2.9] in order to estimate the speckle size. This function corresponds to the normalized autocorrelation function of the intensity and provides a good measurement of the average width of a speckle [Dai84, XMA00, PMC$^+$04, Goo06]. If $I(x_1, y_1)$ and $I(x_2, y_2)$ are two points in the observation plane [see Figure 2.9] the intensity autocorrelation function is defined by [PMC$^+$04, Goo06]

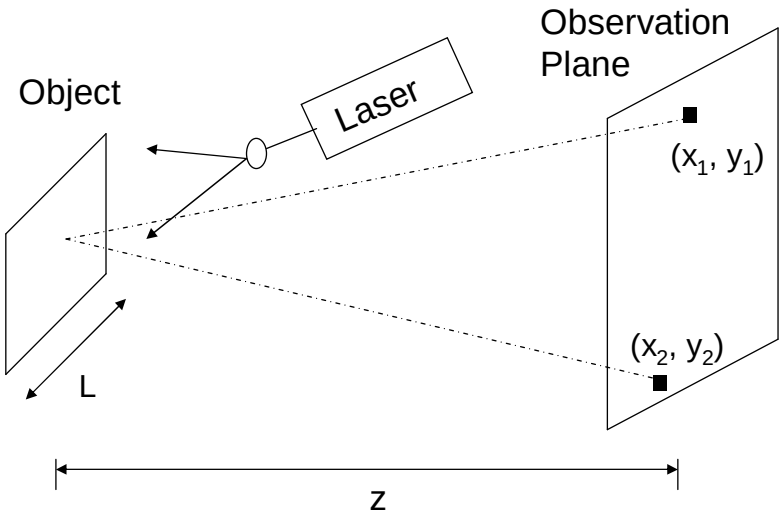

Figure 2.9: Free space geometry for speckle size.

$$R_I(\Delta x, \Delta y) = \langle I(x_1, y_1) I(x_2, y_2) \rangle \ , \tag{2.52}$$

where $\Delta x = x_1 - x_2$ and $\Delta y = y_1 - y_2$ and the $\langle\rangle$ is an average over an ensemble of rough surfaces. If we set $x_2 = 0$, $y_2 = 0$, $x_1 = x$ and $y_1 = x$ we can write

$$R_I(\Delta x, \Delta y) = R_I(x, y) \ . \tag{2.53}$$

Now we can write an expression for the normalized autocovariance function, $C_I(x, y)$,

$$C_I(x, y) = \frac{R_I(x, y) - \langle I(x, y) \rangle^2}{\langle I(x, y)^2 \rangle - \langle I(x, y) \rangle^2} \ . \tag{2.54}$$

Using the Wiener-Khintchine theorem this becomes

$$C_I(x, y) = \frac{\mathrm{FT}^{-1}[|\mathrm{FT}[I(x, y)]|^2] - \langle I(x_1, y_1) \rangle^2}{\langle I(x_1, y_1)^2 \rangle - \langle I(x_1, y_1) \rangle^2}, \tag{2.55}$$

where we have used the fact that autocorrelation of the intensity is given by the inverse Fourier transform of the power spectral density. The width of $C_I(x, y)$ provides us with a good measure of the average width of a speckle [PMC+04,

Kre05, Goo06]. This allows us to measure the average width of speckle in our DH reconstructions.

2.3.3 Speckle in digital holography

We will now investigate speckle in Fresnel DHs. The objects we capture are rough on the scale of the wavelength used and therefore the speckle that arrives on the face of the CCD [see Figure. 2.6] is fully developed as described in the previous sections. Its intensity has a negative exponential probability distribution and it has a speckle index of approximately 1. This of course assumes that the resultant wavefront on the CCD has been sufficiently sampled.

We can accurately calculate the speckle size in a given reconstruction plane using the results found in Section 2.3.2. However, when using the direct method of reconstruction [see Equation 2.17], care must be taken to account for the increased size of the pixels at the reconstruction plane when calculating the speckle size. In the reconstructed field, the pixel size is a function of the distance d and is given by $\Delta\xi_d = \frac{\lambda d}{W_{CCDx}}$ and $\Delta\eta_d = \frac{\lambda d}{W_{CCDy}}$, where $W_{CCDx} = N_x\Delta\xi$ and $W_{CCDy} = N_y\Delta\eta$ (with N_x and N_y being the number of pixels in the x and y directions respectively, and $\Delta\xi$ and $\Delta\eta$ the size of the individual pixels at the sensor in the x and y directions respectively) are the lateral dimensions of the CCD [see Figure. 2.10] [PTZ96]. For the simple case when $W_{CCDx} = W_{CCDy}$, the transversal (perpendicular to the direction of travel) size of the speckle S_x and S_y increases linearly with the distance d from the CCD and is given by

$$S_x = \frac{\lambda d}{W_{CCDx}}, \tag{2.56}$$

in the x direction (y direction is trivial and therefore omitted here) and the speckle size in the direction of propagation increases with the square of the distance [PTZ96],

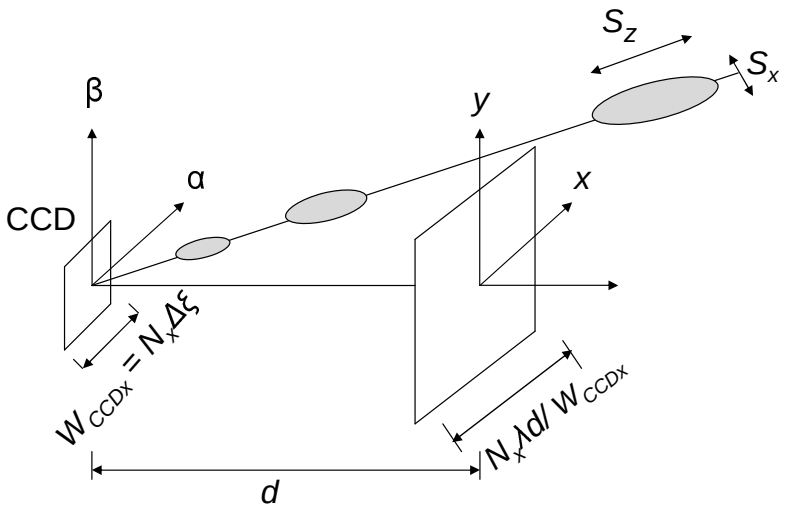

Figure 2.10: Illustration of the changing size of the speckle in a digitally reconstructed wavefront. [Adapted from Pedrini *et al.* [PTZ96]]

$$S_z = \lambda(\frac{d}{W_{CCDx}})^2. \tag{2.57}$$

Looking at Figure. 2.10 we see that speckles increase in size as a function of distance. We also observe that they are larger in the z direction than the (x, y) plane. The minimum speckle size that corresponds to the highest spatial frequency of the pattern and is equal to the resolution limit of the system. In the propagation direction the minimum size is equals the focal depth of the system [Gab70, Yam03].

Pedrini *et al.* [PTZ96] have shown that when an aperture is placed in the hologram plane, effectively reducing the size of the wavefront that is propagated, the speckle size in the reconstruction plane increases. We have confirmed this and the results are shown in Figure 2.11. In Figure. 2.11 (a) we show a zoomed in 100×100 pixel region of a DH (in this case the stormtrooper DH, but any DH will suffice), which was reconstructed using the direct method. The speckle pattern is clearly observable. We have calculated the autocorrelation of this region using the autocorrelation theorem [see Section 2.2.2.4]. This is achieved by subtracting the mean of the region under consideration from each pixel and then applying the

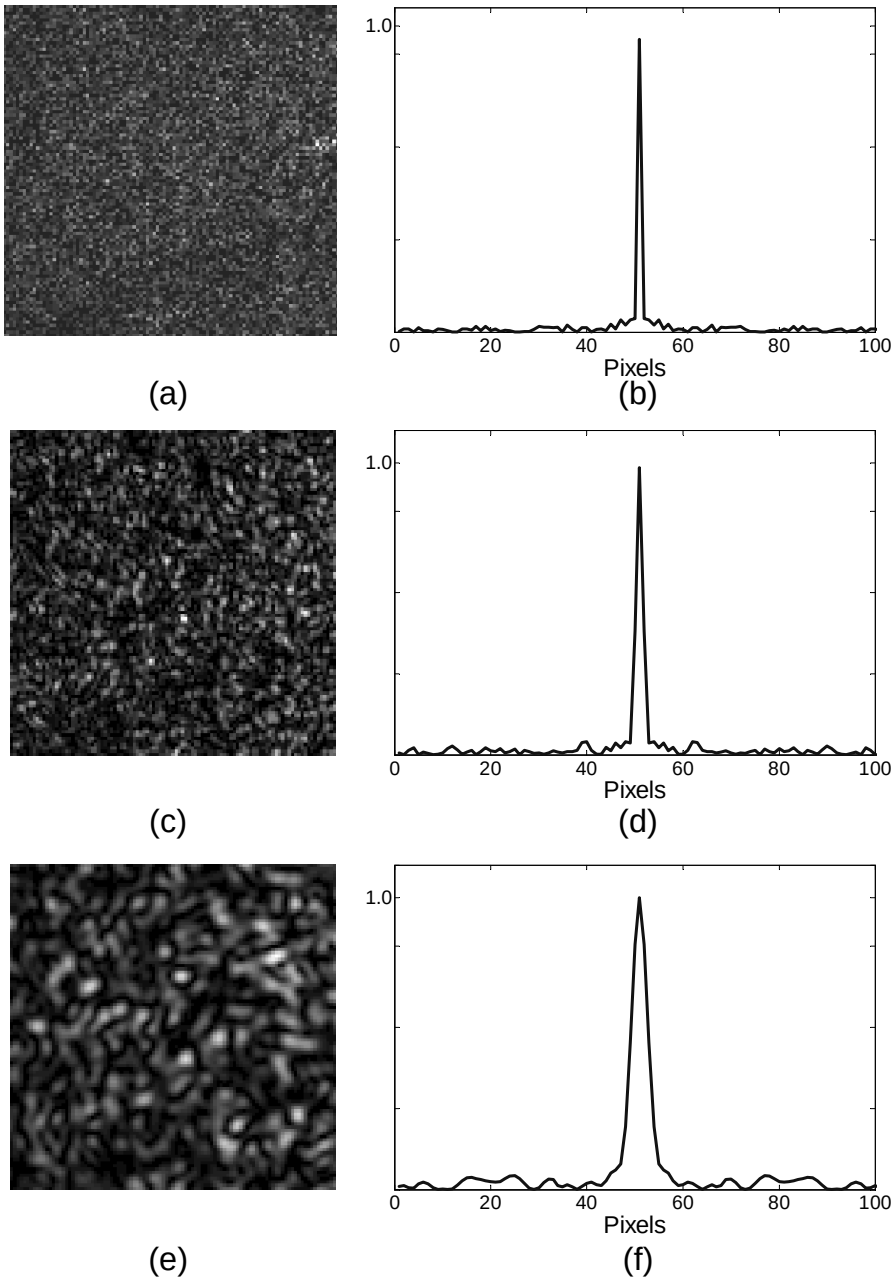

Figure 2.11: Zoomed in area (100×100 pixels) on a DH reconstruction in which (a) 1024×1024, (c) 512×512 and (e) 256×256 sized apertures have been placed at the hologram plane. The corresponding autocorrelation peak for these, which is used to measure average speckle size, is shown in (b),(d) and (f).

FFT algorithm to the result. This is then multiplied by its own complex conjugate and then the inverse FFT algorithm is applied [see Equation refeq:SpeckleSize:4]. Finally, the magnitude of this field is then taken and its center row is displayed in Figure 2.11 (b). The width at 0.5 of this peak gives the average size of the speckle at the reconstruction plane. The width is approximately 1.5 pixels, and the pixels size of our CCD are 9μm. However, we must take into account the new pixel size given by $\Delta\xi_d = \frac{\lambda d}{W_{CCDx}}$. For this experiment $d = 291$mm, $\lambda = 6.33$nm and $W_{CCDx} = 1024 \times 9\mu$m. This results in an actual average speckle size of $1.5 \times 19.9\mu\text{m} = 29.8\mu$m at the reconstruction plane. It is interesting to observe the speckle size increase as the aperture is reduced to first 512×512 pixels [see Figure 2.11 (c) and Figure 2.11 (d)] and then to 256×256 pixels [see Figure 2.11 (e) and Figure 2.11 (f)].

2.3.4 Addition of independent speckle patterns

In this section we analyse the effect of adding together speckle patterns in an effort to reduce their corruptive influence. The result found here is used extensively in Section A) of this thesis, especially in Chapters 3 and 5 as a basis for reducing the speckle index of reconstructions of DHs. The following analysis is given by Goodman [Goo06].

The total intensity for the sum of N independent speckle patterns is

$$I_s = \sum_{n=1}^{N} I_n \ , \tag{2.58}$$

where each I_n has a mean value of $\overline{I_n}$. The mean of the total intensity is therefore

$$\overline{I_s} = \sum_{n=1}^{N} \overline{I_n} \ . \tag{2.59}$$

The second moment of the total intensity is

$$\begin{aligned}\overline{I_s^2} &= \sum_{n=1}^{N}\sum_{m=1}^{N}\overline{I_n I_m} \\ &= \sum_{n=1}^{N}\overline{I_n^2}+\sum_{n=1}^{N}\sum_{m=1,m\neq n}^{N}\overline{I_n I_m}\,, \end{aligned} \tag{2.60}$$

where the independence of $\overline{I_n}$ and $\overline{I_m}$ for $m \neq n$ has been used. We now use the fact that the individual intensity patterns are speckle patterns, and therefore they obey negative exponential probability distributions, for which $\overline{I_n^2} = 2\overline{I_n}^2$. The expression for $\overline{I_s^2}$ becomes

$$\begin{aligned}\overline{I_s^2} &= 2\sum_{n=1}^{N}\overline{I_n}^2+\sum_{n=1}^{N}\sum_{m=1,m\neq n}^{N}\overline{I_n I_m} \\ &= \sum_{n=1}^{N}\overline{I_n}^2+\left(\sum_{n=1}^{N}\overline{I_n}\right)^2 \\ &= \sum_{n=1}^{N}\overline{I_n}^2+\overline{I_s}^2\,. \end{aligned} \tag{2.61}$$

It follows that the variance of the total intensity is

$$\sigma_s^2 = \sum_{n=1}^{N}\overline{I_n}^2, \tag{2.62}$$

and that the speckle index of the total intensity is

$$\alpha = \frac{\sigma_s}{\overline{I_s}} = \frac{\sqrt{\sum_{n=1}^{N}\overline{I_n}^2}}{\sum_{n=1}^{N}\overline{I_n}}\,. \tag{2.63}$$

For the special case of components with equal mean intensities ($\overline{I_n} = I_0,$ all n), which is the case for the developed technique, the result reduces to

$$\alpha = \frac{1}{\sqrt{N}}. \tag{2.64}$$

Therefore the speckle index falls in proportion to $\frac{1}{\sqrt{N}}$ as the number of independent speckle patterns N increases. This result assumes that the N individual speckle patterns are statistically independent. This is an extremely important result for us and it will be used continually through this thesis as a means of reducing the effects of speckle on reconstructions of DHs. We wish to emphasise here that the addition of speckle patterns on a complex amplitude basis does not reduce the speckle index. Each of the complex fields contributed by one of the speckle patterns can be thought of as a random walk in the complex plane. The addition of N random walks simply results in a random walk with more steps [Goo76]. We now introduce the Wigner distribution function, which we use to analyse the contributions presented in Part B of this thesis.

2.4 Wigner distribution function

In this section, we review the properties of the WDF in preparation for Section B) of this thesis. We use the WDF to analyse overcoming partial occlusion effects in reconstructions of DHs [see Chapter 6]. In this case an occlusion is something in the foreground of a scene that occludes one view of a background object of interest in the scene. We have also analysed using occlusions to reduce the effects of the twin image in reconstructions of DHs [see Chapter 7]. Here, the occlusion is a binary mask used to remove the energy of the twin image at the twin image reconstruction plane.

The WDF of a complex optical amplitude distribution provides a graphical means of simultaneously viewing a signal's spatial and spatial frequency distributions, and is particularly useful for visualizing localized signals [Wig32, Bas97,

Loh93, OZK01]. $\Psi\{f(x)\}(x,u)$, which represents the WDF of a signal $f(x)$, is defined in terms of its spatial distribution in the following way

$$\Psi\{f(x)\}(x,u) = \int_{-\infty}^{\infty} f\left(x+\frac{\xi}{2}\right) f^*\left(x-\frac{\xi}{2}\right) \exp[-j2\pi u\xi]\mathrm{d}\xi \tag{2.65}$$

where u represents spatial frequency, * denotes complex conjugation and Ψ denotes the WDF operator. Often a plan view outline of the signal's energy is used for illustration. Such a Wigner chart is shown in Figure. 2.12. The real valued WDF has double the number of dimensions, i.e. a complex 1D signal has a two-dimensional WDF while 2D signals have 4D WDFs.

The WDF is entirely reversible with the exception of a constant phase factor,

$$f(x)f^*(0) = \int_{-\infty}^{\infty} \psi\{f(x)\}(x/2,u)\exp[j2\pi ux]du \tag{2.66a}$$

$$|f^*(0)|^2 = \int \psi\{f(x)\}(0,u)du. \tag{2.66b}$$

An exactly equivalent definition of the WDF can be given using the FT of $f(x)$,

$$\psi\{f(x)\}(x,u) = \int_{-\infty}^{\infty} \mathrm{FT}\{f(x)\}\left(u+\frac{\xi}{2}\right)\mathrm{FT}^*\{f(x)\}\left(u-\frac{\xi}{2}\right)\exp[j2\pi u\xi]d\xi. \tag{2.67}$$

The WDF has many interesting properties [LDM+96].

1. The WDF is real valued,

$$\psi\{f(x)\}(x,u) = \psi^*\{f(x)\}(x,u). \tag{2.68}$$

2. Shifting a signal in x correspondingly shifts its WDF as

$$\psi\{f(x-\xi)\}(x,u) = \psi\{f(x)\}(x-\xi,u). \tag{2.69}$$

3. Parseval's Theorem,

$$\int \psi\{f(x)\}(x,u)dx = |f(x)|^2 = \int \psi\{f(x)\}(x,u)du = |\mathrm{FT}\{f(x)\}(u)|^2. \tag{2.70}$$

4. The WDF has a convolution property,

$$\psi\left\{\int_{-\infty}^{\infty} f(\xi)g(x-\xi)d\xi\right\}(x,u) = \int \psi\{f(x)\}(x-x^{'},u) \tag{2.71a}$$

$$\times\psi\{g(x)\}(x^{'},u)\mathrm{d}x^{'}, \tag{2.71b}$$

$$\psi\{f(x)g(x)\}(x,u) = \int_{-\infty}^{\infty} \psi\{f(x)\}(x,u-u^{'}) \tag{2.71c}$$

$$\times\psi\{g(x)\}(x,u^{'})\mathrm{d}u^{'}. \tag{2.71d}$$

5. The WDF is bilinear; When two signals are added, the WDF of the sum is given by the sum of the individual WDFs plus an additional cross term,

$$\begin{aligned}\psi\{f(x)+g(x)\}(x,u) = \quad & \psi\{f(x)\}(x,u)+\psi\{g(x)\}(x,u) \\ & + \int_{-\infty}^{\infty} 2\Re\left[f\left(x-\tfrac{\xi}{2}\right)g^{*}\left(x+\tfrac{\xi}{2}\right)\right]\exp[-j2\pi u\xi]\mathrm{d}\xi.\end{aligned} \tag{2.72}$$

6. The projection of the WDF normal to the u-axis (i.e. integrating along u) gives the spatial intensity distribution of our signal and the projection normal to the x-axis gives the frequency spectrum,

$$|f(x)|^2 = \int_{-\infty}^{\infty} \psi\{f(x)\}(x,u)\mathrm{d}u, \quad |F(u)|^2 = \int_{-\infty}^{\infty} \psi\{f(x)\}(x,u)\mathrm{d}x. \tag{2.73}$$

We note that it is possible for the energy of two signals that have been added together to overlap in the projection along x and not to overlap in the projection along u or vice versa. If the signals do not overlap in the projection that we are interested in, we may omit the cross-term in Equation 2.72 in all of the Wigner analyses.

In physical reality, we may only ever view the spatial intensity distribution of a signal, shown on the left of Equation 2.73 above. We may rotate, x shear and u shear the WDF of the signal using a variety of optical systems [Bas97] and then view the new spatial intensity distribution. For example, a FT [Goo05] rotates the WDF ($x \rightarrow u, u \rightarrow -x$) and then we integrate along the new u. This is equivalent to the right hand side of Equation 2.73. We note that if two signals are added and the resultant WDF, see Equation 2.72 above, is integrated along u, we obtain the fundamental equation of holography,

$$\begin{aligned} |f(x)+g(x)|^2 &= \int_{-\infty}^{\infty} \psi\{f(x)+g(x))\}(x,u)du \\ &= |f(x)|^2 + |g(x)|^2 + 2\Re[f(x)g^{'}(x)]. \end{aligned} \tag{2.74}$$

7. The Fresnel transform (FST) has the following effect on the WDF of a signal, $\psi\{F_{\lambda d}\{f(x)\}(x^{'})\}(x^{'},u^{'}) = \psi\{f(x)\}(x+\lambda du,u)$. The effect of applying a FST to the signal can be expressed in terms of a matrix operating on the phase space coordinate vector.

$$\begin{bmatrix} x^{'} \\ u^{'} \end{bmatrix} = \begin{bmatrix} 1 & \lambda d \\ 0 & 1 \end{bmatrix} \begin{bmatrix} x \\ u \end{bmatrix}. \tag{2.75}$$

This matrix is known as the ABCD matrix or the ray-transfer matrix. The

FST causes a shearing of a signal's WDF along the x direction as shown in Figure. 2.12 (b) and (c) where we have shown the resultant Wigner chart for the original object signal after propagation of 0.1m and 0.2m respectively.

8. Signal localisation; If the FT of a function is finite in extent then the spatial distribution must have an infinite extent. This implies that our bandlimited signal must be sampled over all of space since it exists over its entire extent. However, in many practical problems it is assumed with a very large degree of accuracy that a signal is bounded within some finite region in both the spatial and spatial frequency domains. The spatial extent, W, and the frequency extent, B, are defined such that,

$$f(x) \approx 0 \qquad |x| > W/2 \tag{2.76a}$$

$$\mathrm{FT}\{f(x)\}(u) \approx 0 \qquad |u| > B/2 \tag{2.76b}$$

and therefore, the signal energy is negligible outside these spatial and spatial frequency regions.

9. Sampling; In Figure. 2.12 (a) we show the WDF of a localised signal $f(x)$ in which the signal's energy lies within a rectangular area. The signal $f(x)$ is completely determined if it is sampled equidistantly in x with sample space T such that the Nyquist criteria is satisfied. Therefore the number of samples, N, required to completely describe $f(x)$ is $N = \frac{W}{T} \geq WB$. Clearly, for the most efficient uniform sampling $T = 1/B$ and $N = WB$, the space-bandwidth product of the signal [OZK01, LDM$^+$96]. In general signals may have an irregular shaped WDF such as the case shown in Figure. 2.12 (b). This shape is the result of applying a Fresnel Transform to the signal with regular WDF shown in Figure. 2.12 (a). Such a signal could be fully described

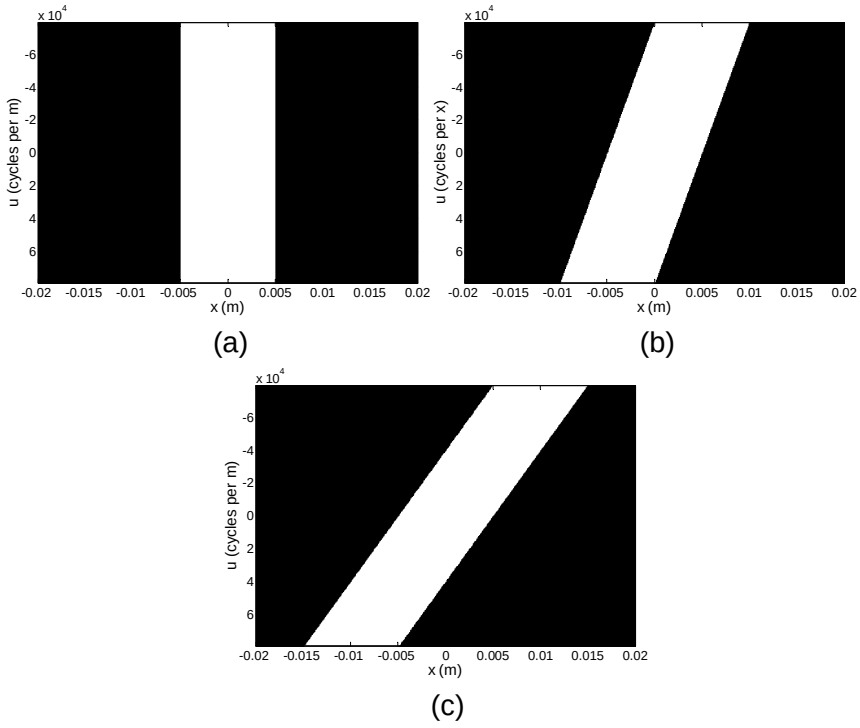

Figure 2.12: Wigner chart of a propagating signal showing (a) the wavefield immediately after the object, (b) the Wigner chart after propagation a distance 0.1m (c) the Wigner chart after propagation of a distance 0.2m. Object size for this example is 0.01m and the wavelength of the light is 633nm.

with a number of samples less than the space-bandwidth product [LDM+96], but this would require non-uniform sampling in the space domain. We note that the WDF of a sampled signal has been investigated in detail by Stern and Javidi [SJ04c, SJ04b].

Ideal sampling is accomplished by multiplying the signal by a train of Dirac delta functions or a comb function defined by

$$\delta_T(x) = \sum_{n=-\infty}^{\infty} \delta(x - nT), \tag{2.77}$$

where T is the sampling interval and $\delta(x)$ represents the Dirac delta function. This is equivalent to convolving the signals WDF, $\psi\{f(x)\}(x,u)$, with $\psi\{\delta(x)\}(x,u)$, the WDF of the comb function. We note that

$$\psi\{\delta_T(x)\}(x,u) = \frac{1}{2T}\sum_n\sum_q (-1)^{qn}\delta\left(x - \frac{nT}{2}\right)\delta\left(x - \frac{q}{2T}\right). \tag{2.78}$$

10. Ray tracing, the WDF and the corner coordinate matrix (CCM); The WDF offers a unified interpretation of wave optics, geometrical optics and quantum optics. Ray tracing is a widely used application of geometrical optics and involves following the paths of light rays as they pass through an optical system. For a specific ray with known position (x) and direction (spatial frequency u) we may map any change in position and direction due to an optical element, including free space, using the ray transfer matrix for that optical element. We have shown above, in the case of free space propagation in the paraxial approximation, that the ray transfer matrix may also be used to map changes in the WDF of a signal. This has lead to the development of the CCM [HS05a], a 2D array containing a series of $x-u$ coordinates that define the boundary of a localized signal in phase space. For example, for the signal in Figure. 2.12 (a) we will have a CCM

$$\mathbf{S} = \begin{bmatrix} -W/2 & W/2 & W/2 & -W/2 \\ B/2 & B/2 & -B/2 & -B/2 \end{bmatrix}. \tag{2.79}$$

After Fresnel propagation a distance d_1, the signals WDF is shown in Figure 2.12 (b), and after a further propagation to distance d_2, the signals WDF is shown in Figure 2.12 (c). The new corner coordinates are given by the following,

$$\mathbf{S}' = \begin{bmatrix} 1 & \lambda d \\ 0 & 1 \end{bmatrix} \mathbf{S}. \tag{2.80}$$

These ideas have lead to an optimisation of all FST algorithms [HS05a]. We note that Equation 2.79 and 2.80 may easily be extended for an arbitrary number of coordinates [HS05b].

11. The WDF of a rectangular function; We define the rect function as,

$$eq : wdf_r ec_d ef \quad \begin{array}{ll} \text{rect}\left(\frac{W}{2}\right) & = 1 \qquad \forall |x| < \frac{w}{2} \\ & = 0 \qquad \forall |x| > \frac{w}{2}. \end{array} \tag{2.81}$$

The WDF of rect(x/w) has been investigated in the context of diffraction [RMOM03] from a thin slit and is given by

$$\psi\left\{\text{rect}\left(\tfrac{x}{w}\right)\right\}(x,u) \quad = \quad \tfrac{\sin(u[-2|x|+w])}{u}, \qquad |x| < \tfrac{w}{2}, \tag{2.82}$$

which is a type of sinc function in u for the range of x values allowed. The scale of this sinc function, $p(x,w)$ is a function of both the width of the rect function and the value of x. For values of x that are much less than w the sinc function will be very narrow. As x approaches the boundary the sinc functions broadens in u. This effect is due to diffraction at the boundaries. In this thesis we will assume that $w \gg \lambda$ and that we may therefore ignore the effect of diffraction at the edges. In this case we may write

$$\psi\left\{\text{rect}\left(\tfrac{x}{w}\right)\right\}(x,u) = \delta(u), \qquad |x| < \tfrac{w}{2}. \tag{2.83}$$

We note that this approximation is in conflict with the existence conditions of the WDF [Bas97], but it will simplify the analysis given in Chapter 6 considerably while at the same time retaining a high degree of accuracy.

We use these properties to investigate occlusions in Chapters 6 and 7.

2.5 Summary

In this chapter, we have discussed the first holograms created by Gabor and subsequently discovered some of their properties. We investigated capturing DHs using in-line, off-axis and PSI setups, and given some conditions that should be met in order to sufficiently capture a DH. We also reviewed two numerical algorithms that are used to reconstruct DHs. Part A of this thesis investigates ways to reduce the corruptive effect of speckle on reconstructions of DHs. In order to address this problem a sound foundation in the theory of speckle is needed. Therefore, we have discussed the first-order statistical properties of speckle. This enabled us to discover that the speckle inherent in our DHs is fully developed speckle with a speckle index of 1. We reviewed the second-order statistical properties of speckle and determined the average size of speckles in an intensity pattern. We have used this result to determine the size of the speckle in our DHs in Chapter 5. We also reviewed the propagation of a speckle pattern when reconstructing a DH using the discrete Fresnel transform. We saw that the size of the speckle changes as a function of the distance of propagation and the size of the recording CCD. We also saw that the addition of independent speckle patterns could reduce the speckle index by $\frac{1}{\sqrt{N}}$, where N is the number of patterns. This is an important result and is used in Chapters 3, 5. Part B uses the WDF to analysis both partial occlusions [see Chapter 6] and the twin image problem [see Chapter 7] in digital holography. Therefore, we have reviewed the WDF and looked at some of its properties. In the next chapter, we will look at the first contribution this thesis makes to the field of digital holography, when we introduce a new technique, called the DFF, which reduces the speckle content in reconstructions of DHs.

Chapter 3

Discrete Fourier filter for speckle reduction

3.1 Introduction

In this chapter we introduce a new DSP technique for the reduction of speckle in reconstructions of DHs. Dainty and Welford [DW71] optically reduced speckle in image plane hologram reconstructions by rotating a circular aperture in the Fourier plane of the image. Hariharan and Hegedus [HH74] extended the method by superimposing the exposures from band passed filtered images of a diffuse object. By interpreting our DH as the complex wavefield at a particular intermediate plane in the coherent imaging speckle removal system, we can apply the discrete analog of this process to DHs. Furthermore, this DSP technique, which we call discrete Fourier filtering (DFF), offers a number of considerable advantages both to its optical counterpart and to other existing DSP methods. These advantages are discussed after the analysis is presented. The work in this chapter is based on an earlier publication by the author [MHM+07].

The optical setup in Figure. 3.1(a) is that used in Refs. [DW71, HH74]. The

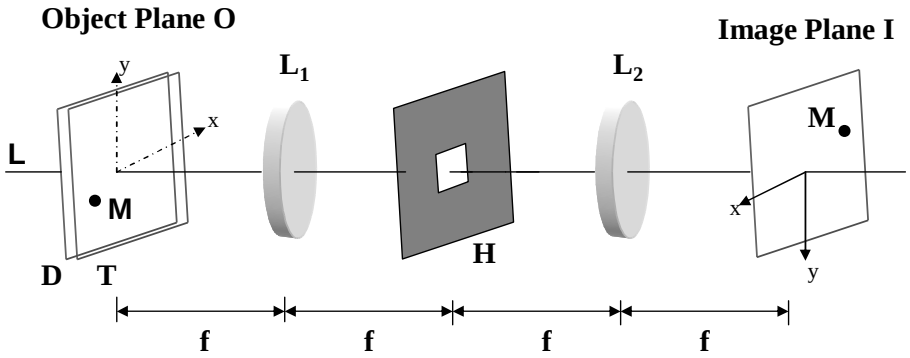

Figure 3.1: Optical setup for coherent imaging.

wavefront emanating from the diffuse object propagates through the 4f system in which an aperture is placed in the Fourier plane. The aperture is moved between each of several exposures, and the intensities in the image plane are integrated over the exposures. This leads to a speckle-reduced image plane signal. The effect of capturing the DH introduces an extra aperture between the object plane and the first lens, namely the recording CCD sensor. We assume for simplicity that the effect of this is only to bandlimit the object wavefield. We then simulate the rest of the setup in the paraxial regime to a high degree of accuracy.

3.2 Analysis

The following analysis is based on previous work done by Lowenthal and Arsenault [LA70] and Hariharan and Hegedus [HH74], and for convenience follows their notation. A plane, $f(\mathbf{r})$, immediately in front of a diffuse non-uniform object, which is illuminated by a coherent beam can be expressed as the product of two terms

$$f(\mathbf{r}) = t(\mathbf{r})d(\mathbf{r}), \tag{3.1}$$

where $d(\mathbf{r})$ is a uniform diffuser, $t(\mathbf{r})$ is a transparency that modulates the diffuser,

and $\mathbf{r}$ is a vector (x, y) in the plane in front of the object. The image plane amplitude $g(\mathbf{r})$ is defined as $g(\mathbf{r}) = f(\mathbf{r}) \star h(\mathbf{r})$, where $h(\mathbf{r})$ is the amplitude impulse response of the imaging system and $\star$ denotes a convolution. It will be shown that the average power spectrum of the image intensity is related to the autocorrelation of the image intensity [Pap65]. We will also show that the power spectrum of the image intensity can be spilt into two terms. The first being the power spectrum of the image itself and the second being the power spectrum of the speckle, which we want to reduce. The autocorrelation of $f(\mathbf{r})$ can be written [LA70]

$$R_{ff}(\mathbf{r}_1, \mathbf{r}_2) = \langle f(\mathbf{r}_1) f^*(\mathbf{r}_2) \rangle = \langle t(\mathbf{r}_1) d(\mathbf{r}_1) t^*(\mathbf{r}_2) d^*(\mathbf{r}_2) \rangle \tag{3.2}$$

where $\langle f(\mathbf{r}_1) f^*(\mathbf{r}_2) \rangle$ is an expectation, which is defined as $\langle \mathrm{X} \rangle = \int_{-\infty}^{\infty} x P_{\mathrm{x}}(x) \mathrm{d}x$, where $P_{\mathrm{x}}(x)$ is the probability density function for X having a value of x. Since t is not a random function, it can be extracted from the expectation, as in

$$R_{ff}(\mathbf{r}_1, \mathbf{r}_2) = t(\mathbf{r}_1) t^*(\mathbf{r}_2) \langle d(\mathbf{r}_1) d^*(\mathbf{r}_2) \rangle = t(\mathbf{r}_1) t^*(\mathbf{r}_2) R_{dd}(\mathbf{r}_1, \mathbf{r}_2). \tag{3.3}$$

$d(\mathbf{r})$ is considered to be stationary and Gaussian with zero mean and its autocorrelation may be approximated by a delta function

$$R_{dd}(\mathbf{r}_1, \mathbf{r}_2) = \langle d(\mathbf{r}_1) d^*(\mathbf{r}_2) \rangle = \delta(\mathbf{r}_1 - \mathbf{r}_2). \tag{3.4}$$

If j exposures are made with a shift of the aperture between them, the resultant intensity $I(\mathbf{r})$ at any point in the image is the sum of the intensities at this point due to the individual j exposures,

$$I(\mathbf{r}) = \sum_j I_j(\mathbf{r}), \tag{3.5}$$

where $I_j(\mathbf{r}) = |g_j(\mathbf{r})|^2$, where $g_j(\mathbf{r}) = f(\mathbf{r}) \star h_j(\mathbf{r})$, and where $h_j(\mathbf{r})$ is the impulse response of the system for the jth position of the aperture in the Fourier plane.

Due to the linearity of convolution, the autocorrelation $R_{II}(\mathbf{r}_1, \mathbf{r}_2)$ of the image intensity can be written as

$$\begin{aligned} R_{II}(\mathbf{r}_1, \mathbf{r}_2) &= \sum_{m,n} R_{I_m I_n}(\mathbf{r}_1, \mathbf{r}_2) \\ &= \sum_{m,n} \langle |g_m(\mathbf{r}_1)|^2 |g_n(\mathbf{r}_2)|^2 \rangle \end{aligned} \tag{3.6}$$

where the summation is taken over all values of m and n, and each term is the result of an expectation.

For two complex, Gaussian variables X_1 and X_2, with zero mean, the expectation $\langle |X_1|^2 |X_2|^2 \rangle$ is given by a theorem of Reed [Ree62] to be

$$\langle |X_1|^2 |X_2|^2 \rangle = \langle |X_1|^2 \rangle \langle |X_2|^2 \rangle + |\langle X_1 X_2^* \rangle|^2. \tag{3.7}$$

As we are dealing with expectations, the autocorrelation of the image intensity can be re-written as

$$\begin{aligned} R_{II}(\mathbf{r}_1, \mathbf{r}_2) &= \sum_{m,n} \langle |g_m(\mathbf{r}_1)|^2 \rangle \langle |g_n(\mathbf{r}_2)|^2 \rangle \\ &\quad + \sum_{m,n} |\langle g_m^*(\mathbf{r}_1) g_n(\mathbf{r}_2) \rangle|^2 \\ &= \sum_{m,n} \langle I_m(\mathbf{r}_1) \rangle \langle I_n(\mathbf{r}_2) \rangle \\ &\quad + \sum_{m,n} |R_{g_m g_n}(\mathbf{r}_1, \mathbf{r}_2)|^2. \end{aligned} \tag{3.8}$$

The average power spectrum of the image intensity is $\Omega(\mathbf{u}, \mathbf{u})$, where $\Omega(\mathbf{u}_1, \mathbf{u}_2)$ is the double FT of the autocorrelation of the image intensity [LA70] [see Appendix A] given by,

$$\begin{aligned} \Omega(\mathbf{u}_1, \mathbf{u}_2) &= F\{R_{II}(\mathbf{r}_1, \mathbf{r}_2)\} \\ &= F\{\sum_{m,n} \langle I_m(\mathbf{r}_1) \rangle \langle I_n(\mathbf{r}_2) \rangle\} \\ &\quad + F\{\sum_{m,n} |R_{g_m g_n}(\mathbf{r}_1, \mathbf{r}_2)|^2\} \end{aligned} \tag{3.9}$$

where F is the double FT operator, defined by Lowenthal and Arsenault [LA70] as $F\{R_{II}(\mathbf{r}_1,\mathbf{r}_2)\} = \int_{-\infty}^{\infty}\int_{-\infty}^{\infty} R_{II}(\mathbf{r}_1,\mathbf{r}_2)e^{-i2\pi(\mathbf{u}_1\cdot\mathbf{r}_1-\mathbf{u}_2\cdot\mathbf{r}_2)}\mathrm{d}\mathbf{r}_1\mathrm{d}\mathbf{r}_2$.

The first term in Equation 3.9 is the power spectrum that would be given by a spatially incoherent object having the same intensity as the object under consideration. As the average intensity in the image plane is the same as that which would be given by an incoherent object, this term is considered to be the power spectrum of the image. Therefore we conclude that the other term represents the power spectrum of the speckle [LA70]. We label the first term, the power spectrum of the image, as $\Omega_1(\mathbf{u}_1,\mathbf{u}_2)$ and the second term, the power spectrum of the speckle, as $\Omega_2(\mathbf{u}_1,\mathbf{u}_2)$.

It has also been shown by Lowenthal and Arsenault [LA70] that the average intensity $\langle I(\mathbf{r})\rangle$ in the image of a coherently illuminated diffuse object is given by the relation $\langle I(\mathbf{r})\rangle = |t(\mathbf{r})|^2 \star |h(\mathbf{r})|^2$. This result means that $\Omega_1(\mathbf{u}_1,\mathbf{u}_2)$ can be given by

$$\begin{aligned}\Omega_1(\mathbf{u}_1,\mathbf{u}_2) &= \sum_{m,n}[T(\mathbf{u}_1)\star T^*(-\mathbf{u}_1)][H_m(\mathbf{u}_1)\star H_m^*(-\mathbf{u}_1)] \\ &\quad \star[T(-\mathbf{u}_2)\star T^*(\mathbf{u}_2)][H_n(-\mathbf{u}_2)\star H_n^*(\mathbf{u}_2)]\end{aligned} \tag{3.10}$$

where $T(\mathbf{u})$ is the FT of $t(\mathbf{r})$, and $H(\mathbf{u})$ is the FT of $h(\mathbf{r})$. We now evaluate the other term $\Omega_2(\mathbf{u}_1,\mathbf{u}_2)$ which gives the power spectrum of the speckle [HH74]. For two linear systems with input $f(\mathbf{r})$, impulse responses $h_m(\mathbf{r})$, $h_n(\mathbf{r})$ and outputs $g_m(\mathbf{r})$, $g_n(\mathbf{r})$ respectively, the cross-correlation of the outputs can be written in terms of the cross-correlation of the inputs. Using this result and the right hand side of Equation 3.9, we have [LA70]

$$\Omega_2(\mathbf{u}_1,\mathbf{u}_2) = \sum_{m,n} F\{|R_{ff}(\mathbf{r}_1,\mathbf{r}_2)\star_{\mathbf{r}_1} h_m(\mathbf{r}_1)\star_{\mathbf{r}2} h_n^*(\mathbf{r}_2)|^2\} \tag{3.11}$$

where the subscripts $\mathbf{r}_1$ and $\mathbf{r}_2$ mean that the convolution operation is carried out on the variable $\mathbf{r}_1$ and $\mathbf{r}_2$ respectively, the other variable being treated as a

constant, and $R_{ff}(\mathbf{r}_1, \mathbf{r}_2)$ is the autocorrelation function of the object amplitude $f(\mathbf{r})$.

Now, $\Omega_2(\mathbf{u}_1, \mathbf{u}_2)$, which is the power spectrum of the speckle, can be written as,

$$\begin{aligned} \Omega_2(\mathbf{u}_1, \mathbf{u}_2) &= \sum_{m,n} [\Gamma(\mathbf{u}_1, \mathbf{u}_2) H_m(\mathbf{u}_1) H_n^*(-\mathbf{u}_2)] \\ &\quad \star [\Gamma^*(-\mathbf{u}_1, -\mathbf{u}_2) H_m^*(-\mathbf{u}_1) H_n(\mathbf{u}_2)] \end{aligned} \tag{3.12}$$

where $\Gamma(\mathbf{u}_1, \mathbf{u}_2)$ is the double FT of $R_{ff}(\mathbf{r}_1, \mathbf{r}_2)$.

Finally, if Equation 3.12 is rewritten with $\mathbf{u}$ replacing $\mathbf{u}_1$ and $\mathbf{u}_2$ to obtain the average power spectrum of the speckle, $\Gamma(\mathbf{u}_1, \mathbf{u}_2)$ becomes the average power spectrum of the object amplitude, which has been shown to be a constant and is equal to the total power in the signal [LA70]. The power spectrum of the speckle is rewritten as

$$\Omega_2(\mathbf{u}, \mathbf{u}) = |R_{tt}(0)|^2 \sum_{m,n} [H_m(\mathbf{u}) H_n^*(\mathbf{u})] \star [H_m^*(-\mathbf{u}) H_n(-\mathbf{u})]. \tag{3.13}$$

From this equation Lowenthal and Arsenault [LA70] have shown that the manner in which the speckle spatial frequencies are distributed does not depend on the signal $t(\mathbf{r})$, but only on the coherent transfer function of the system. Using this result and modeling our system's aperture as a 2D rect function, Equation 3.13 becomes

$$\begin{aligned} \Omega_2(\mathbf{u}, \mathbf{u}) &= |R_{tt}(0)|^2 \\ &\quad \sum_{m_x, m_y, n_x, n_y} \left[\text{rect}\left(\tfrac{u_x - m_x \Delta u_x}{w_x}, \tfrac{u_y - m_y \Delta u_y}{w_y} \right) \text{rect}\left(\tfrac{u_x - n_x \Delta u_x}{w_x}, \tfrac{u_y - n_y \Delta u_y}{w_y} \right) \right] \\ &\quad \star \left[\text{rect}\left(\tfrac{u_x - m_x \Delta u_x}{-w_x}, \tfrac{u_y - m_y \Delta u_y}{-w_y} \right) \text{rect}\left(\tfrac{u_x - n_x \Delta u_x}{-w_x}, \tfrac{u_y - n_y \Delta u_y}{-w_y} \right) \right] \end{aligned} \tag{3.14}$$

where $\mathbf{u} = u_x \hat{x} + u_y \hat{y}$, and Δu_x, Δu_y is the displacement of the aperture between two exposures in the x and y directions respectively. w_x is the width of the rect

function in the x direction and w_y is the width of the rect function in the y direction. This reduces to

$$\Omega_2(\mathbf{u},\mathbf{u}) = |R_{tt}(0)|^2 \sum_{m_x,m_y,n_x,n_y} [1 - \frac{|u_x - \Delta u_x(m+n)|}{w_x - \Delta u_x|m-n|}][1 - \frac{|u_y - \Delta u_y(m+n)|}{w_y - \Delta u_y|m-n|}]. \tag{3.15}$$

If $w_x - \Delta u_x|m-n| \leq 0$ or $w_y - \Delta u_y|m-n| \leq 0$ then the entire expression goes to 0. In the limiting case of $\Delta u_x = 0$ and $\Delta u_y = 0$, the power spectrum of the speckle is at its maximum, being the same as the power spectrum of the speckle given by a single aperture. When $\Delta u_x \geq w_x$ and $\Delta u_y \geq w_y$, so that the two positions of the aperture do not overlap, the power spectrum of the speckle is reduced to half the value of the limiting case [HH74]. However, the power spectrum of the image does not follow this trend. It follows that for n exposures the power spectrum of the speckle is $\frac{1}{n}$ times that obtained using a single exposure. For maximum efficiency we have set $\Delta u_x = w_x$ and $\Delta u_y = w_y$. Since we are limited by the finite extent of the FT of our DH, we are limited in the number of independent exposures. It should be noted that the smaller the exposure the greater the loss in resolution in the reconstructed image. However, using basic Fourier theory one may deduce that the bandwidth of the reconstruction intensity is twice the extent of the rect function. For a more thorough analysis of the optical system, please refer to Lowenthal and Arsenault [LA70] and Hariharan and Hegedus [HH74].

Figure 3.2(b) illustrates how our simulations were performed. In order to relate the digital system back to an optical one, Figure. 3.2(a) shows the optical system. Here the object plane is the diffuse stormtrooper object, and the position of the captured hologram is also shown. The first step is to simulate the propagation from the hologram plane to the Fourier plane, from here on referred to as the Fourier domain to distinguish it from the optical case, as shown in Figure. 3.2(b). This can be achieved efficiently in one step using a single discrete linear canonical transform

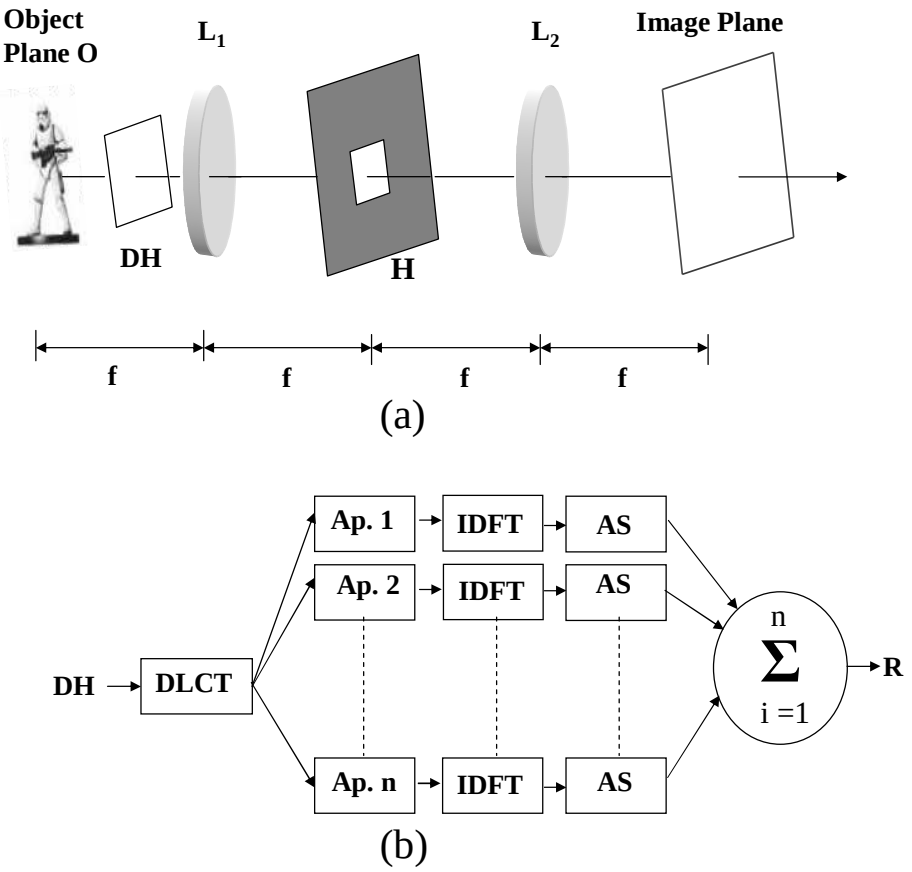

Figure 3.2: Schematic diagram of how an optical setup, (a), relates to our discrete setup,(b). DLCT: discrete linear canonical tranform, IDFT: inverse discrete Fourier transform, Ap.: Aperture, and AS: absolute value of the output squared.

(DLCT). A number of methods to efficiently implement this transform are outlined by Hennelly and Sheridan [HS05a]. Of course it could also be achieved by Fresnel transforming to a reconstruction plane, and then using a DFT to propagate to the Fourier domain. The Fourier domain data are then filtered and then inverse discrete Fourier transformed to the image plane where their intensities are stored. This is repeated n times and the resulting n intensities are summed. It is noted that a computational speed up can be attained using our knowledge of basic Fourier theory. We know that the bandwidth of the reconstruction intensity is twice the

extent of the rect function [see Equation 2.82 in Section 2.4]. This means that we only need to pad each of the Fourier filters with zeros up to twice the size of the aperture used. This ensures that as the aperture is reduced in size we achieve a speed up in terms of the computational speed of the algorithm.

3.3 Metrics

In this section, we introduce a number of metrics to evaluate the effectiveness of our technique. These metrics will be used in subsequent speckle reduction chapters. The first metric we use measures the speckle content of speckle patterns and is called the speckle index [Lim81, Goo06]. We use the speckle index to evaluate the reduction in speckle after application of a speckle reduction technique. It is calculated as the ratio of standard deviation to the mean in a homogenous area of a speckle image (in this thesis a reconstructed DH)

$$\alpha = \frac{\sigma(I(m,n))}{\mu(I(m,n))} \tag{3.16}$$

where $\sigma(I(m,n))$ denotes the standard deviation of the homogenous area $I(m,n)$, $\mu(I(m,n))$ denotes the mean of this area, and m and n are numbers of pixels. The closer the speckle index is to 0 the better the speckle reduction achieved.

We also introduce a metric to calculate the effect on resolution of our technique. The resolution chart [see Figure. 3.3(a)] we use is modeled on the U.S. Air Force (USAF) 1951 three-bar resolving power test chart. It is 2048 $\times$ 2048 pixels in size (matching the resolution of our DHs). The smallest details on the chart [see Figure. 3.3(b)] are just a single pixel in width. We define the resolution level as

$$R = 1/X, \tag{3.17}$$

where X is the width of the smallest bars on the resolution chart that can be

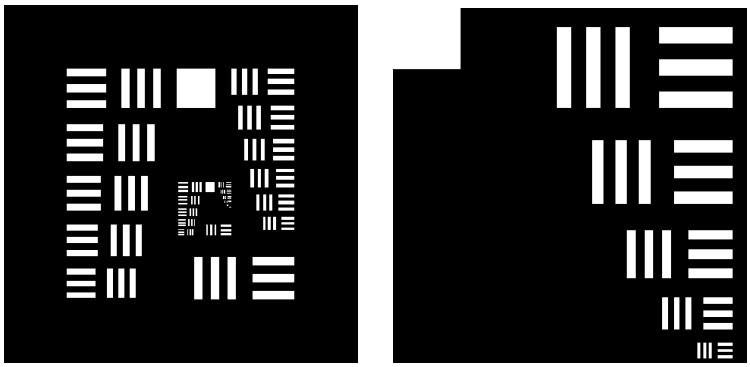

Figure 3.3: (a) USAF 1951 3-bar resolving power test chart (2048 × 2048 pixels in size), (b) zoomed in 115 × 115 pixel region of the chart showing the smallest details on the chart.

resolved. A speckle reduction technique with given parameters (i.e., neighborhood size for mean and median filters) is said to cause no loss in resolution if the smallest three bars (both vertical and horizontal) can be resolved. The technique is thus classified as being at resolution level $\frac{1}{1}$. It follows that if the smallest three bars cannot be resolved, but the next smallest can, then the technique for given parameters is classified as being at resolution level $\frac{1}{2}$.

Finally, we introduce a metric to quantify the effect of the method on the underlying image data in terms of edge preservation. To this effect an edge preservation metric introduced by Sattar *et al.* [SFSL97] is used;

$$\beta = \frac{\Gamma(\Delta s - \overline{\Delta s}, \widehat{\Delta s} - \overline{\widehat{\Delta s}})}{\sqrt{\Gamma(\Delta s - \overline{\Delta s}, \Delta s - \overline{\Delta s}) \times \Gamma(\widehat{\Delta s} - \overline{\widehat{\Delta s}}, \widehat{\Delta s} - \overline{\widehat{\Delta s}})}}, \tag{3.18}$$

where $\Delta s(i,j)$ is a high pass filtered version of $s(i,j)$ (the original test pattern without added speckle) obtained using the standard approximation of the Laplacian operator. Therefore, β is a normalised cross correlation between two Laplacian images. $\overline{\Delta s(i,j)}$ is the mean of $\Delta s(i,j)$, $\widehat{s(i,j)}$ denotes the speckle reduced image,

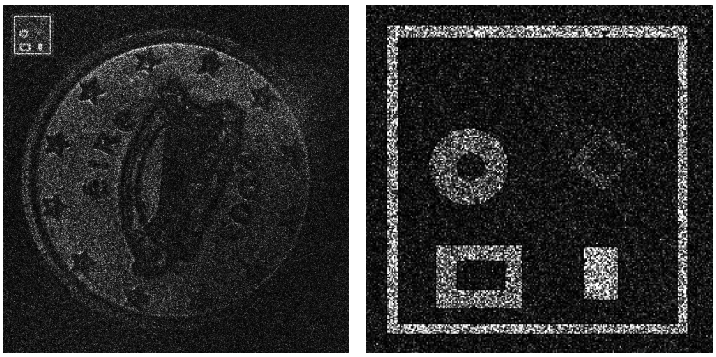

Figure 3.4: (a) A DH reconstruction of a coin object with added test image and resolution strips, and (b) zoomed in section (a) showing the test image.

and

$$\Gamma(s_1, s_2) = \sum_{(i,j)} s_1(i,j) \times s_2(i,j). \tag{3.19}$$

The range of possible values that β can take on is between -1 and 1. Squared correlation describes the proportion of variance in common between the two variables and allows us to transform a correlation into a percentage (by multiplying the resulting value by 100) [Rum76]. Therefore, we use the square of β and the closer this is to 1 the better the edge preservation.

We have inserted the test image into a real reconstructed DH [see the top left of Figure 3.4(a)]. The test image is a binary image containing curves and straight lines in various orientations and is 256×256 pixels in size [see Figure 3.4 (b)]. As speckle is approximately additive in the natural logarithm, we add the test image to the natural logarithm of the reconstructed DH wavefield and this is then exponentiated. Care is taken to ensure that the maximum grayscale value of the added test image after the exponentiation operation is still less than the maximum value of the DH reconstruction. Having ground truth data (in the form of the test

Figure 3.5: The original reconstruction is shown in (a), and the result of applying the DFF technique is shown in (b).

pattern without added speckle) allows us to quantitively evaluate the DFF.

3.4 Results and discussion

Figure 3.5 shows the results of the DFF technique applied to a DH of a stormtrooper object. In Figure 3.5(a), the original reconstruction is shown. It is 2048×2048 pixels in size, and has a speckle index of approximately 1.0. The application of the DFF to a reconstruction of this DH is shown in Figure 3.5(b). In this example we have set the width of the aperture, $h(r)$, to 256 pixels in size (resulting in 64 apertures used at the Fourier domain). This results in a reduced speckle index of 0.2 and a resolution level of $\frac{1}{4}$. It is clear that the technique has succeeded in reducing the speckle content in this reconstruction.

The effectiveness of the DFF is now quantified is terms of speckle index, resolution and edge preservation. The resolution chart is 2048×2048 pixels in size (matching the resolution of our DHs) and is modeled on the USAF 1951 3-bar resolving power test chart. Figure 3.6 (a) shows a zoomed in section (115×115

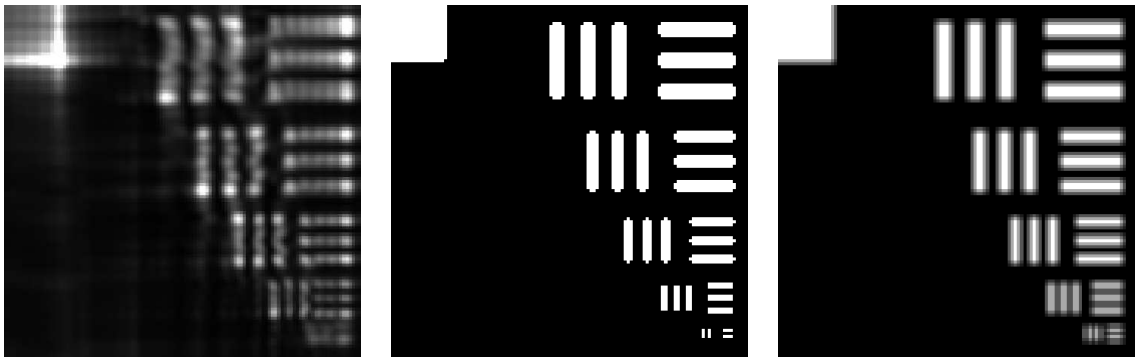

Figure 3.6: Zoomed in results of resolution chart after application of the (a) the DFF technique with aperture width of 512, (b) median filter with a neighborhood size of 3×3, and (c) mean filter with a neighborhood size of 3×3.

pixels in size) of the resolution chart after application of the DFF technique with aperture size of 512×512. Figures 3.6 (b) and (c) show the same zoomed in section after application of the mean and median filters respectively (with a neighborhood region sizes of 3×3). For the parameters given, all of these techniques have a resolution level of $\frac{1}{2}$. In this manner we quantitatively measure the effectiveness of the DFF against the mean and median filters.

A graph of the results of speckle index verses resolution loss for the DFF technique, and the median and mean filters, is shown in Figure 3.7. The techniques have been applied to a reconstruction of a DH of the stormtrooper figure. It shows that the speckle index can be reduced by nearly half with no loss in resolution using the DFF technique. In comparison, using either the median or mean filters to achieve a similar reduction in speckle index will result in a drop to a resolution level of $\frac{1}{2}$. At each resolution level the discrete Fourier filter consistently has a lower speckle index than either the median or mean filters. It is important to note that any level of speckle reduction can be achieved by a given technique, but

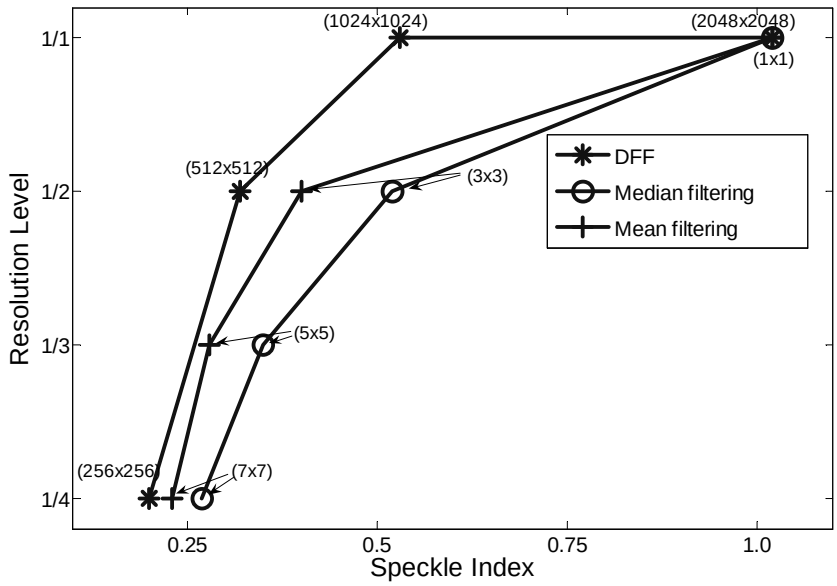

Figure 3.7: Graph showing the speckle index against resolution results of DFF technique (points are labeled with the size of the aperture width used), and the median and the mean filters (points are labeled with the neighborhood sizes used).

this needs to be checked against the destructive effect the technique has on image details.

We have also investigated the effect the DFF has on edges by using the edge preservation metric introduced above. Figure 3.8 shows how the DFF performed against the median and the mean filters. It has performed better than both the mean and median filters in terms of edge preservation. For example, applying the DFF with a 256×256 pixel aperture to the coin DH with added test pattern results in a speckle index of $\alpha = 0.1851$ and an edge preservation of $\beta^2 = 0.0312$. In contrast, a mean filter with neighbourhood region size of 9×9 results in a speckle index of $\alpha = 0.1805$ and an edge preservation of $\beta^2 = 0.0059$, and a median filter with neighbourhood region size 9×9 results in a speckle index of of $\alpha = 0.2120$ and an edge preservation of $\beta^2 = 0.0011$. In the given example all methods were parameterized to give approximately the same speckle index and it

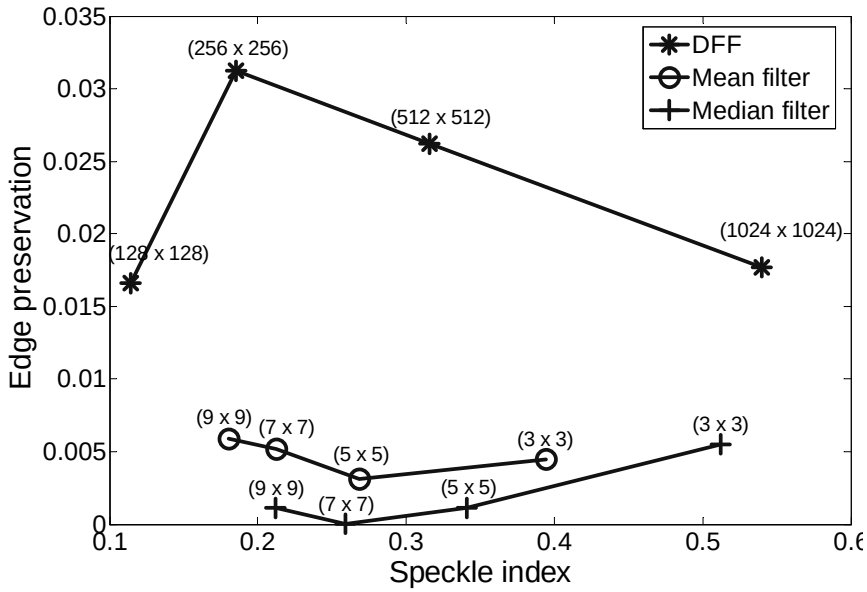

Figure 3.8: Graph showing the speckle index against edge preservation results of DFF technique (points are labeled with the size of the aperture width used), and the median and the mean filters (points are labeled with the neighborhood sizes used).

is clear that DFF has performed best [see Figure 3.8]. Please refer to Appendix B for tables detailing the speckle index, resolution and edge preservation results presented here. We have also investigated the use of overlapping filters, but found that they produce no benefit in terms of a reduced speckle content [see Appendix C].

We now look at the reconstructions of DHs after application of the DFF, the mean filter and median filter. For comparison the original reconstruction without any speckle reduction technique applied is once again shown in Figure 3.9 (a). Next to it, the DFF technique is shown in Figure 3.9 (b). The aperture has been set to 512×512 pixels. This results in a resolution level of $\frac{1}{2}$. Figures. 3.9(c) and (d) show the median and mean filter respectively (with neighbourhood regions set at 3×3), also with resolution level of $\frac{1}{2}$. The DFF has successfully reduced

the speckle to a lower level than either the median or mean filters for the same resolution level. Figure 3.10 shows the same reconstructions, but this time we have zoomed into a 100×100 pixel area on the chest of the reconstruction of the stormtrooper DH. This is a homogenous area of the DH and it is clear to see the destructive effect the speckle causes by looking at Figure 3.10 (a). In an area which should be smooth, we see that both bright and dark speckles are present. The DFF has reduced the speckle content to 0.31 and thus significantly smoothed this region [see Figure3.10 (b)]. At the same resolution level of $\frac{1}{2}$ the median filter has only reduced the speckle index to 0.51 and the mean filter to 0.39 [see Figs. 3.10 (c) and (d) respectively].

The DFF is now tested on three DHs captured using three different architectures. All of the DHs are corrupted by fully developed speckle patterns and therefore have a speckle index of approximately 1.0. The first DH is of a die object and like the stormtrooper DH was captured using PSI [see Chap. 2.2.2.3]. A reconstruction from it is shown in Figure 3.11(a). After application of the DFF with aperture size 256×256 pixels the speckle index is reduced to 0.17 and the resultant image is shown in Figure 3.11 (b). The second DH is of a 2 cent euro coin and was captured using the in-line setup described in Chap. 2.2.2.1 [see Figure 3.11 (c)]. After application of the DFF with aperture size 256×256 pixels the speckle index is also reduced to 0.17. The resultant image is shown in Figure 3.11 (d). This illustrates the generic nature of the DFF. It can be applied to two different DH architectures and reduce the speckle in them in a consistent manner. By filtering in the FT domain and using non-overlapping filters we ensure that the speckle patterns that are added together are statistically independent. The results we have gotten are close to the theoretical result we would expect to get when $N = 64$ (the number of apertures when the size is set to 256×256) and the speckle index is calculated as $\alpha = \frac{1}{N}$, which results in a speckle index of 0.125.

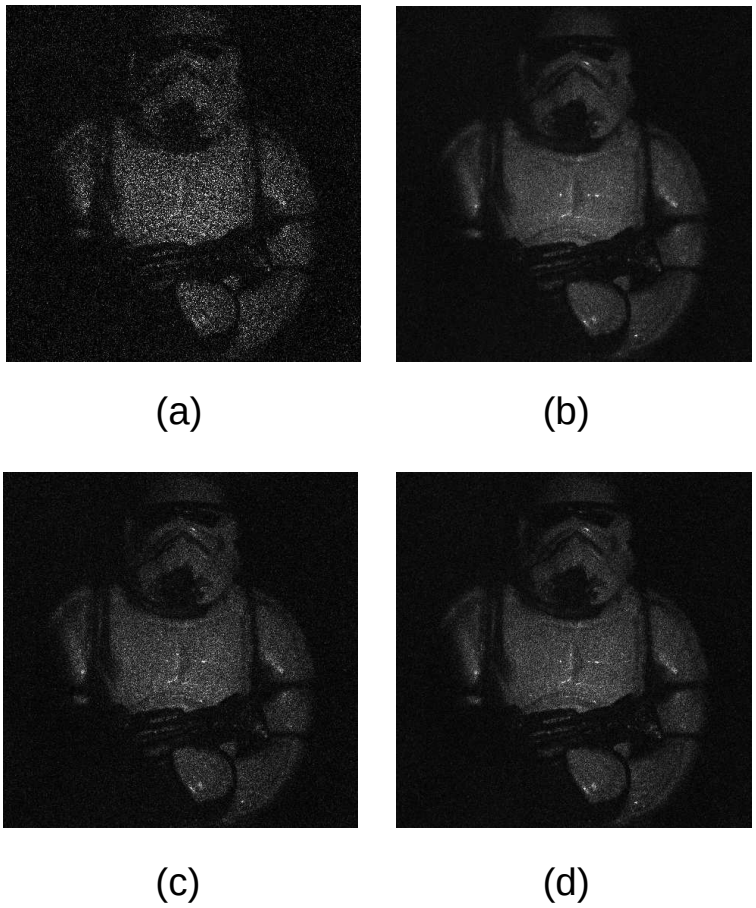

Figure 3.9: Results of applying different speckle reduction techniques to a DH of a stormtrooper figure. (a) The original reconstruction, (b) the DFF with an aperture size of 512×512, (c) median filter with neighbourhood region size of 3×3 and (d) mean filter also with neighbourhood region size of 3×3.

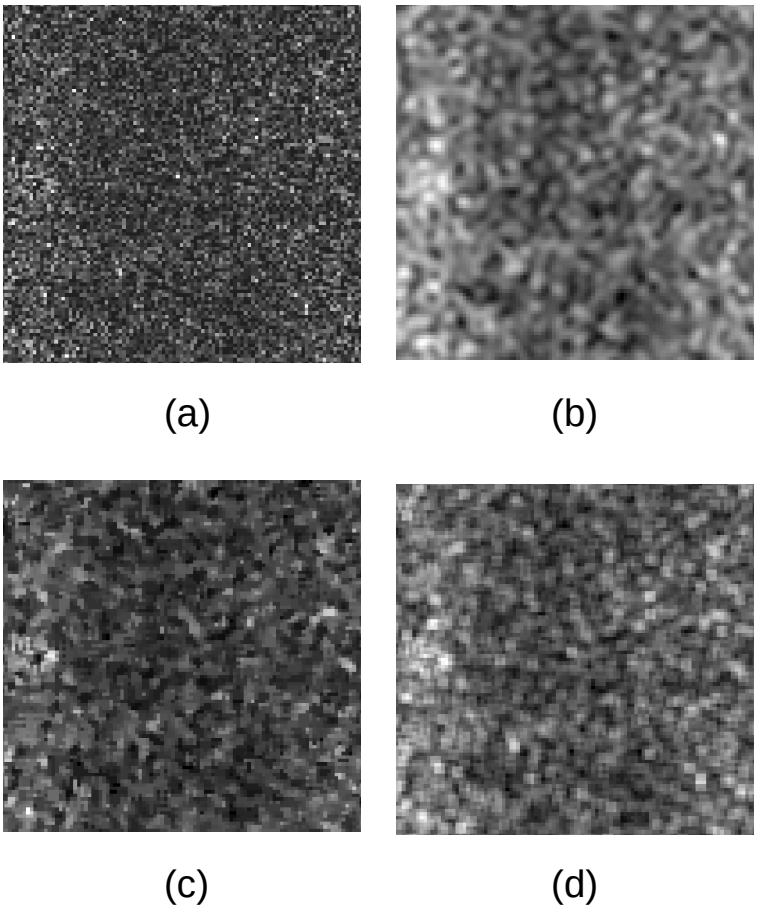

Figure 3.10: Zoomed in area of the chest of the stormtrooper DH showing (a) the original reconstruction, (b) the DFF with an aperture size of 512×512, (c) median filter with neighbourhood region size of 3×3 and (d) mean filter also with neighbourhood region size of 3×3.

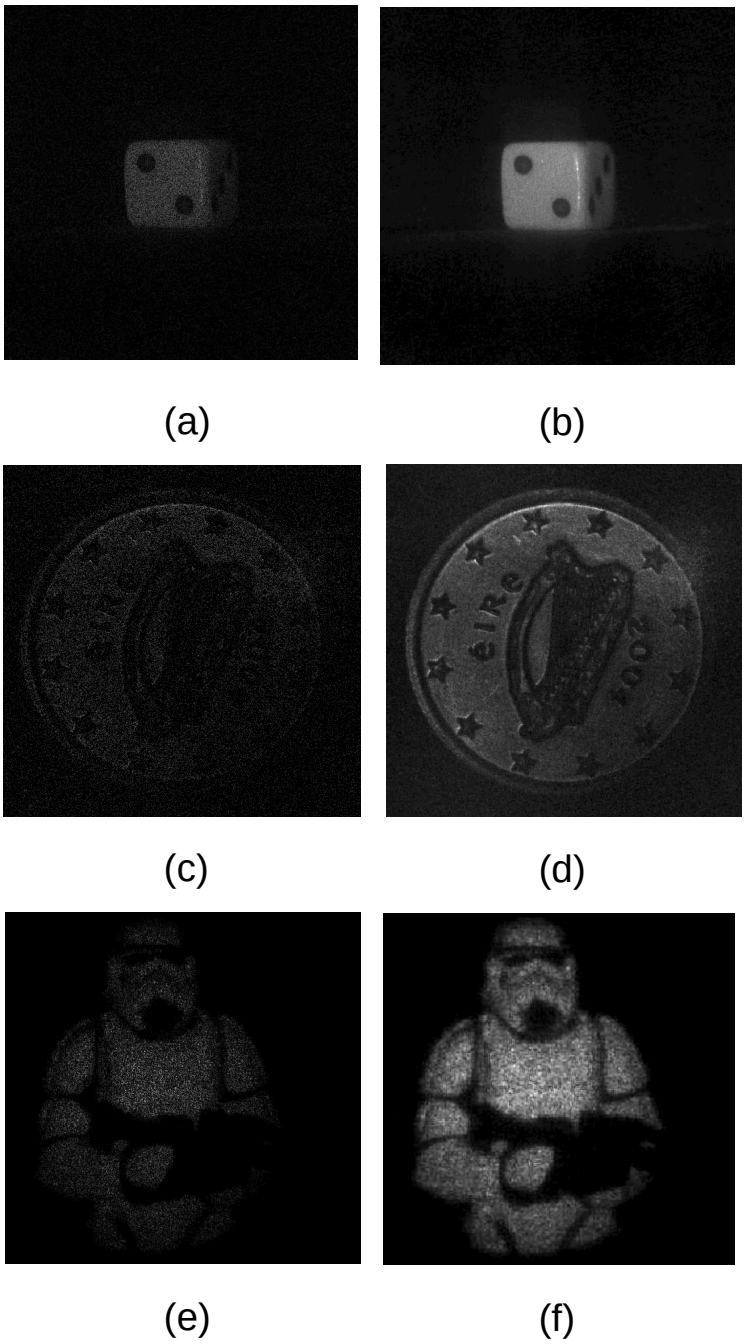

Figure 3.11: Original reconstructions for (a) PSI DH, (c) in-line DH and (e) off-axis DH. (b), (d) and (f) show the DFF applied to these reconstructions.

The third and final DH is also a stormtrooper figure, but this time captured using the off-axis setup described in Chap. 2.2.2.2[see Figure 3.11 (e)]. As this is an off-axis DH the resolution reduced to 1024×1024. Applying the DFF with a 128×128 aperture (so that once again $N = 64$) reduces the speckle index to 0.29 [Figure 3.11 (f)]. The reason for this is that the energy of the power spectrum of this DH does not take up the full bandwidth in the Fourier domain. Therefore a number of the apertures in the Fourier domain do not contribute to a reduction in the speckle index. To illustrate this Figure 3.12 (a) shows the power spectrum of a reconstruction of the PSI die object DH, Figure 3.12 (b) shows the power spectrum of the in-line coin object DH and Figure 3.12 (c) shows the power spectrum of a off-axis DH of the same object. It is clear from these figures that the energy is spread over the entire Fourier domain for the PSI and in-line DHs, but that their are large areas in which there is little or no energy in the Fourier domain for the off-axis DH. This explains the higher speckle index for the off-axis DH.

Finally, we note that the DFF has been employed as the speckle reduction technique in a number of areas in digital holography: segmentation [EMF+07], extraction of shape information [EMH+06a, EMH+06b] and extended focus imaging [EHN08].

3.5 Summary

A new DSP technique that reduces the speckle content in reconstructed DHs has been presented. It was shown that the speckle index can be reduced by half with no loss of resolution, and further reductions in speckle can be achieved with some loss in resolution. Furthermore, the DFF technique was shown to be superior to the mean and median filters in terms of edge preservation. An important benefit of this technique is that it requires no preprocessing of the input DHs, and thus

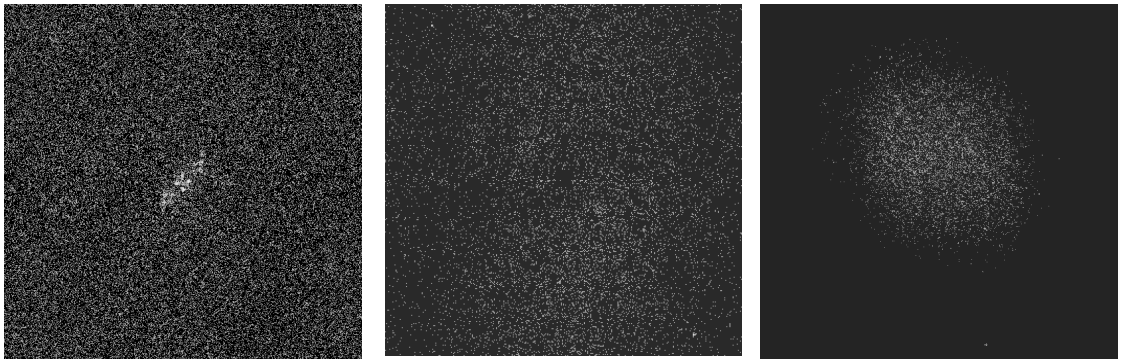

Figure 3.12: Power spectrum of a reconstruction of a (a) PSI DH, (b) in-line DH (DC terms removed) and (c) off-axis DH.

can be applied to all existing DHs. See Appendix D, where we present some initial work in which the DFF is used to reduce speckle content in DH reconstructions of an object embedded between layers of biological tissue. In the next chapter we offer a comprehensive analysis of applying wavelets to the problem of speckle reduction in reconstructions of DHs.

Chapter 4

Speckle reduction using wavelets

4.1 Introduction

This chapter presents a comprehensive analysis of applying standard wavelets to the problem of speckle reduction in reconstructions of in-line DHs. Wavelets are a good candidate for noise reduction as the wavelet transform is good at energy compaction, with the resulting small coefficient more likely to be due to noise and the large coefficient due to important signal features [Jan01]. These small coefficients can be thresholded without overly affecting significant features of the image.

In 2007, Do and Javidi [DJ07] reduced speckle in reconstructions of DHs using wavelets. However, the focus of their paper was directed towards the use of independent component analysis in fusing multiple reconstructed holographic images together that are at different distances from the CCD and therefore they did not quantify their speckle reduction results. Sharma *et al.* [SSJM08] also applied wavelets to the problem of speckle reduction in DHs. However they only investigated using a single mother wavelet, the Symlet wavelet, and did not mention anything concerning the resulting resolution of the reconstructions. Previously,

wavelets were applied to the problem of speckle reduction in replay holograms by Yu *et al.* [YAW96]. They used hard thresholding and an iterative method to obtain an optimal threshold value. We investigate the use of both soft and hard thresholding combined with four different thresholding schemes (i.e., fixed form [DJKP95], balance sparsity norm [MZK01], square-root balanced sparsity norm, and sqtwolog [YXLH06, LJYY07], which are all available in the Matlab Wavelet toolbox [Inc06]). The naming convention adopted in this chapter is that the threshold type can be either soft or hard, and that the thresholding scheme can be fixed form, balance sparsity norm, square-root balanced sparsity norm, and sqtwolog. We test our technique on real valued intensities of DH reconstructions. We have quantified our results using a combination of three metrics; speckle index, edge preservation and resolution. We note that part of the work in this chapter has already been published in [MMM+08].

4.2 Analysis

Wavelets are families of orthonormal basis functions, but unlike Fourier transform basis functions, they do not need to have infinite duration. The wavelet transform can be expressed in its 2-D continuous form as

$$\mathrm{WT}_{c,\xi,\eta}\{f(x,y)\} = \frac{1}{c}\int\int f\left(x-\xi, y-\eta\right)\Psi^*\left(\frac{x}{c},\frac{y}{c}\right)\mathrm{d}x\mathrm{d}y. \tag{4.1}$$

Here $f(x,y)$ represents the 2-D signal or function, $\Psi(x,y)$ is the 2-D mother wavelet, c is a global scaling factor and (ξ,η) are shift variables for the correlation. All the wavelet decomposition functions can be found by scaling the mother wavelet and shifting the signal. When the mother wavelet is dilated, it accesses lower frequency information, and when it is contracted, it accesses higher frequency information in the signal.

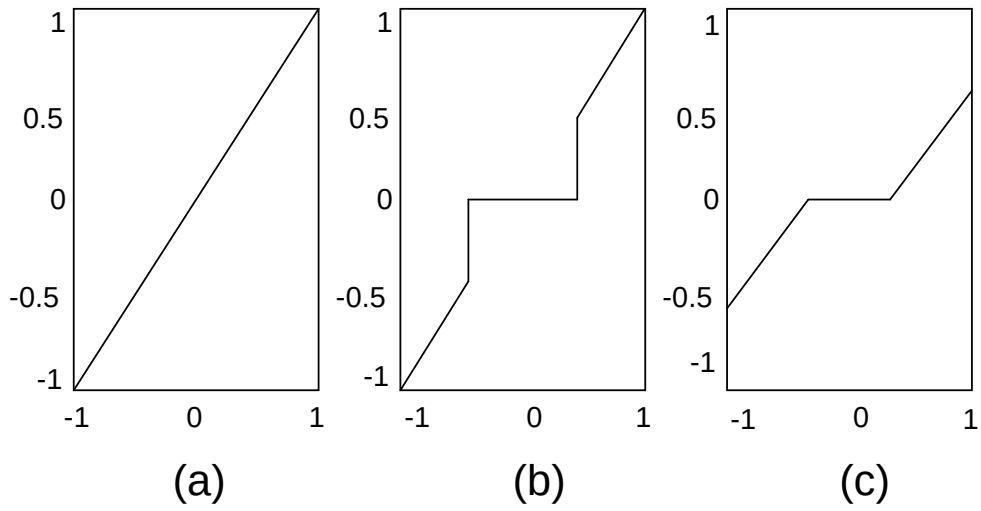

Figure 4.1: The results of applying a threshold of 0.4 to an original signal (a). (b) shows the signal after hard thresholding, and (c) shows the signal after soft thresholding. Figure adapted from Matlab [Inc06]

We use the discrete stationary wavelet transform (SWT) [NS95] to reduce noise in reconstructions of DHs corrupted by speckle. Wavelets have been used to successfully to recover signals from data corrupted by additive Gaussian noise [LGO+96]. Although speckle is not an additive noise, it has been demonstrated that when a speckled image is captured by a finite aperture (i.e., a CCD) and logarithmically transformed, it can be approximated to additive Gaussian noise [AA76]. Discrete SWT denoising involves decomposition, level dependent thresholding and reconstruction by inverse transforming. The natural logarithm of the DH reconstruction is taken before wavelet analysis is applied. Then a mother wavelet is chosen (in these experiments we test the full set of wavelets available in the Matlab toolbox [Inc06]) and the wavelet decomposition of the input is computed at level N. The detail level coefficients for each level 1 to N are thresholded using hard and soft thresholding [Don95]. Using hard thresholding the signal is x if $|x| > t$, and is 0 if $|x| \leq t$. In contrast, soft thresholding sets to zero those elements of the signal

whose absolute values are lower than the computed threshold, and then shifts the nonzero coefficients towards 0. Therefore the soft threshold signal is $\text{sgn}(x)(|x|-t)$ if $|x| > t$ and is 0 if $|x| \leq t$ (where $\text{sgn}(x)$ is the signum function). Unlike hard thresholding, soft thresholding does not produce discontinuities not already present in the signal. This is illustrated in Figure 4.1 in which discontinuities are observed at $\pm t$ in the hard thresholding case. The threshold value, $\lambda_{i,j}$, is calculated in each orientation i ($i = 1$ =horizontal, $i = 2$ =vertical, $i = 3$ =diagonal) at each level j ($j = 1, 2, ..., N,$ where N = number of levels). The wavelet coefficients are then thresholded using $\lambda_{i,j}$ to remove noise energy. The appropriate λ $(3 \times N)$ matrix is obtained using one of four potential methods [Inc06]:

1) fixed form [DJKP95]:

$$\lambda_{i,j} = s_{i,j}\sqrt{2log(X_{i,j})}, \tag{4.2}$$

where s is the standard deviation of detail coefficient in orientation i at level j and $X_{i,j}$ is the number of pixels in the detail coefficient in orientation i at level j,

2) balanced sparsity norm: $\lambda_{i,j}$ is calculated so that the ratio of remaining signal energy to original signal energy (remaining + noise energy) is equal to the ratio of the number of zero coefficients after thresholding and the total number of coefficients,

3) square-root balanced sparsity norm: $\lambda_{i,j}$ is the square-root of balanced sparsity norm, and finally

4) sqtwolog:

$$\lambda_{i,j} = \sqrt{2log(X_{i,j})}, \tag{4.3}$$

where $X_{i,j}$ is the length (number of pixels) of the detail coefficients in orientation i at level j. After thresholding, the signal is reconstructed using the original

approximation coefficients at level N and the modified detail coefficients of levels 1 to N. Finally, the logarithmic operation is reversed by exponentiation.

4.3 Metrics

We use speckle index and edge preservation [see Section 3.3] in this chapter. We also employ a new resolution metric in order to allow for automatic detection of the image resolution using an FFT based search algorithm. This was not required in the previous chapter as the resolution is easily predicted by the size of the aperture used in the DFF.

The new resolution metric is in the format of two embedded resolution strip patterns, one horizontal and one vertical [see the bottom left and the top right of Figure 4.2 (a)] into a real DH. For both the horizontal and the vertical cases there are 10 sub-strips (each 10 pixels wide) and each a sampled sine wave of a different frequency. The ten strips present in the resolution chart are at ten different spatial frequencies as shown in Figure 4.2 (b). For the vertical case, the highest frequency can be seen at the top of Figure 4.2 (b) and corresponds to the maximum frequency, f_{max}, of the image, which is given by $\frac{1}{2sp}$, where sp is the pixel size of our camera (i.e., 9μm $\times$ 9μm in this example). Proceeding from the top to the bottom of Figure 4.2 (b), the frequencies shown are given by $\frac{c}{10} \times f_{max}$, where c takes integer values from 10 down to 1. The lowest frequency in the chart is therefore $0.1f_{max}$.

The resolution strips are embedded into a reconstructed DH in the same way as the test image is embedded in Section 3.3, once again making sure that the maximum grayscale value of the added strips after the exponentiation operation is still less than the maximum value of the DH reconstruction. The strips are no longer sampled versions of perfect sine waves due to the exponential operation.

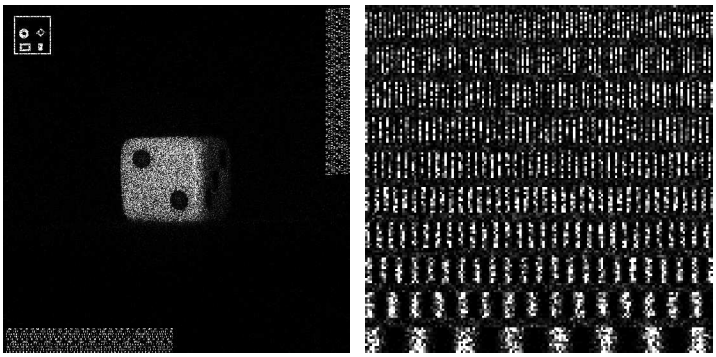

Figure 4.2: (a) A DH reconstruction of a die object with embedded test image and resolution strips and (b) zoomed in section of (a) showing a section of the vertical resolution strips.

However they have fundamental frequencies at the same frequencies of the original sine waves. Importantly, these strips are now corrupted by a coherent speckle noise. In order to test for the presence of a particular frequency we isolate each particular sub-strip (of which there are 10 for both the horizontal and vertical cases) and create 10 1-D vectors by integrating along the 10 pixel width. This allows us to check for resolution in DHs corrupted by speckle noise. The Fourier transform of the 10 1-D vectors are computed and we search for the presence of a peak in the fundamental frequency region for that sub-strip. If the peak has a power greater than some predefined threshold, we conclude that the resolution for this sub-strip has been maintained. Figure 4.3 (a) shows the presence of five fundamental frequencies (resolution levels in the horizontal direction looking from right to left). The predefined threshold we set corresponds to our own ability to visually identify the sub-strips. In Figure 4.3 (b) a graph of the result of searching for the presence of the fifth lowest fundamental frequency is shown. The two highest spikes in Figure 4.3 (b) correspond to the fifth lowest fundamental

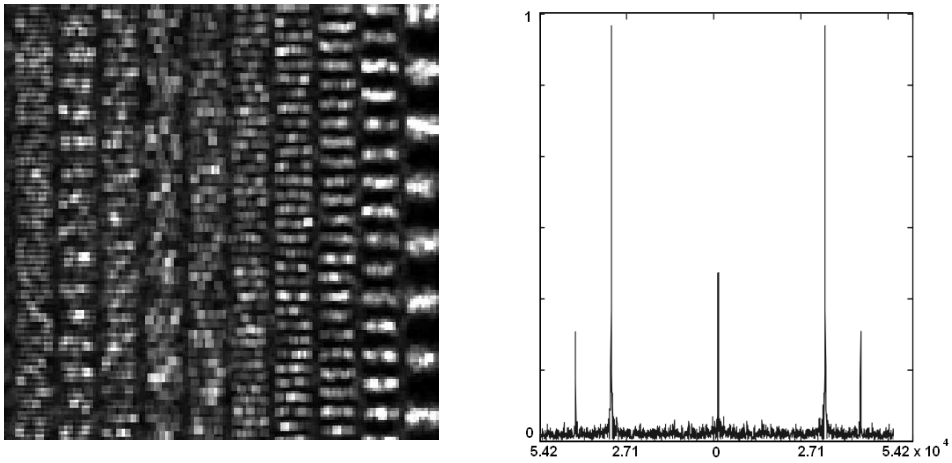

Figure 4.3: This figure shows presence of certain fundamental frequencies. (a) Shows the horizontal resolution chart after speckle reduction, and (b) shows the result of the check done to see if the fifth lowest fundamental frequency is present (it is). The two highest spikes represent this frequency. Note the presence of the DC term (in the middle) and another frequency due to the embedding process.

frequency in the chart. The DC terms at the zero frequency is also visible, plus frequencies due to the embedding process. It should be noted that when searching for the presence of frequencies, we begin with the lowest and search through to the highest in sequence. The search is terminated when we encounter the first frequency below the predefined threshold.

We have combined these three metrics in order to create an overall metric that was particularly useful as over 2000 tests were carried out making a manual inspection of the results very difficult. The overall metric, ω, is defined as

$$\omega = (1 - \alpha) \times \beta^2 \times \left(\frac{hr + vr}{2} \right), \tag{4.4}$$

where hr is the horizontal resolution and vr is the vertical resolution. The overall metric is a measure that incorporates all three metrics. We have assigned each

of the individual metrics equal importance, and therefore a direct comparison of different speckle reduction methods can be carried out. This allows us to decide on a best performing wavelet and thresholding scheme and thus display the relevant images. However, a summary of the results for each separate metric are also provided in tabular form in the next section, and more complete results can be found in Appendix F.

4.4 Results and discussion

Figures 4.4 and 4.5 show the results for the best mother wavelet from each family for each level and for each thresholding scheme (i.e., fixed form [DJKP95], balance sparsity norm [MZK01], square-root balanced sparsity norm, and sqtwolog [YXLH06, LJYY07]) for both soft and hard thresholding. The wavelet families we tested are the Haar, Daubechies (Db), Coif, biorthogonal (bior) and reverse biorthoganal (rbio) wavelets. The Db1, bior1.1 and rbio1.1 wavelets are identical to the Haar wavelet, and as these performed best in the respective family group, their results are omitted from the graph. We have plotted the results for the best performing mother wavelet from each of the following families; Db, Coif, bior, rbio, along with the Haar wavelet. Regardless of the chosen thresholding scheme, or whether soft or hard thresholding was used, the best mother wavelets for each family (omitting the bior1.1 and rbio1.1 mother wavelets) are almost consistently Db2, Coif1, bior1.3, and rbio1.3. The only exception is the case for soft thresholding using the sqtwolog thresholding scheme when Coif5 outperforms Coif1 [see Figure 4.4 (d)]. From these results we see that the Haar mother wavelet consistently outperforms all the other wavelets regardless of the chosen thresholding scheme. There is a single exception to this when a sqtwolog thresholding scheme is used for hard thresholding. Here the bior1.3 is a superior choice. However, we

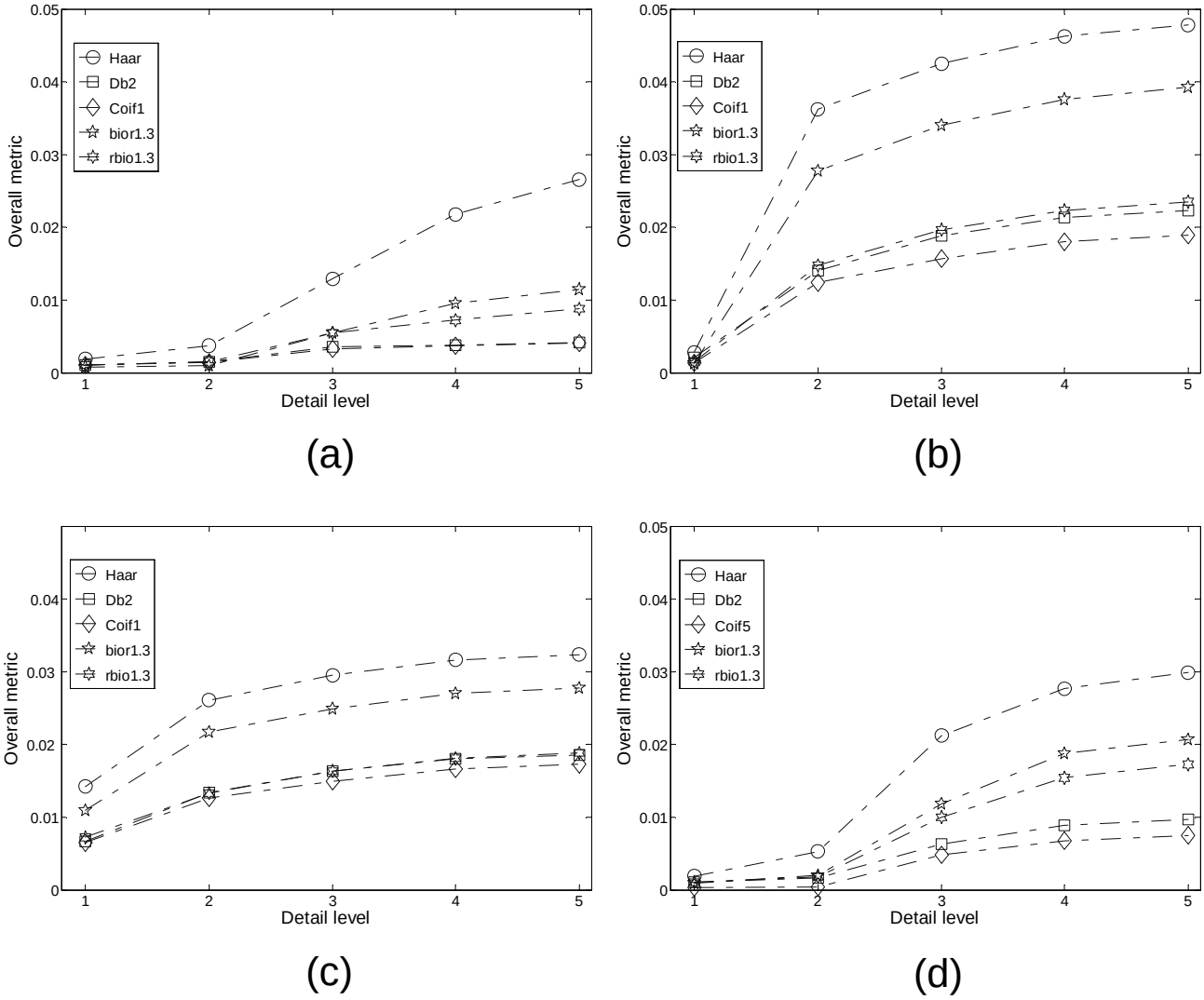

Figure 4.4: This results for soft thresholding using (a) fixed form, (b) balance sparsity norm, (c) square-root balanced sparsity norm, and (d) sqtwolog.

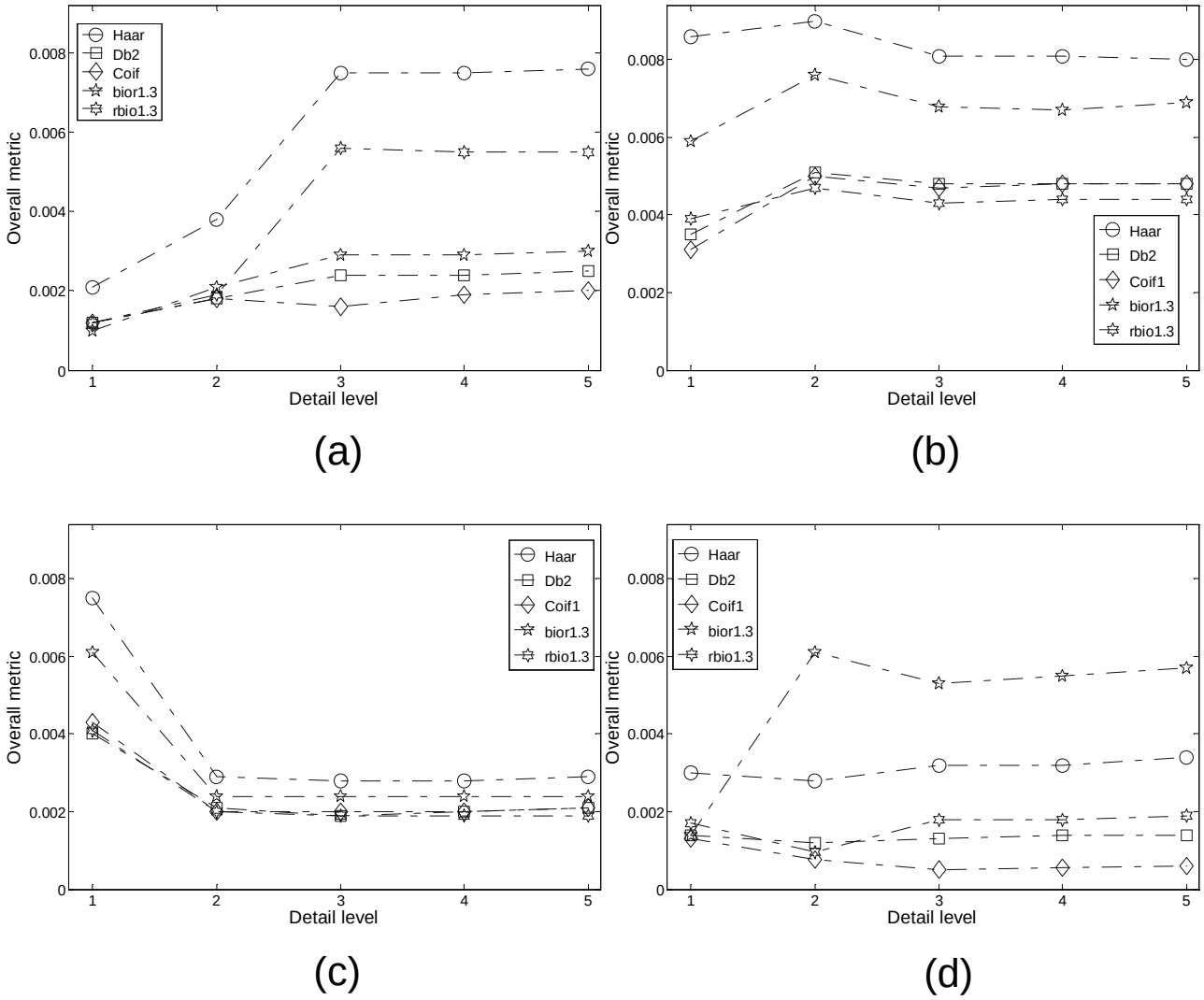

Figure 4.5: This results for hard thresholding using (a) fixed form, (b) balance sparsity norm, (c) square-root balanced sparsity norm, and (d) sqtwolog. Note that the overall metric, ω, for these results is lower by an order of magnitude than for those of soft thresholding.

noted that the overall results for this thresholding scheme are poor.

Our results indicate that soft thresholding outperforms hard thresholding in all cases. The best soft thresholding overall metric result is 0.0478. This is for a balance sparsity norm thresholding scheme and is achieved by the Haar wavelet at detail level 5. This compares very favorably to the best overall metric result for hard thresholding of only 0.009. This was achieved once again using Haar wavelet and a balance sparsity norm thresholding scheme, but this time at detail level 2. It is noted that for the soft thresholding results a trend emerges; as the detail levels increase so does the overall metric, ω, for all of the mother wavelets. The same trend is not found for hard thresholding. A possible reason for the poor performance of the hard thresholding scheme is that the thresholds are computed in a level dependent fashion. This means that level j can in fact reduce the speckle index more than level $j+1$ depending on where and in what level of detail the majority of the speckle noise resides. Consider the case where a threshold x_{11} is applied to the horizontal detail of a level 1 decomposition. For level 2 decomposition, thresholds y_{11} and y_{12} are applied to horizontal details at level 1 and 2 respectively. $x_{11} > y_{11}$ and $x_{11} > y_{12}$. If speckle resides in the intermittent band of frequency, then it is kept rather than lost by the remove or preserve policy of hard thresholding. Using hard thresholding also means that there is the potential for false positive removal too. In this case high frequency information such as edges can be inadvertently removed. Soft thresholding reduces those intermittent detail values rather than keeps or removes them entirely. We also note that in the hard thresholding case the overall metric values do not change significantly after detail level 2, with the exception of a fixed form thresholding scheme when the values do not change significantly after detail level 3. Figures 4.6 and 4.7 show the best results for both soft thresholding and hard thresholding respectively, for each wavelet family tested. We have used an in-line DH that is 2048×2048 pixels in

size. We also show the best reconstructions (in terms of ω) for all four thresholding schemes using both soft thresholding [see Figure 4.8] and hard thresholding [see Figure 4.9].

Figure 4.10 shows the results for the best performing soft thresholding wavelet (Haar using balance sparsity norm scheme) and the best performing hard thresholding wavelet (Haar using balance sparsity norm scheme) against the mean filter, median filter and the DFF [MHM+07]. The results clearly show that in terms of the overall metric, ω, soft and hard thresholding are superior to all three other methods. In particular it is noticeable that for soft thresholding ω improves significantly at each subsequent detail level. The DFF outperforms both the mean and median filters and performs comparatively against the best hard thresholding wavelet, however it is significantly worse than the best soft thresholding wavelet. The mean filter slightly outperforms the median filter. Table 1.1 shows the individual metric values, including the finer speckle index, edge preservation and resolution results, for the best soft thresholding wavelet, the best hard thresholding wavelet, the median filter, the mean filter and the DFF. It is interesting to note that both soft and hard thresholding achieve full resolution [see Table 1.1] for all levels (except detail level 1 in the case of soft thresholding). We also note that the speckle index reduces at each subsequent level for soft thresholding, but this trend is not found in the case of hard thresholding.

Looking at Table 5.3, it appears that the Haar wavelet using balance sparsity norm scheme and soft thresholding should be the obvious choice when choosing a speckle reduction technique. In fact, the excellent results the Haar wavelet achieves are due to the structure of the resolution charts and and test pattern. Both consist mainly of horizontal and vertical lines that particularly suit the form of the Haar mother wavelet, which is a step function. Figure 4.11 demonstrates this by showing the when the test pattern is replaced by an image of Lena, the Haar

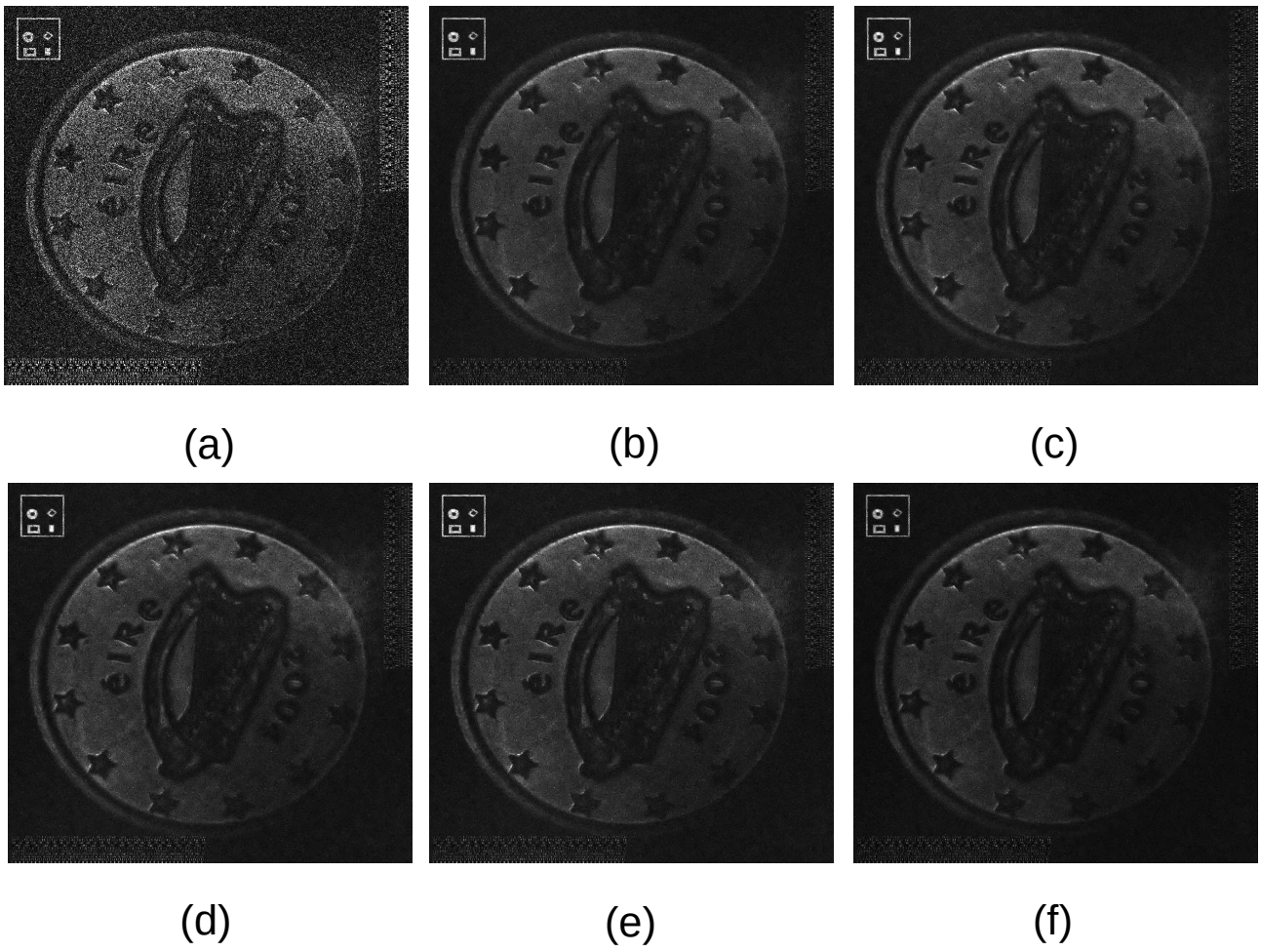

Figure 4.6: The best of each wavelet family using soft thresholding. In all cases the best performing thresholding scheme was a balance sparsity norm one at detail level 5. (a) original reconstruction (no filtering), (b) Haar, (c) Db2, (d) Coif1, (e) bior1.3, and (f) rbio1.3.

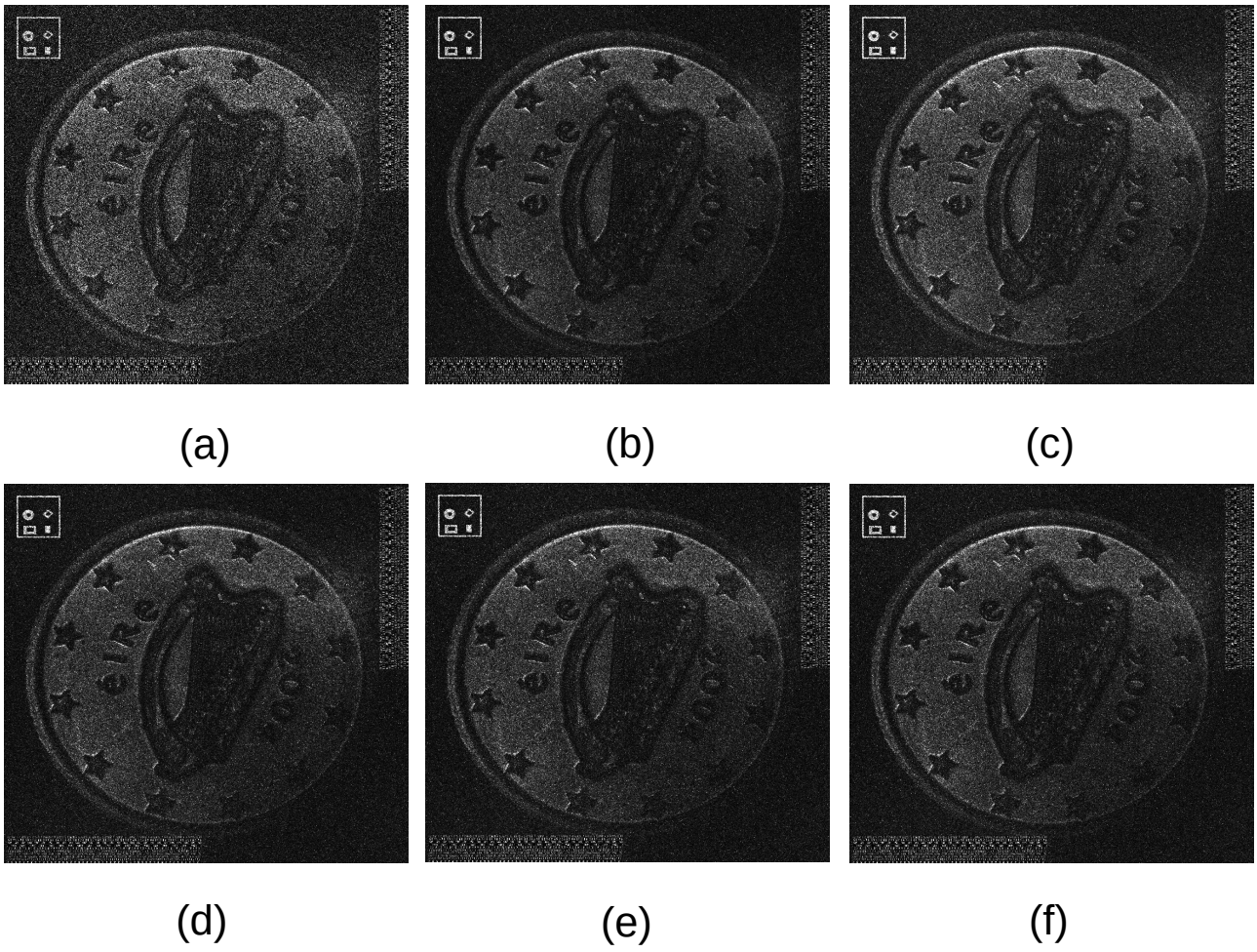

Figure 4.7: The best of each wavelet family using hard thresholding. In all cases the best performing thresholding scheme was a balance sparsity norm one at detail level 2. (a) original reconstruction (no filtering), (b) Haar, (c) Db2, (d) Coif1, (e) bior1.3, and (f) rbio1.3.

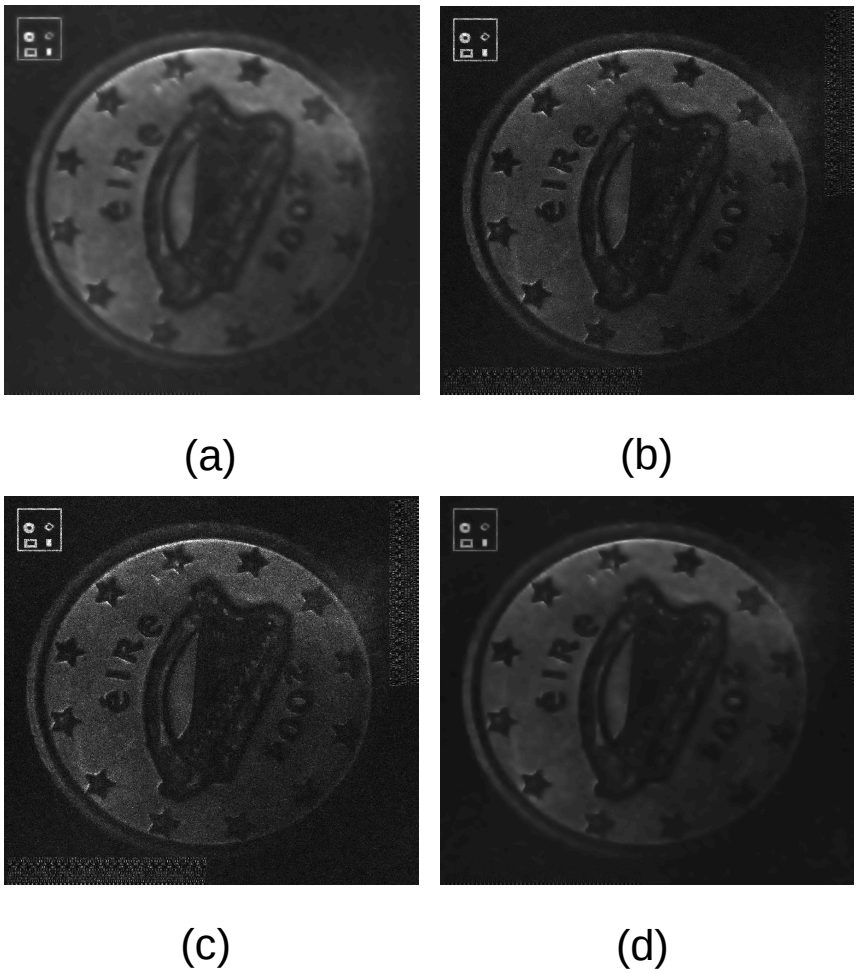

Figure 4.8: The best results for soft thresholding using the following thresholding schemes: (a) fixed form, (b) balance sparsity norm, (c) square-root balanced sparsity norm, and (d) sqtwolog. For soft thresholding the best result is consistently Haar detail level 5, regardless of the thresholding scheme used. Note that in (a) and (d) the resolution bars are not visible. In fact they are still present, but have been adversely affected by fixed form and sqtwolog thresholding [see Appendix F for more details].

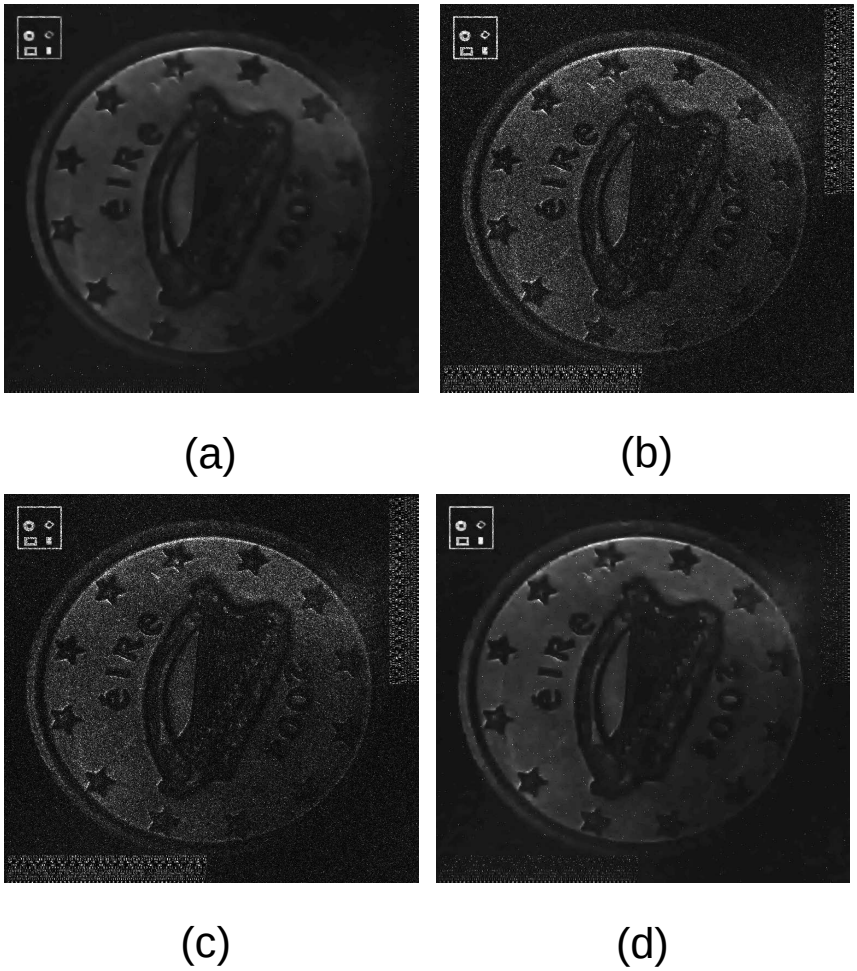

Figure 4.9: The best results for hard thresholding using the following thresholding schemes: (a) fixed form (detail level 5), (b) balance sparsity norm (detail level 2), (c) square-root balanced sparsity norm (detail level 1), and (d) sqtwolog (detail level 5). Note that one again the resolution bars are not visible in (a) and (d). They are still present, but have been adversely affected by fixed form and sqtwolog thresholding [see Appendix F for more details].

Technique	**Detail level / Aperture**	**Speckle index**	**Edge preservation**	**Resolution (H,V)**	**Overall metric (ω)**
Haar (Soft)	1	0.5238	0.0083	$0.7, 0.7$	0.0028
Haar (Soft)	2	0.3355	0.0545	$1, 1$	0.0362
Haar (Soft)	3	0.2727	0.0585	$1, 1$	0.0425
Haar (Soft)	4	0.2461	0.0614	$1, 1$	0.0463
Haar (Soft)	5	0.2374	0.0626	$1, 1$	0.0478
Haar (Hard)	1	0.5388	0.0186	$1, 1$	0.0086
Haar (Hard)	2	0.7253	0.0328	$1, 1$	0.0090
Haar (Hard)	3	0.7515	0.0324	$1, 1$	0.0081
Haar (Hard)	4	0.7503	0.0324	$1, 1$	0.0081
Haar (Hard)	5	0.7501	0.0322	$1, 1$	0.0080
Median filter	3×3	0.5121	0.0055	$0.5, 0.5$	0.0013
Median filter	5×5	0.3410	0.0011	$0.3, 0.3$	0.000022
Median filter	7×7	0.2593	0.000047	$0.2, 0.2$	0.0000063
Median filter	9×9	0.2120	0.0011	$0.1, 0.1$	0.000009
Mean filter	3×3	0.3945	0.0045	$0.5, 0.5$	0.0014
Mean filter	5×5	0.2685	0.0031	$0.3, 0.3$	0.000068
Mean filter	7×7	0.2124	0.0052	$0.2, 0.2$	0.000082
Mean filter	9×9	0.1805	0.0059	$0.1, 0.1$	0.000048
DFF	1024×1024	0.5398	0.0177	$0.8, 0.8$	0.0065
DFF	512×512	0.3156	0.0262	$0.4, 0.4$	0.0072
DFF	256×256	0.1851	0.0312	$0.2, 0.2$	0.0051
DFF	128×128	0.1142	0.0166	$0.1, 0.1$	0.0015

Table 4.1: Results for the best soft thresholding wavelet, best hard thresholding wavelet, median filter, mean filter and the DFF.

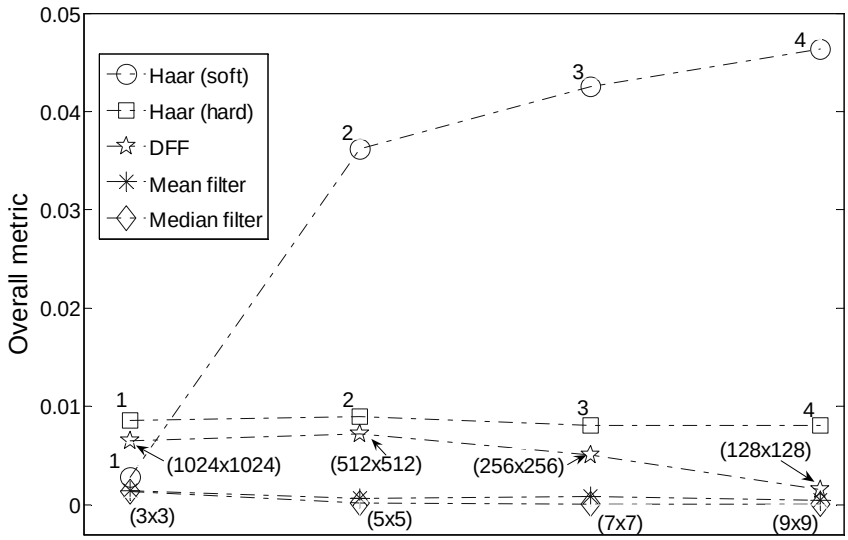

Figure 4.10: The results for the best soft thresholding wavelet (parameter indicates detail level), best hard thresholding wavelet (parameter indicates detail level), DFF (parameter indicates aperture size), mean filter (parameter indicates neighbourhood region size) and median filter (parameter indicates neighbourhood region size). Note that the best soft thresholding wavelet is the Haar mother wavelet using a balance sparsity norm thresholding scheme and the best hard thresholding wavelet is also the Haar mother wavelet using a balance sparsity norm thresholding scheme. DFF, discrete Fourier filter.

wavelet performs very poorly ($\beta^2 = 0.008$) in comparison to the DFF ($\beta^2 = 0.143$), mean filter($\beta^2 = 0.047$) and median filter ($\beta^2 = 0.025$). This illustrates the fact that care needs be taken in order to make sure that the choice of wavelet matches the input well.

Figure 4.13 shows the resultant reconstructions, in terms of the best ω value, for each technique tested. These results suggest that Figure 4.13 (b) (i.e., Haar wavelet at detail level 5 using soft thresholding and a balanced sparsity norm thresholding scheme) is superior to all the other techniques investigated when

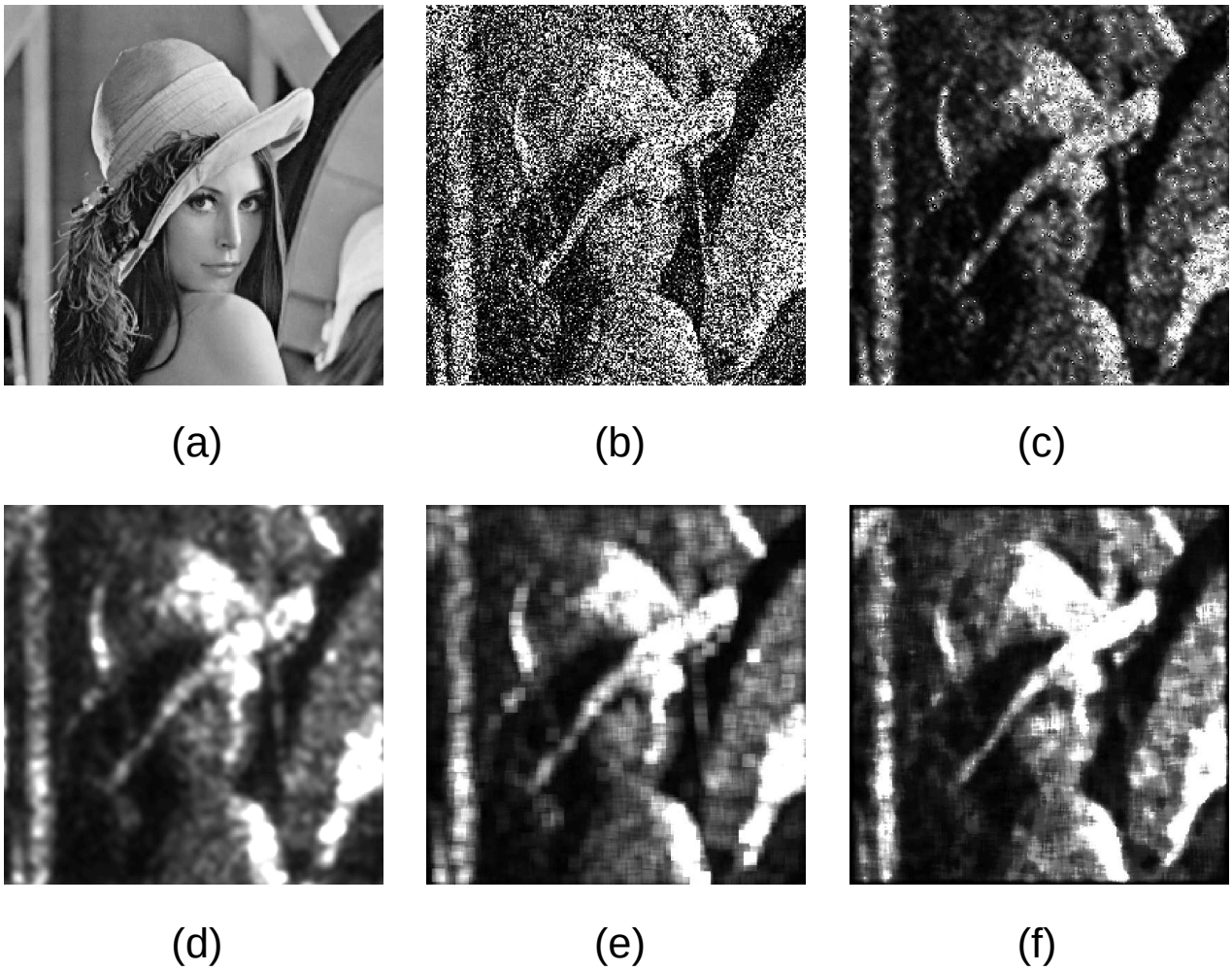

Figure 4.11: Images of the best performing (a) Lena image, (b) Lena image corrupted with speckle, (c) Haar wavelet, with soft thresholding and a balance sparsity norm scheme results in the worst edge preservation value of 0.008, (d) DFF (aperture size 512×512) achieves the overall best edge preservation of 0.143, (e) mean filter (neighbourhood size 9×9) results in edge preservation of 0.047, and (f) median filter (neighbourhood size 9×9) results in edge preservation of 0.025.

compared using our overall metric, which takes into account not only speckle index, but also the adverse impact on edges and resolution too. However, we also note that the reconstruction in Figure 4.13 (b) has a reduced speckle index of 0.2374, whereas all the other reconstructions have higher speckle indexes, and therefore, qualitatively it also looks better. This difference would not be as noticeable if all images were displayed with equivalent speckle indices.

In Figure 4.12 we show the results for the best performing thresholding scheme (balanced sparsity norm thresholding) using soft thresholding in terms of speckle index [see Figure 4.12 (a)] and edge preservation [Figure 4.12 (b)]. The speckle index results decrease (improves) from detail level 1 through to detail level 5 and the edge preservation results increase (improve) in the same manner. The only exception is a decrease for the Db2 mother wavelet between detail level 4 and detail level 5. A graph for resolution is not shown as full resolution (both horizontal and vertical) is achieved by all wavelets from detail level 2 onwards. At detail level 1, the Haar and rbio1.3 wavelets have a horizontal and vertical resolution of 0.7, and the Db2, Coif1, and Bior1.3 have a resolution of 0.6. A full list of results for the best performing soft thresholding wavelet, the best hard performing thresholding wavelet, the median filter, the mean filter and the DFF is shown in Table 14.

It is important wavelets with DHs that have been captured using other optical architectures. Therefore, we have tested them on phase-shifting interferometry (PSI) [YZ97, MHM$^+$07] DHs and off-axis DHs. Our PSI DHs are, like our in-line DHs, 2048×2048 pixels in size. The result of applying the best soft thresholding wavelet (Haar at detail level 5 using a balanced sparsity norm scheme) is shown in Figure 4.14 (a) and (b). While the technique performs well for PSI, it is clear that using the same parameters the technique has not performed well for the off-axis case [see Figure 4.14 (c) and (d)]. The reconstruction is blurred, the explanation for which is that the off-axis DH, at 1024×1024 pixels in size, has only a quarter of the

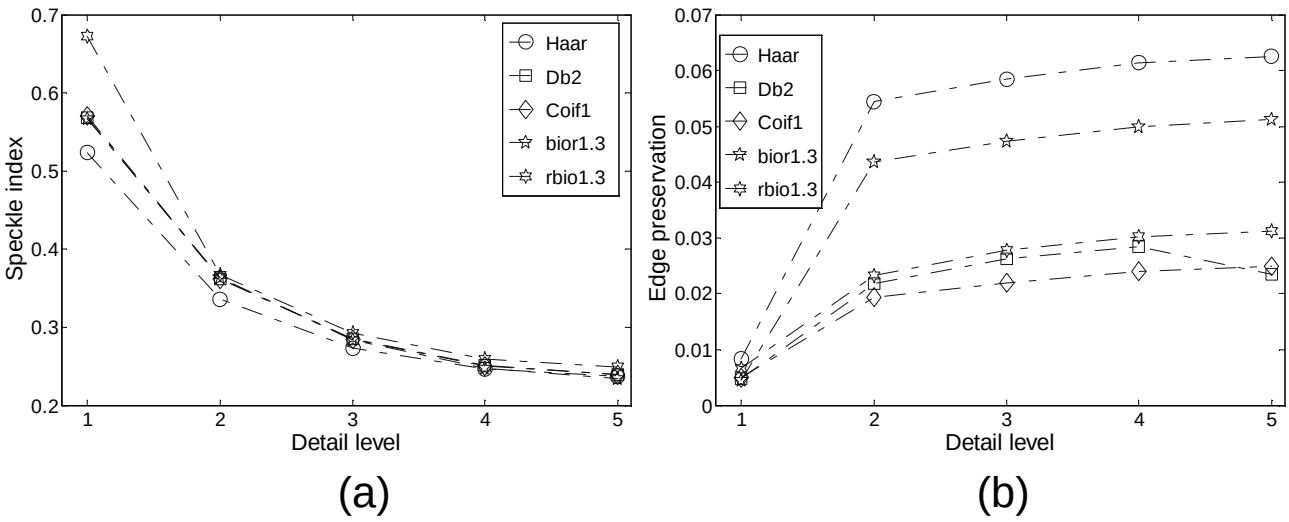

Figure 4.12: The results for soft thresholding and the best performing wavelet thresholding scheme (balanced sparsity norm thresholding) in terms of (a) speckle index, and (b) edge preservation.

resolution of the PSI DH. Furthermore, in the case of off-axis digital holography, objects must be placed at much greater distances from the CCD resulting in a larger speckle size [see Section 2.2.2.2]. Finally, in Figure 4.15 we show the result of the best soft thresholding wavelet applied to two in-line DHs [see Figure 4.15 (b) and (d)] and a PSI DH [see Figure 4.15 (f)]. The benefit of speckle reduction can be readily seen in the case of the PSI DH in that the lego logo is visible in Figure 4.15 (f) and not in the unprocessed version [see Figure 4.15 (e)].

Soft thresholding optimally recovers a signal from data corrupted by additive Gaussian noise [Don95]. We therefore expected it to perform better than hard thresholding and the results presented here corroborate that. The best of the Db, bior and rbio families usually give the same result as the Haar mother wavelet. Therefore, the only real alternative to the Haar mother wavelet is the Coif family of wavelets. However, in our tests the Haar mother wavelet has outperformed the Coif family of wavelets across every thresholding scheme. Although Figure 4.4

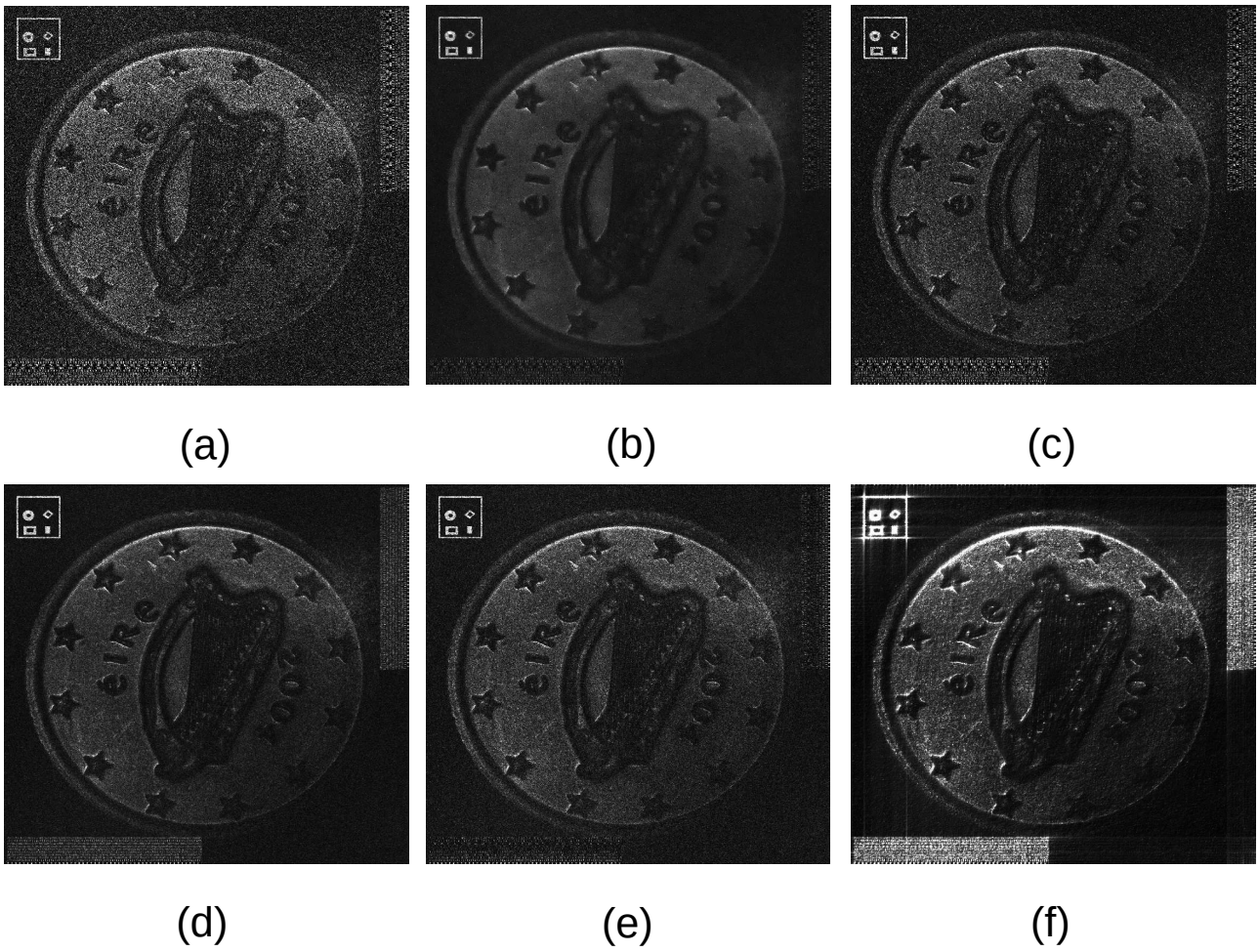

Figure 4.13: This figure shows (a) the original coin DH, and the best result in terms of the overall metric, ω, for (b) Haar wavelet at level 5 (using soft thresholding and a balance sparsity norm scheme, (c) Haar wavelet at level 2 (using hard thresholding and a balance sparsity norm scheme, (d) mean filter (neighbourhood size 3×3), (e) median filter (neighbourhood size 3×3), and (f) discrete Fourier filter (aperture size 512×512).

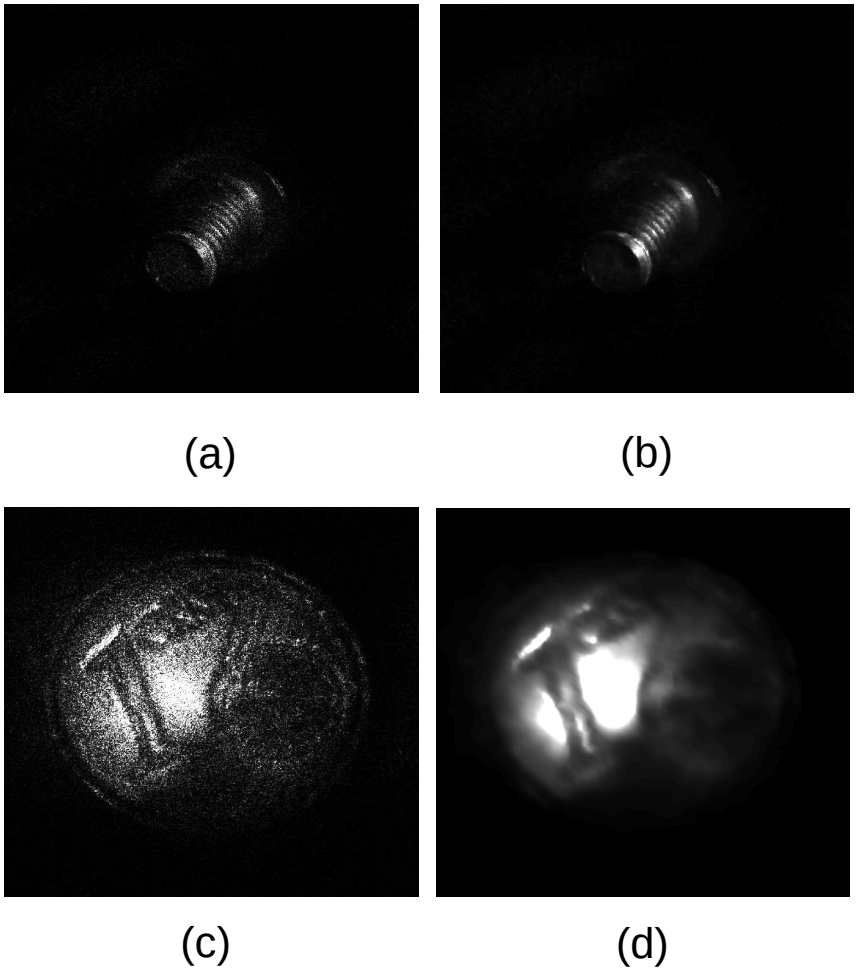

Figure 4.14: Effect of applying the wavelet plus thresholding scheme found (Haar at detail level 5 using a balanced sparsity norm scheme and soft thresholding) to a PSI DH and an off-axis DH. (a) original reconstruction of the PSI DH (no filtering), (b) wavelet filtered version of (a), (c) original reconstruction of an off-axis DH, and (d) wavelet filtered version of (c).

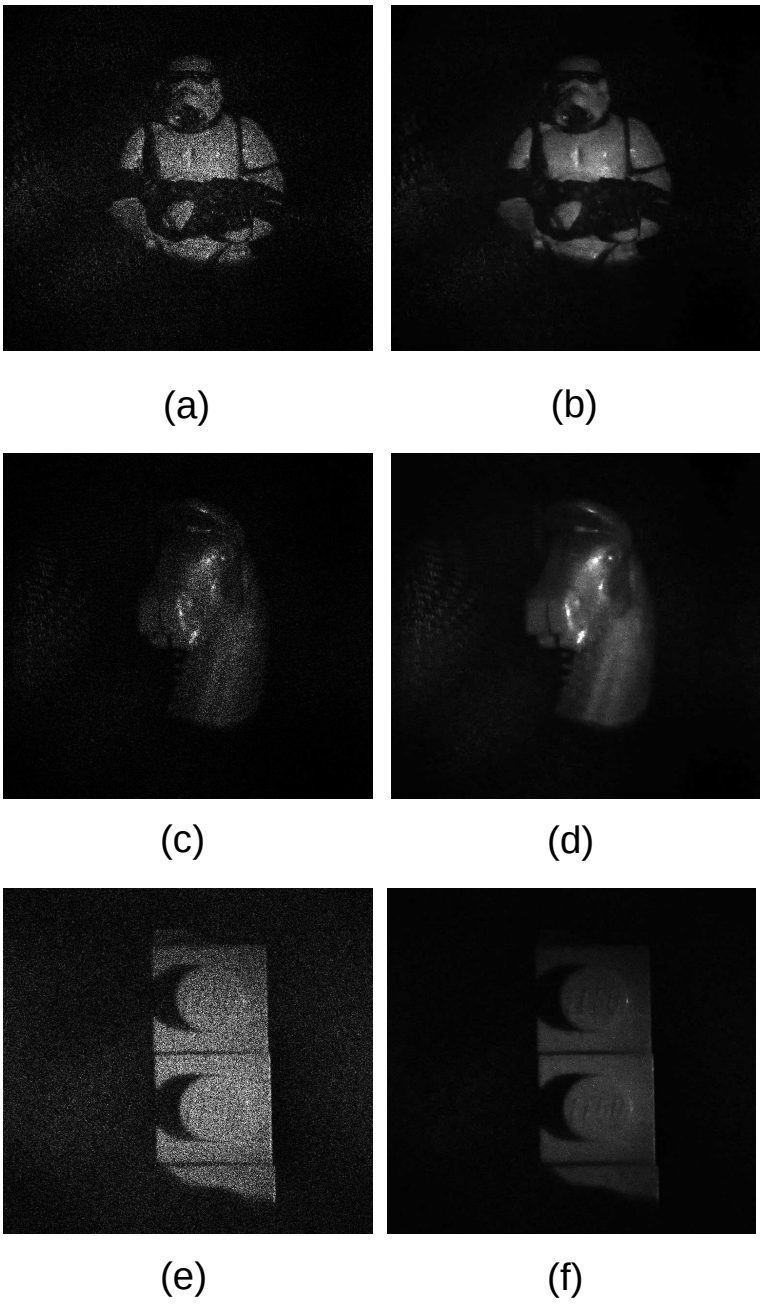

Figure 4.15: Effect of applying the wavelet plus thresholding scheme found (Haar at detail level 5 using a balanced sparsity norm scheme and soft thresholding) to two more in-line DHs and another PSI DH. (a) and (c) are the original reconstruction of in-line DHs (no filtering), (b) and (d) are wavelet filtered versions of these, (e) is the reconstruction of a PSI DH, and (f) wavelet filtered version of (e).

(b) indicates that there is a large difference between the best performing wavelet, the Haar wavelet, and the worst performing wavelet, Coif1, qualitative viewing of Figure 4.6 (b) and (d) suggests a strong similarity between the results. The success of the Haar wavelet can be attributed to the fact that the inserted test image used to calculate edge preservation is made up of a large number of straight edges. Also, the resolution bars are all vertical and horizontal straight edges. As the Haar wavelet is a step function, it matches the input image well. This was demonstrated when we switched the test pattern used for edge preservation calculation with an image of Lena [see Figure 4.11] resulting in the Haar wavelet performing performing worse than the DFF, mean and median filters. In general, the performance of any wavelet will depend on how well the mother wavelet matches the input signal. Therefore, depending on the input image that needs to have speckle reduced, another wavelet other than the Haar could be more suitable.

4.5 Summary

We have presented the first comprehensive analysis of applying wavelets to the problem of speckle reduction in reconstructions of in-line DHs. In the current set of tests, the Haar wavelet using soft thresholding and a balanced sparsity norm thresholding scheme was shown to be superior to the DFF technique, and the mean and median filters in terms of speckle reduction, edge preservation and resolution. However, we note that this was in large part due to the choice of resolution charts and test pattern used to calculate edge preservation. Qualitative results were also provided for PSI DHs and off-axis DHs. An important benefit of using wavelets (and the DFF, mean and median filters) is that no preprocessing of the input DHs is required, and thus they can be applied to all existing DHs. In the next chapter we introduce a 3D filtering technique that successfully reduces speckle using a

convolution based framework and Gaussian filtering on DH 3D intensity fields.

Chapter 5

Speckle reduction using three dimensional filtering

5.1 Introduction

In this chapter we report on a new DSP technique that reduces speckle in reconstructions of DHs. This is achieved by convolving the 3D intensity pattern (the intensity of the propagated DH at a series of different distances) with a 3D point spread function in all three dimensions (x,y,z). This 3D filtering method is based on the fact that the addition of different independent speckle images on an intensity basis reduces the speckle content.

We begin by investigating the most basic 2D case, (x,y), where the DH reconstruction planes are laterally shifted and added together. If the shift is greater than a speckle correlation area (average speckle size), then the overlying speckle patterns will be statistically independent [see Section 2.3.4]. Adding together a number of shifted copies of the 2D intensities, each differently weighted in the sum, may be described by a 2D convolution. Convolution provides a framework for the application of different kinds of filters, e.g., Gaussian filter. Convolution

also provides a framework for extension to the case of 3D filtering. In this case we reconstruct a series of intensities at a range of different distances. If the sampling distance along z is at least as large as the speckle size in the z direction we may assume that each reconstruction has an independent speckle pattern.

It is important to note that the idea of adding shifted intensities for speckle reduction in holography has precedent. In 1975, Gama [Gam75] used a vibrating source during optical replay of holographic reconstructions of diffuse objects to reduce the speckle contrast pattern. He showed that for certain classes of objects, resolution was not affected. This was true when the object used was a grating and the source was vibrated in a direction parallel to the lines of the grating. Gama implemented his technique by reflecting the hologram reconstruction beam off a mirror that was attached to a loudspeaker to create the needed oscillations. Thus the oscillating image was time averaged. We can effectively simulate this vibration numerically when we average along particular vectors in the 2D plane. We note that shifting the object wavefield in the reconstruction plane of a DH is exactly equivalent to tilting the reference beam during replay of an optical hologram [Kre05].

Recently, Pen *et al.* [PXL+11] introduced a method to reduce coherent noise in digital holographic phase contrast microscopy by slightly shifting the specimen under investigation and at each shift capturing a DH, each with different speckle pattern. By adding reconstructions from these DHs together the speckle content was reduced. Another method by the same group introduced an approach based on polarization to reduce speckle noise in off-axis DHs [XZR+11]. Once again multiple DHs are obtained by rotating the linear polarization state of both illumination and reference beams simultaneously. Speckle is suppressed by adding together reconstructions from these DHs on an intensity basis. Nomura *et al.* [NONN08] proposed a different method of reducing speckle by superposing the intensities of

reconstructed DHs recorded at different wavelengths. They used a wavelength-tunable laser and they captured their DHs in the range 567 to 624 nm, with an interval of 8nm. They then added together reconstructions from each of the captured DHs on an intensity basis, thus reducing the speckle content.

We propose to reduce speckle in a similar way, by convolving the reconstructed wavefield intensity in the third dimension, i.e., by modifying the distance parameter (or wavelength-distance product, $\lambda \times d$) used in a series of different reconstructions rather than capturing a series of different holograms. There is an important distinction between the method proposed by Nomura *et al.* [NONN08] and the method that we are proposing. In the former cases each recording with a different wavelength produces an identical reconstructed image with an independent speckle pattern. In our case reconstructing the same recorded DH using a series of different distances gives independent speckle patterns but also defocuses the reconstructed image. A drawback of the approaches by Pen *et al.* [PXL$^+$11], Xiao *et al.* [XZR$^+$11], and Nomura *et al.* [NONN08] is that they all require the capture of multiple DHs and therefore are not suited to the capture of dynamic scenes. Our technique does not suffer the same drawback.

To the best of our knowledge this is the first time that 3D filtering of a reconstructed speckle field has been investigated. The resulting degradation of the image produced by 3D filtering is investigated using a resolution chart. The technique does not require any change to the optical apparatus for capturing DHs and can therefore be applied to all existing DHs. Finally, we note that the work in this chapter has been accepted for publication in Optics Communication [MHM13].

5.2 Analysis

An analysis of the technique is now presented. In Section 5.2.1 the convolution framework, upon which our technique is built, is discussed. Then we address the issue of generating a 3D signal along with the required sampling intervals needed for convolving such a signal [see Section 5.2.2]. The differences between reconstruction with the direct and spectral methods and possible implications for our approach are treated in Section 5.2.2.1. Then in Section 5.2.3 we discuss speckle size in 3 dimensions and compare the expected sizes given by theory to the sizes numerically calculated using autocorrelation in all three dimensions. Finally, the model we have developed is presented Section 5.2.4.

5.2.1 Convolution and filtering

Convolution of 2D signals f and g can be written as

$$(f * g)(x, y) = \int_{-\infty}^{\infty} \int_{-\infty}^{\infty} f(u, v) g(x - u, y - v) du dv, \tag{5.1}$$

where u and v are position variables. We can convert this to the discrete case and let f represent the image and g the kernel, and now in order to differentiate the continuous case from the discrete case there is a change in variable names to r and s for the position variables. The output image, $h[x, y]$ is defined as

$$h[n_x, n_y] = f[n_x, n_y] * g[n_x, n_y] = \sum_{r=-\infty}^{\infty} \sum_{s=-\infty}^{\infty} f[r, s] g[n_x - r, n_y - s]. \tag{5.2}$$

In practice the convolution is calculated over finite intervals [see its 3D version in Equation 5.4 below] where the summation covers the range of samples $-N_x/2$ to $(N_x/2) - 1$ in the x direction and $(-N_y/2)$ to $(N_y/2) - 1$ in the y direction. In general the discrete convolution of two signals f and g with common sampling

intervals T_x and T_y and number of samples $(N_x f, N_y f)$ and $(N_x g, N_y g)$ will also have the sampling intervals T_x and T_y but will have a number of samples $(N_x f + N_x g - 1, N_y f + N_y g + 1)$. If both f and g have large dimension the convolution can be implemented in a fast straightforward manner by first zero padding both f and g up to a size $(N_x f + N_x g - 1, N_y f + N_y g + 1)$, then implementing an FFT algorithm to both. The results are multiplied and an inverse FFT is computed. This is possible as convolution in the spatial domain reduces to multiplication in the Fourier domain [see Section 2.2.2.4]. Alternatively if one of, or both, f and g have small dimensions, direct implementation of Equation 5.2 over finite intervals can be calculated in an efficient time. The *conv2* function in MATLAB [MAT04], which we make use of in the results section of this chapter, is an example of such an algorithm.

Convolution in 2D is often used in image processing to reduce noise. However, as we are using DHs, it is possible to create a 3D signal by calculating the intensity pattern at a sequence of different distances within a certain range around the correct object distance. For such a signal we can perform 3D filtering using 3D convolution with a suitable 3D kernel. 3D convolution in the continuous case can be written as

$$(g * f)(x, y, z) = \int_{-\infty}^{\infty} \int_{-\infty}^{\infty} \int_{-\infty}^{\infty} f(u, v, w) g(x - u, y - v, z - w) du dv dw, \quad (5.3)$$

and the discrete bounded case can be formulated as

$$h[n_x, n_y, n_z] = \sum_{r=-\frac{N_x}{2}}^{\frac{N_x}{2}-1} \sum_{s=-\frac{N_y}{2}}^{\frac{N_y}{2}-1} \sum_{t=-\frac{N_z}{2}}^{\frac{N_z}{2}-1} f[rT_x, sT_y, tT_z] g[n_x T_x - rT_x, n_y T_y - sT_y, n_z T_z - tT_z], \quad (5.4)$$

where f is the 3D signal, g the 3D kernel and T_x, T_y and T_z the sampling periods in the (x,y,z) directions, respectively.

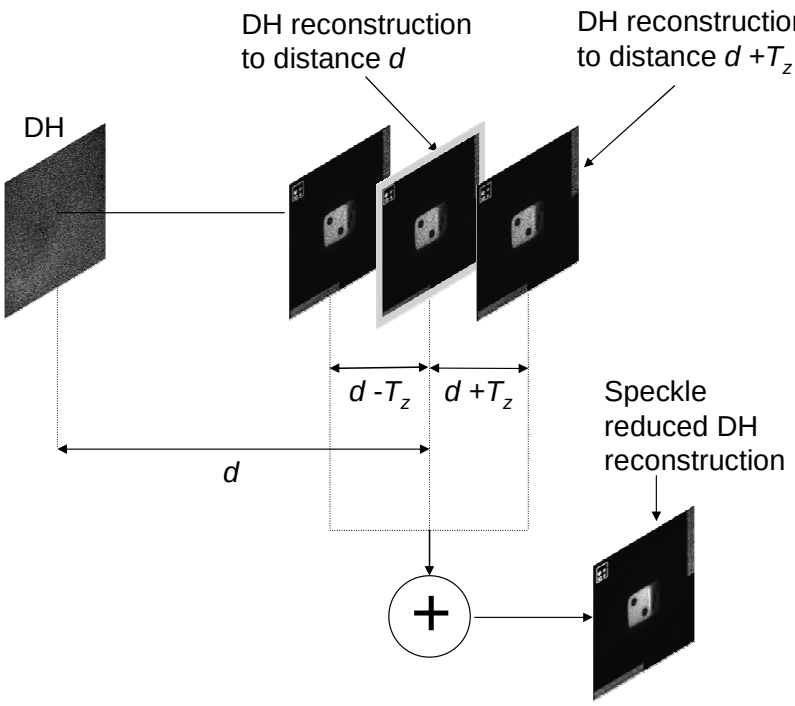

Figure 5.1: Visualisation of the process of filtering in 1D in the z direction. Pictured are the three reconstructions given by distances d, $d - T_z$, and $d + T_z$. A speckle reduced reconstruction is shown after the addition of these reconstructions on an intensity basis. We note that in reality d is much larger with respect to T_z than depicted here.

Figure 5.1 illustrates the idea in which three reconstructions are computed using d, the correct reconstruction distance, $d - T_z$, and $d + T_z$, where T_z is the step size needed to produce a statistically independent speckle pattern. All three intensity reconstructions are added together (and the result divided by three) to produce a speckle reduced image. In this case the signal $g(x, y, z) = \text{Rect}(z/2T_z)$ and the discrete kernel matrix is a simple block filter ($[1, 1, 1]\frac{1}{3}$). This example shows one dimensional filtering along the z direction only. Instead of using a hard edge filter, we can decide on a kernel based on important image feature directions, use a Gaussian filter, or other image processing filters such as a Laplacian filter. For the

Method	T_x	T_y	T_z
Direct	$\frac{d\lambda}{N_x\Delta\xi}$	$\frac{d\lambda}{N_y\Delta\eta}$	$\lvert d(\frac{1}{1+\frac{d\lambda}{min(N_x,N_y)^2 min(\Delta\xi,\Delta\eta)^2}}) - d(\frac{1}{1-\frac{d\lambda}{min(N_x,N_y)^2 min(\Delta\xi,\Delta\eta)^2}})\rvert$
Spectral	$\Delta\xi$	$\Delta\eta$	$\lvert d(\frac{min(N_x,N_y)}{min(N_x,N_y)+1}) - d(\frac{min(N_x,N_y)}{min(N_x,N_y)-1})\rvert$

Table 5.1: Direct and spectral reconstruction method parameters. T_x: Sampling interval in x, T_y: Sampling interval in y, T_z: Sampling interval in z (depth of focus), $\Delta\xi$: sensor pixel size in x, $\Delta\eta$: sensor pixel size in y, N_x, N_y: number of pixels on the sensor in x and y respectively, d: distance that we numerically propagate, λ: wavelength of the light used.

images and kernels of interest in this chapter we found the most efficient method of calculating the filtered image was to numerically reconstruct the intensity patterns at a sequence of different distances. We then implement 2D convolution on each of these images independently (we deal with kernels that are separable in x, y and z), and finally to multiply each resulting image one by a specific weight that depends on the z component of the 3D kernel, before adding them all together. We note that for more complicated larger filters or for specific directional filters it may be more efficient to use a 3D FFT algorithm in which the product of the 3D DFT of the intensity stack and the 3D DFT of the kernel is computed and then an inverse 3D DFT operation applied. Finally, a 2D slice can be extracted from this 3D signal to retrieve the filtered image.

5.2.2 Numerical computation of the 3D intensity field

Discrete convolution with a 3D filter kernel requires a discrete 3D signal. When constructing such a signal, careful consideration needs to be given to the discrete sampling intervals in all three dimensions. We must also take into account that the sampling intervals of a reconstructed DH differ depending on the choice of reconstruction algorithm chosen. Table 5.1 gives the equations used to calculate

sampling intervals in the x, y and z directions [Kre05]. As can be seen from the table, the sampling intervals in x and y (T_x and T_y) are proportional to the reconstruction distance, d, when using the direct method and is the same size as the sensor pixels when using the spectral method. If we wish to upsample the reconstructed wavefield, i.e. to achieve a smaller T_x and T_y, different methods may be applied in the case of the two algorithms. In the case of the direct method we can simply zeropad the DH before reconstructing; N_x and N_y will increase and therefore T_x and T_y will decrease accordingly. In the case of the spectral method if we first upsample the DH we will consequently upsample the reconstruction since the sampling interval is conserved. This can be achieved by zeropadding in the Fourier domain. In both cases the output window will remain unchanged and only the sampling interval will be reduced. The output window size for both methods is discussed in more detail in the next subsection.

In order to decide which sampling interval we should choose along the z direction, we use the concept of depth of focus given by Kreis [Kre05]. Our assumption is that the depth of focus is related to the rate of change along the z direction and therefore the correct sampling rate in the Nyquist sense. In order to ensure sufficient sampling, the 3D intensity signal should be made up of a number of 2D reconstructions that are centered on the optimum reconstruction distance and are separated in space by T_z. Before computing these 2D reconstructions the original DH should have been zero-padded sufficiently (in the spatial domain when using the direct method of reconstruction and in the spatial frequency domain when using the spectral method). For our calculations we further reduced sampling interval, T_z, to a quarter of its size in order to further ensure sufficient sampling of the 3D intensity field. As can be seen in Table 5.1 T_z needs to be smaller to closer distances than at distances further out, as the wavefield changes more quickly at short distances. Nonetheless, we choose a constant value of T_z determined by the

reconstruction distance, d, and the length of the shortest side of the sensor. We believe this is acceptable because T_z does not appreciably change over the range in which we calculate our discrete 3D signal.

5.2.2.1 Direct and spectral methods of reconstruction

We now briefly discuss the differences between the direct and spectral methods of reconstruction in the context of calculating a 3D field. Both methods calculate the Fresnel transform in different ways, allowing us to numerically simulate free space propagation of light in the paraxial approximation. They differ primarily in the output range that they display and the sampling rate at the output plane. For the direct method the output is proportional to the distance, whereas the spectral method has an output range equal to the size of the CCD camera. However, the manner in which these approaches calculate planes in the z direction is important for the work presented in this chapter. Figure 5.2 (a) shows a visualisation of the direct reconstruction method. The output range is proportional to the reconstruction distance $\lambda d/T_x$ in the x direction and $\lambda d/T_y$ in the y direction. For the spectral method, shown in Figure 5.2 (b), the output window is the width of the CCD $N_y T_y$ [HKMP10]. These details are important when it comes to choosing a reconstruction method to use for 3D filtering. A general rule of thumb is that if the object is much larger than the CCD, then the direct method should be employed. Otherwise costly zero padding of the DH needs to be done as a pre-processing step before reconstruction to ensure no aliasing. There are $N_x N_y$ lines emanating from the DH and cutting through the x,y,z coordinate system; in the case of the direct method they emanate from the centre and spread out and for the case of the spectral method they are all horizontal and parallel to each other. These lines therefore cut through and sample the 3D speckle field differently.

In Section 2.3.3 we discussed the size and shape of speckle grains in digital

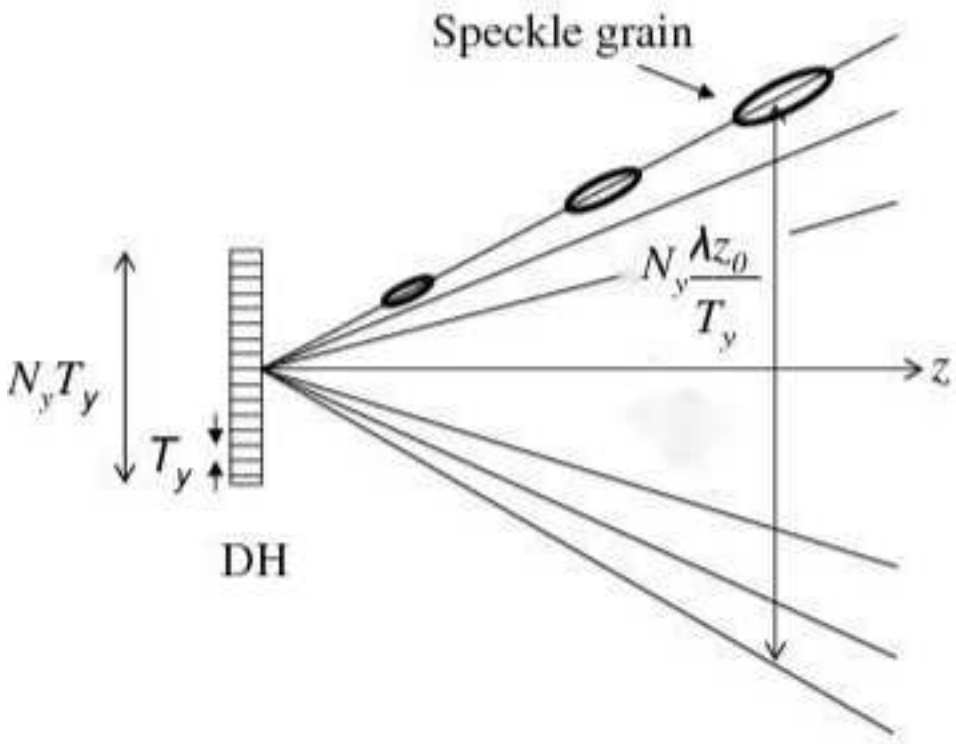

(a)

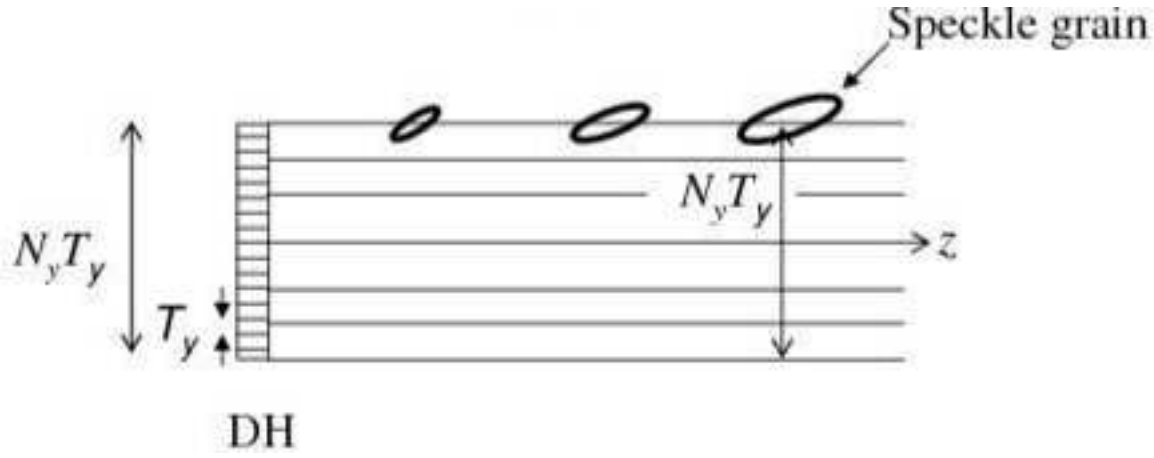

(b)

Figure 5.2: Output width when reconstructing with the (a) direct method and the (b) spectral method. Also shown is the difference between how both methods average along lines when we sum a series of reconstructions in the z direction. In the case of the direct method averaging occurs along lines that are parallel with the direction of the speckle, whereas in the case of the spectral method the lines cut through the speckle. Adapted from Hennelly et al. [HKMP10].

holography [PTZ96]. Assuming this holds true for both the direct and spectral methods, Figure 5.2 (a) shows that for the direct method the speckle grains line up along the lines emanating from the CCD plane and therefore we expect that the calculated speckle size should closely match that given by the theory [LK90]. However, for the spectral method [see Figure 5.2 (b)] the lines cut through the speckle grains and thus we expect that the calculated speckle size may be smaller than that predicted by theory. In the next section we test this hypothesis and discuss how it affects our filtering algorithm.

5.2.3 Speckle size and independent speckle patterns

The addition of independent speckle patterns on an intensity basis will reduce the speckle index by $1\sqrt{N}$ where N is the number of independent speckle patterns [see Section 2.3.4]. As we discussed in the previous section, a discrete convolution returns a value for a particular image sample that is given by the weighted sum of some region of the input image samples. In the case of a 3D convolution, this region has three dimensions. The extent of this region in each dimension and the weighting values depend on the extent and type of the kernel that we use for convolution. In order to ensure a reduction in the speckle index by an amount $1/\sqrt{N}$, N statistically independent speckles need to fit inside this region, and therefore to achieve this reduction, the physical extent of the kernel should be at least as large as the average speckle size in the given dimension. Therefore when choosing an appropriate kernel in order to provide a desired speckle reduction, our first consideration must be the size of the average size of the speckles in the image in all three dimensions and this will directly influence our choice of the kernels extent in these three dimensions.

Table 5.2 gives expressions for the theoretical speckle size in the x and y directions [Goo06] and the z direction [LK90]. As long as d is large compared with the

Direction	Equation
x	$S_x = 0.9\lambda(\frac{d}{W_{CCDx}})$
y	$S_y = 0.9\lambda(\frac{d}{W_{CCDy}})$
z	$S_z = \frac{7.31\sqrt{2}\lambda d^2}{\sqrt{{W_{CCDx}}^4+{W_{CCDy}}^4}}$

Table 5.2: Speckle size. S_x, S_y and S_z are the speckle sizes in x,y and z respectively. d: distance of the object to the sensor, λ: wavelength of the light used, W_{CCD}: width of the sensor in a particular direction.

size of the sensor, then the speckle will have a much greater size in the z direction than in the x or y directions.

We employ auto-correlation to determine the physical size of the speckle in a numerical reconstruction of a digital hologram of a planar test object (a resolution chart object which is discussed in detail in Section 5.3) and to test whether this approximates the theoretical values in Table 5.2. A uniform square feature in the reconstructed image is extracted and auto-correlated. It is clear from Tables 5.1 and 5.2 that the direct method produces a reconstructed image with a sampling interval approximately equal to one average speckle size. For the given parameters it turns out that the same us true for the spectral method. In order to ensure an accurate auto correlation we decided to upsample the reconstruction. We interpolated the reconstruction of the DH by a factor of 4. For the resolution chart hologram the expected speckle size in the x and y directions is 7.16μm and 9.59μm, respectively. Application of the direct method to this hologram without interpolation provides a reconstructed image with a sampling interval of 7.96μm and 1.06μm in x and y, which is approximately equal to the speckle size in x and y. After interpolation, the sampling interval reduces to 1.99μm and 2.66μm, which is significantly less than the speckle size. Similarly direct application of the spectral method to the hologram without interpolation provides a reconstructed image

Direction	Theoretical Size	Direct method	Spectral method
x	7.16μm	7.88μm	7.88μm
y	9.59μm	9.59μm	9.59μm
z	729μm	638μm	396μm

Table 5.3: Theoretical and measured speckle sizes for the USAF resolution chart DH

with a sampling interval of 6.45μm and 6.45μm in x and y (as the pixel sizes have equal extent in x and y), which once again is close to the size of the speckle in x and y. After interpolation the sampling interval reduces to 1.61μm and 1.61μm, respectively, which is, again, significantly less than the speckle size.

For the 2D case the average 2D speckle size was calculated by measuring the width of the autocorrelation peak of the intensity in the reconstruction plane [Kre05, Goo06] [see Section 2.3.2]. We found that the width at half the height of the peak matched the theoretical value well for the speckle size in the x and y directions [see Figures 5.3 and 5.4] and that there were no differences in the calculated sizes between the direct and spectral methods of reconstruction [see Table 5.3]. This was expected since both methods, numerically calculate the same field, the primary difference between them is the sampling rate and output window size.

Calculating the speckle size in the z direction was not so straightforward, but a solution we found was to save a row of pixels that run through the same homogeneous section of the resolution chart used in the 2D case at a stack of reconstruction planes around the optimum reconstruction distance in the z direction. These 1D rows of pixels were then stacked to create a 2D matrix. We note that the speckle index of this 2D area was found to be approximately 1.0. The normalized auto-correlation of a homogeneous area within this intensity speckle pattern was then calculated. Figure 5.5 clearly shows that the measured speckle size is indeed

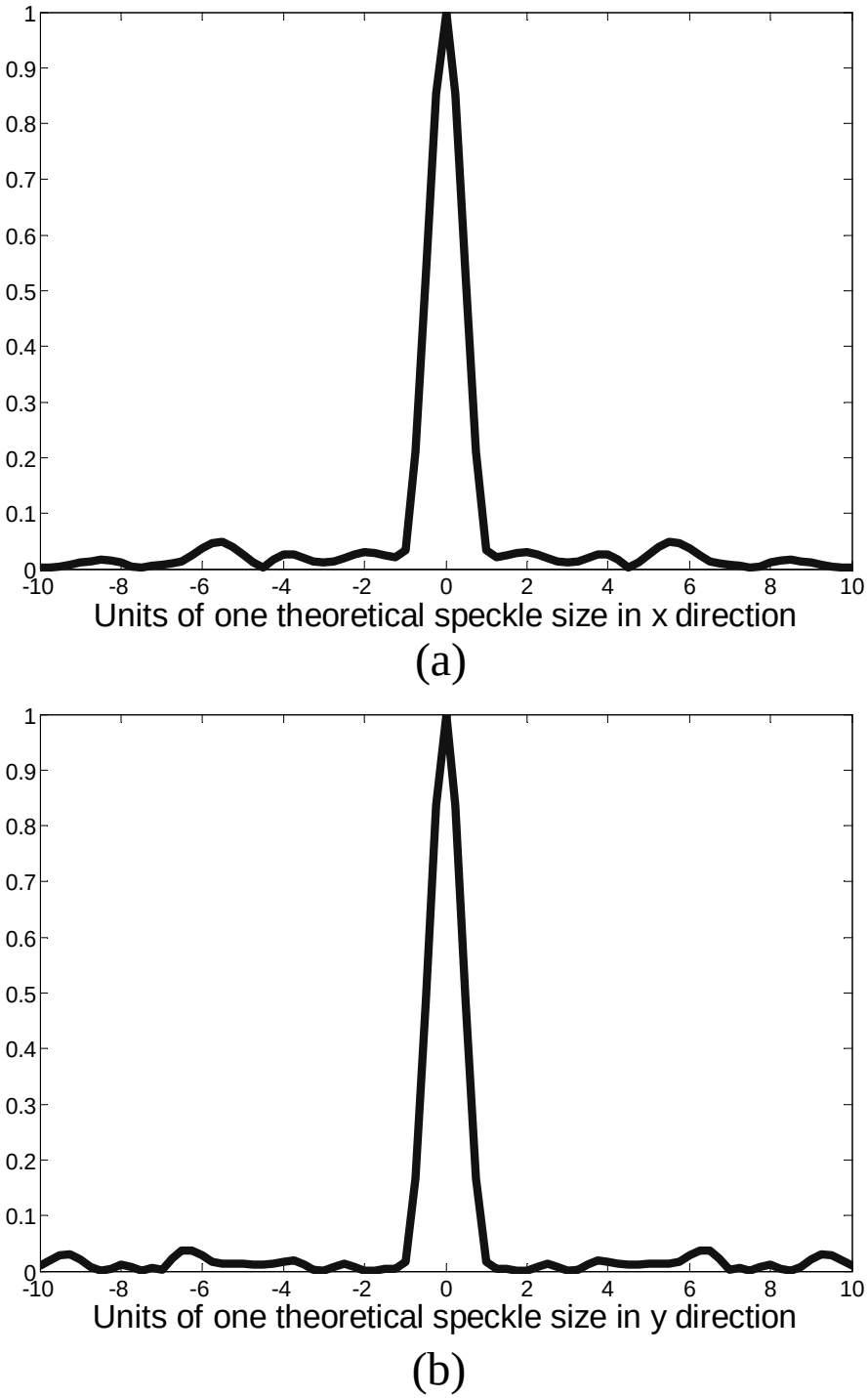

Figure 5.3: 2D speckle size when the direct method of reconstruction is used. Visualization of the speckle size in the (a) x direction and (b) y direction for the USAF resolution chart DH. The measured speckle is 1.1 the size of the theoretical size in the x direction and in the y direction matches closely the theoretical size.

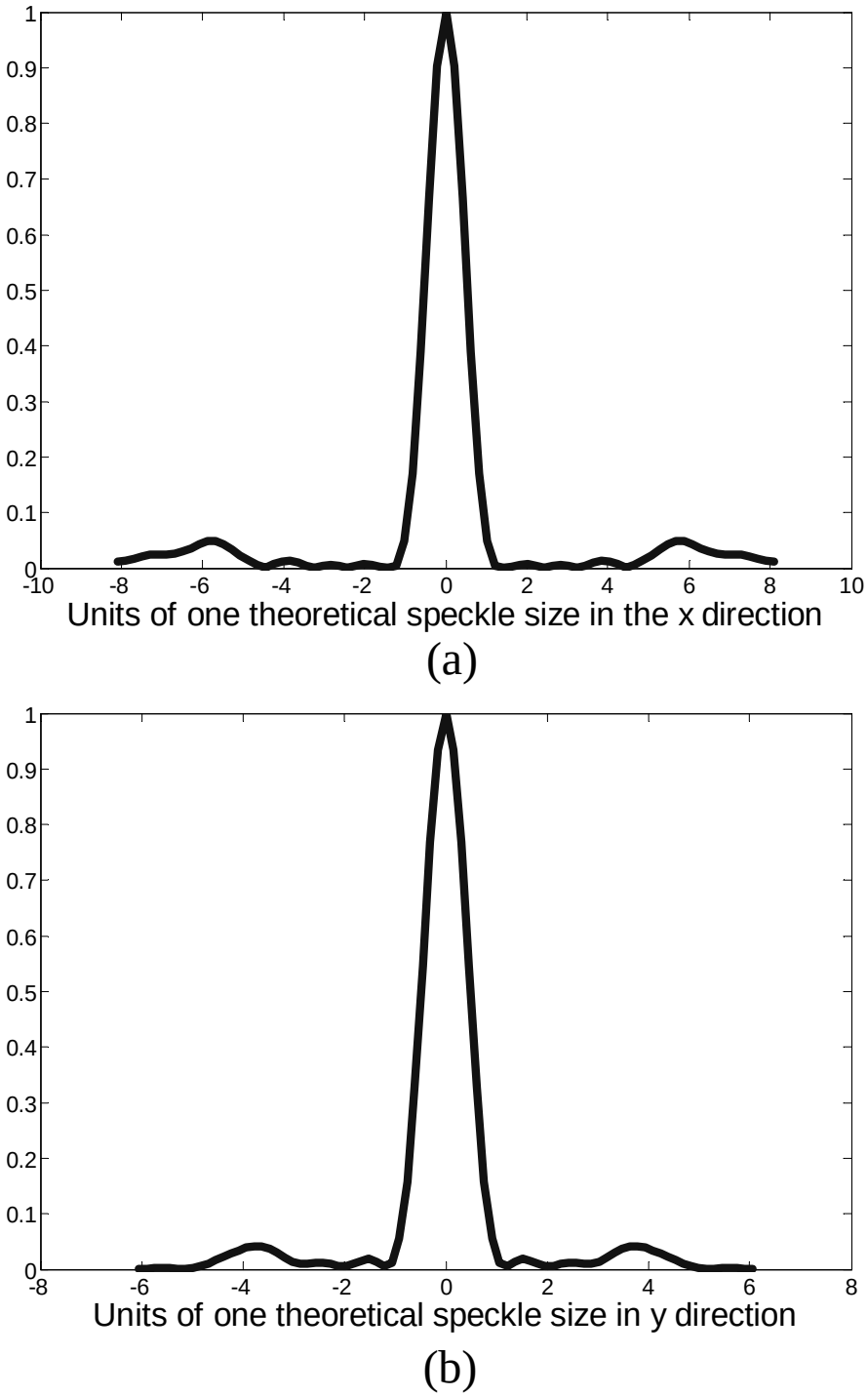

Figure 5.4: 2D speckle size when the spectral method of reconstruction is used. Visualization of the speckle size in the (a) x direction and (b) y direction for the USAF resolution chart DH. The measured speckle is 1.1 the size of the theoretical size in the x direction and in the y direction matches closely the theoretical size.

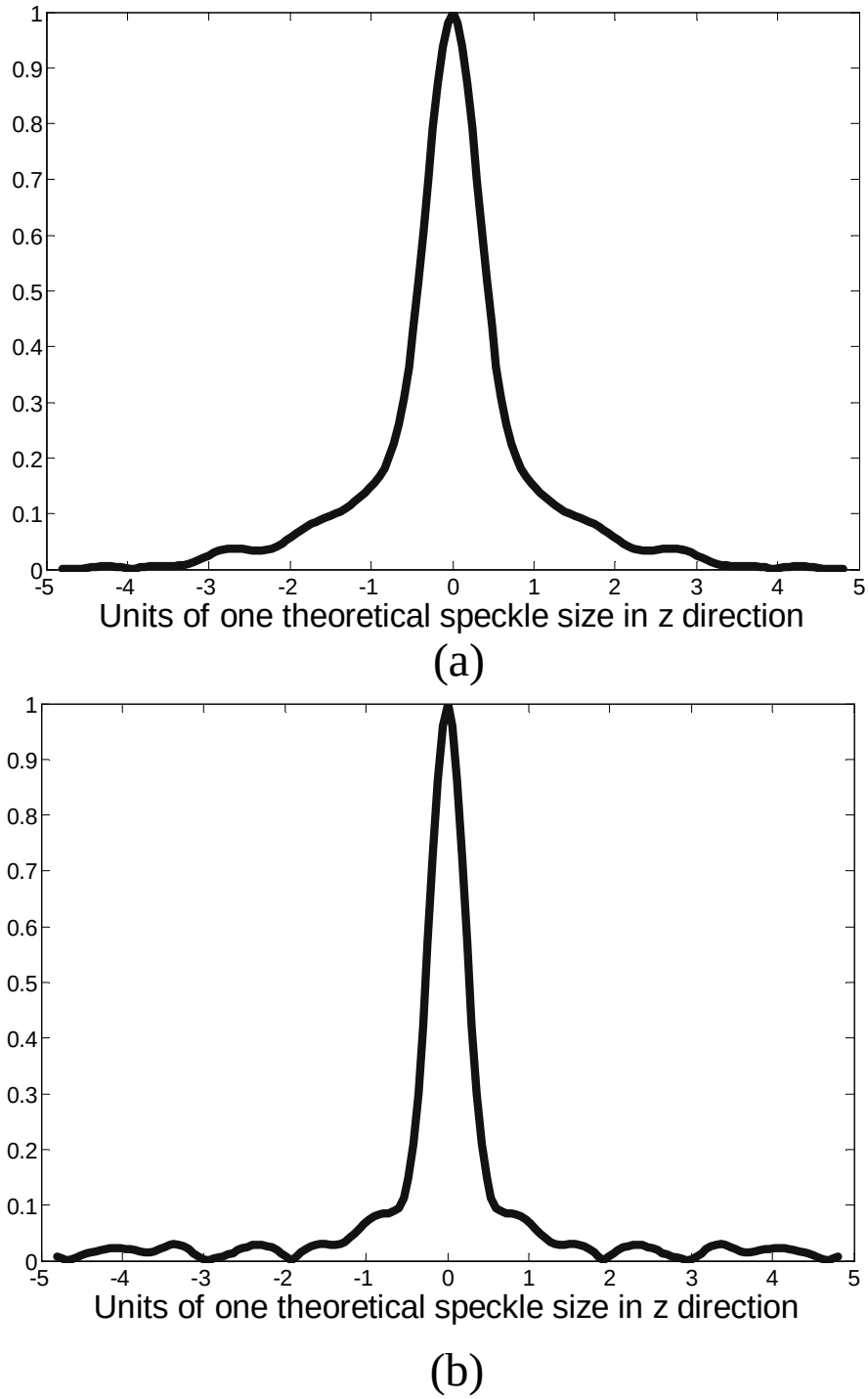

Figure 5.5: 3D speckle size. Visualization of the speckle size in the z direction for the USAF resolution chart DH using (a) direct method and (b) spectral method. The measured speckle is 0.87 the size of the theoretical size in the z direction for the direct method and 0.54 the size of the theoretical size in the z direction for the spectral method

smaller when the spectral method is used to reconstruct than when the direct method is used. This confirms what was hypothesized in the previous section that averaging along different lines [see Section 5.2.2.1] in the z direction has an effect on the calculated speckle size for each method. Table 5.3 gives the full list of theoretical versus measured speckle sizes in the x, y and z directions for the USAF resolution chart. This suggests that using Gaussian kernels with a smaller extent in the z direction when reconstructing the 3D field with the spectral method can reduce the speckle index just as much as when using a kernel with a larger extent when the 3D field was calculated with the with the direct method. However, in contrast to the direct method, stacks of images that are reconstructed using the spectral method are not aligned in the z direction and this affects the speckle index and indeed the amount of blurring in the final image. In this chapter we make no allowance for this and only use the theoretically predicted speckle length in z to derive the size of the Gaussian kernels created to filter the speckle field. Consequences of this phenomenon will be investigated in future work.

5.2.4 Gaussian filtering and our model

Gaussian filtering is often chosen for image de-noising [GW02]. The advantage of the Gaussian kernel over the rectangular kernel (mean filtering) is that no nulls occur in the frequency domain. This can be explained as follows; the FT of a *Rect* function is a *Sinc* function which contains a series of null (zero value) points in its two dimensional distribution. Since convolution in space with a *Rect* function is equivalent to multiplication in frequency by a *Sinc* function we can expect the FT of the filtered image to contain a number of null frequencies which will inevitably distort the image. Alternatively the FT of a Gaussian function is also a Gaussian function which reduces smoothly in value, but does not contain null points. A 3D Gaussian distribution has the following form

$$G(x,y,z) = A \exp\left[-\left(\frac{x^2}{2\sigma_x^2} + \frac{y^2}{2\sigma_y^2} + \frac{(z-z_0)^2}{2\sigma_z^2}\right)\right] \tag{5.5}$$

where σ_x, σ_y and σ_z are the standard deviations in the (x,y,z) directions, A is a normalization factor $1/(\sqrt{2\pi\sigma_x}\sqrt{2\pi\sigma_y}\sqrt{2\pi\sigma_z})$ and z_0 is the reconstruction distance. There exists no obvious direct relationship between the size of the Gaussian kernel and the number of independent speckles that will be averaged together resulting from the convolution. In order to simplify our analysis we attempt to apply an approximately direct relationship between the standard deviation of the Gaussian function and the reduction in speckle index. To do this we empirically investigate 2D Gaussian filtering of a test hologram of a USAF resolution chart with a range of different standard deviation values. Our assumption is that our model will be similar to the model used for predicting the speckle index when multiple independent speckle patterns are added together. In that case the speckle index is given by $1/\sqrt{M}$ where M statistically independent images are added together [Goo06]. In this case we assume that Gaussian filtering will result in a speckle index given by $1/\sqrt{M_x}$, where M_x is a linear function of σ_x. In order to derive this function we use two expected values. The first is when $\sigma_x \to 0$, the speckle index, C, should be 1 indicating no speckle reduction. Thus as the Gaussian function narrows to approximate a Dirac delta function, it allows the input to pass through unimpeded and there will only be one independent speckle pattern giving $C = 1$. Upon investigation of our experimental measurements a second point of interest was chosen, this time with $\sigma_x = S_x$ and $C \approx \frac{1}{2}$. Therefore we conclude that an approximate model for the speckle index resulting from 1D Gaussian filtering in the x direction is given by

$$C = \frac{1}{\sqrt{1 + \frac{3\sigma_x}{S_x}}}. \tag{5.6}$$

A similar model can be used for 1D filtering in both the y and z directions. Extension to the 2D case is given by the product of the 1D values,

$$C = \frac{1}{\sqrt{1 + \frac{3\sigma_x}{S_x}}} \times \frac{1}{\sqrt{1 + \frac{3\sigma_y}{S_y}}} \tag{5.7}$$

and it follows that the 3D case is given by,

$$C = \frac{1}{\sqrt{1 + \frac{3\sigma_x}{S_x}}} \times \frac{1}{\sqrt{1 + \frac{3\sigma_y}{S_y}}} \times \frac{1}{\sqrt{1 + \frac{3\sigma_z}{S_z}}}. \tag{5.8}$$

The theoretical values for the speckle index resulting from 1D, 2D and 3D Gaussian filtering will be presented in Section 5.4 and as will be readily seen they closely agree with the experimental results.

Finally, we note that the result of the convolution of a 3D image with a 3D kernel is another 3D image, with each slice being a smoothed version of itself. It is possible to reduce the computational complexity of the operation if only one slice, say the original reconstruction plane, is required. The convolution can be calculated for this slice, resulting in one of the summations from Equation. 5.4 not having to be computed. If the kernel is separable, which means that it can be described by the multiplication of a number of 1D vectors (2 for a 2D kernel, 3 for a 3D kernel), then the convolution can be broken into a number of parts. A 2D Gaussian kernel is an example of a kernel that can be separated into two 1D kernels. This can significantly reduce the computational complexity of the operation, although it requires some extra storage space to keep intermediate computations. Finally, when dealing with large 3D images and kernels, it might also be computationally less expensive to compute the DFT of both signals and then the convolution operation reduces to a multiplication operation. The final result being the inverse DFT of this multiplication. As efficiency was not the primary focus of this work, such considerations are only noted here, but were not

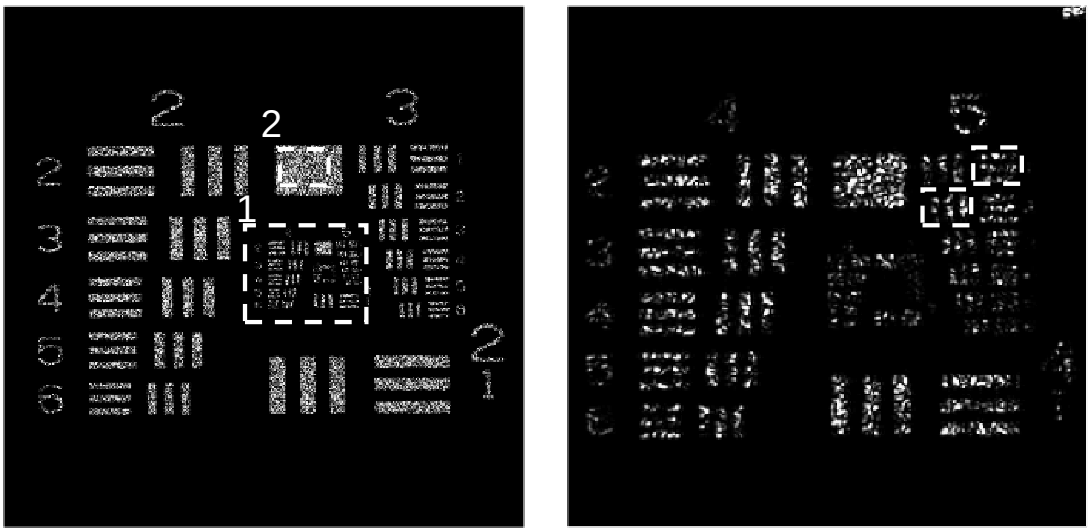

Figure 5.6: The USAF resolution chart used to quantify the loss of resolution. (a) The full chart, and (b) a zoomed in section of smaller details (these are marked with region of interest box 1 in (a)). The chart has a fully developed speckle pattern (speckle index is calculated on the homogeneous section marked with region of interest box 2 in (a)) and using visual inspection the minimum resolvable bars in x and y is highlighted by the two dashed white lined rectangles in (b).

implemented.

5.3 Metrics

A reduction in speckle contrast often comes at the expense of a reduction in resolution. In order to take both factors into consideration we use speckle index [see Section 3.3] and a resolution metric to quantify the results. Figure 5.6 shows a reconstruction of a DH (with no speckle reduction applied) of a USAF resolution chart, purchased from Edmund Optics, which is opaque except for the transparent

areas [KHP+09]. Deciding upon the resolution is a subjective process involving visual inspection. In order to ensure a consistent measurement of resolution across the entire data set we define a set of measurement criteria for the detection of a minimum value. The minimum resolvable set of lines must obey the following rules;

1. There should be clear separation between the bars in a given group of three, i.e., the contrast between the bars and the space between the bars should be strong enough to preclude any doubt that there is a gap between the bars.

2. Individual bars do not need to be contiguous and can be corrupted by speckle noise.

3. Each set of bars with a lower resolution than the chosen set should also be resolvable.

4. A set of bars is not penalized if a neighboring set of bars blurs into it.

5. If it is not clear what the resolution is between two sets of bars then the lower resolution is chosen.

When no speckle reduction is applied the resolution, seen in Fig. 5.6 (b), in the x direction (vertical bars) is group 5 element 1, or 35.91 line pairs per millimeter, and the resolution in the y direction (horizontal bars) is group 5 element 2, or 32 line pairs per millimeter. The resolution, R, which denotes the of the number of lines per millimeter is given by $R = 2^{G+(E-1)/6}$, where G is the group and E the element within that group. Groups 2 and 3 both containing elements 1 through 6 are clearly visible in Figure 5.6 (a). For the remainder of the paper the resolution is given in line pairs per millimeter.

We now discuss the expected theoretical resolution for the resolution DH. The approximate bandwidth limit for a DH system is imposed by the aperture of the

camera, $W_{CCDx,y}$, the wavelength of the laser used in the system, λ, and the object camera distance, z_0 [KHP+09];

$$\text{Bandwidth}_{x,y} \cong \frac{W_{CCDx,y}}{\lambda z_0}, \tag{5.9}$$

where the x, y subscript denotes that the equation is valid for both the x and the y parameters. We can rewrite the equation above in terms of system parameters

$$\text{Bandwidth}_x \cong \frac{N_x \Delta\xi}{\lambda z_0}, \tag{5.10}$$

$$\text{Bandwidth}_y \cong \frac{N_y \Delta\eta}{\lambda z_0}. \tag{5.11}$$

Therefore we can expect a complex image that is recorded by a DH system will have a frequency range in f_x and f_y (spatial frequency coordinates corresponding to x and y respectively) given by;

$$|f_x| \lessapprox \frac{N_x \Delta\xi}{2\lambda z_0}, \tag{5.12}$$

$$|f_y| \lessapprox \frac{N_y \Delta\eta}{2\lambda z_0}. \tag{5.13}$$

The maximum recoverable spatial frequency is given by

$$f_{x_{max}} \cong \frac{N_x \Delta\xi}{2\lambda z_0}, \tag{5.14}$$

$$f_{y_{max}} \cong \frac{N_y \Delta\eta}{2\lambda z_0}. \tag{5.15}$$

We note that the maximum recordable frequency is directly proportional to the camera width in the direction of interest and is inversely proportional to the wavelength and the camera object distance. We also note that there are at least three

other factors that further reduce the bandwidth of the system [KHP+09]; these include (i) the averaging effect of the pixel, which for a Fresnel system amounts to an averaging of the complex reconstruction; (ii) the effect of sampling which can result in overlapping replicas of the reconstruction; and (iii) the pixel quantization, which can lead to errors in the reconstructed image [PH11]. Furthermore, we expect the speckle noise (and indeed other sources of noise) to further impact on resolution. Thus, it should be stated that the limits given above in Equations. 5.14 and 5.15 are approximate and should be treated as upper limits. In practice we can expect that the maximum recordable frequencies will be less than the values determined by Equations. 5.14 and 5.15.

The unit of lines per millimeter can be related to maximum recoverable frequency of the system. This unit is based on the number of bright and dark line pairs that can be found in a length of 1mm. Equations 5.14 and 5.15 can be interpreted as the number of bright and dark lines that can be found in a length of 1m, assuming that all of the parameters in the equations are defined in meters. Therefore we can redefine the theoretical maximum frequencies in terms of the pairs per millimeter as follows

$$f_{x_{max}} \cong \frac{N_x \Delta\xi}{2\lambda z_0}, \tag{5.16}$$

$$f_{y_{max}} \cong \frac{N_y \Delta\eta}{2\lambda z_0}. \tag{5.17}$$

For the resolution chart DH, the parameters of which are defined in Table 5.4 (DH 1), and we can calculate the values of the theoretical maximum frequencies to be

$$f_{x_{max}} \cong 62.85(\text{line pairs / mm}), \tag{5.18}$$

$$f_{y_{max}} \cong 46.95(\text{line pairs / mm}). \tag{5.19}$$

DH	$\lambda(\mu\text{m})$	$\Delta\xi(\mu\text{m})$	$\Delta\eta(\mu\text{m})$	N_x	N_y	$z_0(\text{m})$
1	0.785	6.45	6.45	1392	1040	0.091
2	0.785	6.45	6.45	1392	1040	0.279
3	0.785	6.45	6.45	1392	1040	0.3
4	0.785	6.45	6.45	1392	1040	0.394
5	0.785	3.45	3.45	2448	2050	0.105

Table 5.4: Parameter details for DHs used in the experiments. The numbers 1 through 5 are labels for DHs of the USAF resolution chart, two screws, a toy spindle, a stormtrooper object and two small chairs. λ: wavelength of the light used, $\Delta\xi$: sensor pixel size in x, $\Delta\eta$: sensor pixel size in y, N_x, N_y: number of pixels on the sensor in x and y respectively, z_0: distance of the object to the sensor.

As expected the experimental values of 35.91 and 32 lines pairs / mm respectively fall some way short of the expected theoretical maximum values. We add one final note. If we are correct in our previous assumption that the speckle noise will impact on the maximum recordable frequencies, then we can expect that speckle reduction may increase the number of line pairs per millimeter that can be observed in the image.

5.4 Experimental results

In order to test our approach, reconstructions of the resolution chart DH introduced in the previous section were used to quantify the improvement in speckle contrast and the resulting loss in resolution. We investigated 1D filtering in the x, y and z directions separately, 2D filtering in the x y plane, and finally full 3D filtering in all three spatial directions. In all cases resolution results are provided separately for x and y. We provide evidence that our model closely approximates the theory in

DH	$S_x(\mu\text{m})$	$S_y(\mu\text{m})$	$S_z(\mu\text{m})$
1	7.16	9.59	729
2	21.2	29.4	6800
3	23.6	31.6	7900
4	31	41.5	13600
5	8.74	10.43	1000

Table 5.5: Theoretical speckle size for each DH. S_x, S_y and S_z are the sizes in x, y and z respectively. These values are calculated using Equations in Table 5.2, and the DH parameters given in Table 5.4.

terms of speckle reduction for a given number of independent speckle patterns. We also provide evidence that an improvement in the depth of focus can be achieved when filtering in the z direction, if the object of interest has an appreciable extent in this direction.

Following our analysis with the resolution chart DH, we investigate the performance of the method on a number of different holograms. Tables 5.4 and 5.5 provide details such as sensor pixel sizes, number of pixels on the sensor, reconstruction distances, wavelength of the light used during capture and the theoretical speckle sizes (based on Equations in Table 5.2) for the DHs tested in this paper. Table 5.6 gives details of the sampling intervals in and around the reconstruction plane used in all three directions for both reconstruction methods (direct and spectral method). We note here again that the sampling interval in the z direction is calculated using the concept of depth of focus given by Kreis [Kre05]. In Section 5.2.2.1 we postulated that the effective speckle size could be smaller in the z direction when the images are stacked using the spectral method because the direction of the lines along which the averaging occurs in the z direction is different to the direction of the speckle and indeed in Section 5.2.3 we measured a slightly

	Direct Method			Spectral Method		
DH	$T_x(\mu\text{m})$	$T_y(\mu\text{m})$	$T_z(\mu\text{m})$	$T_x(\mu\text{m})$	$T_y(\mu\text{m})$	$T_z(\mu\text{m})$
1	7.96	10.66	161.64	6.45	6.45	175.19
2	24.39	32.65	1500	6.45	6.45	536.54
3	26.23	35.1	1800	6.45	6.45	576.92
4	34.45	46.11	3000	6.45	6.45	757.69
5	9.71	11.59	240.37	3.45	3.45	101.95

Table 5.6: Sampling intervals in x, y and z for both the direct and spectral methods for the DHs used in this paper. T_x: Sampling interval in x, T_y: Sampling interval in y, T_z: Sampling interval in z (given by the depth of focus). We note that these are the calculated theoretical sampling intervals and that these are reduced further to ensure sufficient sampling of the 3D field.

smaller speckle size. For the experiments carried out on the resolution chart DH we do not adapt the size of the Gaussian kernels to take this into account as the difference in speckle size was quite small due to the small camera object distance (0.091m) at which the resolution chart was recorded. For larger camera object distances this effect is more pronounced and the size of the filter used should be adapted accordingly if the spectral method is used to reconstruct the DH. As all of our tests were carried out on the resolution chart DH, we determined the width of the Gaussian kernel based on the dimensions of the theoretical speckle size (given in Table 5.5, DH 1). Table 5.6, by giving values for the depth of focus for all DHs used, also gives an insight into the size of the sampling period need to ensure sufficient sampling is performed. The values in Tab 5.6 were calculated using the equations given in Table 5.1 and the parameters in Table 5.4. In the following sections tests are carried out with the resolution chart DH and using both the direct and the spectral method of reconstruction.

5.4.1 1D filtering

Our initial tests involve filtering with Gaussian kernels that have extent in only one direction (x, y or z). Figure 5.7 (a) plots the resolution in x and y for 1D filtering in the x direction. Initially the resolution in x is better than that in y due to the fact that the CCD is rectangular and is larger in the x direction (0.009m versus 0.0067m) [KHP$^+$09]. We observe an improvement in the y resolution, before a slight dip, and then the resolution remains constant at 35.91 line pairs per mm. It is an interesting phenomenon that the resolution can increase through filtering (as was predicted in Section 5.3), but it can be attributed to an improvement in image quality brought about by the reduction in speckle. As expected, the resolution in x steadily degrades as the width of the Gaussian filter increases until, when $\sigma_x = 5$ (units of S_x), only 4.49 line pairs per mm can be observed. Figure 5.8 shows the effect on speckle index when filtering in the x, y and z directions using both the direct and the spectral methods of reconstruction. It confirms that our model reflects the actual speckle index very well. We note that there are small differences between the direct and spectral methods with the latter method having a slightly smaller speckle index. Figure 5.9 shows a section of the resulting resolution chart after filtering is applied only in the x direction. Figure 5.7 (b) plots the resolution in x and y for 1D filtering in the y direction. This time we observe an improvement in resolution in the x direction from 35.91 line pairs per mm up to 45.25 line pairs per mm. However this degrades to 32 lines as the filter size reaches larger sizes (for $\sigma_y = 4.5S_y$ to $5S_y$). The reason for this is that sets of 3 vertical bars start to blur into each other, thus reducing the resolution. Figure 5.7 (c) plots the resolution in x and y for 1D filtering in the z direction. As we are averaging along a direction that is orthogonal to both x and y there is no improvement in resolution as the filter kernel size increases, only a degradation. We note that for this method of filtering there was more noise between pairs of bars that we consider resolved than

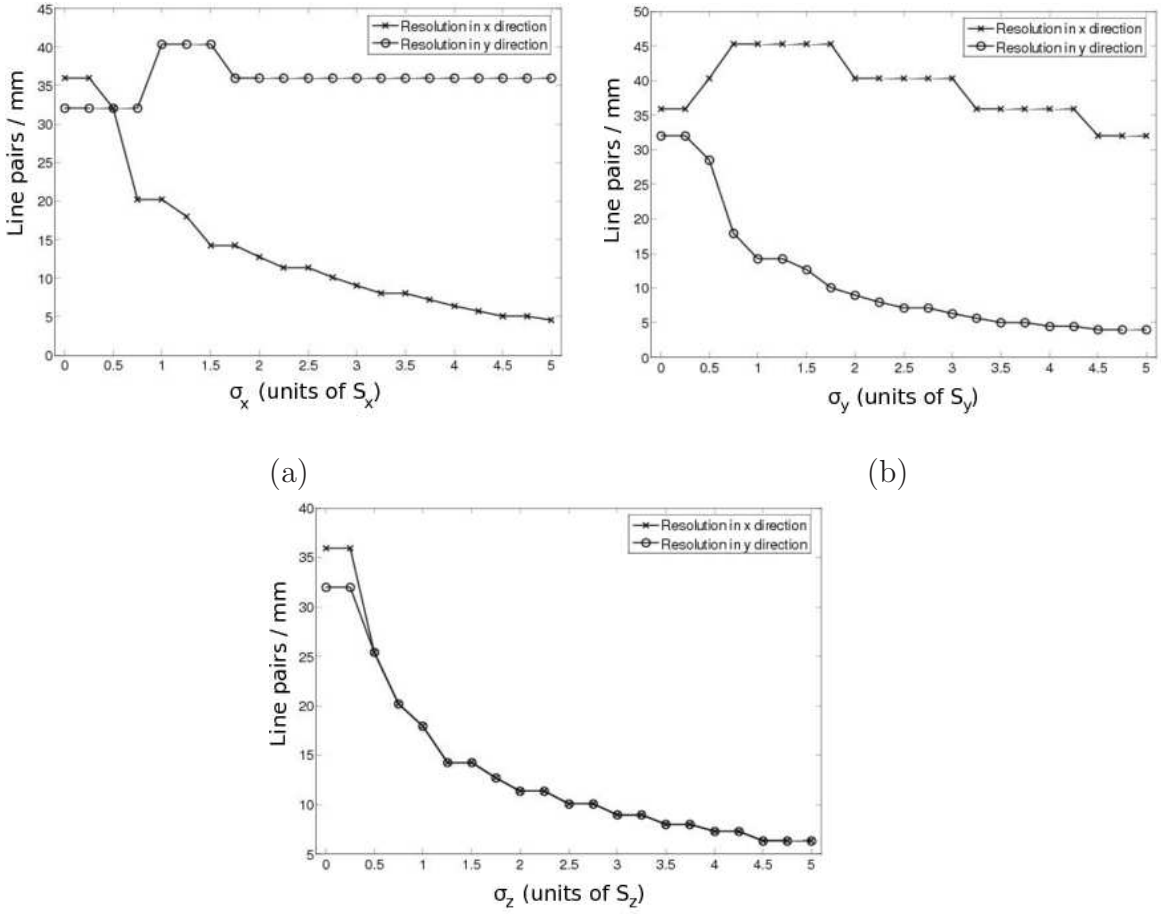

(a) (b)

(c)

Figure 5.7: Resolution in x and y when filtering only in the x direction (a), only in the y direction (b) and only in the z direction (c). These results are applicable to both the direct and spectral methods of reconstruction as the resolution was the same regardless of which method was chosen.

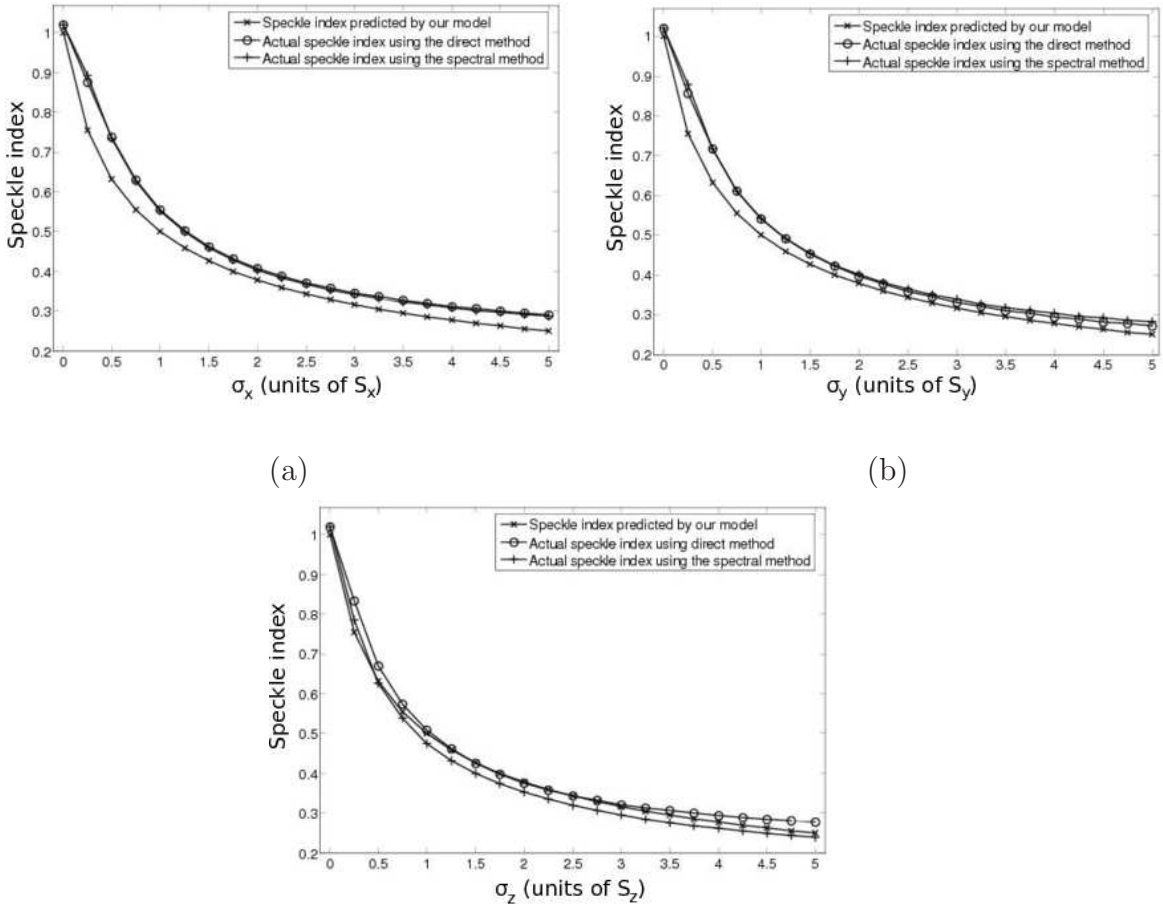

Figure 5.8: Speckle index when filtering only in the x direction (a), only in the y direction (b) and only in the z direction (c).

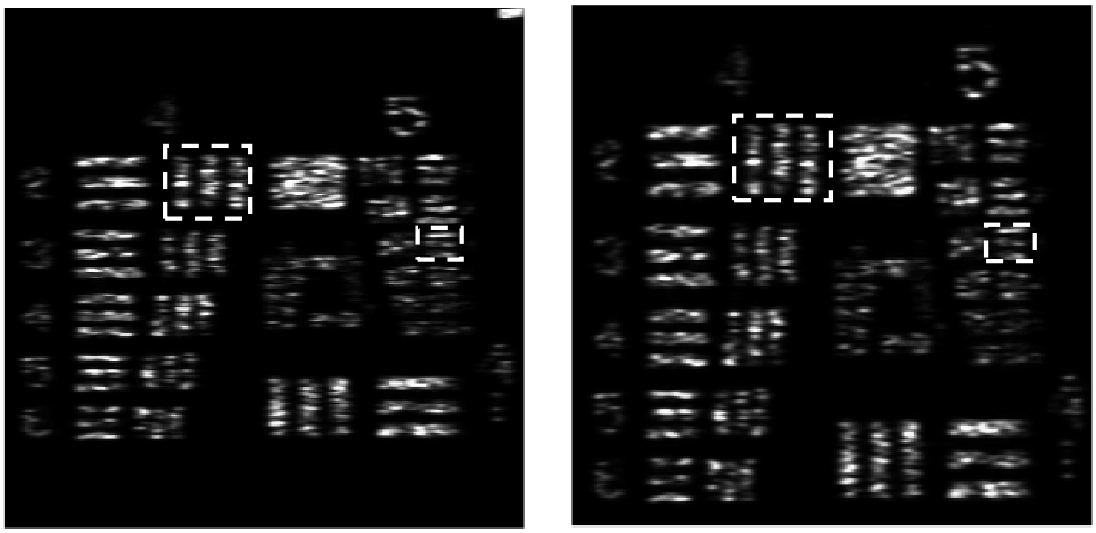

Figure 5.9: Filtering only in the x direction with $\sigma_x = 1.25S_x$ (a) Using the direct method of reconstruction, and (b) using the spectral method of reconstruction. In both reconstruction cases the x resolution is 17.95 line pairs per mm and the y resolution is 40.31 line pairs per mm. The speckle contrast was reduced to a speckle index of 0.5025 in the case of the direct method and 0.4984 for the spectral method.

for the similar 1D x and y filtering. We also note that for larger filter kernels this method outperforms the previous two conditions in at least one direction and if the desired goal is to have good resolution in both x and y directions, this could be the method of choice in the event only 1D filtering is to be carried out. If improved resolution is required is another direction then the Gaussian kernel can be rotated as required.

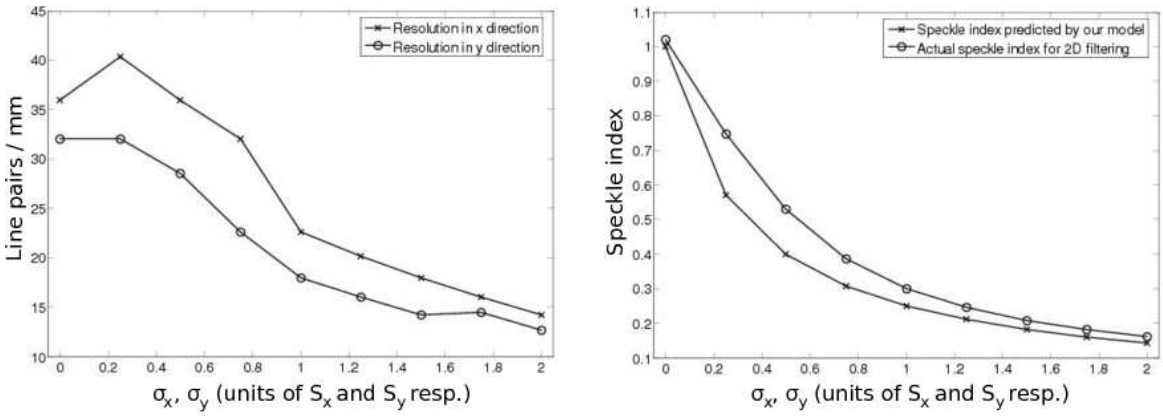

(a) (b)

Figure 5.10: (a) Resolution in x and y when filtering in 2D. These results are applicable to both the direct and spectral methods of reconstruction as the resolution was the same regardless of which method was chosen. (b) Graph showing the expected theoretical value of the speckle index versus the actual speckle index when filtering in 2D in x and y. As there were only negligible differences in speckle index between the direct and spectral reconstruction methods, only the direct method is plotted here

5.4.2 2D filtering

In this section, we take the next logical step and filter using a Gaussian kernel with extent in both the x and y direction. Figure 5.10 (a) plots the resolution in x and y for 2D filtering in the x and y directions. The resolution in x is better than that in y due to the larger extent of the sensor in the x direction for all tests conducted. We note an initial improvement in the x direction resolution from 35.91 line pairs per mm (with no filtering) to 40.31 line pairs per mm, and thereafter as the filter kernel increases in size the resolution reduces. At first the resolution in the y direction remains the same as when no filtering is applied at 35.91 line pairs per mm, but then resolution degrades at approximately the same rate as

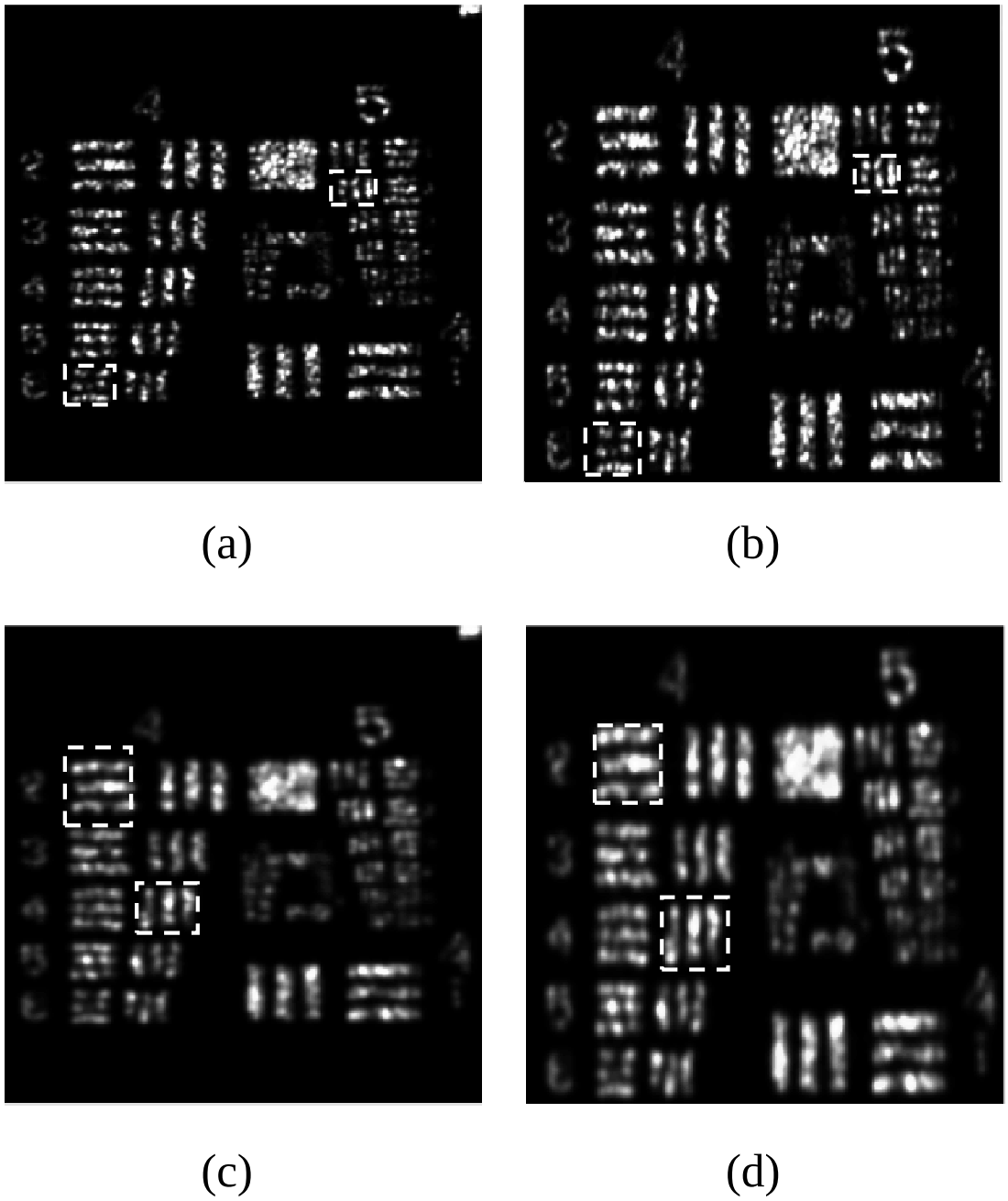

Figure 5.11: Filtering in 2D in the x and y directions with M_x and M_y set to 2. (a) Using the direct method of reconstruction (speckle index = 0.5292), and (b) using the spectral method of reconstruction (speckle index = 0.5285). In both cases the x resolution is 35.92 line pairs per mm and the y resolution is 28.51 line pairs per mm. Filtering in 2D in the x and y directions with $\sigma_x = \frac{S_x}{4}$ and $\sigma_y = \frac{S_y}{4}$. (c) Using the direct method (speckle index = 0.3005), and (d) using the spectral method (speckle index = 0.3005). In both cases the x resolution is 22.63 line pairs per mm and the y resolution is 17.96 line pairs per mm.

that in x. If maintaining resolution in both x and y directions is important, then 2D filtering provides large gains over 1D filtering. Figure 5.10 (b) plots the actual speckle index achieved when filtering in 2D against the expected theoretical speckle index. The model once again approximates the theoretical expected speckle index values well. Figure 5.11 (a) and (b) shows that with σ_x and σ_y set to $\frac{S_x}{2}$ and $\frac{S_y}{2}$, respectively, the x resolution is 40.31 line pairs per mm and the y resolution is 32 line pairs per mm, and the speckle index is approximately 0.52. In comparison, if we were to filter in 1D in any direction and our aim was to achieve a similar speckle index (i.e., a value close to 0.5), the best case would be filtering in the x direction which provides 20.15 line pairs per mm in x resolution, while of course having better resolution in the y direction at 40.31 line pairs per mm. Comparing 2D filtering with 1D filtering is difficult, but a general rule of thumb is that if resolution is required in both spatial directions then 2D filtering should be chosen over 1D filtering. Furthermore, due to the separability of the Gaussian kernel, the 2D filter can be implemented as a pair of orthogonal 1D Gaussians, which reduces the computational complexity from $O(n^2)$ to $O(2n)$.

5.4.3 3D filtering

In this section, we take advantage of the inherent 3D nature of DHs and and filter using a Gaussian kernel with support in the x, y and z directions. Figure 5.12 (a) plots the resolution in x and y for 3D filtering, where σ_x, σ_y and σ_z are increased by equal multiples of S_x, S_y and S_z, respectively. The resolution in x is better than that in y for the first two kernel sizes, but after that the resolution is the same in both directions. The trend is for resolution to degrade in both directions as the kernel size increases in x, y and z. Figure 5.12 (b) plots the actual speckle index achieved when filtering in 3D against the expected theoretical speckle index. We note that there are larger differences between the model and

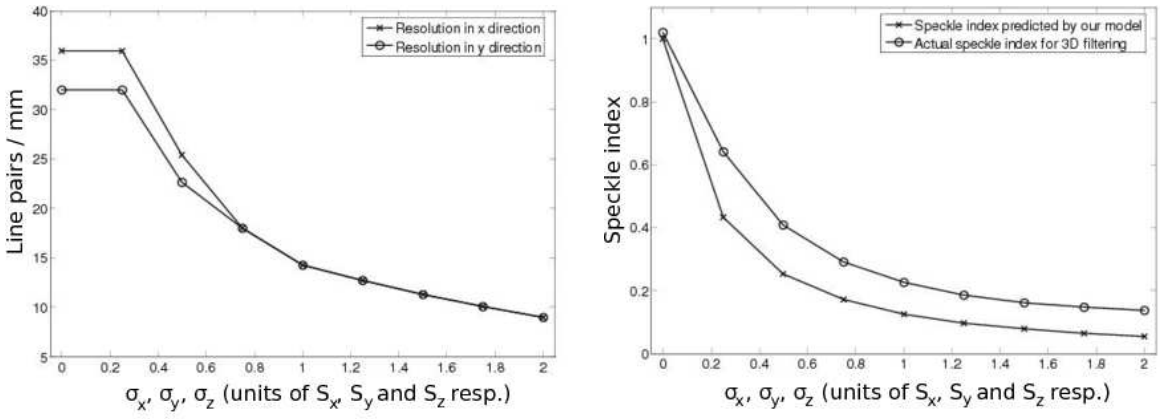

(a) (b)

Figure 5.12: (a) Resolution in x and y when filtering in 3D. These results are applicable to both the direct and spectral methods of reconstruction as the resolution was the same regardless of which method was chosen. (b) Graph showing the expected theoretical value of the speckle index versus the actual speckle index when filtering in 3D in the x, y and z directions.

theoretical expected speckle index values than for the 1D or 2D filtering cases. Figure 5.13 shows a result for 3D filtering when σ_x, σ_y and σ_z are set to $\frac{S_x}{2}$, $\frac{S_y}{2}$ and $\frac{S_z}{2}$, respectively. If resolution in both the x and y directions is important then 3D filtering outperforms 1D filtering. For this example the speckle index is approximately 0.4 for both reconstruction methods and the resolution in x is 25.4 line pairs per mm and resolution in y is 22.63 line pairs per mm. In comparison, if we were to filter in 1D in any direction and our aim was to achieve a similar speckle index (i.e., a value close to 0.4), the best case would be filtering in the z direction which provides 14.25 line pairs per mm in both the x and y directions. However, when compared with 2D filtering, 3D filtering performed slightly worse for every test, when the criteria is to have good resolution in both the x and y directions coupled with a low speckle index. We note that the USAF resolution DH is a planar object and thus has no extent in the z direction. We expect 2D

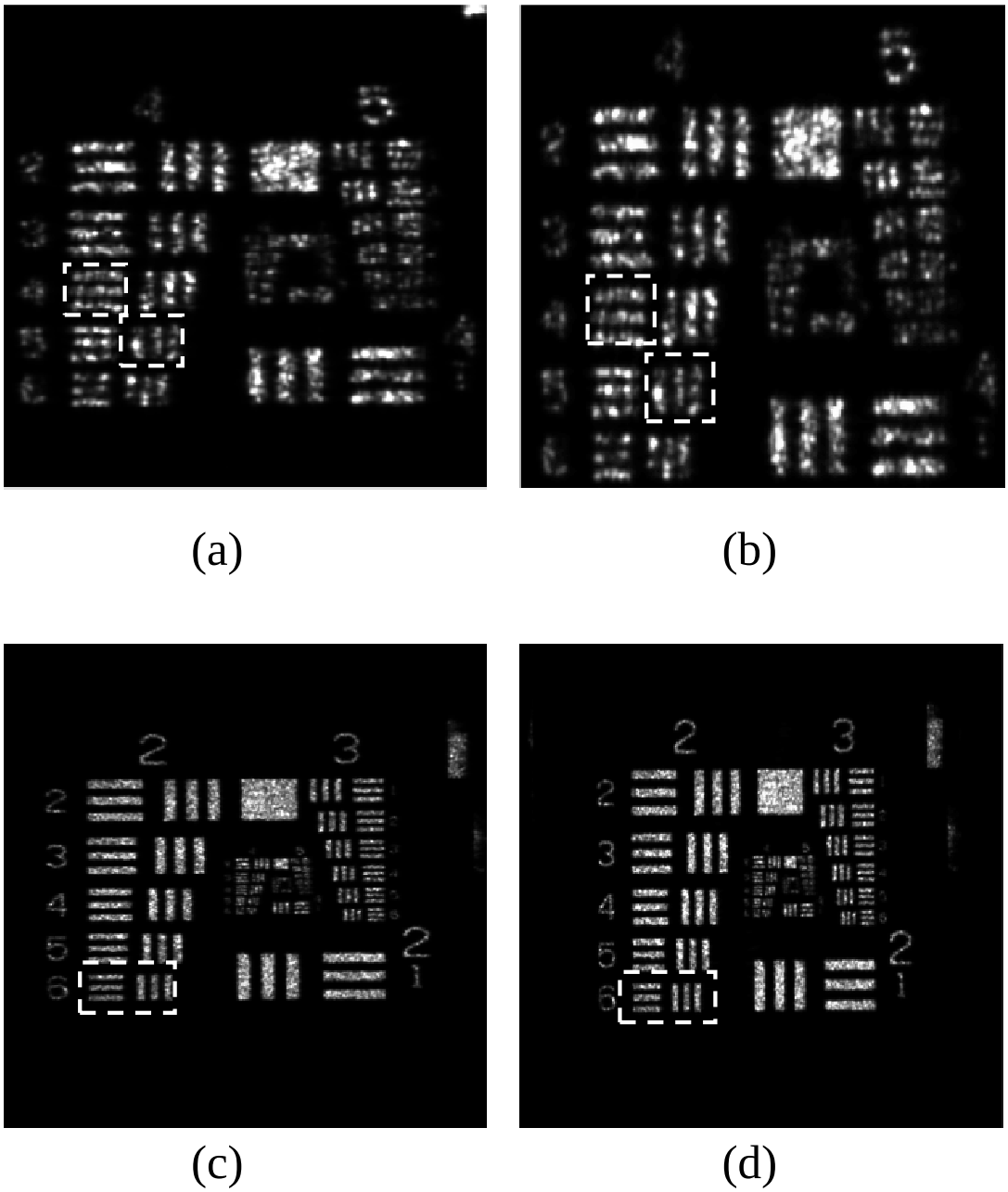

Figure 5.13: Filtering in 3D in the x, y and z directions with $\sigma_x = \frac{S_x}{2}$, $\sigma_y = \frac{S_y}{2}$ and $\sigma_z = \frac{S_z}{2}$. (a) Using the direct method of reconstruction (speckle index = 0.4079), and (b) using the spectral method of reconstruction (speckle index = 0.4037). In both reconstruction cases the x resolution is 25.4 line pairs per mm and the y resolution is 23.63 line pairs per mm. Filtering in the x, y and z directions with $\sigma_x = \frac{S_x}{4}$, $\sigma_y = \frac{S_y}{4}$ and $\sigma_z = \frac{S_z}{4}$. (c) Using the direct method of reconstruction (speckle index = 0.2252), and (d) using the spectral method of reconstruction (speckle index = 0.2267). In both reconstruction cases the x and y resolution is 14.25 line pairs per mm.

filtering to perform extremely well on such an object. This does not, however, mean that 3D filtering should be dismissed, as it can perform well if the object has extent in the z direction. Then we actually observe, with astute positioning of the filter, an improvement in the depth of focus too.

We also performed 2D and 3D filtering on in-line DHs 2-4 from Table 5.4. Figure 5.14 shows the results when filtering was applied to a stormtrooper DH for the 2D and 3D cases for with different sized Gaussian kernels. In the following exemplar figures the original reconstruction is shown with no speckle reduction applied, then the result of applying 2D filtering with $\sigma_x = 2S_x$ and $\sigma_y = 2S_y$ and finally the result of applying 3D filtering with $\sigma_x = 1.75S_x$, $\sigma_y = 1.75S_y$ and $\sigma_z = 1.75S_z$. The resulting speckle index for the reconstructions with 2D filtering applied is ≈ 0.14 (theoretical value given by our model is 0.16) and for the reconstructions with 3D filtering applied is ≈ 0.09 (theoretical value is 0.064). For these settings the 3D filtering result [Figure 5.14 (d)] is slightly more blurred, but has a lower speckle index, than the 2D filtering result [Figure 5.14 (c)]. Similar figures are shown for a DH of two bolts [see Figure 5.15] and a DH of a small spindle object [see Figure 5.16].

Although our quantitative results using the resolution chart DH revealed no benefit in choosing 3D filtering over 2D filtering, the ability to average in another dimension can be advantageous under certain circumstances. Filtering in the z direction with objects that have extent in that direction can improve the depth of focus of resulting image. To illustrate this we investigated filtering a DH of two small chairs in the z direction and provide qualitative evidence that the depth of focus is indeed improved. The DH was recorded with the parameters shown in row 5 in Table 5.4. The same laser was used to record this hologram as in the case of the resolution chart but the recording distance was a little further from the camera at 0.105m. We note that the expected speckle size is a little

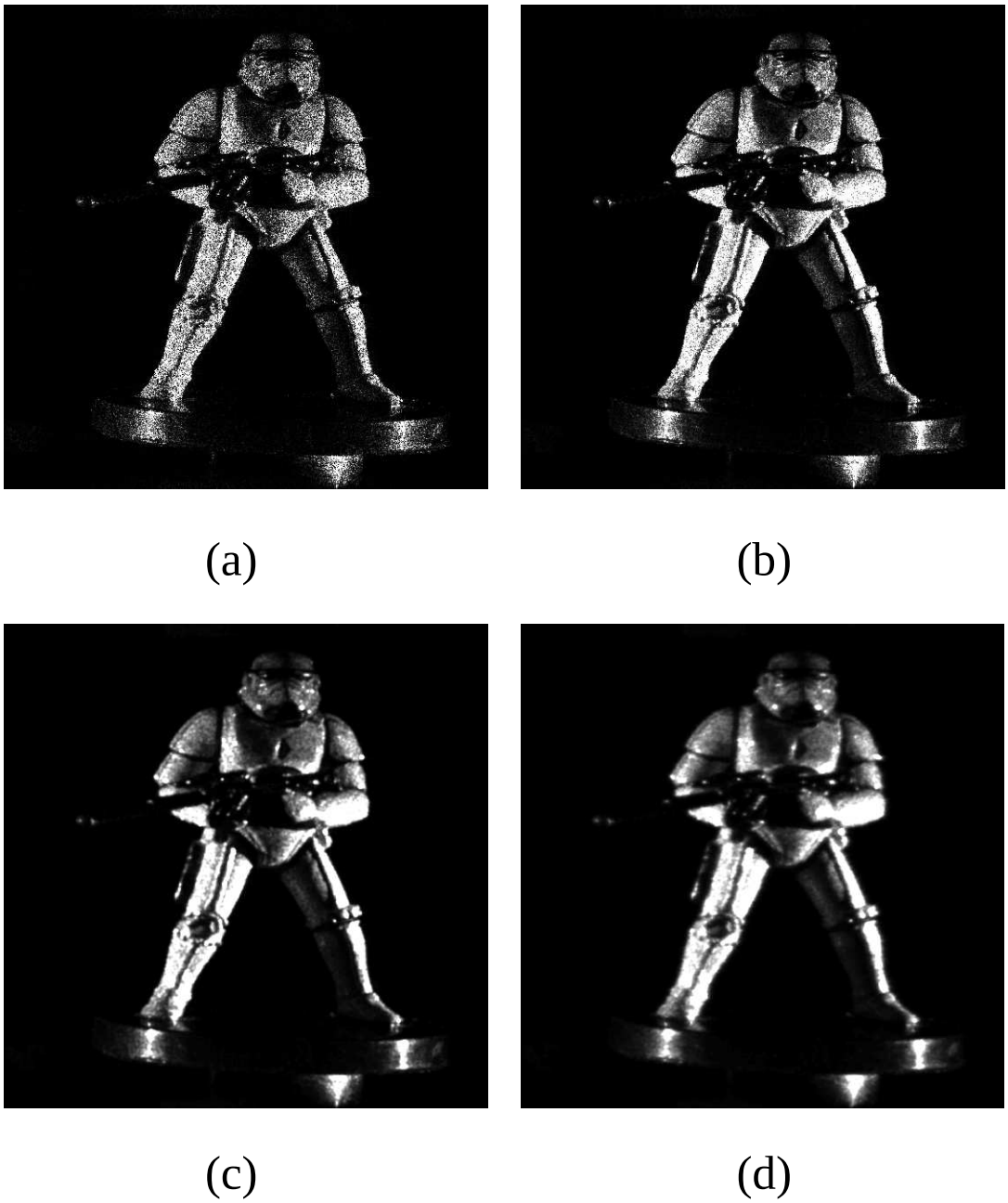

Figure 5.14: Filtering in 2D and 3D applied to an in-line DH of a stormtrooper object. (a) the original reconstruction with no speckle reduction applied, (b) 2D filtering applied with parameters $\sigma_x = 0.5S_x$ and $\sigma_y = 0.5S_y$ resulting in a speckle index of 0.4916, x resolution of 35.92 line pairs per mm and y resolution of 28.51 line pairs per mm. (c) 2D filtering applied with parameters $\sigma_x = 2S_x$ and $\sigma_y = 2S_y$ resulting in a speckle index of 0.1253, x resolution of 16 line pairs per mm and y resolution of 14.25 line pairs per mm, and (d) 3D filtering applied with parameters $\sigma_x = 1.75S_x$, $\sigma_y = 1.75S_y$ and $\sigma_z = 1.75S_z$ resulting in a speckle index of 0.0975, x resolution of 10.08 line pairs per mm and y resolution of 10.08 line pairs per mm.

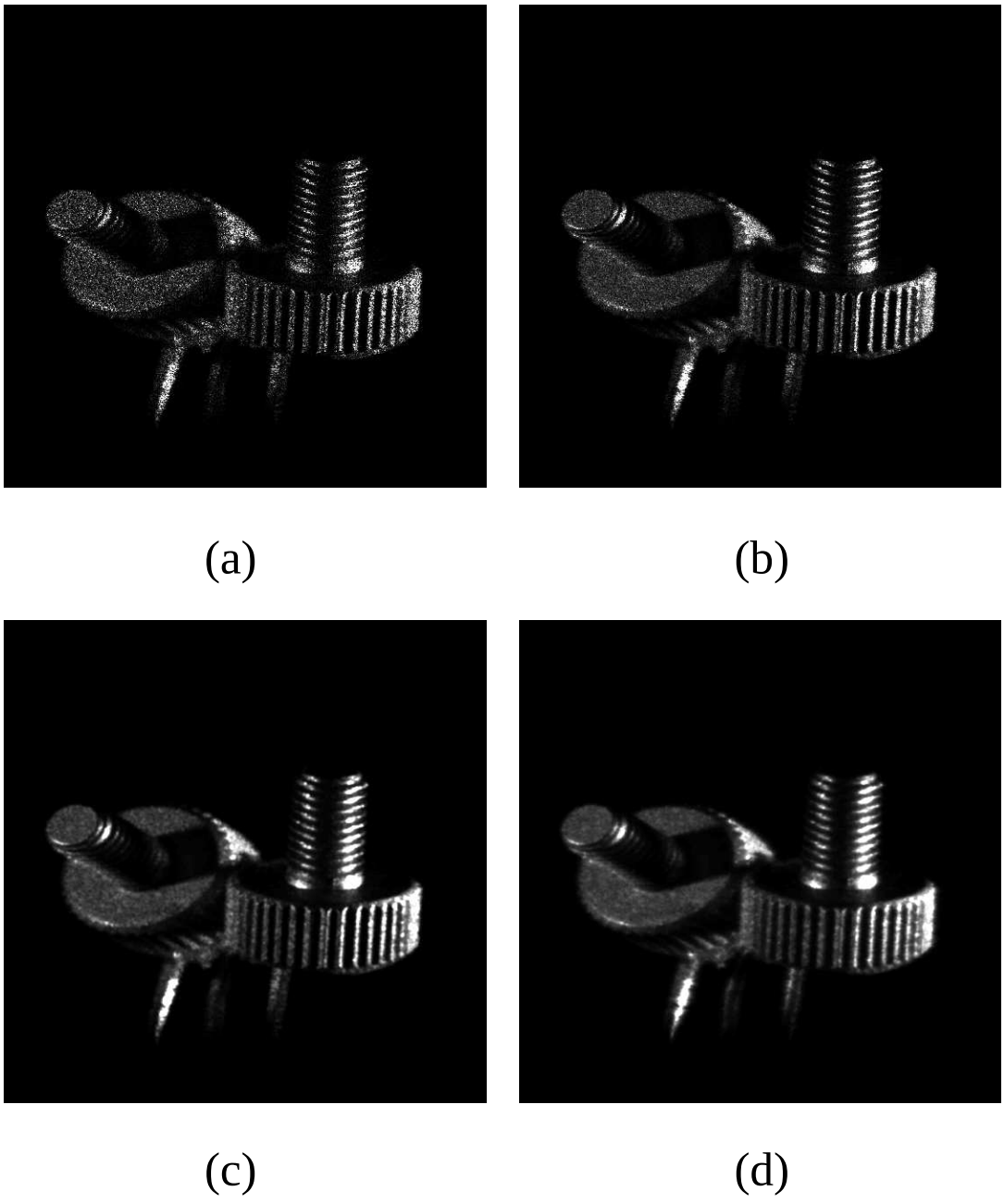

Figure 5.15: Filtering in 2D and 3D applied to an in-line DH of two bolt objects. (a) the original reconstruction with no speckle reduction applied, (b) 2D filtering applied with parameters $\sigma_x = 0.5S_x$ and $\sigma_y = 0.5S_y$ resulting in a speckle index of 0.5076, x resolution of 35.92 line pairs per mm and y resolution of 28.51 line pairs per mm. (c) 2D filtering applied with parameters $\sigma_x = 2S_x$ and $\sigma_y = 2S_y$ resulting in a speckle index of 0.1344, x resolution of 16 line pairs per mm and y resolution of 14.25 line pairs per mm, and (d) 3D filtering applied with parameters $\sigma_x = 1.75S_x$, $\sigma_y = 1.75S_y$ and $\sigma_z = 1.75S_z$ resulting in a speckle index of 0.1611, x resolution of 10.08 line pairs per mm and y resolution of 10.08 line pairs per mm.

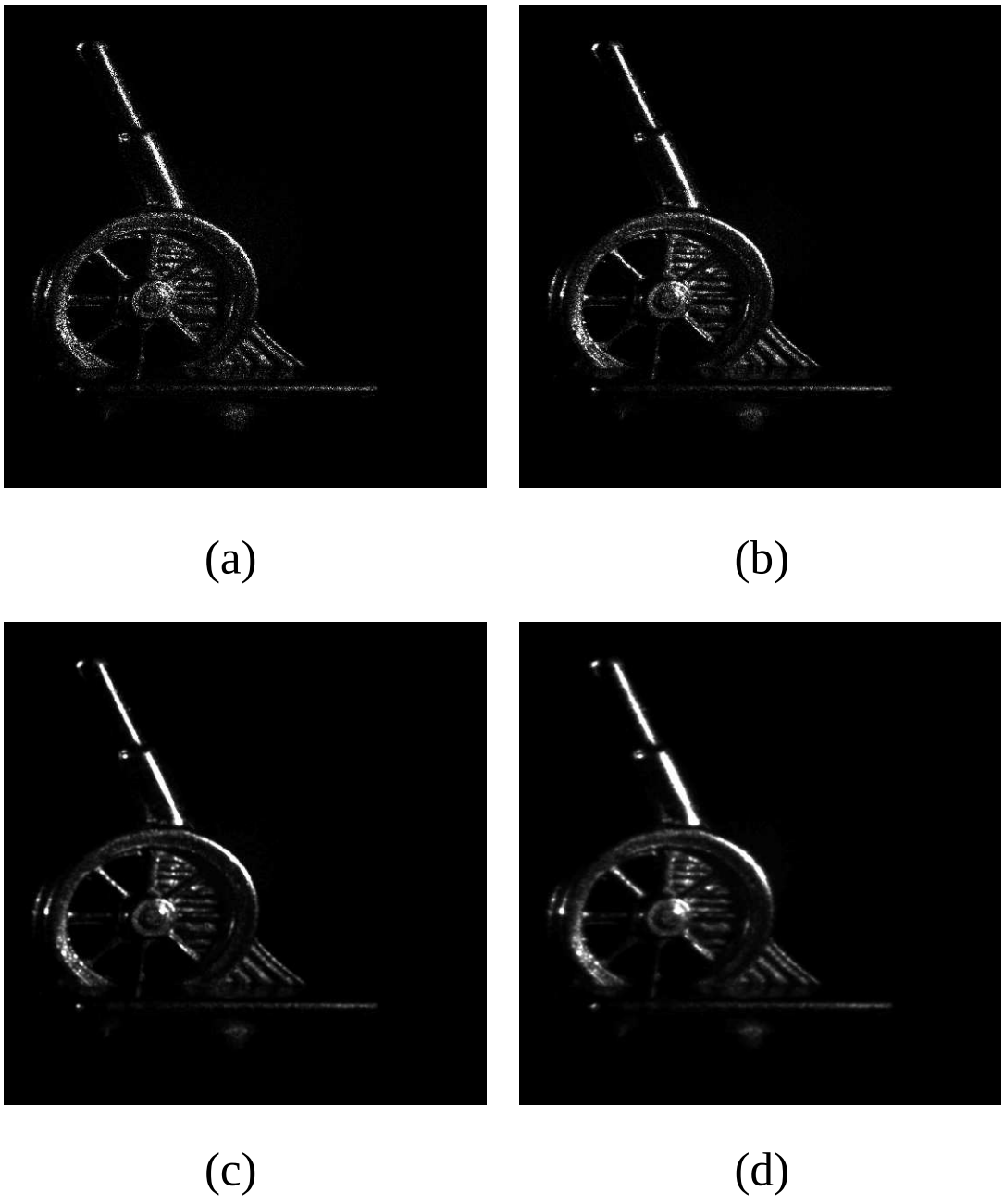

Figure 5.16: Filtering in 2D and 3D applied to an in-line DH of a spindle object. (a) the original reconstruction with no speckle reduction applied, (b) 2D filtering applied with parameters $\sigma_x = 0.5S_x$ and $\sigma_y = 0.5S_y$ resulting in a speckle index of 0.5308, x resolution of 35.92 line pairs per mm and y resolution of 28.51 line pairs per mm. (c) 2D filtering applied with parameters $\sigma_x = 2S_x$ and $\sigma_y = 2S_y$ resulting in a speckle index of 0.1722, x resolution of 16 line pairs per mm and y resolution of 14.25 line pairs per mm, and (d) 3D filtering applied with parameters $\sigma_x = 1.75S_x$, $\sigma_y = 1.75S_y$ and $\sigma_z = 1.75S_z$ resulting in a speckle index of 0.1258, x resolution of 10.08 line pairs per mm and y resolution of 10.08 line pairs per mm.

larger than for the resolution chart as shown in Table 5.5. The speckle size in the x and y directions are given by 8.74μm and 10.43μm respectively, while S_z is equal to 1mm. This particular object has a large depth; The front of the object is in focus at a reconstruction distance of 0.0975m as shown in Figure 5.17 (a), while the back of the object is in focus at a reconstruction distance of 0.1125m as shown in Figure 5.17 (b), which gives us an object depth of 1.5cm and a mid-point reconstruction distance of $z_0 = 0.105$m. Both of these reconstructions were calculated after first zero padding the DH up to a size of 6150×7344 pixels and reconstructing using the direct method. The resulting image in Figure 5.17 (a) has a pixel size of 3.61μm and 3.02μm in the x and y dimensions respectively, and in Figure 5.17 (b) has a pixel size of 4.16μm and 3.48μm in the x and y dimensions respectively. In both Figure 5.17 (a) and (b) we show zoomed in regions of the reconstruction which highlight small features in the front and back parts of the object. We note that no filtering was applied to either of these reconstructions.

It is interesting to apply our 3D filtering algorithm with a Gaussian filter that has a standard deviation that is wide enough to cover a large range of the full object depth. We implement the method with $\sigma_x = S_x$, $\sigma_y = S_y$ and $\sigma_z = 7S_z$. The result of using this 3D filter using the direct method is shown in Figure 5.18 (a), where we have chosen the reconstruction distance to be the midpoint object distance $z_0 = 0.105$m. We can see that the effect of the wide z filter significantly blurs the image. While this filter will ensure that all of the object will come into focus as part of the summation, it will also ensure that each part will go significantly out of focus as well and the out of focus contribution to the final summation is much greater. The result of this filter is a blurred image. However this problem can be overcome adapting the Gaussian filter. We redefine the filter with a delay in the z direction with a delay parameter $f(x, y)$ that is a function of x and y.

$$G(x,y,z) = A \exp\left[-\left(\frac{x^2}{2\sigma_x^2} + \frac{y^2}{2\sigma_y^2} + \frac{(z-f(x,y))^2}{2\sigma_z^2}\right)\right] \tag{5.20}$$

with normalization factor A defined as before.

This delay parameter $f(x,y)$ is given by the distance at which that part of the image at location (x,y) approximately comes into focus. This can be implemented using the algorithm presented in Ref [EHN08]. The intensity of the reconstructed image is calculated over a series of distances and the variance of the image is calculated at each location (x,y) for a particular block size. This is repeated for each reconstruction distance. For a given value of x and y the variance is compared across the sequence of intensity reconstructions. When the variance is at a maximum we take the corresponding distance to be the in focus distance for that part of the image and we set $f(x,y)$ equal to that value. In our case we use a block size of 400×400 pixels. The depth map calculated, $f(x,y)$, is shown in Figure 5.18 (b). Applying the standard 3D Gaussian filter, defined above in Equation 5.5, using z_0 equal to the middle distance 0.105m and using $\sigma_x = S_x$, $\sigma_y = S_y$ and $\sigma_z = 7S_z$ we obtain the speckle reduced image shown in Figure 5.18 (a). We can see that this image is out of focus and of poor quality. However using the improved filter defined in Equation 5.20 with the variable delay with $\sigma_x = S_x$, $\sigma_y = S_y$ and $\sigma_z = S_z$ we obtain the considerably improved image shown in Figure 5.18(c). Further speckle reduction can be achieved at the expense of some blurring by increasing the filter size. In Figure 5.18 (d) we show the result for $\sigma_x = 2S_x$, $\sigma_y = 2S_y$ and $\sigma_z = 2S_z$. Comparing these latter two results with Figure 5.18 (a) demonstrates that the filter with the variable delay affords a much improved resulting from us being able to employ a more controlled and narrower filter in the z direction. We note that the improved filter employing the variable depth parameter is not without disadvantage. It necessitates the calculation of a depth map $f(x,y)$ as described above, which requires the calculation of multiple

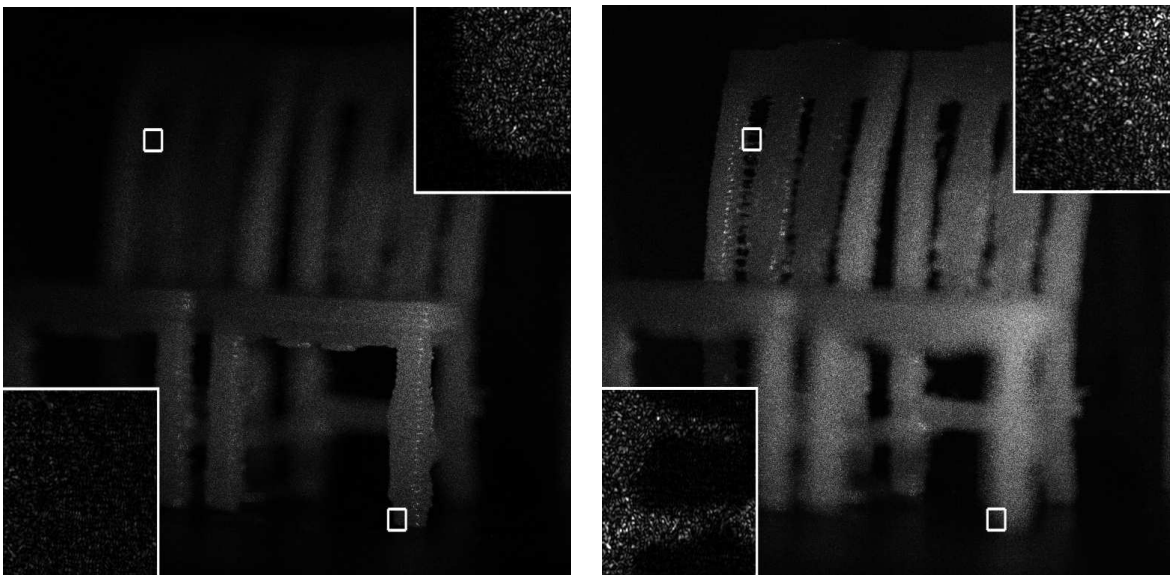

(a) (b)

Figure 5.17: Reconstructions of a DH of two small chairs with (a) front in focus, and (b) back in focus.

reconstruction depths prior to even beginning the filtering process. This can be time intensive and for the two results shown in Figure 5.18 (a), the overall process required approximately two hours on a modern computer processor.

5.4.4 Comparison with other techniques

Here we present results of a comparison between the best performing filter from this chapter, the 2D filter, other standard speckle reduction techniques (mean and median filters), the DFF [see Section 3] and the best performing wavelet from Appendix A. Figure 5.19 shows exemplar results for the case when all have reduced speckle to approximately half. 2D filtering has outperformed the other techniques, achieving a similar level of speckle reduction but maintaining a higher resolution. The next best performing technique is the DFF, followed by the mean, median filters and Haar mother wavelet (at detail level 2 using soft thresholding with a

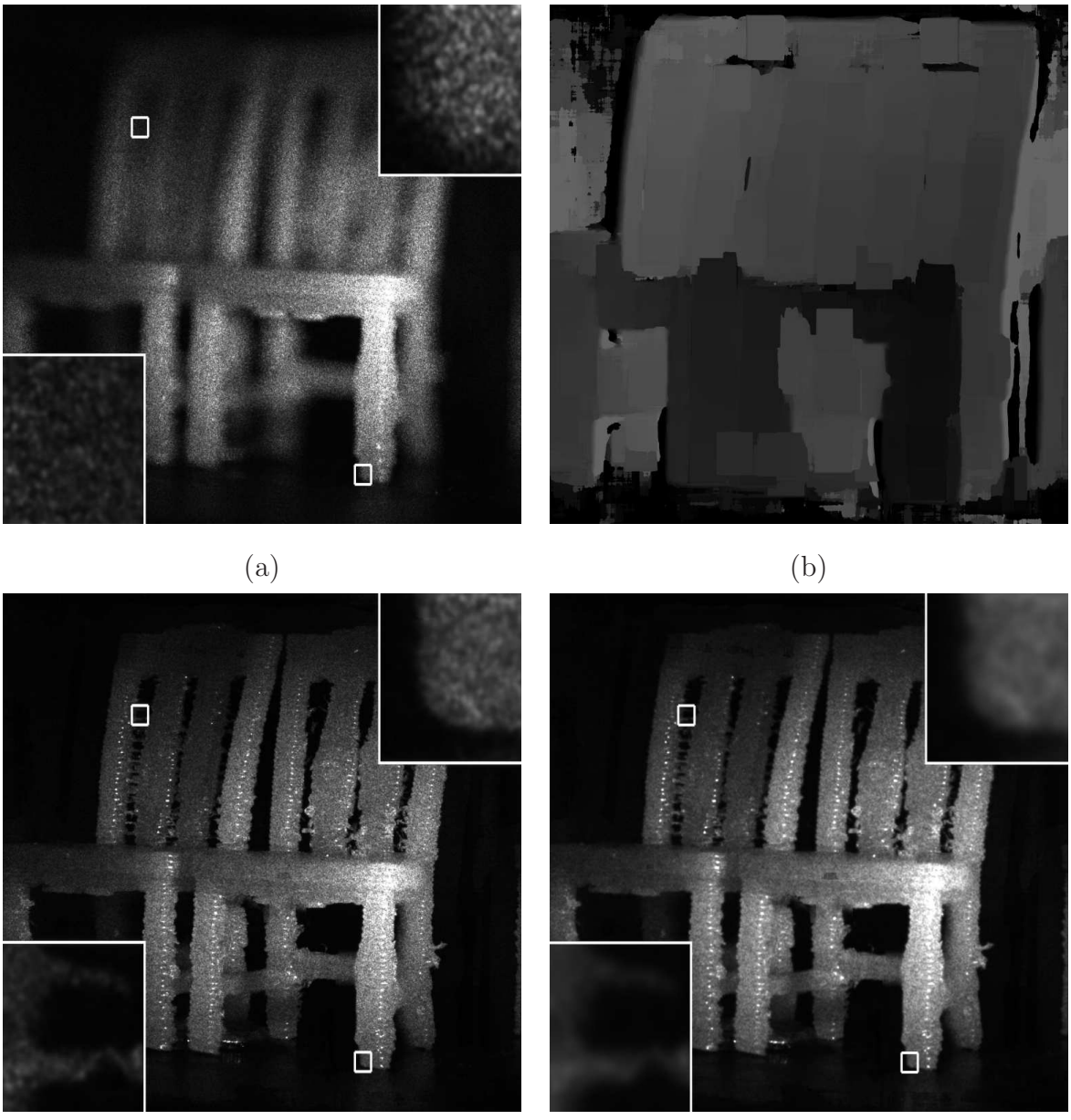

(a) (b)

(c) (d)

Figure 5.18: (a) Result of filter with size $\sigma_x = S_x$, $\sigma_y = S_y$ and $\sigma_z = 7S_z$, (b) the depth map,$f(x, y)$ [EMN+05, MLJ04], (c) filter of size $\sigma_x = S_x$, $\sigma_y = S_y$ and $\sigma_z = S_z$, using the delay in z described in Equation 5.20 and (d) filter size of $\sigma_x = 2S_x$, $\sigma_y = 2S_y$ and $\sigma_z = 2S_z$, also using the delay in z from Equation 5.20.

balance sparsity norm scheme). Table 5.7 provides a more comprehensive set of results.

5.5 Summary

In this chapter, we have reported on a Gaussian filtering technique to reduce speckle in digital holograms. Our main contribution was to use the inherent 3D nature of DHs to construct suitable 3D filters to reduce the speckle content. Using a convolution approach, a large set of quantitative results were generated for the 1D, 2D and 3D cases to show the effectiveness of the technique. We demonstrated that a reduction of the speckle content could be attained, while at the same time resolution improved in directions orthogonal to the filtering direction. We also provided qualitative evidence that 3D filtering can have a positive impact on the depth of focus of the resulting filtered image. In the following, we provide more details of the main findings in this work.

The model developed was shown to predict the reduction in speckle contrast well in the x and y directions, but performed less well for the z direction case. This is primarily because tuning the model parameters were optimized on data taken from 2D filtering. Nonetheless, the general trend of the reduction in speckle contrast is also approximated well for filtering in z.

We also discussed the expected theoretical maximum recoverable frequencies and how these values relate the observable line pairs / mm in the image. We pointed to the fact that the theoretical values are upper limits as there are at least three factors that further reduce the bandwidth of the system; (i) the averaging effect of the pixel, which for a Fresnel system amounts to an averaging of the complex reconstruction; (ii) the effect of sampling which can result in overlapping replicas of the reconstruction and (iii) the pixel quantization, which can lead to

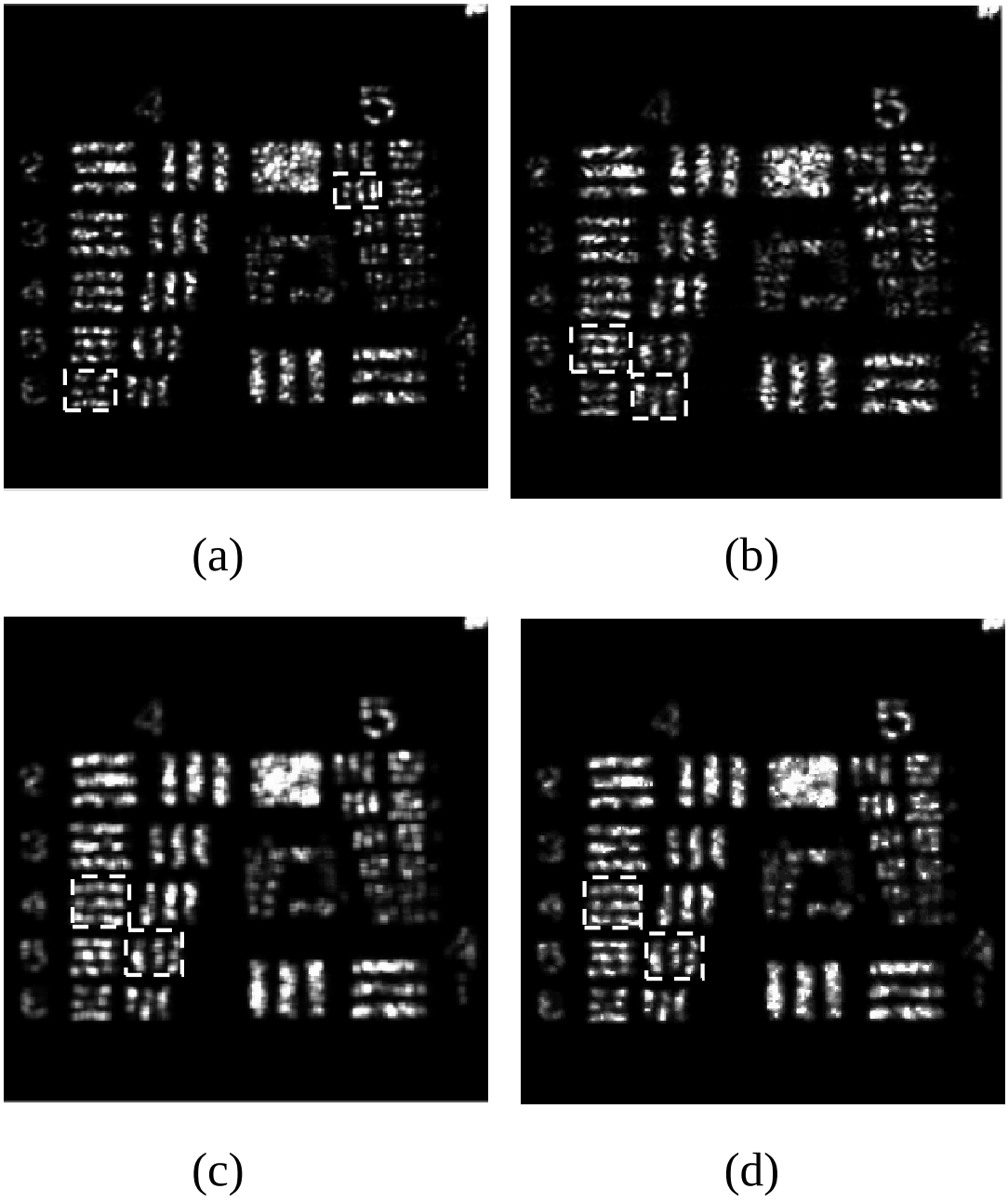

Figure 5.19: Visual comparison of 2D filtering verses the DFF, mean filter and wavelet denoising. (a) Filtering in 2D in the x and y directions with M_x and M_y set to 2 resulting in a speckle index of = 0.5292 and x and y resolution of 35.92 and 28.51 line pairs per mm, respectively, (b) DFF with a square aperture (768×768 pixels) resulting in a speckle index of = 0.5231 and x and y resolution of 28.51 and 25.4 line pairs per mm, respectively, (c) 3×3 mean filter resulting in a speckle index of = 0.4742 and x and y resolution of 25.4 and 22.62 line pairs per mm, respectively, and finally (d) Haar wavelet at resulting in a speckle index of = 0.5362 and x and y resolution of 25.4 and 22.62 line pairs per mm, respectively.

Technique	SI	RES x	RES y
2D filtering ($\mathbf{M_x = 2, M_y = 2}$)*	**0.52**	**35.92**	**28.51**
2D filtering ($M_x = 3, M_y = 3$)	0.37	32	22.62
2D filtering ($M_x = 4, M_y = 4$)	0.3	22.62	17.96
2D filtering ($M_x = 5, M_y = 5$)	0.24	20.16	16
DFF ($\mathbf{768 \times 768}$)*	**0.52**	**28.51**	**25.4**
DFF (512×512)	0.42	25.4	20.15
DFF (256×256)	0.23	17.95	16
DFF (128×128)	0.14	8.97	8.97
Haar (detail level 1)	0.66	35.92	25.4
Haar (detail level 2)*	**0.53**	**25.4**	**22.62**
Haar (detail level 3)	0.47	20.15	16
Haar (detail level 4)	0.45	16	14.25
Mean filter ($\mathbf{4 \times 4}$)*	**0.47**	**25.4**	**22.62**
Mean filter (5×5)	0.39	22.62	17.95
Mean filter (7×7)	0.29	20.15	16
Mean filter (9×9)	0.23	17.95	14.25
Median filter (4×4)	0.54	25.4	22.62
Median filter (5×5)	0.46	22.62	20.15
Median filter (7×7)	0.35	20.15	17.95
Median filter (9×9)	0.29	17.95	16

Table 5.7: Comparison of 2D filtering versus various speckle reduction techniques. Results in bold marked with an * can be viewed in Figure 5.19. SI: speckle index, RES x: resolution in the x direction, RES y: resolution in the y direction.

errors in the reconstructed image [PH11]. Furthermore, we postulated that the speckle noise could further impact on resolution and showed that by reducing speckle noise it was possible to increase the resolution of the image.

We discussed the shape and orientation of the speckle in the 3D intensity field and postulated that the spectral method averages along lines that cut through the speckle grains. This suggests that the effective speckle size in the z direction is smaller when using the spectral method to reconstruct over when the direct method is used. A numerical calculation of the speckle size confirms this. However, using the spectral method to filter in the z direction has the disadvantage that reconstructions at each subsequent plane are not aligned as the field is expanding. This of course can have a negative effect on the resulting resolution.

When filtering in the x direction only, resolution in the y direction initially improved (over a non-filtered reconstruction) and then after a slight degradation was maintained, all the while resolution in the x direction decreased steadily with increasing kernel size. Filtering in the y direction produced similar effects, with an observed slight improvement in x resolution, followed by a slight degradation and leveling off, but this time with some further resolution loss. This was due to the design of the resolution chart itself, which allows for the blurring of the vertical resolution bars into each other and was not a discovery that warranted further investigation. 2D filtering in x and y directions resulted in a slight improvement in x resolution and no change to the y resolution, before a steady decrease in resolution for both x and y. There was no initial improvement in resolution in either direction for 3D filtering and as the kernel size was increased resolution decreased steadily in both directions. As expected, in terms of resolution and speckle index, 2D filtering outperformed both 1D and 3D filtering when the criteria was to maintain resolution in both the x and y directions and achieve a certain level of speckle reduction. This is because the test object was planar and it can

be reasonably asserted that the results might favour 3D filtering if the test object were to have an appreciable extent in the z direction.

Finally, we provided qualitative evidence that 3D filtering can have a positive impact on the depth of focus of the resulting filtered image. Using a DH of two small chairs with extent in the z direction, we showed that both the front and the back of the chairs could be in focus more after filtering, with the added benefit of a reduced speckle contrast, than when no filtering is applied.

The first chapter in Part B of this thesis is presented in the next chapter. It concerns overcoming partial occlusions in reconstructions of DHs.

Chapter 6

Occlusions in digital holography

6.1 Introduction

We explore the potential use of DHs for 3D scene reconstruction, where particular regions of interest are occluded under certain views. The study of occlusions in digital holography has been actively researched of late. For the case of digital hologram watermarking [KJ03, KL05, OA07], occlusions are considered attacks and occur in the hologram plane, resulting in a direct loss of data at that plane. The integration of computer graphics and holograms has also been investigated, necessitating the study of occlusion effects [BZG+05, Bim06]. Occluding certain parts of the a reconstruction plane in an effort to reduce the effects of the out-of-focus twin image has been studied previously [PFFT98, DFFD05] [see Chapter 7 for contribution to this topic]. Another technique, which attempts to overcome the problems of foreground occlusions in a complex scene is integral imaging, which uses the concept of ray phase space to reconstruct the occluded images. It is based on ray optics and uses different view perspectives with a microlens array [HJ05, JPDH06, HHJ07]. This is a passive sensor as opposed to active sensing as in digital holography. For a more thorough review of occlusions in

digital holography and other imaging systems see Section 1.1.3. The work in this chapter has emanated from a collaborative effort between the author, Conor P. Mc Elhinney and Bryan M. Hennelly [MEH+06b, MEH+06a, HME+06].

A technique that uses the inherent properties of DHs to improve the viewing of certain regions of interest in the presence of occlusion in now presented. We have previously simulated the addition of occlusions in free space [EMM+05] (i.e., in the region between the object of interest and the camera) and here we use this technique to model lightless opaque and light diffracting opaque occlusions as they occur in nature. In our simulated experiments, we use optically-captured digital holograms of real-world objects. We show that by reconstructing the entire hologram it is possible to overcome the problems of foreground occlusions in a scene. This is achieved by propagating the wavefront to the calculated in-focus plane of the object of interest. However, for the purpose of this chapter, we investigate finding a subset of pixels that can successfully reconstruct partially occluded background objects, by selectively incorporating information from additional views of the scene. There are three reasons why this is useful. The first is that different windows in the hologram plane give different perspectives. In situations where a light diffracting opaque occlusion is present, the reconstruction plane of the object of interest may be corrupted by non-physical light emanating backwards from the occlusion. The non-physical light is present because DH reconstruction algorithms [see Section 2.2.3] do not distinguish between forward or backwards traveling light. This light acts as a noise and can saturate features on the object of interest. By careful selection of windows from the hologram plane, the influence of this noise can be reduced and features that are not discernable when the whole hologram is used to reconstruct, become visible. The second benefit is that the computational complexity of hologram reconstruction is reduced if less pixels are used to reconstruct the scene. The third benefit is that reducing the numbers of pixels

that have to be sent over a communication channel will produce increased communication efficiency. The second and third benefits are investigated thoroughly in [MEH+06b], but omitted here.

6.2 Wigner distribution function

We now present an analysis of digital holography using the WDF, and then apply WDF theory to the problem of investigating occlusions in reconstructions of DHs.

6.2.1 The WDF and Digital Holography

Following from the analysis given in Section 2.4, we now describe the WDF of a rectangular occlusion. The transmission function of a rectangular occlusion of width w may be written as

$$\text{occlusion}(x) = 1 - \text{rect}\left(\frac{x}{w}\right). \tag{6.1}$$

Using Equations 2.72 and 6.1 we may calculate the WDF of the occlusion to be

$$\begin{aligned} \psi\{\text{occlusion}(x)\}(x,u) &= \psi\left\{1 - \text{rect}\left(\frac{x}{w}\right)\right\}(x,u) \\ &= \delta(u) - \psi\left\{rect\left(\frac{x}{w}\right)\right\}(x,u) \\ &- \cos(\pi x k) sinc(wk). \end{aligned} \tag{6.2}$$

As long as $w \gg \lambda$, we may ignore the effect of diffraction at the edges and use the following approximation for ease of analysis,

$$\psi\{\text{occlusion}(x)\}(x,u) = \delta(u), \qquad |x| > \tfrac{w}{2}. \tag{6.3}$$

We are now in a position to discuss digital holography from the perspective of Wigner and to analyze (i) the effect of taking different windows within our hologram for reconstruction and (ii) the effect of occlusions on a digital holography system.

In the following we consider (without any loss of generality) such a system to be summarised by a single camera capable of measuring the complex amplitudes at the individual pixel positions. The wavefield emanating from an object, in the plane just after the object (plane of focus) is denoted $O(x)$ and has a WDF denoted by $\psi\{O(x)\}(x,u)$. The Wigner chart for the signal will be of the form shown in Figure 7.2(a). After Fresnel propagation the signal's chart now takes the form shown in Figure 7.2(b) and the WDF of the propagated signal is given by $\psi\{O(x)\}(x+\lambda du,u)$. Capture by the CCD is equivalent to multiplying by a comb function (sampling interval equal to T, the distance between the pixels), which has been convolved by a rect function with width equal to that of a CCD pixel, w_p. This is followed by multiplying by a rect function of size (i.e., side-length), w_c and position, x_0, of the CCD aperture. Thus the CCD function is given by

$$CCD(x-x_c)=\left[\delta_T(x)*\text{rect}\left(\frac{x}{w_p}\right)\right]\times\text{rect}\left(\frac{x-x_c}{w_c}\right). \tag{6.4}$$

Using Eqs 2.69, 2.71a, 2.71b, 2.82 and 2.83 we may calculate the WDF of CCD(x) given Equation 6.4. It is

$$\left[\psi\{\delta_T(x)\}(x,u)\ast^x\psi\left\{\text{rect}\left(\frac{x}{w_p}\right)\right\}(x,u)\right]\ast^u\psi\left\{\text{rect}\left(\frac{x}{w_c}\right)\right\}(x-x_c,u), \tag{6.5}$$

where the superscript on the asterisk denotes the coordinate vector along which the 1-D convolution takes place. Capturing the DH is equivalent to multiplying our complex signal by CCD(x). The WDF is therefore equivalent to a convolution of the WDFs along the u axis,

$$\psi\{O(x)\}(x - \lambda du) *^u \psi\{\mathrm{CCD}(x)\}(x, u). \tag{6.6}$$

Recently, Wigner analysis has found a significant application in digital holography. The generalized sampling theorem [SJ04c, SJ04b], which can be derived from Equations 2.78 and 6.6 above, allows us to improve the capacity of any digital holographic system [SJ04a]. Simply stated, we need only ensure that the CCD bandwidth is greater than the local bandwidth of the incident signal even if this local bandwidth lies far outside the bandwidth of the CCD. From this point on, we will assume that the optical recording is set up to ensure that no aliasing occurs in the process and that the sampling is ideal (i.e. the pixels are ideal delta functions). Thus we will entirely ignore the effect of sampling. Numerical implementations of the FSTs will also assumed to be ideal. The true effect of CCD sampling and numerical Fresnel may be found in great detail [Kre05], but these effects have little impact on the results presented. As such, recording is summarised as convolving the signals WDF with Equation 2.83. The position of the WDF of the rect function can shift in x depending on the centre of the CCD (hologram) window. In the next sub-section, we discuss lightless opaque and light emitting opaque occlusions using the WDF. In the latter case, we show how astute positioning of the camera (or equivalently a choice of some sub-section of the CCD recording) can lead to a higher signal to noise ratio in numerical object reconstruction.

6.2.2 The WDF and occlusions

We consider first the case of an lightless opaque planar occlusion of width w_o positioned a distance d_1 from the object and a position d_2 from the CCD. The plane of the occlusion is normal to the axis of propagation. The occlusion may be modelled with the aid of a rect function as shown in Equation 2.83. We may change the lateral position of the occlusion by setting $x \to x - x_o$ in Equation 2.83

where x_0 is the position of the center.

The object wavefield has a Wigner chart shown in Figure 7.2(a). The object has a width **W** and at each position over this width we assume rays of light to be traveling in all directions over a range of angles proportional to the bandwidth **B**. The power of the light in a given position-direction is represented by the height of the WDF at that coordinate. Since we are considering the general case we may use the plan view of a square WDF for illustrative purposes. $O(x)$, with WDF $\psi\{O(x)\}(x,u)$, propagates a distance d_1. The CCM, defining the shape, is given by Equation 2.79. After propagation the WDF becomes $\psi\{O(x)\}(x+\lambda d_1 u, u)$. The resulting Wigner chart is shown in Figure 6.1(a) and the new CCM is defined by Equation 2.80 where we set $d = d_1$. In this plane the wavefield is multiplied by occlusion $((x-x_o)/w_o)$. The WDF of the occlusion, $\psi\{occlusion(x/w_o)\}(x,u)$ is defined with an approximation in Equation 6.2 and is illustrated in Figure 6.1(b). Using Equations 2.69, 2.71 we may define the WDF of the wavefield immediately after the occlusion as

$$\psi\{O(x)\}(x^{'},u) *^{u} \psi\left\{\text{rect}\left(\text{occlusion}\left(\tfrac{x^{'}}{w_o}\right)\right)\right\}(x^{'}-x_o,u), \tag{6.7}$$

where $x^{'} = x + \lambda d$. Taking the definition of the WDF of the occlusion given in Equation 6.2 we illustrate the new Wigner chart in Figure 6.1(c). We now require two CCMs. The coordinates for these two CCMs can be easily derived using geometry on the original CCM.

The signal now propagates a distance d_2 and there is further shearing along the x-axis. The Wigner chart is shown in Figure 6.1 (d). The two new CCMs may be calculated by finding the product of the old CCMs with the Fresnel matrix in Equation 2.80. The WDF of the signal at this point is

$$\psi\{O(x)\}(x^{''},u) *^{u} \psi\left\{\text{rect}\left(\text{occlusion}\left(\tfrac{x^{'}}{w_o}\right)\right)\right\}(x^{''}-x_o,u), \tag{6.8}$$

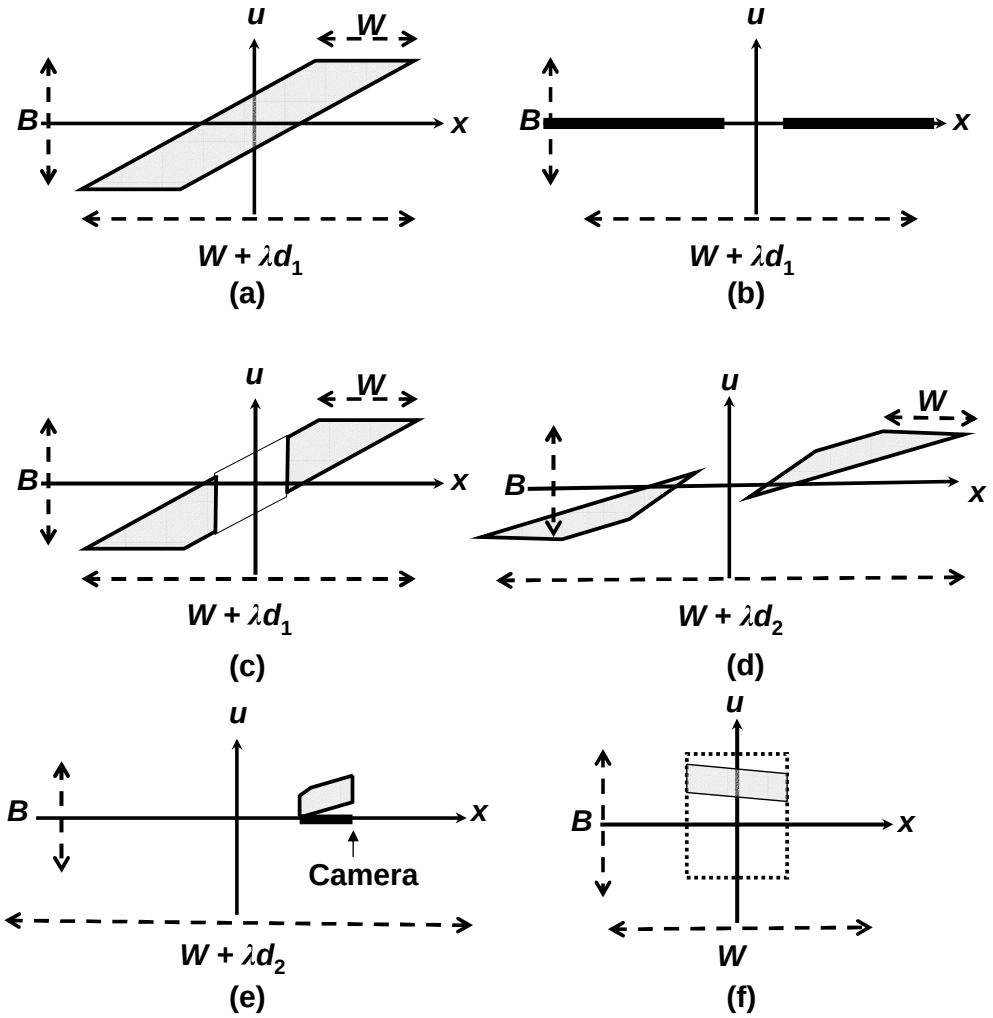

Figure 6.1: (a) Wigner chart of the object signal after propagating a distance d_1 to the occlusion, (b) the occlusion Wigner chart, (c) the Wigner chart of the occluded wavefront obtained by convolving (a) and (b), (d) the Wigner chart after the occluded wavefield propagation of a distance d_2 to the CCD plane, (e) the Wigner chart of the CCD and the captured wavefield, and (f) the Wigner chart of the reconstructed signal against the total reconstructed signal.

where $x^{''} = x+\lambda(d_1+d_2)u$. The signal is then multiplied by CCD$(x-x_c)$, the CCD transmission function. Based on previous discussions concerning CCD sampling it is sufficient for present analysis to assume ideal sampling and interpolation and describe the CCD only using CCD$(x) = \text{rect}(x/w_c)$. We show the WDF of such a signal in Figure 6.1(e) with the approximation that it is a delta function over some region of space as in (Equation 2.72). In this figure we also show the section of the signal that would be removed by this finite delta function after convolution along u. Once again the new CCM may be found by applying geometry in an obvious fashion to the old CCMs. The WDF of the signal after capture by the CCD is given by

$$\begin{aligned}\psi\{\text{hol}(x^{''})\}(x^{''},k) &= \left[\psi\{O(x)\}(x^{''},k) *^k \psi\left\{\text{rect}\left(\text{occlusion}\left(\frac{x^{'}}{w_o}\right)\right)\right\}(x^{''}-x_o,k)\right] \\ &*^k \psi\{\left\{\text{rect}\left(\text{rect}\left(\frac{x^{''}}{w_o}\right)\right)\right\}(x^{''}-x_c,k). \qquad (6.9)\end{aligned}$$

A numerical FST of distance $-(d_1+d_2)$ is then applied to the signal. Assuming the numerical transform to be ideal, the reconstructed signal is given by $\psi\{hol(x^{''}\}(x-\lambda(d_1+d_2),k)$. The intensity can be found using Equation 2.72. The Wigner chart for this signal is illustrated in Figure 6.1(f), plotted against the backdrop of the original Wigner chart. We have recovered a certain amount of the signals energy in phase space. We may interpret this in one sense as having recovered a specific range of angles for different positions. As we vary the position of the camera x_c, and its width, w_c we may vary the range of angles recovered for each x. In certain cases the recovered angles will not exist because they have been removed by the occlusion. The effect of the occlusion will vary depending on the position and size of the camera. We note that while we have made large approximations in our illustrations, Equation 6.9 is free of these approximations if we use the correct definitions of the WDF of a rect function.

When we consider the case of a light emitting opaque occlusion we immediately find an application of the theory outlined above. In this case we have the sum of two signals to deal with; as before we have the occluded wavefield a distance d_2 from the CCD and we have a second signal that lies within the occlusion. If these two complex signals are recorded and an inverse Fresnel used to return to the in-focus plane of the first object we find that non-physical light from the second object will be present as a source of noise. Not only will the intensity of this the second signal be a source of noise but so will its interference with the desired wavefield. We now demonstrate how to increase the signal to noise ratio for the desired signal by appropriate choice of CCD position.

The bilinear property (v) above implies that the WDF of the sum will be given by the sum of the WDFs plus some cross term. From property (xii) we know that for a given projection the cross term will exist only in the region of overlap of the signals for that projection. We show the Wigner charts of the two signals in Figure 6.2(a). We have the occluded WDF as before and now we also have a second wavefield. At this point we have three CCMs: two describing the first signal and one for the second. After propagation a distance d_2 both signals are sheared along the x-axis and the new CCMs may be easily calculated as before. The Wigner charts of the sheared wavefields are illustrated in Figure 6.2(b). A CCD then captures the wavefield in some region and the resulting Wigner chart is shown in Figure 6.2(c). The new CCMs can be calculated geometrically. Had the entire wavefield been captured and an inverse numerical FST applied to return to the plane of the first object, the Wigner chart would look like that shown in Figure 6.2(d). In this case we have recovered all of the information that we can for the first object but it overlaps with the second signal and it is saturated with the second signals' intensity and their common interference. In Figure 6.2(e) we show the Wigner chart for the CCD hologram having been inverse Fresnel transformed.

We can see that while we have less of our signals energy we have an even smaller amount of the corrupting signals energy. Thus, by changing our CCD position (or equivalently the region of the recorded hologram that we use in our reconstruction) we may recover multiple projections each with a higher signal to noise ratio for a given region and over a different angle of view. We demonstrate these results using experimental data in the next section.

6.3 Results and discussion

Any complex scene can contain foreground objects that occlude one's view of background objects of interest. Digital holography provides a novel way to overcome these occlusions by permitting unobstructed reconstructions of desired objects to be computed [EMM+05]. The 3D objects used in our simulations were reconstructed from DHs of a die object. They were captured using the PSI described in Section 2.2.2.3. The DHs are represented as a 2048×2048 complex-valued matrix.

In order to demonstrate the ability of digital holography to overcome problems of occlusion, we simulated the addition of a light diffracting opaque occlusion to a scene containing a die object. This simulation provides a demonstration of the situation depicted in the Wigner chart in Figure 6.1. The simulated experimental set-up is shown in Figure 6.3. This is the part of the optical apparatus from Figure 2.6 in Section 2.2.2.3 between the object and camera. It depicts a situation where a foreground occlusion is obstructing the view of a background object of interest. Each pixel in the occlusion has a phase value chosen with uniform probability from the range $[0, 2\pi)$, which simulates a diffuse reflective object. The occlusion was positioned 260mm from the object. The object was placed 325mm from the camera (hologram plane). The hologram plane describes a 2D complex-valued signal representing a coherent wavefront that was incident on, and

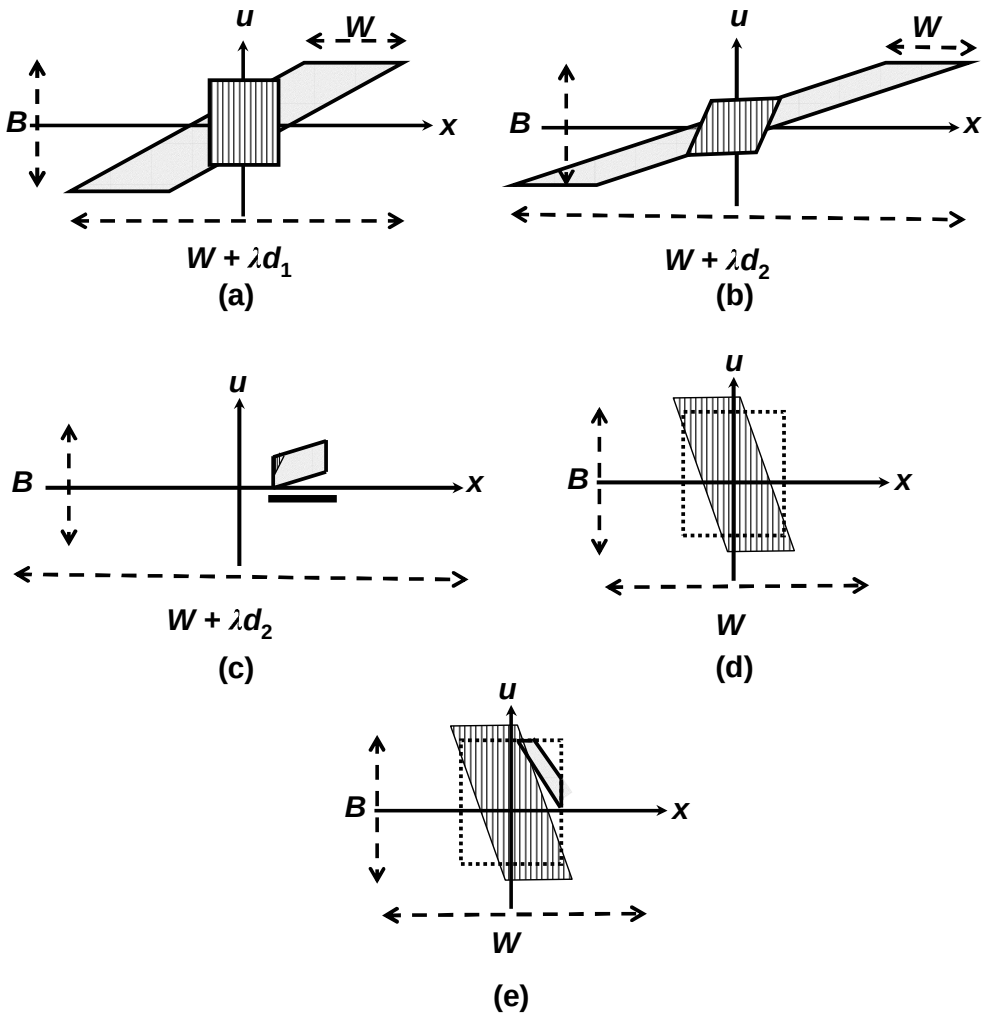

Figure 6.2: (a) The Wigner chart of both the occluded wavefield (having already propagated a distance d_1 and the second wavefield), (b) the two Wigner charts after propagation to the CCD plane, (c) the Wigner charts after propagation to the CCD and the result of convolution with the signal's WDF, (d) the Wigner chart of the reconstructed signals in the plane of the first object, if the CCD had been large enough to capture the entire wavefields during recording, and (e) reconstruction using the signal in (c) plotted against total reconstruction.

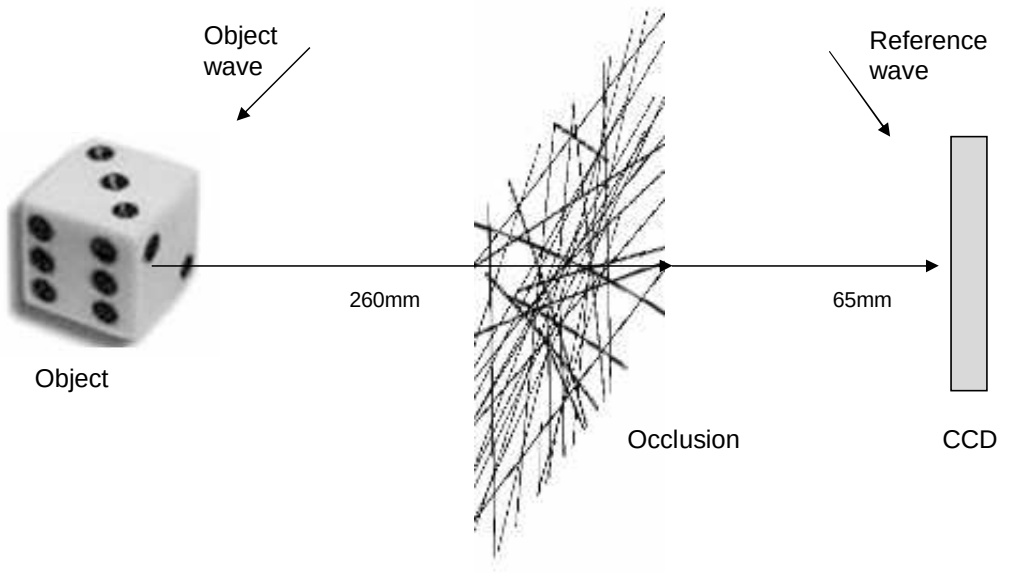

Figure 6.3: Simulated experimental set-up with an occlusion positioned at 260mm from the object.

reflected from, a diffuse 3D object. By applying the discrete Fresnel transform [see Section 2.2.3] to this DH, we can generate the whole complex wavefield in any plane.

In this simulation, we demonstrate how DHs, through Fresnel propagation to the correct distance, have the ability to overcome the problems of foreground occlusions, which can be present in a scene. In Figure 6.4 (a), both the object and the occlusion are in focus simultaneously, as would be the case under the weak perspective model. Figure 6.4(b) shows the object wavefront 260mm from the camera, where the lightless opaque occlusion was positioned. In Figure 6.4 (c), we see the reconstruction of the object using the full hologram. Although the quality of this reconstruction is not equivalent to a reconstruction of the unoccluded die, object information that is not visible due to the occlusion in the weak perspective model, becomes visible through the use of digital holography and Fresnel propagation to the object plane.

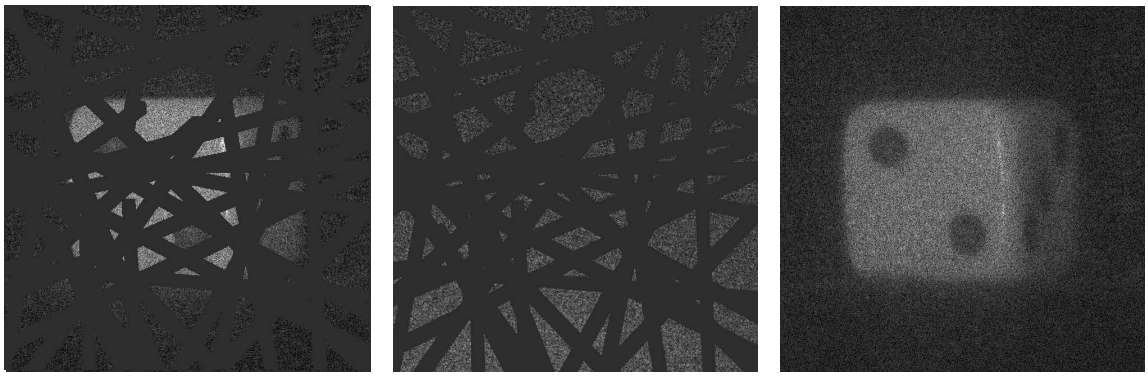

Figure 6.4: Occlusion positioned at 260mm from 3D object, (a) shows a weak perspective view of the scene, (b) shows the occlusion plane, (c) shows the reconstruction along the optical axis of the die.

We will now investigate task specific scene reconstruction using a subsection of the hologram. The task we are interested in is one of trying to reveal a hidden feature on an occluded object, and we achieve this by taking a subset of pixels (a window) from the hologram and reconstructing from that perspective. This is equivalent to changing the position of the camera and provides a demonstration of the situation depicted in the Wigner chart in Figure 6.2. By taking a smaller window from the hologram plane, we can reduce the effects of the out of focus occluding object on the background object of interest, and thus it is possible to reveal features that had been saturated by noise, and therefore not visible. In order to verify this phenomena, we deal with a situation using experimentally recorded PSI data. We have two object wavefields at two different distances from the hologram plane. The wavefield from the background object has been occluded by the presence of the foreground object [see Figure 6.5]. When propagating to the reconstruction plane of the background object, non-physical light from the foreground object saturates this reconstruction. In Figure 6.6(a), the entire hologram is used

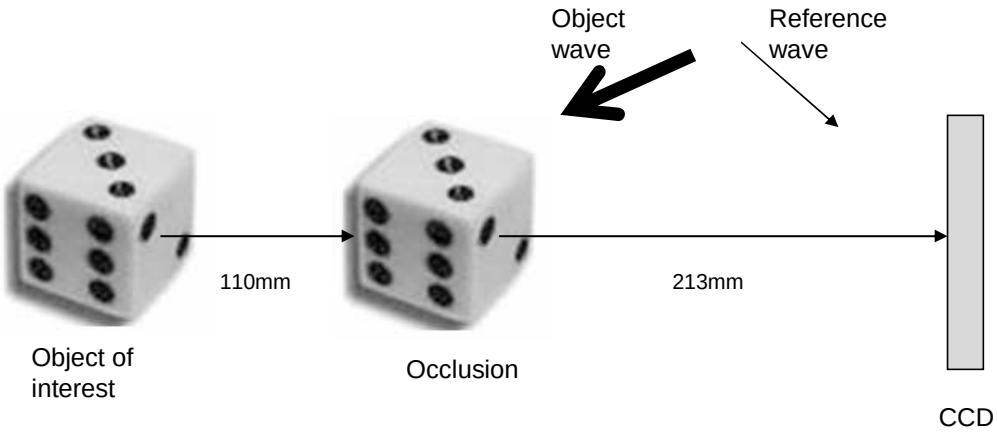

Figure 6.5: Simulated experimental set-up where one die acts as an occlusion to a second die.

to reconstruct the object of interest. However, the three dots that are on the right side of the die have been completely saturated by the out of focus occluding object, and cannot be discerned. When the top right corner (1024×1024 pixels, compared with the available 2048×2048 pixels) of the hologram is used to reconstruct the object, as is shown in Figure 6.6 (b), at least two of the "dots" come into view.

We argue that the ability to reveal hidden features of a partially occluded object is one of the benefits of using smaller windows in the hologram plane for reconstructing. It should be noted that this is only relevant if a light diffracting opaque occlusion is present. This is due to the fact the the out-of-focus light from the foreground occlusion can saturate background object features. In the case of an lightless opaque occlusion, smaller windows will not have any benefit over using the entire hologram in revealing object features.

6.4 Summary

The nature of lightless opaque and light diffracting opaque occlusions, and the effect of reconstructing subwindows from the hologram plane, has been analyzed

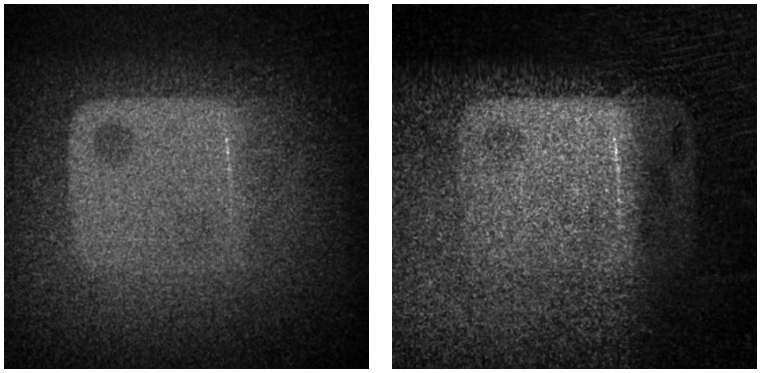

Figure 6.6: Advantage of using a smaller window of pixels over the entire set of pixels when reconstructing an occluded object, (a) reconstruction using the entire set of pixels, (b) reconstruction of the scene using a top right 1024×1024 windows of pixels.

thoroughly using the Wigner chart. We have shown that in the presence of a light diffracting opaque occlusion, using a subset of pixels in the DH to reconstruct can have the benefit of revealing hidden features on a partially occluded object. In the next chapter, we use an occlusion to remove the effects of the out-of-focus twin image.

Chapter 7

Occluding the twin image

7.1 Introduction

Since its discovery by Gabor [Gab48] in 1948, images obtained using in-line holographic techniques have been affected by the presence of the out-of-focus twin image and the zero order terms. After the invention of the laser methods were developed to cleverly evade the twin image by using new experimental off-axis architectures [LU62] [see Section 2.2.2.2]. However, this placed greater demands on the resolution of the film. Indeed for certain radiation sources these off-axis experimental architectures have no physical implementation or only crude and expensive equivalents. In these cases, one must rely upon the initial Gabor architecture and the out-of-focus twin image remains a problem that must be dealt with. This is true for many cases including: x-ray holography, gamma-ray holography and electron holography [see Section 1.1.3]. In the case of digital holography, the in-line architecture [see Section 2.2.2.1] also suffers from the out-of-focus twin image and we now present a technique for its removal. For a more thorough review of literature relating to the twin image problem see Section 1.1.3.

In Section 1.1.3 we discussed some previous work by Pedrini *et al.* [PFFT98]

who successfully eliminated a large portion of the twin image in a DH by bringing the real image to focus and filtering the out-of-focus twin image around this image. We also discussed of the work by Denis *et al.* [DFFD05] who used an iterative scheme to filter out the effects of the twin images (we use the plural as they were dealing with multiple objects) in DHs of particle fields. As they were dealing with multiple objects at different depths, it was necessary to iteratively repeat the process a number of times to successfully reduce the effects of the twin images. We propose the use of a similar technique for macroscopic objects. We discuss for the first time the relative spreading of the unwanted out-of-focus twin image and the wanted image and how to manage this spreading in the numerical reconstruction techniques. We use the Wigner chart to provide us with first order approximations. While this chapter focuses on digital holography, we note that it may be applied to other holographic fields including x-ray, electron, and gamma ray holography.

7.2 Analysis of the technique

We recall from Section 2.2 that a complex signal $h(x, y)$ incident on the CCD can be given by the sum of two wavefields

$$h(x, y) = R(x, y) + O(x, y). \tag{7.1}$$

The CCD records the real-valued intensity $|h(x, y)|^2$, which may be written as

$$|h(x, y)|^2 = |O(x, y)|^2 + |R(x, y)|^2 + O(x, y)R^*(x, y) + O^*(x, y)R(x, y). \tag{7.2}$$

where $O(x, y)R^*(x, y)$ and $O^*(x, y)R(x, y)$ are the real and virtual images respectively. In this chapter we use the terms *wanted image* and *twin image* to make it clear that we want one image over another. In practice these are completely

interchangeable as it does not matter which we remove and which we keep. The point is that when either of these terms are reconstructed, they are corrupted by an out-of-focus version of the other. $|O(x,y)|^2$ and $|R(x,y)|^2$ are the DC terms. In some cases this is far noisier than the unwanted out-of-focus-twin image. However, a number of methods have been developed to successfully remove the DC terms [KJ97, DMS03, ZLG04, GLCC07].

We also recall from Section 2.4 that the WDF of a complex optical amplitude distribution provides a graphical means of simultaneously viewing a signal's spatial and spatial frequency distributions, and is particularly useful for visualizing localized signals [Wig32, Bas97, Loh93, OZK01]. $\Psi\{f(x)\}(x,u)$, which represents the WDF of a signal $f(x)$, is defined in terms of its spatial distribution in the following way

$$\psi\{f(x)\}(x,u) = \int_{-\infty}^{\infty} f\left(x+\frac{\xi}{2}\right) f^*\left(x-\frac{\xi}{2}\right) \exp(-j2\pi u\xi)\mathrm{d}\xi \tag{7.3}$$

where u represents spatial frequency, * denotes complex conjugation and ψ denotes the WDF operator. We use the Wigner chart to give a graphical view of the signals and also as an aid to explain our technique. However, unlike the previous chapter, we have this time computed the exact Wigner chart using an object of width 0.01m, a camera of width 0.0148m (calculated by multiplying the pixel pitch, 7.4μm (the pixel pitch of one of the CCDs that we use to record the digital holograms in this thesis) by the number of pixels, 2000), and a wavelength of 633nm. The wavefield immediately after the object is shown in Figure. 7.1 (a). From the figure we note that the signal's spatial extent is finite, but that its bandwidth is infinite. After propagation of 0.2m using the FST the signal is shown to have spread out [see Figure. 7.1 (b)]. We recall that the FST has the following effect on the WDF of a signal:

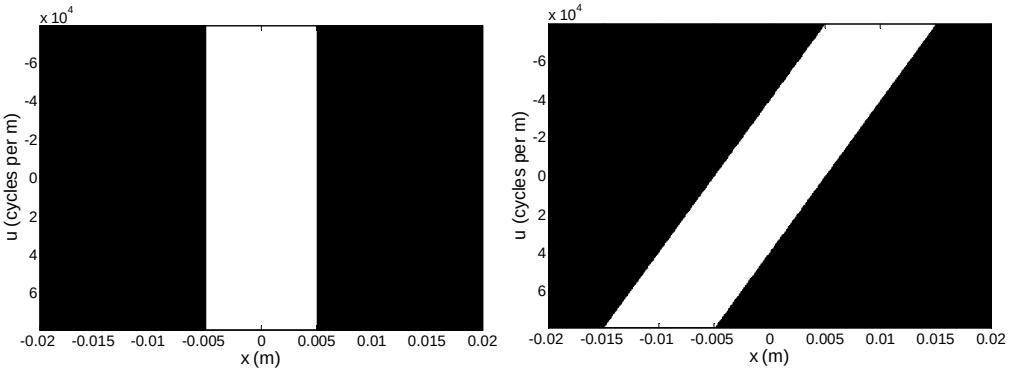

Figure 7.1: Wigner chart of a propagating signal with (a) the wavefield immediately after the object and (b) the Wigner chart after propagation a distance of 0.2m.

$$\psi\{F_{\lambda d}\{f(x)\}(x^{'})\}(x^{'},u^{'}) = \psi\{f(x)\}(x+\lambda du,u). \tag{7.4}$$

The affect of applying a FST to a signal can be expressed in terms of the ABCD matrix operating on the phase space coordinate vector,

$$\begin{bmatrix} x^{'} \\ u^{'} \end{bmatrix} = \begin{bmatrix} 1 & \lambda d \\ 0 & 1 \end{bmatrix} \begin{bmatrix} x \\ u \end{bmatrix}. \tag{7.5}$$

Figure 7.2 (a) shows the WDF of the CCD which we is limited in both spatial distribution and spatial frequency. The FST causes a shearing of a signal's WDF along the x direction as shown in Figure 7.2 (b). The CCD can only capture a finite area of this sheared wave field. Figure 7.2 (c) shows the part of the propagated signal that is captured by the CCD, and Figure 7.2 (d) shows the twin image which is the $O^{*}(x,y)R(x,y)$ term from Equation 7.2 and is present due to the fact that the CCD can only capture intensity.

The WDF of the CCD is denoted as $\psi\{\text{CCD}(x)\}(x,u)$ and the WDF of the wavefield emanating from the object is $\psi\{O(x)\}(x,u)$. After Fresnel propagation

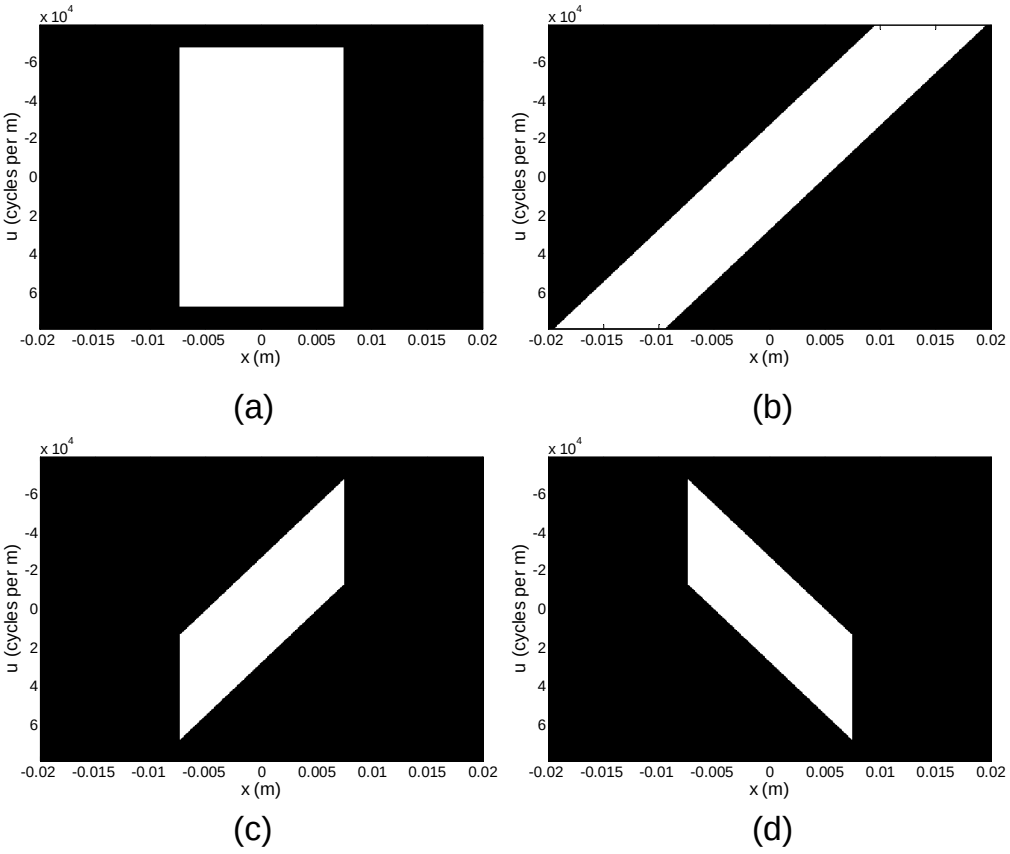

Figure 7.2: Wigner chart of (a) the CCD, limited in both spatial distribution and spatial frequency, (b) the Wigner chart after propagation a distance 0.289m ensuring no aliasing, (c) the captured object signal, and (d) the twin image signal that is present due to the fact that the CCD only captures intensity.

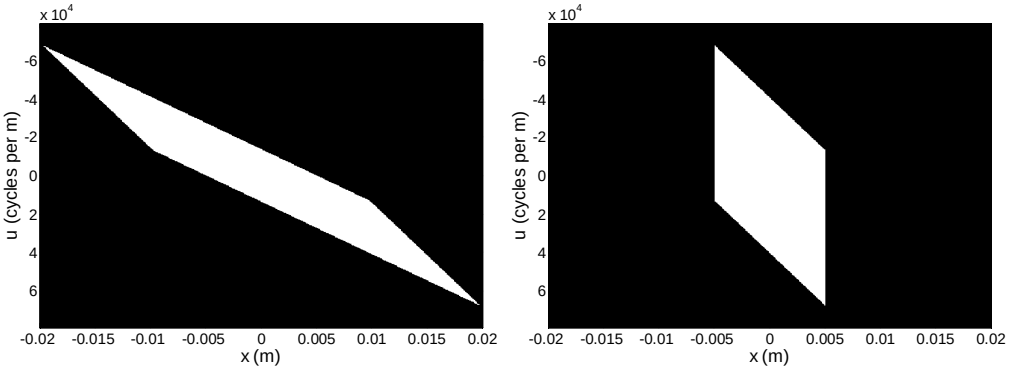

Figure 7.3: Wigner chart of (a) the wanted image signal at the twin image in-focus plane and (b) the twin image at its in-focus plane. Note that the twin image has a narrower spatial distribution and can be removed by occlusion, leaving a large portion of the wanted image signal intact.

the signal's chart now takes the form shown in Figure. 7.2(b) and the WDF of the propagated signal is given by $\psi\{O(x)\}(x-\lambda du, u)$. Capturing the DH is equivalent to multiplying the complex signal by the CCD signal CCD(x). The resultant WDF is therefore equivalent to a convolution of the WDFs along the u axis,

$$\psi\{\text{hol}(x)\}(x,u) = \psi\{O(x)\}(x+\lambda du, u) *^u \psi\{\text{CCD}(x)\}(x,u), \tag{7.6}$$

However, as we have seen from Equation 7.2 above, the twin image will also be present as the CCD can only capture intensity. Therefore, our captured DH is

$$\begin{aligned}\psi\{\text{hol}(x')\}(x',u) &= \psi\{O(x)\}(x+\lambda dk, u) *^u \psi\{\text{CCD}(x)\}(x,u) \\ &+ \psi\{O^*(x)\}(x+\lambda dk, u) *^u \psi\{\text{CCD}(x)\}(x,u). \end{aligned}\tag{7.7}$$

and as Figures 7.2 (c) and (d) show, the spatial distribution and spatial frequency distribution of these two signals cannot be easily separated. The technique we

use is to propagate both signals to the in-focus plane of the twin image, thus localizing its spatial distribution so that a simple occlusion can remove it. In the process some of the wanted image signal is lost, but the majority is kept and when it is propagated to its in-focus plane the noise from the twin image is no longer present. The Wigner chart of the signals after they have been propagated to the in-focus plane are shown in Figure 7.3 (c) and (d). These are then multiplied by a rectangular lightless opaque planar occlusion (see Equation 6.3 from Section 6) and the resultant WDF is given by

$$\begin{aligned}\psi\{\text{WantedMinusTwin}(x)\}(x,u) &= [\psi\{O(x)\}(x) *^u \psi\{\text{CCD}(x)\}(x,u)] \\ &*^u \text{W}\{\text{occlusion}\left(\frac{x}{w_o}\right)(x,u)\} \\ &+ [\psi\{O^*(x)\}(x) *^u \psi\{\text{CCD}(x)\}(x,u)] \\ &*^u \text{W}\{\text{occlusion}\left(\frac{x}{w_o}\right)(x,u)\}. \end{aligned} \tag{7.8}$$

where w_o is the width of the occlusion. If the width of the occlusion is large enough to cover the spatial distribution of the twin image then the second term goes to zero. Propagating the resultant signal back to the in-focus plane of the wanted image results in a reconstruction that is free from the corrupted effect of the twin image.

The Wigner chart also provides a graphical means to illustrate how much padding of the DH is needed to ensure that no aliasing occurs when the signal is propagated back to the wanted image using the angular spectrum method of simulating the Fresnel Transform which was discussed in Section 2.2.3 [see Figure 7.3 (a)]. The angular spectrum method [MZK97, MGF+99] for propagation has a constant output window size which is equal to the input window size. The object signal will be wrapped within the reconstruction window if the reconstruction window is not large enough to contain the entire spatial support of the object.

Therefore, using the angular spectrum method we have to pad the DH with zeros to ensure that the reconstruction window is at least as large as the spatial extent of the object signal at the reconstruction plane of the twin image. We have calculated this spreading for an object with size 0.01m positioned at 0.289m from the CCD. It is clear from the Wigner chart that in order to avoid aliasing in this scenario, the DH should be padded to twice its size. In the next section we further motivate the application of our technique by providing results of experiments we have carried out on both in-line and PSI DHs.

7.3 Results and discussion

Depending on the resolution requirements, it may be necessary to choose a Gabor in-line DH setup [see Section 2.2.2.1]. In these cases the resultant DHs will invariably suffer from the presence of the unwanted out-of-focus twin image. Using the technique described in the previous section we now demonstrate the benefits of our technique for removal of this unwanted noise. Figures 7.4 (a) and (b) show the in-focus reconstruction of the twin image and the in-focus wanted image respectively. The zero order terms have been removed, but both images are still corrupted by each others out-of-focus signals and speckle. Figure 7.4 (c) shows the occluding mask that has been created just large enough to occlude the in-focus twin image. Figure 7.4 (d) shows the after effect of the twin image plane multiplied by the mask. It has been cropped to 2900×2900 pixels for display purposes, but in fact had to be padded to 4096×4096 in order to ensure no aliasing. The signal is then propagated back to the in-focus wanted image plane and is shown in Figure 7.4 (e). Zoomed in versions of the improvement in image quality are shown in Figures 7.5 (a) through (f).

Figure 7.6 shows the effects of sampling and the copies of the image that it

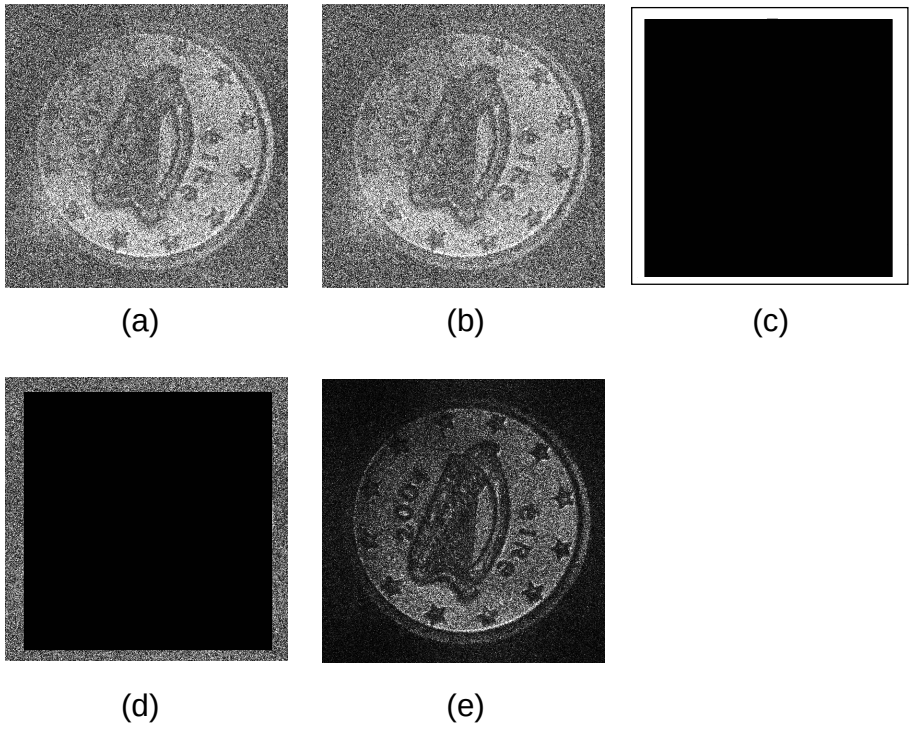

Figure 7.4: (a) Twin image, (b) wanted image corrupted by out-of-focus twin image (minus the DC terms), (c) the occluding mask, (d) the twin image plane after multiplication by the occluding mask, and, (e) the wanted image (minus the out-of-focus twin image and the DC terms.) Note all reconstructions are cropped to 2900×2900 pixels in size and all have the same display settings, except (c), which is a binary image.

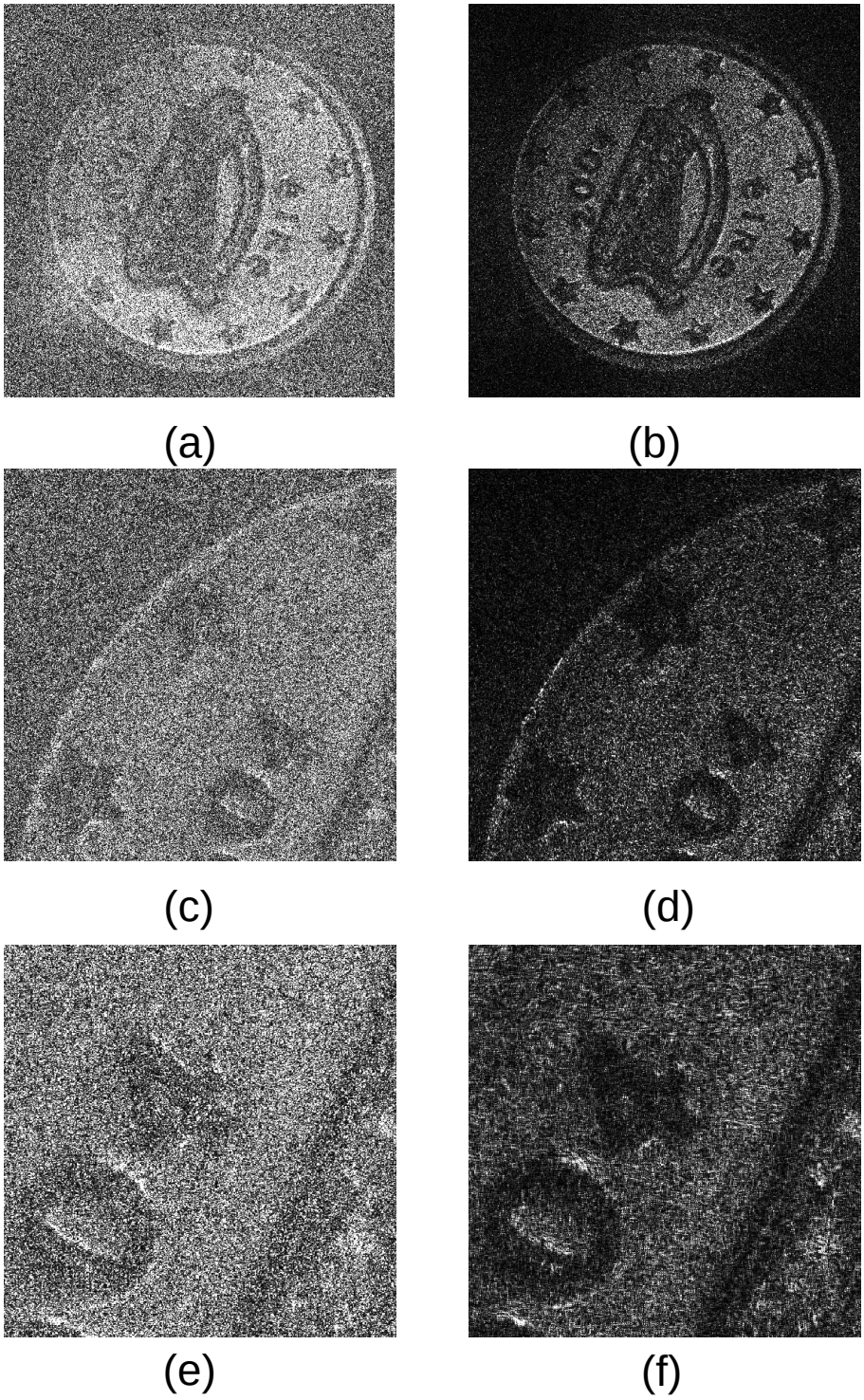

Figure 7.5: (a) Wanted image corrupted by out-of-focus twin image (minus the DC terms), (b) the wanted image (minus the out-of-focus twin image and the DC terms.), (c) zoomed in version of (a) (1000×1000 pixels), (d) zoomed in version of (b), (e) zoomed in version of (a) (500×500 pixels), (f) zoomed in version of (b).

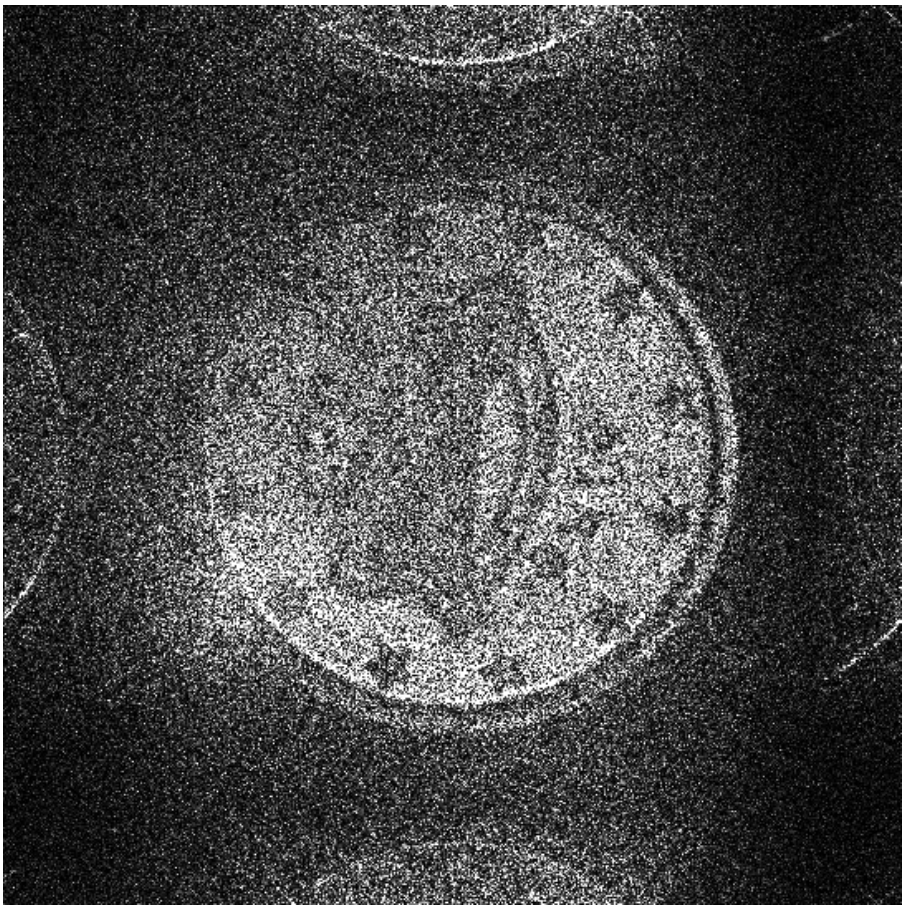

Figure 7.6: Wanted image of coin DH showing aliasing effects (4096×4096 pixels in size)

creates. It shows that in order to localize the spatial distribution of either the wanted or twin image, sufficient padding at the DH plane is required, but not so much as to introduce the sampling copies of the image. Using the analysis in the previous section and the Wigner chart as an aid we can determine the spreading of the wanted image signal at the point when the twin image has been brought to focus so that it can be removed.

7.4 Summary

We have presented a DSP technique for removing the corruptive effect of the twin image in digital holography. The WDF was used to provide a theoretical grounding for the technique and we saw how the Wigner chart can be used as an add to indicate the amount of padding needed to capture the wanted image without aliasing effects. The application of this technique allows for the use of in-line DHs instead of PSI or off-axis DHs. In-line DHs are single shot DHs and are therefore suited to the capture of dynamic scenes unlike PSI DH which are multi-shot DHs. Although off-axis DHs are also single shot, they are restricted to using only a quarter of the camera's bandwidth and therefore in-line DHs post-processed with our technique could be used instead. A disadvantage is that the technique cannot be used for digital holographic microscopy as removing the twin image corrupts the phase. Another disadvantage is that it is computationally expensive involving an additional application of the spectral method of reconstruction and determination of the correct occlusion mask. At its core the technique brings to focus the twin image and occludes it using a binary mask. The remaining wanted images' signal energy is then propagated back to the DH plane and resulting in a DH minus the twin image. All subsequent reconstructions of the DH are free of the contaminating effects of the twin image. This results in much clearer, noise free (except for the presence of the speckle) reconstructions.

Chapter 8

Conclusion

This thesis detailed a number of contributions to the improvement of reconstruction of DHs. These contributions are divided into two categories: A) speckle reduction in reconstructions of DHs, and, B) modeling and overcoming partial occlusion effects in reconstructions of DHs, and, using occlusions to reduce the effects of the twin image.

8.1 General discussion

The first area in which this thesis makes a contribution is in the area of speckle reduction in reconstructions of DHs. Iwai and Asakura [IA96] classified the principles of speckle reduction into five categories: 1) control of spatial coherence, 2) control of temporal coherence, 3) temporal averaging based on spatial sampling, 4) spatial integration at the detector, and 5) digital image processing. In this thesis, we have investigated new techniques for reducing speckle content in reconstructions of DHs are in category 5. We note that some of our methods are based on simulating earlier optical methods that fall into some of the other categories. For instance in Chapter 5 we introduced a new DSP technique that was inspired

by earlier work by Gama [Gam75] who reduce the spatial coherence of the reconstruction beam. Chapter 3 followed the work of Dainty and Welford [DW71] and Hariharan and Hegedus' [HH74], whose work is categorized in the third category. We note that within the first four categories there are numerous techniques that could also be adapted into the fifth category of digital image processing in the future. We discuss some of these in Section 8.2.

Image quality assessment plays an important role in many image processing applications. A lot of research has been carried out in an effort to develop objective image quality metrics that correlate with perceived quality measurement, unfortunately with only limited success [WBL02]. Peak signal-to-noise ratio and mean squared error are two of the most popular objective image quality metrics, but they are criticized for not matching up well with perceived qualtity [WBL02]. Wang *et al.* [WBL02] suggest that the best way to assess the quality of an image is to use a subjective process, called the mean opinion score. They then state however that the mean opinion score method is too inconvenient, slow and expensive for practical usage. In this thesis, we have not actively used subjective processes to decide on the quality of an image. We instead have relied on a number of well known objective metrics, namely speckle index, edge preservation and resolution [MHM+07, SFSL97]. Of course, depending on the particular application that requires a level of speckle reduction, the use of subjective expert analysis could well be needed to ensure optimum results are achieved.

This thesis has contributed a number of techniques to the general field of speckle reduction in DHs and we expect that each of them will be used in future varied applications. According to the objective metrics that we have employed, the use of wavelets in Chapter 4 is superior to the DFF [see Chapter 3]. However, we argue that there are certain situations in which wavelets would not necessarily be the optimum choice. For instance, the DFF can potentially produce speckle reduced

DH reconstructions of natural scenes of a better quality (in the subjective sense), than could be produced by the Haar mother wavelet, whose simple step edge design is not suitable to naturally occurring shapes and curves [see Figure 4.11]. Likewise, if important features are orientated a certain way, then the 2D and 3D filtering techniques presented in Chapter 5 could be the best choice for a given application. In fact when we later captured a DH of a USAF resolution chart for Chapter 5 the 2D filtering technique performed best. Unlike the automatic detection of the image resolution using an FFT based search algorithm that was applied in Chapter 4, this subjective visual inspection process revealed different outcomes in terms of maintained resolution. This issue of calculating resolution is one which, in the opinion of the author, deserves further attention. It would be helpful for a standard to emerge that could then be used in an objective way by all researchers. Once we used 3D filtering we observed an advantage over the other techniques in the thesis due to the resulting increase in the depth of focus of the resulting reconstructions [see Figure 5.18].

An important question naturally arises when using a given speckle reduction technique, and that is: What level of speckle reduction should one strive for? For the purpose of this thesis speckle has been considered a noise and therefore the answer is that we should try to reduce it as much as possible. However, we have seen that reduction of speckle can result in loss of resolution and edge blurring. These effects have to be taken into account when choosing a speckle reduction technique for a particular application. The techniques developed in this thesis are generic and are designed to be used in multiple situations. Depending on the application domain, the use of subjective expert analysis may need to be used to determine the optimum level of speckle reduction. However, in the absence of subjective analysis, the objective quantitative metrics we have employed are a suitable indication of the performance of the various techniques we have developed

in this thesis.

We note that all of our techniques require only a single DH to reduce the speckle effect. This means that our techniques can reduce the speckle content in reconstructions of DHs of dynamic scenes. We demonstrated this in Appendix D when we used a transmissive single shot in-line digital holographic setup to capture an object embedded between two layers of tissue, and then used the DFF to reduce the speckle of subsequent reconstructions.

The second area in which this thesis makes a contribution to is the area of occlusions in digital holography. In Chapter 6 we investigated the nature of different types of opaque occlusions and the effect of reconstructing only certain parts of the DH using the Wigner chart [Wig32, Bas97]. The motivation of this research was to reconstruct a subset of the DH in order to reveal hidden features on a partially occluded object [EMM$^+$05, MEH$^+$06b, MEH$^+$06a]. With the aid of the Wigner Chart we were able to show that the properties of DHs allow for the overcoming of partial occlusions under certain circumstances. We went on to verify our theory in a simulated experiment in which a subset of pixels was used to reconstruct an object, and these pixels were chosen in such a way as to reveal occluded features on the object. In Section 8.2.4 we propose to extend this work by integrating its benefits with that of an object recognition algorithm. In this thesis we also investigated the use of occlusions for the purpose of removing the twin image. In 1996 Pedrini *et al.* [PFFT98] successfully eliminated a large portion of the twin image in a DH by bringing the real image to focus and filtering out the out-of-focus twin image around this image. The filtering process can be thought of as an occlusion at the reconstruction plane. Following on from this work, we instead brought the twin image plane to focus [see Chapter 7] and directly occluded the twin image. This had the added benefit of entirely removing the twin image's energy. The technique worked well with in-line DHs who by their nature are severely corrupted

by the out-of-focus twin image, but we also found that the technique worked for PSI DHs. These DHs are also affected by the out-of-focus twin image due to problems of non-perfect alignment and tuning of optical equipment in the experiment capture phase. This technique should facilitate the the ability to choose inline DHs over PSI DHs in future applications. This is especially important for applications that require the capture of dynamic scenes.

8.2 Future work

In this section, we highlight a number of ideas for future work. One of these has already been partially developed and in this case the reader is directed to the initial results achieved in the relevant Appendix.

8.2.1 Discrete Fresnel filter

The discrete Fresnel filter is similar to the DFF in that it produces independent speckle patterns and adds those patterns together to reduce the speckle content of the DH reconstruction. However, it has one main disadvantage over the DFF in that the different speckle patterns it produces are all representations of different perspectives of the object under consideration. This suggests that the discrete Fresnel filter can only work on 2D objects. However, as the resolution of the todays' CCDs is still quite limited, only small angular perspectives can be achieved in DHs. This means that the reduction in speckle can be more beneficial than the resultant blur that occurs when different perspectives of the image are superposed. In fact, the addition of different perspectives to reduce speckle was previously employed in an integral imaging system that used coherent light [RA03]. Like the DFF, this technique simulates an optical technique that falls into the third category called spatial sampling given by Iwai and Asakura [IA96] [see Section 1.1.2]. Although

outperformed by the DFF, the discrete Fourier filter technique has performed well when compared with the mean and median filters in terms of speckle index, resolution and edge preservation. Please see Appendix E for some initial results.

8.2.2 Extension of the Discrete Fourier filter

In Chapter 3 we introduced the DFF and showed it was superior to the mean and median filters in terms of resolution and speckle index. However, we observed that in terms of the edge preservation metric [SFSL97], the DFF performed poorly. We suggested that this could be due to the fact the the filter used in the Fourier domain is a simple bandpass filter. In future work, we propose to investigate complex, Butterworth [HV93] and Chebyshev [MOL01] filters in an effort to improve the quality of DH reconstructions.

8.2.3 Speckle reduction by simulation of other optical methods

In this thesis, we have detailed a number of methods to reduce the speckle content in reconstructions of DHs that simulate optical techniques for the reduction of speckle in holography. However, there are many other optical techniques for reducing speckle that could be digitized and used for digital holography. In particular, we propose to investigate the use of random shaped and sized apertures in the hologram plane. Yu and Wang [YW73] studied this in 1973 and concluded that the speckles in reconstructed images can be completely eliminated by using a moving random mask at the hologram plane, without losing image resolution. The use of moving diffusers to average out the effect of speckles has been popular [Sch71]. The introduction of a moving diffuser into the object beam during hologram recording results in a number of independent speckle patterns being in-

tegrated in the hologram plane. We will investigate ways to simulate this effect during the reconstruction stage of digital holography. There are many more optical techniques for reducing speckle that could be digitized [see references in [IA96]]. We suggest that some or all of these could be digitized in the future.

8.2.4 Object recognition of partially occluded objects in reconstructions of DHs

One of the main challenges in pattern recognition is overcoming the effects of partial occlusions is a system [Ull93, JPDH06]. In most cases, algorithms are developed and applied to the partially occluded object in an effort to complete the missing parts. Recently, Javidi *et al.* [JPDH06] used a 3D integral imaging system to overcome the effects of partial occlusions. They found that the performance of the proposed recognition system with 3D volumetric reconstruction for occluded objects was superior to the performance of the correlation of occluded 2D images. Using the theoretical foundations laid in Chapter 6, we propose a digital holographic pattern recognition system to overcome the effects of partial occlusions. Javidi and Tajahuerce [JT00] initially proposed a 3D object recognition using digital holography in 2000 and this was extended to distortion-tolerant object recognition with digital holography the following year [FTCJ01]. We suggest that this work could be extended to incorporate the recognition of partially occluded objects in 3D scenes captured using digital holography.

8.3 Outlook

Digital holography is a relatively new imaging technique that shows a lot of promise for the future. Its inherent 3D properties coupled with the fact that phase information is readily available and given that DHs can be electronically

stored, transmitted, compressed, and processed, mean that it has been adopted in many fields of science, including: metrology [PZT95b, PZT95a], particle analysis [AKJ97, OZ00, MY00, PM03, SDF+07], microscopy [ZY98, CMD99, XPMA01, PT02, FGA+05, MRM+05], and, pattern recognition [JT00, FTCJ01, KJ04, JK05]. In using DHs, all of these fields (with the possible exception of microscopy, due to the use of a large objective lens), suffer from the corruptive effects of speckle. In certain cases where in-line DHs are used they also suffer from the effects of the out-of-focus virtual image. We envisage that the contributions made in this thesis, in the area of speckle reduction and twin image suppression, will be of benefit to these and other fields that use DHs.

We previously pointed out that speckle is present in all coherent imaging systems, i.e., ultra sound imaging [GCS05], SAR imaging [USB03] and optical coherent tomography (OCT) imaging [AKF04]. We have also hinted at the possibility of using some of the our speckle reduction techniques in these and other areas could be investigated in the future. This is based on the fact that as long as the speckle that is corrupting these imaging systems is fully developed speckle, our techniques will work in exactly the same manner in which they work for DHs. We intend to investigate the use of these techniques with these other imaging systems in the near future.

Finally, it could be very advantageous to develop speckle reduction techniques that reduce speckle at the hologram plane, rather than at the reconstruction plane. This would have the benefit that every reconstruction of a speckle reduced DH would display reduced speckle. We have been unable to find other works, whether optical or digital, that reduce speckle in this way. However, in 2006, Shortt *et al.* studied the compression of DHs using wavelets [SNJ06b] and nonuniform quantization [SNJ06a]. This compression was done at the DH plane, not the reconstruction plane. Also, Darakis and Soraghan [DS06a] compressed PSI DHs by

applying standard JPEG compression to the four interferograms rather than the DH itself. These works benefited from applying their techniques to the DH or the interferograms directly. We suggest that new speckle reduction techniques could be developed to reduce speckle at the DH plane that will have huge benefits in terms of computational time for certain applications that rely on the multiple rendering of speckle reduced DH reconstructions (i.e., depth independent segmentation of DHs [EMF+07]), although we add a word of caution that a viable way to do this has not been yet found.

Chapter 9

Appendix A

This appendix is taken from Lowenthal and Arsenault [LA70], and is included here for convenience.

If a nonuniform diffuse object has a complex amplitude $f(r)$, the Fourier transform of which is $F(u)$, we define the average power spectrum as the average illuminance in the Fourier plane of the optical system,

$$\bar{S}_f(u) = \langle |F(u)|^2 \rangle. \tag{9.1}$$

Since

$$F(u) = \int_{-\infty}^{\infty} f(r) e^{-2\pi i u \cdot r} \mathrm{d}r, \tag{9.2}$$

where $\mathrm{d}r$ is an element of the area $\mathrm{d}x\mathrm{d}y$, we have

$$\bar{S}_f(u) = \int_{-\infty}^{\infty} \int_{-\infty}^{\infty} \langle f(r_1) f^*(r_2) \rangle e^{-2\pi i u \cdot (r_1 - r_2)} \mathrm{d}r_1 \mathrm{d}r_2. \tag{9.3}$$

The ensemble average inside the brackets is the autocorrelation $R_{ff}(r_1, r_2)$ of $f(r)$. We can therefore write

$$\bar{S}_f(u) = \int_{-\infty}^{\infty}\int_{-\infty}^{\infty} R_{ff}(r_1, r_2) e^{-2\pi i u \cdot (r_1 - r_2)} \mathrm{d}r_1 \mathrm{d}r_2. \tag{9.4}$$

If the double Fourier transform of $R_{ff}(r_1, r_2)$ is

$$F\{R_{ff}(r_1, r_2)\} = \Gamma(u_1, u_2), \tag{9.5}$$

then the average power spectrum is equal to the double Fourier transform of the autocorrelation, with $u_1 = u_2$

$$\bar{S}_f(u) = \Gamma(u_1, u_2). \tag{9.6}$$

After some algebra, Eq. 9.4 may be written

$$\bar{S}_f(u) = \int_{-\infty}^{\infty} \bar{\rho f}(\tau) e^{-2\pi i u \cdot \tau} \mathrm{d}\tau. \tag{9.7}$$

with $r_1 - r_2 = \tau, r_2 = r$, and

$$\bar{\rho f}(\tau) = \int_{-\infty}^{\infty} R_{ff}(r + \tau, r) \mathrm{d}r. \tag{9.8}$$

The quantity $\bar{\rho f}(\tau)$ is the average autocorrelation. Equation 9.7 states that the average autocorrelation and the average power spectrum are a Fourier transform pair, which means that they satisfy the Wiener-Khinchin theorem. These two quantities, respectively, defined by Eqs. 9.4 and 9.8 are the two-dimensional space analogs of the same quantities used in signal theory [Pap65]. But in optics, the existence of the Fourier plane gives a special meaning to the average power spectrum.

Chapter 10

Appendix B

The results of speckle index and resolution for the DFF technique [VZW$^+$05] are given in Table 10.1 and for the median and mean filters are given in Table 10.2.

Discrete Fourier filtering technique		
Aperture	Speckle index	Resolution
2048	1.02	1 (no loss)
1024	0.5398	1 (no loss)
512	0.3156	$\frac{1}{2}$
256	0.1851	$\frac{1}{4}$
128	0.1142	$\frac{1}{8}$

Table 10.1: This table shows the results of speckle index verses resolution for the DFF technique.

The results of speckle index and edge preservation for the DFF technique are given in Table 10.3 and for the median and mean filters are given in Table 10.4.

	Median filter		Mean filter	
Neighbourhood	Speckle index	Resolution	Speckle index	Resolution
(1×1)	1.02	1 (no loss)	1.02	1 (no loss)
(3×3)	0.51	$\frac{1}{2}$	0.39	$\frac{1}{2}$
(5×5)	0.34	$\frac{1}{4}$	0.27	$\frac{1}{4}$
(7×7)	0.26	$\frac{1}{7}$	0.21	$\frac{1}{7}$

Table 10.2: This table shows the results of speckle index verses resolution for the median and the mean filters.

Discrete Fourier filtering technique		
Aperture	Speckle index	Edge preservation
1024	0.54	0.018
512	0.31	0.026
256	0.18	0.031
128	0.11	0.017

Table 10.3: This table shows the results of speckle index and edge preservation for the DFF technique.

	Median filter		Mean filter	
Neighbourhood	Speckle index	Edge pres.	Speckle index	Edge pres.
(3×3)	0.51	0.0055	0.39	0.0045
(5×5)	0.34	0.0011	0.27	0.0031
(7×7)	0.26	0.000047	0.21	0.0052

Table 10.4: This table shows the results of speckle index and edge preservation for the median and the mean filters.

Chapter 11

Appendix C

In Hariharan and Hegedus' [HH74] paper on the reduction of speckle in coherent imaging, they give the analysis for a continuously moving aperture in the Fourier plane of a 4f imaging system [see Figure 3.1 in Chapter 3]. They conclude that the power spectrum of the speckle can be reduced by between 33 and 50 per cent, if a continuously moving aperture is used rather than simply sampling the independent positions that the aperture can take on. However, according to Dainty and Welford [DW71], the power spectrum of the speckle is only effected by the number of independent positions that the aperture can take on in the Fourier plane. Furthermore, we know from Goodman [Goo06] [see Chap. 2.3.4] that it is only through the addition of independent speckle patterns on an intensity basis that we can achieve a $\frac{1}{\sqrt{N}}$ reduction in the speckle index. In this section a simple experiment is run in order to determine whether the improved speckle reduction Hariharan and Hegedus spoke off could be achieved using overlapping blocks. The experiment setup is the same as shown in Figure 3.1(b), except that this time the apertures are allowed to overlap each other. Depending on the amount of overlap this can result in many more reconstructions to sum up in order to create the final reconstruction. We investigated a non-overlapping approach verses an overlapping

approach. Figure 11.1(a) shows the reconstruction obtained when a 1024×1024 aperture is used, and Figure 11.1(b) shows the reconstruction obtained when the same size aperture, but with a step size (indicates the level of overlap) of 128 pixels. In order to calculate the number of samples taken in the Fourier plane the following equation is used

$$S = (\frac{h - w}{s} + 1)^2 \tag{11.1}$$

where h is the width of the hologram (in this experiment, $h = 2048$), w is the width of the aperture (in this experiment, $w = 1024$), and s is the step size. Therefore, the number of samples used to create the reconstruction in Figure 11.1(b), which used a step size of 128 pixels, was 81, compared with only 4 used the non-overlapping case [shown in Figure 11.1(a)]. However, as can be seen from Figure 11.1, there is no noticeable reduction in the speckle content for the overlapping case. The results of different step sizes, along with their effect on speckle index (once again calculated on a homogenous area of the stormtrooper reconstruction) is shown in Table 11.1. These results show that there is no advantage in using overlapping filters with the DFF technique. It confirms Dainty and Welford [DW71] and Goodman's [Goo06] assertion that the reduction in speckle that can be obtained depends entirely on the number of independent speckle patterns that are added together.

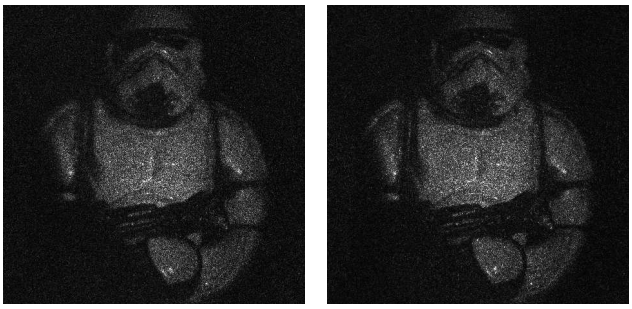

(a) (b)

Figure 11.1: A non-overlapping reconstruction with aperture size 1024 pixels is shown in (a), and, an overlapping approach with aperture size 1024 and step size 128 is shown in (b).

Overlapping discrete Fourier filtering technique		
Aperture	Speckle Index	Step size
1024	0.53	1024
1024	0.53	512
1024	0.54	256
1024	0.56	128

Table 11.1: This table shows the results of incorporating overlapping filters with the discrete Fourier filtering technique.

Chapter 12

Appendix D

Optical imaging of biological tissue in the visible and near-infrared has become an important area of research due to the many benefits it possesses compared to other tomographic techniques. Radiation at these wavelengths is non-ionizing, and so offers the possibility of non-invasively imaging structures within the body, for example, in mammography [DVG06] and brain imaging [SBS02]. One of the stated aims of these spectroscopy techniques is to provide 3D mapping of tissue structures using non-invasively light [DVG06]. The relative cost of building such systems is also much lower than its counterparts (e.g. functional magnetic resonance imaging or computed axial tomography scans), and in many cases is less bulky, allowing it to be used in bedside monitoring [BRRO05]. The work in this appendix has emanated from a collaborative effort between the author and Aoife Cuddihy.

Many techniques have been developed in the area of optical tomography [ZT02]. Optical tomography is used to generate full 3D images from measurements taken from sources and detectors widely spaced over the surface of an object. Both coherent [DF03] and diffuse light [GHA05] have been used in optical tomography. Two such techniques include optical coherence tomography (OCT) [HSL$^+$91] and noninvasive optical imaging by speckle ensemble (NOISE) [RA03]. OCT oper-

ates strictly in the reflection mode and is an interferometric method that utilizes spatially coherent illumination with a low temporal coherence. The latter property enables focusing on layers of biological tissue with sub-micron accuracy. A layer at a particular depth may be isolated through adjustment of the optical set-up [HSL+91]. However, it is not ideal for recording dynamic scenes as only one layer at a time may be recorded. NOISE requires the use of coherent illumination in order to generate multiple images of an object using a microlens array (MLA), each with an independent speckle noise. These sub-images are superimposed to strengthen the image of the object, which is common to all of the images, while the various speckles average out in the process. However, although diffraction of the object wavefield occurs, it is not regarded as an interferometric technique, and so does not take full advantage of the complex wavefront scattered by the object. Furthermore, due to the need to capture an array of sub-images the resolution is low. Each of the images captured by the MLA will contain slightly different perspectives of the object. When these are added together, not only will the speckle average out, but blurring along the edges of the object will occur.

We investigate the use of digital holography and the DFF for imaging an object embedded between two layers of biological tissue. It overcomes the disadvantage of OCT in that dynamic scenes can be recorded, and overcomes the disadvantages of the NOISE [RA03] technique in terms of resolution and unnecessary blurring of the edges caused by multiple perspectives of the object being added together. The method is based on a transmissive single shot in-line digital holographic setup to record the complex wavefield emanating from the front tissue surface. The wavefield is reconstructed at the depth of interest using the discrete Fresnel approximation method [see Chap. 2.2.3]. The DFF [MHM+07] from the previous chapter is then applied to this complex reconstruction to reduce the effects of the noise caused by the front scattering layer. We compare our developed technique

with the NOISE [RA03] technique described above.

Digital holography offers significant advantages over 2D imaging methodologies due to its ability to generate a large number of different angular perspectives of an object off-line. The most commonly used techniques for capturing DHs include in-line PSI and off-line DH [Kre05] [see Section 2.2.2]. While PSI has the advantage of removing the d.c.-components and the out-of-focus twin image that are inherent in holography, it requires multiple sequential captures of the scene. This makes the technique unsuitable for the capture of dynamic scenes. The off-line technique only involves one capture and is therefore suitable for dynamic scenes. It also allows for simple removal of the d.c.-components and out-of-focus twin image, but this time at the expense of resolution. We use the simplest of all architectures: an transmissive single shot in-line digital holographic setup. We remove the d.c.-components by computing the Fourier transform of the DH and removing the lower (center) frequencies before inverse Fourier transforming back to the DH plane [KJ97]. Our technique does not overcome the problem of the out-of-focus twin image, but its negative effects are outweighed by the superior resolution we achieve in our DHs. Furthermore, the twin image could be removed using the technique given in Chapter 7. A single shot in-line digital holography setup was recently used to perform 3D object recognition and distortion tolerant 3D object recognition [KJ04, JK05].

The setup for the new technique is shown in Figure 12.1. A linearly polarized helium-neon (633.6 nm) laser beam is expanded and collimated, and divided into object and reference beams. The object beam illuminates a reference object placed at a distance of approximately $d = 350\,\text{mm}$ from a Kodak KAI-4021 camera, with 2032×2048 pixels, each having dimension $7.4\mu\text{m} \times 7.4\mu\text{m}$. As with all coherent imaging systems the resultant reconstructions suffer from speckle. In order to improve the image of the object it is important to reduce the speckle content in

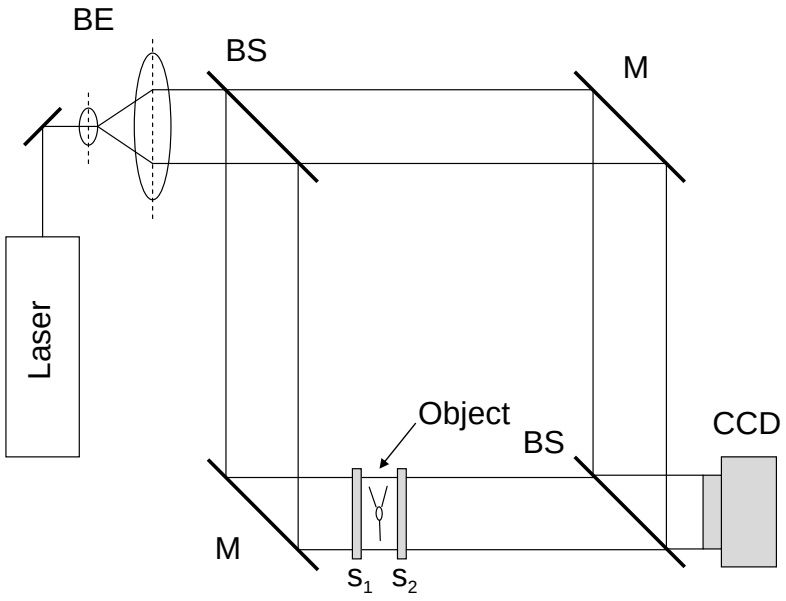

Figure 12.1: Experimental setup for single shot in-line digital holography DH: BE, beam expander;BS, beam splitter; M, mirror; O, object; s_1, s_2, scattering layers.

these reconstructions.

While any speckle reduction technique could be used, we have used the DFF [MHM+07] as it has been shown to be superior to the mean and median filters in terms of speckle index, resolution and edge preservation. The plane, $f(\mathbf{r})$, immediately in front of layer S_2 on the CCD side [see Figure 12.1], can be expressed as the product of two terms, $f(\mathbf{r}) = t(\mathbf{r})d(\mathbf{r})$, where $d(\mathbf{r})$ is a uniform diffuser, $t(\mathbf{r})$ is a transparency that modulates the diffuser, in our case the object, O [see Figure 12.1], and $\mathbf{r}$ is a vector (x, y) in the plane in front of layer S_2. In Chapter 3 it was shown that the average power spectrum of the image intensity is related to the autocorrelation of the image intensity [**?**]. It was further shown that the power spectrum of the image intensity can be spilt into two terms; the first being the power spectrum of the image itself and the second being the power spectrum of the speckle, which we want to reduce. The DFF was initially developed to reduce

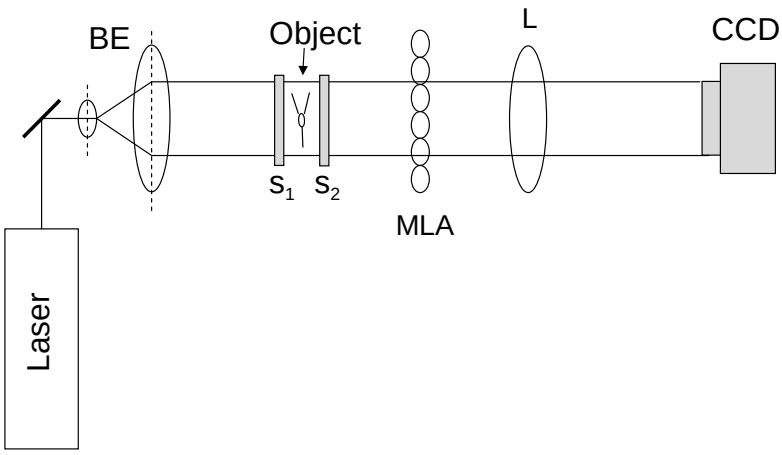

Figure 12.2: Experimental setup for NOISE [RA03] technique: BE, beam expander; s_1, s_2, scattering layers, MLA, microlens array, L, imaging lens.

speckle in reconstructions of DHs of diffuse three-dimensional objects. However, the description of $f(\mathbf{r})$ in this chapter in the context of imaging through two layers of tissue shares the same form as $f(\mathbf{r})$ in Chapter 3. We therefore propose that the DFF can be equally applied to DHs captured using the setup shown in Figure 12.1 to remove noise introduced by the tissue layers.

Two experiments are considered with a view to testing the imaging capabilities of our transmissive single shot in-line digital holography system in conjunction with the DFF technique; (a) embedding an opaque object between layers of plastic, and (b) embedding the same object between layers of bacon [see Figure 12.1]. For comparison, the same experiments were carried out using the NOISE [RA03] technique [see Figure 12.2]. The NOISE technique can be easily implemented by removing the reference beam from the digital holography setup and introducing a MLA and an additional imaging lens after the front scattering layer s_2.

In the first set of experiments a 0.509 ± 0.001 mm thick piece of high density polyethylene (HDPE) was placed 2 mm behind the object. This layer re-

Sample	Average thickness of s_2 (mm) $\pm$0.001mm	Distance of s_2 from the object for the DH experiments (mm) $\pm$0.001mm	Distance of s_2 from the object for the NOISE [RA03] experiments (mm) $\pm$0.001mm
a	0.09	2.5, 7, 16, 30	0, 2.5, 13, 24
b	0.13	2.5, 7, 16, 30	0, 2.5, 13
c	0.25	2.5, 7, 16	0, 2.5, 13
d	0.39	2.5, 7, 16	0, 2.5, 13
e	0.86	2.5, 7	0, 2.5
bacon	2.5	0,3	0,2.5,13

Table 12.1: Thickness and distance of sample layer s_2 from object.

mained constant for the experiment. A number of different polytetrafluoroethylene (PTFE) layers of various thickness were used for s_2 and these were placed at ever increasing distances from the object [see Table 12.1]. The object, a thin piece of metal wire [see Figure 12.3], was placed at a distance of 347 mm from the CCD plane.

For each thickness of layer s_2, a DH was captured with the distances between the object and layer s_2 indicated in Table 12. In order to remove the d.c.-components we Fourier transformed the DH, set the center 200×200 pixels to zero, and then inverse Fourier transformed back to the DH plane [Kre05]. We then reconstructed the DH using the direct method of reconstruction [see Section 2.2.3]. In order to reduce the speckle content in the resultant images the DFF technique is applied with an aperture size of 256×256 pixels. Figure 12.3 (a) shows the resultant image for sample b (thickness 0.13 ± 0.001 mm) at distance 2.5 mm. The object is visible, but heavily corrupted by speckle. Figure 12.3 (b) shows the effect

of applying the DFF. For comparison, Figure 12.3 (c) shows one of the subimages produced by the NOISE [RA03] technique for the same sample and distance. The object is not visible. However when all 128 subimages are added together, the speckle is averaged out and the object becomes visible [see Figure 12.3 (d)]. It is clear that the image of sample b produced by our new technique is much shaper in terms of resolution than that produced by the NOISE technique.

In the second experiment the object is placed between two layers of bacon, both of thickness 2.5 mm. As in the first experiment layer s_1 was placed 2 mm behind the object. In order to produce images in which the object was visible we found that it was necessary to place layer s_2 had to be placed as close to the object as possible (effectively 0 mm away from it). Figure 12.4 (a) shows the resultant image before application of the DFF technique and (b) shows the resultant image after application of the DFF technique (once again with an aperture size of 256×256 pixels). For comparison, Figure 12.4 (c) shows one subimage from the captured image using the NOISE [RA03] technique, and (d) shows the result of averaging the 128 subimages using the NOISE technique. Once again the qualitative results indicate that our new technique the NOISE technique.

In order to quantify the variation in image quality as the diffuser thickness and distance changed for experiment 1 and the tissue distance changed for experiment 2, a correlation metric is employed. A calibrated image was calculated for each experiment. This was done by removing layer s_2 imaging the object. The correlation between the calibrated image and the images produced in each experiment was then calculated. Figure 12.5 (a) shows the results of our technique and Figure 12.5 (b) shows the result of the NOISE technique. Each figure plots the correlation versus the distance of layer s_2 from the object, for each sample, with the correlation normalized with the calibrated images autocorrelation.

In general, we see that with increasing sample thickness and distance from the

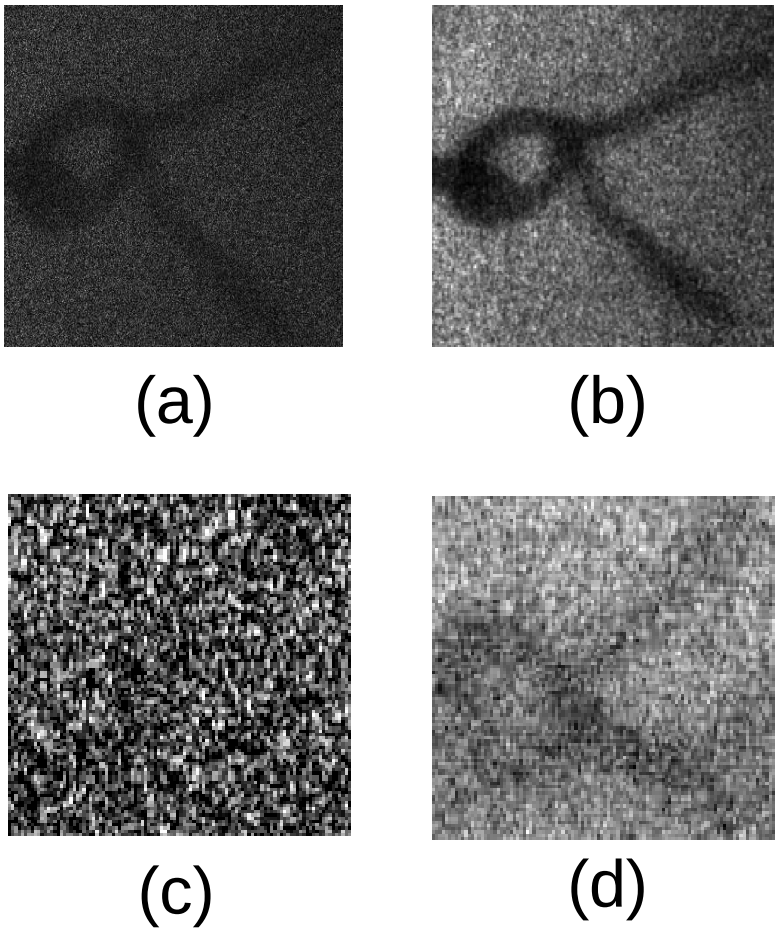

Figure 12.3: (a) Image from our new technique for PTFE sample b at distance 2.5 mm, (b) DFF version of (a) using an aperture size of 256×256 pixels, and for comparision (c) shows one subimage from the NOISE [RA03] technique for the PTFE sample b at distance 2.5 mm, and, (d) shows the resultant image for the NOISE technique in which 128 subimages were averaged for the same sample at distance 2.5 mm.

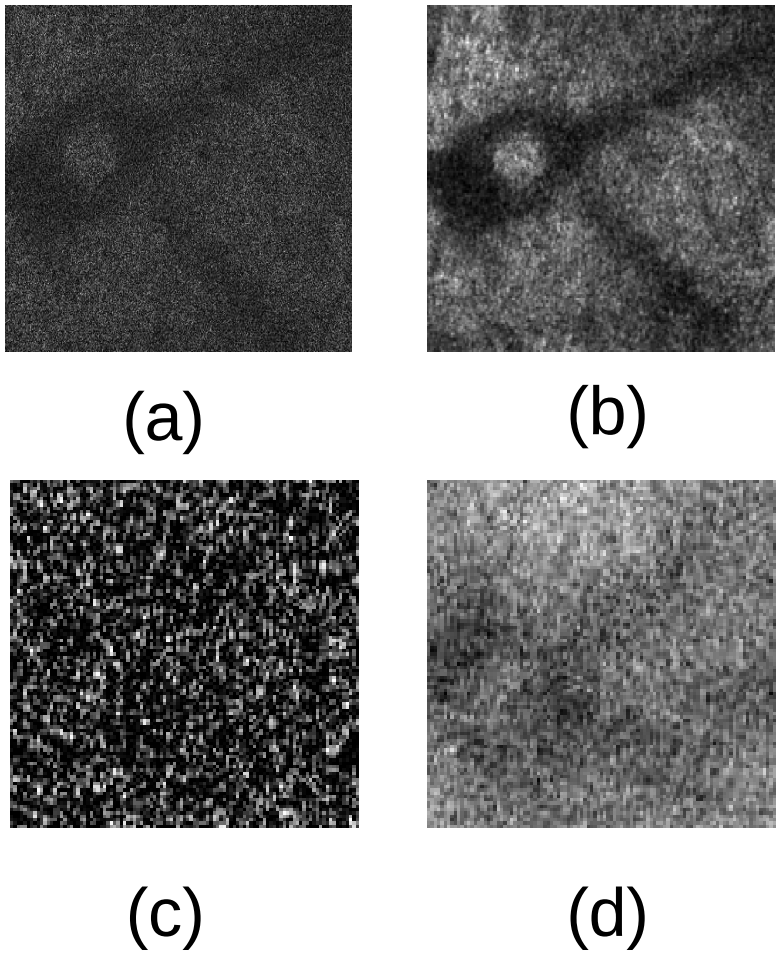

Figure 12.4: (a) Image from our new technique for the bacon sample at distance 0 mm, (b) DFF version of (a), and for comparision (c) shows one subimage of the NOISE [RA03] technique for the bacon sample at distance 0 mm, and, (d) shows the resultant image for the NOISE technique in which 128 subimages were averaged for the same bacon sample at distance 0 mm.

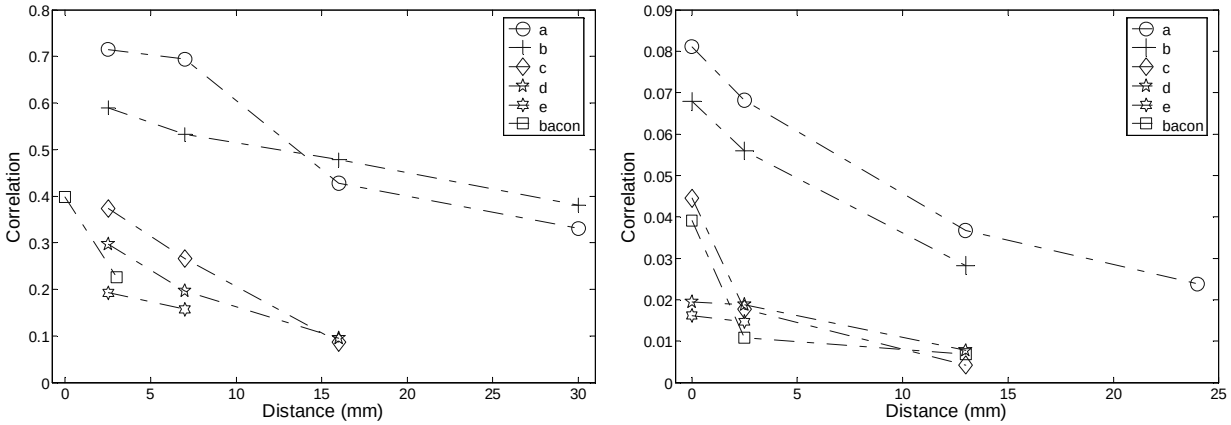

Figure 12.5: (a) Correlation versus distance of layer s_2 from the object for each sample using our new technique, and, (b) correlation versus distance of layer s_2 from the object for each sample using the NOISE [RA03] technique. (Note that our technique outperforms the NOISE by whole order of magnitude in terms of correlation).

object, the correlation decreases. This indicates that the objects shape can no longer be resolved. The correlation values are approximately a factor of 10 times greater for our proposed technique than that of the NOISE technique. This is a considerable improvement. We note that in order to produce images in which the object is visible, the front scattering layer s_2 had to be placed close enough to the object so that the object was visible to the naked eye even in incoherent light. This suggests that a photograph of the object could be taken instead. However, it is noted that a photograph is a 2D imaging technology and our new technique and the NOISE technique are 3D imaging technology. This makes it possible to to generate different perspective views of the object under consideration. If the object is changed for one that has a large depth, it would be possible to create an

extended focused image in which all of the object is in focus [FGA+05, EHN08].

We have demonstrated a new technique for imaging through diffusers and biological tissue. The method uses a single shot in-line digital holography system to record the wavefield emanating from the front scattering layer. Digital algorithms enable us to numerically reconstruct the wavefield at the sub-tissue object depth. The method relies upon our ability to significantly reduce the speckle noise in the reconstructed image which is due to the diffusing nature of the tissue layers and the fact that we have to use coherent light. The speckle reduction algorithm is based on the mathematical properties of diffuse coherent imaging. We have noted the relationship of our method with the recently proposed NOISE [RA03] imaging technique and we offer an experimental comparison between the two methods. It is evident both from the qualitative and quantitative results presented here our new technique offers an improved performance. In fact the correlation values are approximately a factor of 10 times greater for our proposed technique than that of the NOISE technique. Further experimental and analytical work is planned to progress this research.

Chapter 13

Appendix E

An illustration of the discrete Fresnel filter is shown in Figure 13.1. The DH plane is filtered into non-overlapping $m \times m$ blocks. Each of these blocks is numerically propagated to the reconstruction plane where their intensities are stored. In order to ensure that each of the reconstructions is positioned correctly we modify the input linear shift variables to our numerical reconstruction algorithm. This is achieved by modifying the impulse response of the free space propagation [see Chap. 2.2.3] to

$$g_{\alpha,\beta}(x'-\xi, y'-\eta) = \frac{i}{\lambda}\frac{e^{ik}\sqrt{(x'-\alpha-\xi)^2+(y'-\beta-\eta)^2+d^2}}{\sqrt{(x'-\alpha-\xi)^2+(y'-\beta-\eta)^2+d^2}}, \tag{13.1}$$

where α denotes the shift in the x'-direction and β gives the shift in the y'-direction. By modifying the impulse response for each block we can shift the object field in such a way as to line up all of the reconstructions on top of each other [Kre05]. Of course each of the reconstructions give a different perspective of the object, but as the perspectives differences are small due to the size of the CCD used to capture the DHs, the resulting reconstructions when added together produce a single speckle reduced reconstruction. The addition of different perspectives to

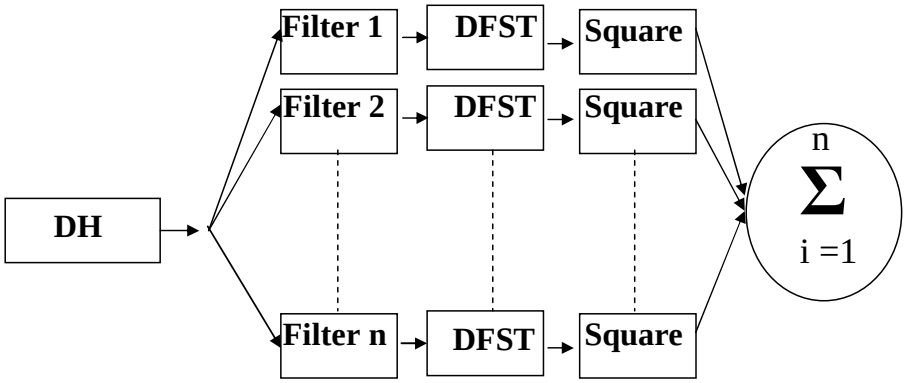

Figure 13.1: Setup for discrete Fresnel filter. DH, digital hologram; DFST, discrete Fresnel transform

reduce speckle was previously employed by Rosen and Abookasis [RA03] using an integral imaging system [RA03]. We reconstruct n blocks and the resulting n intensities are summed in order to reduce the speckle content.

Figure 13.2 shows the results of applying the discrete Fresnel filter to a DH reconstruction of a die object. The die reconstruction is corrupted by a fully developed speckle pattern and has a speckle index of approximately 1.0. It was captured using PSI [see Section 2.2.2.3] and a reconstruction from it is shown in Fig. 13.2(a). Figures. 13.2 (b) through (d) show the result of applying the discrete Fresnel filter with aperture sizes 1024×1024, 512×512 and 256×256 respectively. We have found that the speckle index reduces in approximately the same fashion as that of the DFF, when the same size apertures are used.

In Figure 13.3 we show the results of the discrete Fresnel filter against the DFF, mean and median filters, in terms of the edge preservation metric introduced in Section 3.3. We note that unlike the other techniques, the discrete Fresnel filter improves edges as its aperture size is increased and as speckle reduces. In terms of resolution the discrete Fresnel filter is superior to both the mean and median filters. It matches the DFF except when the largest aperture is used resulting in a horizontal and vertical resolution [see Section 4.3] of 0.7, whereas the DFF has

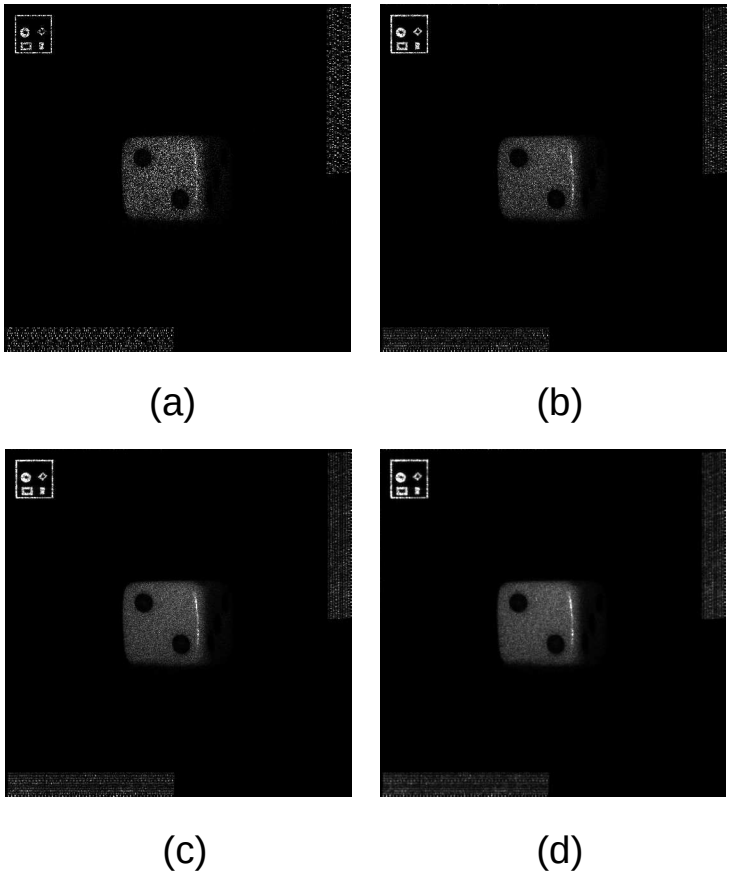

Figure 13.2: (a) Shows the original reconstruction of a die object, (b) shows the result of applying the discrete Fresnel filter technique to (a) with aperture 1024×1024, (c) shows the result of applying the discrete Fresnel filter technique to (a) with aperture 512×512, and (d) shows the result of applying the discrete Fresnel filter technique to (a) with aperture 256×256.

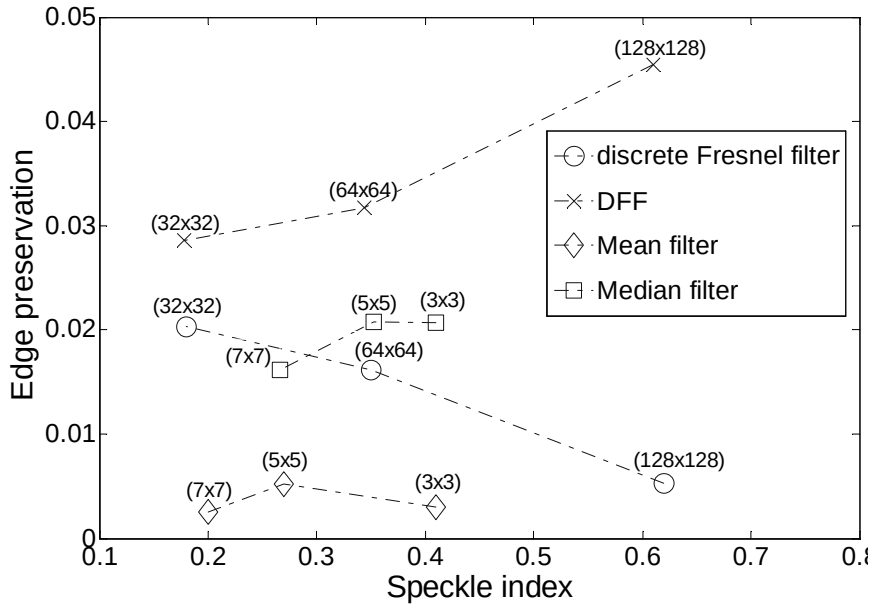

Figure 13.3: Graph showing the speckle index against edge preservation results of the discrete Fresnel filter technique (points are labeled with the size of the aperture width used) DFF technique (points are labeled with the size of the aperture width used), and the median and the mean filters (points are labeled with the neighborhood sizes used).

a better resolution of 0.8 in both directions.

Chapter 14

Appendix F

We present the results for the best performing mother wavelet from each of the following families; Haar, Db, Coif, bior, rbio. Results for the four thresholding schemes for both soft and hard thresholding are presented. The tests were carried out on a DH of a coin with added test pattern and resolution charts [see Chapter 4]. In all of the tables that follow, these abbreviations are used: α = speckle index, β = Edge preservation, hr = vertical resolution, vr = vertical resolution, and ω = overall metric.

Wavelet	**Detail level**	α	β^2	**hr, vr**	ω
Haar	1	0.52396	0.0065	0.6, 0.6	0.0019
DB2	1	0.56835	0.0044	0.6, 0.6	0.0011
Sym2	1	0.56835	0.0044	0.6, 0.6	0.0011
Coif1	1	0.57032	0.0044	0.6, 0.6	0.0011
Bior1.3	1	0.56746	0.0031	0.6, 0.6	0.0008
Rbio1.3	1	0.56713	0.0041	0.6, 0.6	0.0011
Haar	2	0.27707	0.0169	0.3, 0.3	0.0037
DB2	2	0.31369	0.0072	0.3, 0.3	0.0015
Sym2	2	0.31369	0.0072	0.3, 0.3	0.0015
Coif1	2	0.31483	0.0067	0.3, 0.3	0.0014
Bior1.3	2	0.31534	0.0051	0.3, 0.3	0.0010
Rbio1.3	2	0.31649	0.0075	0.3, 0.3	0.0015
Haar	3	0.15759	0.0764	0.2, 0.2	0.0129
DB2	3	0.18188	0.0211	0.2, 0.2	0.0035
Sym2	3	0.18188	0.0211	0.2, 0.2	0.0035
Coif1	3	0.18372	0.0204	0.2, 0.2	0.0033
Bior1.3	3	0.18292	0.0335	0.2, 0.2	0.0055
Rbio1.3	3	0.18305	0.0313	0.2, 0.2	0.0051
Haar	4	0.09608	0.1205	0.2, 0.2	0.0218
DB2	4	0.11006	0.0215	0.2, 0.2	0.0038
Sym2	4	0.11006	0.0215	0.2, 0.2	0.0038
Coif1	4	0.11014	0.0210	0.2, 0.2	0.0037
Bior1.3	4	0.10994	0.0536	0.2, 0.2	0.0095
Rbio1.3	4	0.10806	0.0405	0.2, 0.2	0.0072
Haar	5	0.07226	0.1432	0.2, 0.2	0.0266
DB2	5	0.07841	0.0226	0.2, 0.2	0.0042
Sym2	5	0.07841	0.0226	0.2, 0.2	0.0042
Coif1	5	0.07753	0.0221	0.2, 0.2	0.0041
Bior1.3	5	0.07741	0.0623	0.2, 0.2	0.0115
Rbio1.3	5	0.07851	0.0480	0.2, 0.2	0.0088

Table 14.1: Soft thresholding results for fixed form.

Wavelet	**Detail level**	α	β^2	**hr, vr**	ω
Haar	1	0.52381	0.0083	$0.7, 0.7$	0.0028
DB2	1	0.56835	0.0048	$0.6, 0.6$	0.0021
Sym2	1	0.56835	0.0048	$0.6, 0.6$	0.0021
Coif1	1	0.57036	0.0049	$0.6, 0.6$	0.0013
Bior1.3	1	0.56666	0.0044	$0.6, 0.6$	0.0012
Rbio3.1	1	0.6726	0.0066	$0.7, 0.7$	0.0015
Haar	2	0.33553	0.0545	$1, 1$	0.0362
DB2	2	0.36121	0.0219	$1, 1$	0.0140
Sym2	2	0.36121	0.0219	$1, 1$	0.0140
Coif1	2	0.36193	0.0194	$1, 1$	0.0124
Bior1.3	2	0.36328	0.0437	$1, 1$	0.0278
Rbio1.3	2	0.36682	0.0233	$1, 1$	0.0148
Haar	3	0.27277	0.0585	$1, 1$	0.0425
DB2	3	0.28489	0.0262	$1, 1$	0.0188
Sym2	3	0.28489	0.0262	$1, 1$	0.0188
Coif1	3	0.28415	0.0220	$1, 1$	0.0157
Bior1.3	3	0.28317	0.0474	$1, 1$	0.0340
Rbio1.3	3	0.29281	0.0278	$1, 1$	0.0197
Haar	4	0.24611	0.0614	$1, 1$	0.0463
DB2	4	0.25096	0.0284	$1, 1$	0.0213
Sym2	4	0.25096	0.0284	$1, 1$	0.0213
Coif1	4	0.25055	0.0241	$1, 1$	0.0180
Bior1.3	4	0.24767	0.0500	$1, 1$	0.0376
Rbio1.3	4	0.25958	0.0302	$1, 1$	0.0223
Haar	5	0.2374	0.0626	$1, 1$	0.0478
DB2	5	0.23953	0.0235	$1, 1$	0.0223
Sym2	5	0.23953	0.0235	$1, 1$	0.0223
Coif1	5	0.23878	0.0249	$1, 1$	0.0189
Bior1.3	5	0.23499	0.0513	$1, 1$	0.0393
Rbio1.3	5	0.24923	0.0313	$1, 1$	0.0235

Table 14.2: Soft thresholding results for balanced sparsity norm.

Wavelet	**Detail level**	α	β^2	**hr, vr**	ω
Haar	1	0.53973	0.0308	1, 1	0.0142
DB2	1	0.5801	0.0160	1, 1	0.0067
Sym2	1	0.5801	0.0160	1, 1	0.0067
Coif1	1	0.58133	0.0156	1, 1	0.0065
Bior1.3	1	0.57512	0.0256	1, 1	0.0109
Rbio1.3	1	0.58006	0.0172	1, 1	0.0072
Haar	2	0.43385	0.0461	1, 1	0.0261
DB2	2	0.45093	0.0244	1, 1	0.0134
Sym2	2	0.45093	0.0244	1, 1	0.0134
Coif1	2	0.45168	0.0232	1, 1	0.0127
Bior1.3	2	0.45578	0.0399	1, 1	0.0217
Rbio1.3	2	0.45816	0.0245	1, 1	0.0133
Haar	3	0.39592	0.0488	1, 1	0.0295
DB2	3	0.40382	0.0274	1, 1	0.0163
Sym2	3	0.40382	0.0274	1, 1	0.0163
Coif1	3	0.40338	0.0252	1, 1	0.0150
Bior1.3	3	0.40829	0.0422	1, 1	0.0249
Rbio1.3	3	0.41411	0.0278	1, 1	0.0163
Haar	4	0.37948	0.0509	1, 1	0.0316
DB2	4	0.38284	0.0291	1, 1	0.0180
Sym2	4	0.38284	0.0291	1, 1	0.0180
Coif1	4	0.38288	0.0270	1, 1	0.0166
Bior1.3	4	0.38782	0.0441	1, 1	0.0270
Rbio1.3	4	0.39415	0.0298	1, 1	0.0181
Haar	5	0.37373	0.0517	1, 1	0.0324
DB2	5	0.37549	0.0298	1, 1	0.0186
Sym2	5	0.37549	0.0298	1, 1	0.0186
Coif1	5	0.37533	0.0276	1, 1	0.0173
Bior1.3	5	0.38013	0.0449	1, 1	0.0278
Rbio1.3	5	0.38741	0.0307	1, 1	0.0188

Table 14.3: Soft thresholding results for square-root balanced sparsity norm.

Wavelet	**Detail level**	α	β^2	**hr, vr**	ω
Haar	1	0.52393	0.0067	0.6, 0.6	0.0019
DB2	1	0.56832	0.0044	0.6, 0.6	0.0011
Sym2	1	0.56832	0.0044	0.6, 0.6	0.0011
Coif5	1	0.63395	0.0019	0.5, 0.5	0.0003
Bior1.3	1	0.56728	0.0033	0.6, 0.6	0.0008
Rbio1.3	1	0.5671	0.0042	0.6, 0.6	0.0011
Haar	2	0.27714	0.0244	0.3, 0.3	0.0053
DB2	2	0.31377	0.0078	0.3, 0.3	0.0016
Sym2	2	0.31377	0.0078	0.3, 0.3	0.0016
Coif5	2	0.34791	0.0016	0.4, 0.4	0.0004
Bior1.3	2	0.31555	0.0099	0.3, 0.3	0.0020
Rbio1.3	2	0.31652	0.0088	0.3, 0.3	0.0018
Haar	3	0.1579	0.0839	0.3, 0.3	0.0212
DB2	3	0.18218	0.0219	0.3, 0.4	0.0063
Sym2	3	0.18218	0.0219	0.3, 0.4	0.0063
Coif5	3	0.205	0.0152	0.4, 0.4	0.0048
Bior1.3	3	0.18347	0.0413	0.3, 0.4	0.0118
Rbio1.3	3	0.18325	0.0349	0.3, 0.4	0.0100
Haar	4	0.09661	0.1021	0.3, 0.3	0.0277
DB2	4	0.11066	0.0251	0.4, 0.4	0.0089
Sym2	4	0.11066	0.0251	0.4, 0.4	0.0089
Coif5	4	0.11955	0.0193	0.4, 0.4	0.0068
Bior1.3	4	0.11068	0.0527	0.4, 0.4	0.0187
Rbio1.3	4	0.10846	0.0433	0.4, 0.4	0.0154
Haar	5	0.072612	0.1076	0.3, 0.3	0.0299
DB2	5	0.080343	0.0265	0.4, 0.4	0.0097
Sym2	5	0.080343	0.0265	0.4, 0.4	0.0097
Coif5	5	0.084633	0.0206	0.4, 0.4	0.0075
Bior1.3	5	0.07745	0.0562	0.4, 0.4	0.0207
Rbio1.3	5	0.079004	0.0469	0.4, 0.4	0.0173

Table 14.4: Soft thresholding results for sqtwolog.

Wavelet	**Detail level**	α	β^2	**hr, vr**	ω
Haar	1	0.52381	0.0075	0.6, 0.6	0.0021
DB2	1	0.56816	0.0045	0.6, 0.6	0.0012
Sym2	1	0.56816	0.0045	0.6, 0.6	0.0012
Coif1	1	0.57023	0.0045	0.6, 0.6	0.0012
Bior1.3	1	0.56672	0.0038	0.6, 0.6	0.0009
Rbio1.3	1	0.56696	0.0045	0.6, 0.6	0.0012
Haar	2	0.28047	0.0133	0.4, 0.4	0.0038
DB2	2	0.31445	0.0067	0.4, 0.4	0.0018
Sym2	2	0.31445	0.0067	0.4, 0.4	0.0018
Coif1	2	0.31499	0.0065	0.4, 0.4	0.0018
Bior1.3	2	0.31785	0.0073	0.4, 0.4	0.0021
Rbio1.3	2	0.31855	0.0071	0.4, 0.4	0.0019
Haar	3	0.16959	0.0181	0.5, 0.5	0.0075
DB2	3	0.18526	0.0072	0.4, 0.4	0.0024
Sym2	3	0.18526	0.0072	0.4, 0.4	0.0024
Coif1	3	0.18547	0.0050	0.4, 0.4	0.0016
Bior1.3	3	0.19218	0.0071	0.5, 0.5	0.0029
Rbio1.3	3	0.19043	0.0138	0.5, 0.5	0.0056
Haar	4	0.12178	0.0170	0.5, 0.5	0.0075
DB2	4	0.11961	0.0068	0.4, 0.4	0.0024
Sym2	4	0.11961	0.0068	0.4, 0.4	0.0024
Coif1	4	0.11486	0.0054	0.4, 0.4	0.0019
Bior1.3	4	0.13293	0.0067	0.5, 0.5	0.0029
Rbio1.3	4	0.12834	0.0126	0.5, 0.5	0.0055
Haar	5	0.10702	0.0170	0.5, 0.5	0.0076
DB2	5	0.09303	0.0069	0.4, 0.4	0.0025
Sym2	5	0.09303	0.0069	0.4, 0.4	0.0025
Coif1	5	0.08432	0.0053	0.4, 0.4	0.0020
Bior1.3	5	0.10939	0.0068	0.5, 0.5	0.0030
Rbio1.3	5	0.10629	0.0124	0.5, 0.5	0.0055

Table 14.5: Hard thresholding results for fixed form.

Wavelet	**Detail level**	α	β^2	**hr, vr**	ω
Haar	1	0.5388	0.0186	1, 1	0.0086
DB2	1	0.57689	0.0082	1, 1	0.0035
Sym2	1	0.57689	0.0082	1, 1	0.0035
Coif1	1	0.57558	0.0073	1, 1	0.0031
Bior1.3	1	0.59521	0.0146	1, 1	0.0059
Rbio1.3	1	0.58486	0.0094	1, 1	0.0039
Haar	2	0.72536	0.0328	1, 1	0.0090
DB2	2	0.74835	0.0203	1, 1	0.0051
Sym2	2	0.74835	0.0203	1, 1	0.0051
Coif1	2	0.75401	0.0202	1, 1	0.0050
Bior1.3	2	0.75276	0.0309	1, 1	0.0076
Rbio1.3	2	0.75848	0.0194	1, 1	0.0047
Haar	3	0.75152	0.0324	1, 1	0.0081
DB2	3	0.76089	0.0200	1, 1	0.0048
Sym2	3	0.76089	0.0200	1, 1	0.0048
Coif1	3	0.77297	0.0207	1, 1	0.0047
Bior1.3	3	0.7631	0.0286	1, 1	0.0068
Rbio1.3	3	0.78709	0.0200	1, 1	0.0043
Haar	4	0.7503	0.0324	1, 1	0.0081
DB2	4	0.76057	0.0201	1, 1	0.0048
Sym2	4	0.76057	0.0201	1, 1	0.0048
Coif1	4	0.76699	0.0208	1, 1	0.0048
Bior1.3	4	0.76292	0.0286	1, 1	0.0067
Rbio1.3	4	0.78506	0.0203	1, 1	0.0044
Haar	5	0.75016	0.0322	1, 1	0.0080
DB2	5	0.76116	0.0202	1, 1	0.0048
Sym2	5	0.76116	0.0202	1, 1	0.0048
Coif1	5	0.77263	0.0210	1, 1	0.0048
Bior1.3	5	0.75973	0.0287	1, 1	0.0069
Rbio1.3	5	0.78151	0.0203	1, 1	0.0044

Table 14.6: Hard thresholding results for balanced sparsity norm.

Wavelet	**Detail level**	α	β^2	**hr, vr**	ω
Haar	1	0.77794	0.0337	1, 1	0.0075
DB2	1	0.8104	0.0210	1, 1	0.0040
Sym2	1	0.8104	0.0210	1, 1	0.0040
Coif1	1	0.80655	0.0221	1, 1	0.0043
Bior1.3	1	0.80451	0.0311	1, 1	0.0061
Rbio1.3	1	0.81108	0.0215	1, 1	0.0041
Haar	2	0.89736	0.0283	1, 1	0.0029
DB2	2	0.90771	0.0226	1, 1	0.0021
Sym2	2	0.90771	0.0226	1, 1	0.0021
Coif1	2	0.90942	0.0225	1, 1	0.0020
Bior1.3	2	0.90788	0.0264	1, 1	0.0024
Rbio1.3	2	0.91211	0.0223	1, 1	0.0020
Haar	3	0.90021	0.0280	1, 1	0.0028
DB2	3	0.91212	0.0222	1, 1	0.0019
Sym2	3	0.91212	0.0222	1, 1	0.0019
Coif1	3	0.90998	0.0220	1, 1	0.0020
Bior1.3	3	0.90975	0.0261	1, 1	0.0024
Rbio1.3	3	0.91623	0.0222	1, 1	0.0019
Haar	4	0.89861	0.0279	1, 1	0.0028
DB2	4	0.90747	0.0221	1, 1	0.0020
Sym2	4	0.90747	0.0221	1, 1	0.0020
Coif1	4	0.90827	0.0221	1, 1	0.0020
Bior1.3	4	0.90992	0.0262	1, 1	0.0024
Rbio1.3	4	0.91587	0.0223	1, 1	0.0019
Haar	5	0.89717	0.0279	1, 1	0.0029
DB2	5	0.907	0.0222	1, 1	0.0021
Sym2	5	0.907	0.0222	1, 1	0.0021
Coif1	5	0.90735	0.0222	1, 1	0.0021
Bior1.3	5	0.9101	0.0262	1, 1	0.0024
Rbio1.3	5	0.91623	0.0223	1, 1	0.0019

Table 14.7: Hard thresholding results for square-root balanced sparsity norm.

Wavelet	**Detail level**	α	β^2	**hr, vr**	ω
Haar	1	0.52381	0.0085	0.8, 0.7	0.0030
DB2	1	0.5692	0.0049	0.6, 0.7	0.0014
Sym2	1	0.5692	0.0049	0.6, 0.7	0.0014
Coif1	1	0.57167	0.0050	0.6, 0.6	0.0013
Bior1.3	1	0.56672	0.0055	0.6, 0.6	0.0014
Rbio1.3	1	0.56692	0.0049	0.9, 0.7	0.0017
Haar	2	0.27942	0.0077	0.5, 0.5	0.0028
DB2	2	0.32231	0.0037	0.5, 0.5	0.0012
Sym2	2	0.32231	0.0037	0.5, 0.5	0.0012
Coif1	2	0.3236	0.0025	0.4, 0.5	0.0007
Bior1.3	2	0.31804	0.0178	0.5, 0.5	0.0061
Rbio1.3	2	0.31783	0.0028	0.5, 0.5	0.0009
Haar	3	0.16574	0.0059	0.6, 0.5	0.0032
DB2	3	0.20577	0.0032	0.5, 0.5	0.0013
Sym2	3	0.20577	0.0032	0.5, 0.5	0.0013
Coif1	3	0.20696	0.0013	0.5, 0.5	0.0005
Bior1.3	3	0.19406	0.0132	0.5, 0.5	0.0053
Rbio1.3	3	0.19074	0.0026	0.9, 0.8	0.0018
Haar	4	0.10681	0.0055	0.6, 0.5	0.0032
DB2	4	0.14508	0.0032	0.5, 0.5	0.0014
Sym2	4	0.14508	0.0032	0.5, 0.5	0.0014
Coif1	4	0.14529	0.0013	0.5, 0.5	0.0005
Bior1.3	4	0.12783	0.0125	0.5, 0.5	0.0055
Rbio1.3	4	0.12397	0.0022	0.9, 0.9	0.0018
Haar	5	0.08484	0.0056	0.6, 0.5	0.0034
DB2	5	0.12582	0.0032	0.5, 0.5	0.0014
Sym2	5	0.12582	0.0032	0.5, 0.5	0.0014
Coif1	5	0.1237	0.0014	0.5, 0.5	0.0006
Bior1.3	5	0.09844	0.0127	0.5, 0.5	0.0057
Rbio1.3	5	0.10003	0.0023	0.9, 0.9	0.0019

Table 14.8: Hard thresholding results for square-root balanced sparsity norm.

Cited References

[AA76] H. H. Arsenault and G. April. Properties of speckle integrated with a finite aperture and logarithmically transformed. *J. Opt. Soc. Am*, 66:1160, 1976.

[AATA85] H. Ambar, Y. Aoki, N. Takai, and T. Asakura. Mechanism of speckle reduction in laser-microscope images using a rotating optical fiber. *Applied Physics B*, 38(1):71–78, 1985.

[ABT01] A. Achim, A. Bezerianos, and P. Tsakalides. Novel bayesian multiscale method for speckle removal in medical ultrasound images. *IEEE transactions on medical imaging*, 20:772, 2001.

[AKF04] D. C. Adler, T. H. Ko, and J. G. Fujimoto. Speckle reduction in optical coherence tomography images by use of a spatially adaptive wavelet filter. *Optics Letters*, 29:2878, 2004.

[AKJ97] M. Adams, T. Kreis, and W. Jüptner. Particle size and position measurement with digital holography. *Proc. SPIE*, 3098:234–240, 1997.

[AL70] H. Arsenault and S. Lowenthal. Partial coherence in the image of an object illuminated with laser light through a moving diffuser. *Optics Communications*, 1(9):451–453, 1970.

[ATK+08] Y. Awatsuji, T. Tahara, A. Kaneko, T. Koyama, K. Nishio, S. Ura, T. Kubota, and O. Matoba. Parallel two-step phase-shifting digital holography. *Applied Optics*, 47(19):D183–D189, 2008.

[Bar91] J. J. Barton. Removing multiple scattering and twin images from holographic images. *Phys. Rev. Lett.*, 67(22):3106–3109, 1991.

[Bas97] M. J. Bastians. *Application of the Wigner distribution function in optics*. W. Mecklenbrauker, F. Hlawatsch, Eds., Elsevier Science, Amsterdam, 1997.

[BCL02] R. Binet, J. Colineau, and J.-C. Lehureau. Short-range synthetic aperture at 633 nm by digital holography. *Applied Optics*, 41:4775–4782, 2002.

[BFRJ04] N. Bertaux, Y. Frauel, P. Réfrégier, and B. Javidi. Speckle removal using a maximum-likelihood technique with isoline gray-level regularization. *Optics Society of America*, 21(12):2283–2291, December 2004.

[BHG+74] J. H. Bruning, D. R. Herriott, J. E. Gallagher, D. P. Rosenfeld, A. D. White, and D. J. Brangaccio. Digital wavefront measuring interferometer for testing optical surfaces and lenses. *Applied Optics*, 13:2693–2703, 1974.

[BHW65] R. E. Brooks, L. O. Heflinger, and R. F. Wuerker. Interferometry with a holograhically reconstructed comparison beam. *Appl. Phys. Lett.*, 7, 1965.

[Bim06] O. Bimber. Merging graphics and holograms. *Journal of Holography and Speckle*, 3:1–7, 2006.

[BKKJ06] T. Baumbach, E. Kolenović, V. Kebbel, and W. Jüptner. Improvement of accuracy in digital holography by use of multiple holograms. *Applied Optics*, 45(24):6077–6085, 2006.

[BL66] B. R. Brown and A. W. Lohmann. Complex spatial filtering with binary masks. *Applied Optics*, 5(6):967–969, 1966.

[BR51] W. L. Bragg and G. L. Roger. Elimination of the unwanted image in diffraction microscopy. *Nature*, 167:190–191, 1951.

[Bra78] R. N. Bracewell. *The Fourier transform and its applications*. 2nd ed, McGraw-Hill, New York, 1978.

[BRRO05] A. Bozkurt, A. Rosen, H. Rosen, and B. Onaral. A portable near infrared spectroscopy system for bedside monitoring of newborn brain. *BioMedical Engineering OnLine*, 4, 2005.

[BZG+05] O. Bimber, T. Zeidler, A. Grundhfer, G. Wetzstein, M. Mhring, S Kndel, and U. Hahne. Interacting with augmented holograms. *Proc. SPIE*, 5742:41–54, 2005.

[Cau79] H. J. Caulfield. *Handbook of Optical Holography*. Academic Press, New York, 1979.

[CGC01] F. Le Clerc, M. Gross, and L. Collot. Synthetic aperture experiment in the visible with on-axis digital heterodyne holography. *Optics Letters*, 26:1550–1552, 2001.

[CLY+07] G. L. Chen, C. Y. Lin, H. F. Yau, M. K. Kuo, and C. C. Chang. Wavefront reconstruction without twin-image blurring by two arbitrary step digital holograms. *Optics Express*, 15(18):11601–11607, 2007.

[CMD99] E. Cuche, P. Marquet, and C. Depeursinge. Simultaneous amplitude-contrast and quantitative phase-contrast microscopy by numerical reconstruction of fresnel off-axis holograms. *Applied Optics*, 38:6994–7001, 1999.

[CMD00] E. Cuche, P. Marquet, and C. Depeursinge. Spatial filtering for zero-order and twin-image elimination in digital off-axis holography. *Applied Optics*, 39(23):4070–4075, 2000.

[CPC+06] F. Charrière, N. Pavillon, T. Colomb, C. Depeursinge, T. J. Hegera, E. A. D. Mitchell, P. Marquet, and B. Rappaz. Living specimen tomography by digital holographic microscopy: morphometry of testate amoeba. *Optics Express*, 14:7005–7013, 2006.

[Cri85] T. J. Crimmins. Geometric filter for speckle reduction. *Applied Optics*, 24(10):1438–1443, 1985.

[CT65] J. W. Cooley and O. W. Tukey. An algorithm for the machine calculation of complex fourier series. *Mathamatics of Compututation*, 19:297–301, 1965.

[Dai70] J. C. Dainty. Some statistical properties of random speckle patterns in coherent and partially coherent illumination. *Optica Acta*, 17(10):761–772, 1970.

[Dai84] J. C. Dainty. *Laser Speckle and Related Phenomena*. Springer Verlag, Berlin, second edition, 1984.

[Den62] Y. N. Denisyuk. Photographic reconstruction of the optical properties of an object in its own scattered radiation field. *Dokl. Akad. Nauk SSSR*, 144:1275–1279, 1962.

[DF03] C. Dunsby and P. M. W. French. Techniques for depth-resolved imaging through turbid media including coherence-gated imaging. *J. Phys. D: Appl. Phys*, 36:R207–R227, 2003.

[DFFD05] L. Denis, C. Fournier, T. Fournel, and C. Ducottet. Twin image noise reduction by phase retrieval in in-line digital holography. *Proc. SPIE*, 5914:148–161, 2005.

[DJ07] C. M. Do and B. Javidi. Multifocus holographic 3-d image fusion using independent component analysis. *Journal of Display Technology*, 3(3):326–332, 2007.

[DJKP95] D. L. Donoho, I. M. Johnstone, G. Kerkyacharian, and D. Picard. Wavelet shrinkage: asymptopia? *Jour. Roy. Stat. Soc., series B*, 57:301, 1995.

[DJT66] J. B. DeVelis, G. B. Parrent Jr., and B. J. Thompson. Image reconstruction with fraunhofer holograms. *J. Opt. Soc. Am.*, 56(4):423, 1966.

[DK93] B. Dingel and S. Kawata. Speckle-free image in a laser-diode microscope by using the optical feedback effect. *Optics Letters*, 18(7):549–551, 1993.

[DM74] T. H. Demetrakopoulos and R. Mittra. Digital and optical reconstruction of images from suboptical diffraction patterns. *Applied Optics*, 13:665–670, 1974.

[DMS03] N. Demoli, J. Mestrovic, and I. Sovic. Subtraction digital holography. *Applied Optics*, 42:798–804, 2003.

[Don95] D. L. Donoho. De-noising by soft-thresholding. *IEEE Trans. Inform. Theory*, 41:613, 1995.

[DPI96] K. Doh, T.-C. Poon, and G. Indebetouw. Twin-image noise in optical scanning holography. *Optical Engineering*, 35:1550–1555, 1996.

[DPW+96] K. Doh, T. C. Poon, M. H. Wu, K. Shinoda, and Y. Suzuki. Twin-image elimination in optical scanning holography. *Optics & Laser Technology*, 28(23):135–141, 1996.

[DR58] W. B. Davenport and W. L. Root. *An Introduction to the Theory of Random Signals and Noise*. New York: McGraw-Hill, 1958.

[DRM+04] F. Dubois, M.-L. N. Requena, C. Minetti, O. Monnom, and E. Istasse. Partial spatial coherence effects in digital holographic microscopy with a laser source. *Applied Optics*, 43(5):1131–1139, 2004.

[DS06a] E. Darakis and J. J. Soraghan. Compression of interference patterns with application to phase-shifting digital holography. *Applied Optics*, 45(11):2437–2443, 2006.

[DS06b] E. Darakis and J. J. Soraghan. Use of fresnelets for phase-shifting digital hologram compression. *IEEE transactions on Image Processing*, 15(12):3804–3811, 2006.

[DVG06] S. Demos, A. J. Vogel, and A. H. Gandjbakhche. Advances in optical spectroscopy and imaging of breast lesions. *J Mammary Gland Biol Neoplasia*, 11:165–181, 2006.

[DW71] J. C. Dainty and W. T. Welford. Reduction of speckle in image plane hologram reconstruction by use of a moving pupil. *Optics Communications*, 3(5):289–294, 1971.

[EHN08] C.P. Mc Elhinney, B. M. Hennelly, and T. J. Naughton. Extended focused imaging for digital holograms of macroscopic three-dimensional objects. *Applied Optics*, 47(19):D71–D79, 2008.

[EMF+07] C.P. Mc Elhinney, J. B. McDonald, Y. Frauel, A. Castro, B. Javidi, and T. J. Naughton. Depth-independent segmentation of macroscopic three-dimensional objects encoded in single perspectives of digital hologram. *Optics Letters*, 32:1229–1231, 2007.

[EMH+06a] C. P. Mc Elhinney, J. Maycock, B. M. Hennelly, T.J. Naughton, J.B. McDonald, and B. Javidi. Extraction of shape information from three-dimensional objects encoded in a digital hologram. *Proc. ICO Topical Meeting on Optoinformatics/Information Photonoics, St. Petersburg*, pages 42–44, 2006.

[EMH+06b] C. P. Mc Elhinney, J. Maycock, B.M. Hennelly, T.J. Naughton, J.B. McDonald, and B. Javidi. Extraction and reconstruction of shape information from a digital hologram of three-dimensional objects. *Proc. of Irish Machine Vision and Image Processing Conference, Dublin*, pages 76–83, 2006.

[EMM+05] C.P. Mc Elhinney, J. Maycock, J. B. McDonald, T. J. Naughton, and B. Javidi. Three-dimensional scene reconstruction using digital holography. *Opto Ireland Conf. Proceedings*, 5823:48–57, June 2005.

[EMN+05] C.P. Mc Elhinney, J. Maycock, T. J. Naughton, J. B. McDonald, and B. Javidi. Extraction of three-dimensional shape information from a digital hologram. *Proc. SPIE Optics and Photonics, San Diego*, 5908(590805), 2005.

[Exn77] K. Exner. *Sitzungsber, Kaiserl, Akad, Wiss. (Wein)*, 76:522, 1877.

[EZ96] J. H. Elder and S. W. Zucker. Computing contour closure. *Proceedings of the 4th European Conference on Computer Vision*, 1:399–412, 1996.

[FGA+05] P. Ferraro, S. Grilli, D. Alfieri, S. De Nicola, A. Finizio, G. Pierattini, B. Javidi, G. Coppol, and V. Striano. Extended focused image in microscopy by digital holography. *Optics Express*, 13:6738–6749, 2005.

[FH98] S. Fukuda and H. Hirosawa. Suppression of speckle in synthetic aperture radar images using wavelet. *Int. Jou. of Rem. Sen.*, 19:507, 1998.

[Fra79] M. Françon. *Laser Speckle and Application in Optics*. Acedemic, New York, 1979.

[FTCJ01] Y. Frauel, E. Tajahuerce, M. A. Castro, and B. Javidi. Distortion-tolerant three-dimensional object recognition with digital holography. *Applied Optics*, 40:3887–3893, August 2001.

[Gab48] D. Gabor. A new microscope principle. *Nature*, 161(2):77–79, 1948.

[Gab70] D. Gabor. Laser speckle and its elimination. *IBM J. Res. Develop.*, pages 509–514, 1970.

[Gam75] M. A. M. Gama. Speckle reduction by unidirectional averaging. *Optica Acta*, 22:725–730, 1975.

[GCS05] S. Gupta, R. C. Chauhan, and S. C. Saxena. Locally adaptive wavelet domain bayesian processor for denoising medical ultrasound images using speckle modelling based on rayleigh distribution. *IEE Proc.-Vis. Image Signal Process.*, 152(1):129–135, 2005.

[Ger72] R. W. Gerchberg. Holography without fringes in the electron microscope. *Nature*, 240:404–406, 1972.

[GG66] D. Gabor and W. P. Goss. Interference microscope with total wavefront reconstruction. *J. Opt. Soc. Am.*, 56(7):849, 1966.

[GHA05] A. P. Gibons, J. C. Hebden, and S. R. Adridge. Recent advances in diffuse optical imaging. *Phys. Med. Biol.*, 50, 2005.

[GJ73] N. George and A. Jain. Speckle reduction using multiple tones of illumination. *Applied Optics*, 12(6):1202–1212, 1973.

[GK89] J. Gillespie and R. A. King. The use of self-entropy as a focus measure in digital holography. *Pattern Recognition Letters*, 9(1):19–25, 1989.

[GL67] J. W. Goodman and R. W. Lawerence. Digital image formation from electronically detected holograms. *Applied Physics Letters*, 11:777–778, December 1967.

[GLCC07] M. K. Kuo G. L. Chen, C. Y. Lin and C. C. Chang. Numerical suppression of zero-order image in digital holography. *Optics Express*, 15(14), 2007.

[Goo63] J. W. Goodman. Some effects of target-induced scintillation on optical radar performance. *Stanford Electronics Lab. Tech. Rep.*, (2303), 1963.

[Goo65] J. W. Goodman. Some effects of target-induced scintillation on optical radar performance. *Proc. IEEE*, 53:1688–1700, 1965.

[Goo76] J. W. Goodman. Some fundamental properties of speckle*. *J. Opt. Soc. Am.*, 66(11):1145–1150, 1976.

[Goo00] J. W. Goodman. *Statistical Optics*. New York: Wiley, Wiley Classics Library Edition, 2000.

[Goo05] J. W. Goodman. *Introduction to Fourier Optics*. Roberts and Company, Englewood, Colorado, third edition, 2005.

[Goo06] J. W. Goodman. *Speckle Phenomena: Theory and Applications*. Roberts & Company, Englewood, Colorado, 2006.

[GSRC06] J. Garcia-Sucerquia, J. H. Ramírez, and R. Castaneda. Incoherent recovering of the spatial resolution in digital holography. *Optics Communications*, 260:62–67, 2006.

[GSRP05] J. Garcia-Sucerquia, J. H. Ramírez, and D. V. Prieto. Reduction of speckle noise in digital holography by using digital image processing. *Optik*, 116:44–48, 2005.

[GW02] R. C. Gonzalez and R. E. Woods. *Digital Image Processing*. Prentice-Hall, Englewood Cliffs, NJ, 2002.

[HH66] B. P. Hildebrand and K. A. Haines. The generation of three-dimensional contour maps by wavefront reconstruction. *Physics Letters*, 21:422–423, 1966.

[HH74] P. Hariharan and Z. S. Hegedus. Reduction of speckle in coherent imaging by statial frequency sampling. *Optica Acta*, 21(5):345–356, 1974.

[HHJ07] Y. S. Hwang, S.-H. Hong, and B. Javidi. Free view 3-d visualization of occluded objects by using computational synthetic aperture integral imaging. *IEEE journal of display technology*, 3(1):64–70, 2007.

[HJ05] S. H. Hong and B. Javidi. Three-dimensional visualization of partially occluded objects using integral imaging. *IEEE journal of display technology*, 1:354–359, 2005.

[HKMP10] B. M. Hennelly, Damien P. Kelly, D. S. Monaghan, and N. Pandey. Zoom algorithms for digital holography. In T. Fournel and B. Javidi, editors, *Information Optics and photonics: Algorithms, Systems, amd Applications*, pages 187–204. Springer, 2010.

[HME+06] B. M. Hennelly, J. Maycock, C.P. Mc Elhinney, T. J. Naughton, J. B. McDonald, and B. Javidi. Analysis of partially occluded objects encoded in digital holograms using the wigner distribution function. *Proc. SPIE*, 6311:63110M, 2006.

[HNM07] B. M. Hennelly, T. J. Naughton, and John McDonald. Digital holographic superresolution by rotating the object wavefield. *Digital Holography and Three-Dimensional Imaging*, 2007.

[HS05a] B. M. Hennelly and J. T. Sheridan. Generalizing, optimizing, and inventing numerical algorithms for the fractional Fourier, Fresnel, and linear canonical transforms. *J. Opt. Soc. Am. A*, 22(5):917–927, 2005.

[HS05b] B. M. Hennelly and J. T. Sheridan. Tracking the space bandwidth product in optical systems. *Photon Management Research in Ireland Conf. Proc.*, 5827, 2005.

[HSL+91] D. Haung, E. A. Swanson, C. P. Lin, J. S. Schuman, W. G. Stinson, W. Chang, M. R. Hee, T. Flotte, K. Gregory, C. A. Puliafito, and J. G. Fujimoto. Optical coherence tomography. *Science*, 254:1178–1181, 1991.

[Hua71] T. S. Huang. Digital holography. *Proc. IEEE*, 59(9):1335–1346, 1971.

[HV93] C. Herley and M. Vetterli. Wavelets and recursive filter banks. *IEEE Transactions on Signal Processing*, 41(8):2536–2556, 1993.

[IA96] T. Iwai and T. Asakura. Speckle reduction in coherent information processing. *Proceedings of the IEEE*, 84(5):765–781, 1996.

[IB75] C. S. Ih and L. A. Baxter. Improved random spatial phase modulation for speckle elimination. *Applied Optics*, 17(9):1447–1454, 1975.

[Inc06] Mathworks Inc. Wavelet toolbox. *http://www.mathworks.com/products/wavelet/*, 2006.

[Jan01] M. Jansen. *Noise Reduction by Wavelet Thresholding*. Springer Verlag New York Inc., 2001.

[JFH+05] B. Javidi, P. Ferraro, S. H. Hong, S. De Nicola, A. Finizio, D. Alfieri, and G. Pierattini. Three-dimensional image fusion by use of multiwavelength digital holography. *Optics Letters*, 30:144–146, 2005.

[JGSJK+06] W. Xu J. Garcia-Sucerquia, S. K. Jericho, P. Klages, M. H. Jericho, and H. J. Kreuzer. Digital in-line holographic microscopy. *Applied Optics*, 45(5):836–850, 2006.

[JK05] B. Javidi and D. Kim. Three-dimensional-object recognition by use of single-exposure on-axis digital holography. *Optics Letters*, 30:236–238, 2005.

[JPDH06] B. Javidi, R. Ponce-Daz, and S. H. Hong. Three-dimensional recognition of occluded objects by using computational integral imaging. *Optics Letters*, 31(8):1106–1108, 2006.

[JT00] B. Javidi and E. Tajahuerce. Three-dimensional object recognition by use of digital holography. *Optics Letters*, 25(9):610–612, 2000.

[KAJ02] T. Kreis, M. Adams, and W. Jüptner. Aperture synthesis in digital holography. *Proc. SPIE*, 4777:69–76, 2002.

[KES56] P. Kirkpatrick and H. M. A. El-Sum. Image formation by reconstructed wave fronts. i. physical principles and methods of refinement. *J. Opt. Soc. Am.*, 46(10):825, 1956.

[KG96] G. H. Kaufman and G. E. Galizzi. Speckle noise reduction in television holography fringes using wavelet thresholding. *Optical Engineering*, 35:9, 1996.

[KHP+09] D. P. Kelly, B. M. Hennelly, N. Pandey, T. J. Naughton, and W. T. Rhodes. Resolution limits in practical digital holographic systems. *Opt. Eng.*, 48, 2009.

[Kim04] D. Kim. Reduction of coherent artifacts in dynamic holographic three-dimensional displays by diffraction-specific pseudorandom diffusion. *Optics Letters*, 29(6):611–613, 2004.

[KJ97] T. Kreis and W. Jüptner. Suppression of the dc term in digital holography. *Optical Engineering*, 36:2357–2360, 1997.

[KJ03] S. Kishk and B. Javidi. 3d object watermarking by a 3d hidden object. *Optics Express*, 11(8):874–888, 2003.

[KJ04] D. Kim and B. Javidi. Distortion-tolerant 3-d object recognition by using single exposure on-axis digital holography. *Optics Express*, 12(22):5539–5548, 2004.

[KJP91] G. Koren, D. Joyeux, and F. Polack. Twin-image elimination in in-line holography of finite-support complex objects. *Optics Letters*, 16(24):1979–1981, 1991.

[KL05] H. Kim and Y. H. Lee. Optimal watermarking of digital hologram of 3-d object. *Optics Express*, 13(8):2881–2886, 2005.

[KLT+04] Y. L. Kim, Y. Liu, V. M. Turzhitsky, H. K. Roy, R. K. Wali, and V. Backma. Coherent backscattering spectroscopy. *Optics Letters*, 29(16):1906–1908, 2004.

[KMP+10] D. P. Kelly, D. S. Monaghan, N. Pandey, T. Kozacki, A. Michalkiewicz, G. Finke, B. M. Hennelly, and M. Kujawinska. Digital holographic capture and optoelectronic reconstruction for 3d displays. *Int. Jour. of Digital Multimedia Broadcasting*, 2010:1–14, 2010.

[KMY72] M. A. Kronrod, N. S. Merzlyakov, and L. P. Yaroslavskii. Reconstruction of holograms with a computer. *Soviet Physics Technical Physics*, 17:333–334, 1972.

[KPJ93] G. Koren, F. Polack, and D. Joyeux. Iterative algorithms for twin-image elimination in in-line holography using finite-support constraints. *J. Opt. Soc. Am. A*, 10(3):423, 1993.

[Kre05] T. Kreis. *Handbook of Holographic interferometry, Optical and Digital Methods*. Wiley-VCH GmbH & Co. KGaA, Weinheim, 2005.

[KSO06] C. Kohler, X. Schwab, and W. Osten. Optimally tuned spatial light modulators for digital holography. *Applied Optics*, 45(5):960–967, 2006.

[KSSC85] D. T. Kuan, A. A. Sawchuk, T. C. Strand, and P. Chavel. Adaptive noise smoothing filter for images with signal-dependant noise. *IEEE Trans. Pattern Anal. Machine Intell.*, 7, March 1985.

[KSSC87] D. T. Kuan, A. A. Sawchuk, T. C. Strand, and P. Chavel. Adaptive restoration of images with speckle. *IEEE Trans. Acoust., Speech, Signal Process*, 35:373–383, March 1987.

[KYO+96] I. Kodama, M. Yamaguchi, N. Ohyama, T. Honda, K. Shinohara, A. Ito, T. Matsumura, K. Kinoshita, and K. Yada. Image reconstruction from an in-line x-ray hologram with intensity distribution constraint. *Optics Communications*, 125(1), 1996.

[LA70] S. Lowenthal and H. Arsenault. Image formation for coherent diffuse objects: Statistical properties. *J. Opt. Soc. Am.*, 60:1478–1483, 1970.

[Lau14] M. Von Laue. *Sitzungs, Akad. Wiss. (Berlin)*, 44:1144, 1914.

[Lau16] M. Von Laue. *Mitt. Physik. Ges.*, 18:90, 1916.

[LBU03] M. Liebling, T. Blu, and M. Unser. Fresnelets: new multiresolution wavelet bases for digital holography. *IEEE Transactions on Image Processing*, 12(1):29–43, 2003.

[LC86] J. A. Lin and J. M. Cowley. Reconstruction from in-line electron holograms by digital processing. *Optical Engineering*, 19:179–189, 1986.

[LDM+96] A. W. Lohmann, R. G. Dorsch, D. Mendolovic, Z. Zalevsky, and C. Ferreira. Space-bandwidth product of optical signals and systems. *J. Opt. Soc. Am. A*, 13:470–473, 1996.

[Lee81] J. S. Lee. Speckle analysis and smoothing of synthetic aperture radar images. *Comput. Graph. Image Process*, 17:24–32, 1981.

[Lee83] J. S. Lee. Digital image smoothing and the sigma filter. *Comput. Graph. Image Process*, 17:255–269, 1983.

[Lee86] J. S. Lee. Speckle suppression and analysis for synthetic aperture radar images. *Optical Engineering*, 20:636–643, May 1986.

[LF07] T. Latychevskaia and H.-W. Fink. Solution to the twin image problem in holography. *Physics Review Letters*, 98:233901, 2007.

[LGO+96] M. Lang, H. Guo, J. E. Odegard, C. S. Burrus, and R. O. Wells. Noise reduction using an undecimated discrete wavelet transform. *Lecture Notes in Statistics: Wavelets and Statistics*, 3(1):10–12, 1996.

[LHJK93] S. Lindaas, M. Howells, C. Jacobsen, and A. Kalinovsky. X-ray holographic microscopy by means of photoresist recording and atomic-force microscope readout. *J. Opt. Soc. Am. A*, 13(9):1788–1800, 1993.

[Lim81] L. S. Lim. Techniques for speckle noise removal. *Optical Engineering*, 20(5):670–678, 1981.

[Liu90] G. Liu. Object reconstruction from noisy holograms. *Optical Engineering*, 29(1):19–24, 1990.

[LJYY07] Z. Li, S. Jin, W. Yanping, and Y. Yan. The use of discrete wavelets for signal denoising in microchip capillary electrophoresis. *Electronic Measurement and Instruments, 2007. ICEMI 2007*, 3:203–206, 2007.

[LK90] L. Leushacke and M. Kirchner. Three-dimensional correlation coefficient of speckle intensity for rectangular and circular apertures. *J. Opt. Soc. Am. A*, 7(5):827–832, 1990.

[LMP75] D. Leger, E. Mathieu, and J. C. Perrin. Optical surface roughness determination using speckle correlation technique. *Applied Optics*, 14(4):872–877, 1975.

[Loh93] A. W. Lohmann. Image rotation, Wigner rotation and the fractional Fourier transform. *J. Opt. Soc. Am. A*, 10:2181–2186, 1993.

[Løk84] 0. J. Løkberg. Espi-the ultimate holographic tool for vibration analysis? *J. Acoust. Soc. Am.*, 75:1783–1791, 1984.

[LS85] G. Liu and P. D. Scott. Phase retrieval for in line holograms. *Proceedings of the Nineteenth Annual Conference on Information Sciences and Systems (Johns Hopkins U. Press, Baltimore, Md., 1985)*, pages 237–241, 1985.

[LS87] G. Liu and P. D. Scott. Phase retrieval and twin-image elimination for in-line fresnel holograms. *J. Opt. Soc. Am. A*, 4(1):159–165, 1987.

[LU62] E. N. Leith and J. Upatnieks. New techniques in wavefront reconstruction. *J. Opt. Soc. Am. A*, 51:1469–1473, 1962.

[LU63] E. N. Leith and J. Upatnieks. Wavefront reconstruction with continuous-tone objects. *J. Opt. Soc. Amer*, 53:1377, 1963.

[LU64] E. N. Leith and J. Upatnieks. Wavefront reconstruction with diffused illumination and three-dimensional objects. *J. Opt. Soc. Amer.*, 54:1295, 1964.

[LU04] M. Liebling and M. Unser. Autofocus for digital Fresnel holograms by use of a fresnelet-sparsity criterion. *J. Opt. Soc. Am. A*, 21(12):2424–2430, 2004.

[LWP98] Thorsteinn Halldórsson Lingli Wang, Theo Tschudi and Pálmi R. Pétursson. Speckle reduction in laser projection systems by diffractive optical elements. *Applied Optics*, 37(10):1770–1775, 1998.

[Mas02] J. H. Massig. Digital off-axis holography with a synthetic aperture. *Optics Letters*, 27:2179–2181, 2002.

[MAT04] MATLAB version 7.0, The MathWorks Inc., 2004.

[MBA79] K. H. S. Marie, J. C. Bennett, and A. P. Anderson. Digital processing technique for suppressing the interfering outputs in the image from an inline hologram. *Electron Letters*, 15:241–243, 1979.

[McK74a] T. S. McKechnie. Reduction of speckle by a moving aperture: Theory and measurement. *Optik*, 41(1):34–44, 1974.

[McK74b] T. S. McKechnie. Reduction of speckle in an image by a moving aperture-first order statistics. *Optics Communications*, 13(1):35–39, 1974.

[McK74c] T. S. McKechnie. Reduction of speckle in an image by a moving aperture-second order statistics. *Optics Communications*, 13(1):29–34, 1974.

[MEH+06a] J. Maycock, C. P. Mc Elhinney, B. M. Hennelly, T. J. Naughton, J. B. McDonald, and B. Javidi. Reconstruction of partially occluded objects using digital holograms. *Proc. SPIE Photonics Europe, Strasbourg*, 6187(61870V), 2006.

[MEH+06b] J. Maycock, C.P. Mc Elhinney, B. M. Hennelly, T. J. Naughton, J. B. McDonald, and B. Javidi. Three-dimensional scene reconstruction of

partially occluded objects using digital holograms. *Applied Optics*, 45(13):2975–2985, 2006.

[MGF+99] D. Mas, J. Garcia, C. Ferreira, L. M. Bernardo, and F. Marinho. Fast algorithms for free-space diffraction patterns calculation. *Optics Communications*, 164:233–245, 1999.

[MHM+07] J. Maycock, B. M. Hennelly, J. B. McDonald, Y. Frauel, A. Castro, B. Javidi, and T. J. Naughton. Reduction of speckle in digital holography by discrete Fourier filtering. *J. Opt. Soc. Am. A*, 24(6):1617–1622, 2007.

[MHM13] J. Maycock, B. M. Hennelly, and J. B. McDonald. Speckle reduction of reconstructions of digital holograms using three dimensional filtering. *accepted for publication in Optics Communications*, 2013.

[Mid58] D. Middleton. *Introduction to Statistical Communications Theory.* New York: McGraw-Hill, 1958.

[MLJ04] L. Ma, H. Wang Y. Li, and H. Jin. Numerical reconstruction of digital holograms for three-dimensional shape measurement. *Journal of optics A: Pure and applied optics*, 6:396–400, 2004.

[MLJ08] L. Martínez-León and B. Javidi. Synthetic aperture single-exposure on-axis digital holography. *Optics Express*, 16(1):161–169, 2008.

[MMM+08] K. M. Molony, J. Maycock, J. B. McDonald, B. M. Hennelly, and T. J. Naughton. A comparison of wavelet analysis techniques in digital holograms. *Proc. SPIE*, 6994:699412, 2008.

[MNF+02] O. Matoba, T. J. Naughton, Y. Frauel, N. Bertaux, and B. Javidi. Real-time three-dimensional object reconstruction by use of a phase-encoded digital hologram. *Applied Optics*, 41(29):6187–6192, 2002.

[MOL01] R. Mukundan, S. H. Ong, and P. A. Lee. Image analysis by tchebichef moments. *IEEE Transactions on Image Processing*, 10(9):1357–1364, 2001.

[MRM+05] P. Marquet, B. Rappaz, P. J. Magistretti, E. Cuche, Y. Emery, T. Colomb, and C. Depeursinge. Digital holographic microscopy: a noninvasive contrast imaging technique allowing quantitative visualization of living cells with subwavelength axial accuracy. *Optics Letters*, 30(5):468–470, 2005.

[MS67] W. Martienssen and S . Spiller. Holographic reconstruction without granulation. *Physics Letters*, 24A(2):126–128, 1967.

[MY00] S. Murata and S. N. Yasuda. Potential of digital holography in particle measurement. *Optical laser technology*, 32:567–574, 2000.

[MZK97] David Mendlovic, Z. Zalevsky, and N. Konforti. Computation considerations and fast algorithms for calculating the diffraction integral. *Journal of Modern Optics*, 44(2):407–414, 1997.

[MZK01] X. Ma, C. Zhou, and I. J. Kemp. Wavelets for the analysis and compression of partial discharge data. *Conference on Electrical Insulation and Dielectric Phenomena*, pages 329–334, 2001.

[NFJT02] T. J. Naughton, Y. Frauel, B. Javidi, and E. Tajahuerce. Compression of digital holograms for three-dimensional object reconstruction and recognition. *Applied Optics*, 41(20):4124–4132, 2002.

[NJ04] T. J. Naughton and B. Javidi. Compression of encrypted three-dimensional objects using digital holography. *Optical Engineering*, 43(10):2233–2238, 2004.

[NM08] T. Nakatsuji and K. Matsushima. Free-viewpoint images captured using phase-shifting synthetic aperture digital holography. *Applied Optics*, 47(19):D136–D143, 2008.

[NMJ03] T. J. Naughton, J. B. McDonald, and B. Javidi. Efficient compression of Fresnel fields for Internet transmission of three-dimensional images. *Applied Optics*, 42(23):4758–4764, 2003.

[NOK+05] T. Nomura, A. Okazaki, M. Kameda, Y. Morimoto, and B. Javidi. Image reconstruction from compressed encrypted digital hologram. *Optical Engineering*, 44:075801, 2005.

[NONN08] T. Nomura, M. Okamura, E. Nitanai, and T. Numata. Image quality improvement of digital holography by superposition of reconstructed images obtained by multiple wavelengths. *Applied Optics*, 47(19):D38–D43, 2008.

[NS95] G. P. Nason and B. W. Silverman. The stationary wavelet transform and some statistical applications. *Lecture Notes in Statistics: Wavelets and Statistics*, pages 281–299, 1995.

[Nug90] K. A. Nugent. Twin-image elimination in Gabor holography. *Optics Communications*, 78:293–299, 1990.

[OA07] O. E. Okman and G. B. Akar. Quantization index modulation-based image watermarking using digital holography. *J. Opt. Soc. Am. A*, 24(1):354–359, 2007.

[ÖB77] L. A. Östlund and K. Biedermann. Laser speckle reduction: equivalence of the moving aperture method and incoherent spatial filtering. *Applied Optics*, 16(3):685–690, 1977.

[Onu85] L. Onural. Digital decoding of in-line holograms. *Ph.D. dissertation (State University of New York at Buffalo, Amherst, New York, 1985)*, 1985.

[OS85] L. Onural and P. D. Scott. A digital filtering system for decoding in-line holograms. *Proceedings of the IEEE Conference on Acoustics, Speech, and Signal Processing (Institute of Electrical and Electronics Engineers, New York, 1985)*, pages 708–711, 1985.

[OS87] L. Onural and P. D. Scott. Digital decoding of in-line holograms. *Optical Engineering*, 26(11):1124–1132, 1987.

[OZ00] R. B. Owen and A. A. Zozulya. In-line digital holographic sensor for monitoring and characterizing marine particulates. *Optical Engineering*, 39:2187–2197, 2000.

[OZK01] H. M Ozaktas, Z. Zalevsky, and M. A. Kutay. *The Fractional Fourier Transform with Applications in Optics and Signal Processing.* John Wiley & Sons, New York, 2001.

[Pap65] A. Papoulis. *Probability, random variables and stochastic processes.* Mc Graw Hill, 1965.

[PFFT98] G. Pedrini, P. Fröning, H. Fessler, and H. J. Tiziani. In-line digital holographic interferometry. *Applied Optics*, 37:6562–6269, 1998.

[PH11] N. Pandey and B. Hennelly. Quantization noise and its reduction in lensless fourier digital holography. *Appl. Opt.*, 50(7):58–70, 2011.

[PKI+00] T. C. Poon, T. Kim, G. Indebetouw, B. W. Schilling, M. H. Wu, K. Shinoda, and Y. Suzuki. Twin-image elimination experiments for three-dimensional images in optical scanning holography. *Optics Letters*, 25:215–217, 2000.

[PM03] G. Pan and H. Meng. Digital holography of particle fields: reconstruction by use of complex amplitude. *Applied Optics*, 42(5):827–833, 2003.

[PMC+04] Y. Piederriere, J. Le Meur, J. Cariou, J. F. Abgrall, and M. T. Blouch. Particle aggregation monitoring by speckle size measurement; application to blood platelets aggregation. *Optics Express*, 12(19):4596–4601, 2004.

[PPT93] G. Pedrini, B. Pfister, and H. J. Tiziani. Double pulse-electronic speckle interferometry. *Journal of Modern Optics*, 40(34):89–96, 1993.

[PS65] R. L. Powell and K. A. Stetson. Interferometric vibration analysis by wavefront reconstruction. *J. Opt. Soc. Amer.*, 55:1593–1598, 1965.

[PT94] G. Pedrini and H. J. Tiziani. Double-pulse electronic speckle interferometry for vibration analysis. *Applied Optics*, 33(34):7857–7863, 1994.

[PT02] G. Pedrini and H. J. Tiziani. Short-coherence digital microscopy by the use of a lensless holographic imaging system. *Applied Optics*, 41:4489–4496, 2002.

[PTZ96] G. Pedrini, H. J. Tiziani, and Y. Zou. Speckle size of digitally reconstructed wavefronts of diffusely scattering objects. *Jornal of Modern Optics*, 43:395–407, 1996.

[PWV+06] A. Pizurica, A. M. Wink, E. Vansteenkiste, W. Philips, and J. B. Roerdink. A review of wavelet denoising in mri and ultrasound brain imaging. *Current Medical Imaging Reviews*, 2(2):247–260, 2006.

[PXL+11] F. Pan, W. Xiao, S. Liu, F. Wang, L. Rong, and R. Li. Coherent noise reduction in digital holographic phase contrast microscopy by slightly shifting object. *Optics Express*, 19(5):3862–3869, 2011.

[PZT95a] G. Pedrini, Y. Zou, and H. J. Tiziani. Comparision of two reflecting surfaces by using digital holographic interferometry. *Optics Communications*, 118:186–192, 1995.

[PZT95b] G. Pedrini, Y. Zou, and H. J. Tiziani. Digital double-pulsed holographic interferometry for vibration analysis. *Journal of Modern Optics*, 42:367–374, 1995.

[RA03] J. Rosen and D. Abookasis. Seeing through biological tissues using the fly eye principle. *Optics Express*, 11(26):3605–3611, 2003.

[Ram88] V. S. Ramachandran. Perceiving shape from shading. *Scientific American*, 259:76–83, 1988.

[Ras01] P. K. Rastogi. *Digital Speckle Pattern Interferometry and Related Techniques*. John Wiley & Sons, New York, 2001.

[Ray89] L. Rayleigh. On the character of the complete radiation at a given temperature. *Phil. Mag.*, 27(5):460–469, 1889.

[RE98] R. A. Rensink and J. T. Enns. Early completion of occluded objects. *Vision Research*, 13, 1998.

[Ree62] I. S. Reed. On a moment theorem for complex gaussian processes. *IRE Trans. Inf. Theory*, 8:194–195, 1962.

[RMOM03] C. J. Román-Moreno and R. Ortega-Martínez. The Wigner function in paraxial optics ii. Optical diffraction pattern representation. *Mexicana de Fisica*, 49:290–295, 2003.

[Rog94] G. L. Rogers. In-line soft-x-ray holography: the unwanted image. *Optics Letters*, 19(1):67–69, 1994.

[Rum76] R. J. Rummel. *Understanding Correlation*. Honolulu, Department of Political Science University of Hawai, 1976.

[SBS02] G. Strangman, D. A. Boas, and J. P. Sutton. Non-invasive neuroimaging using near-infrared light. *Biol. Psychiatry*, 52:679–693, 2002.

[Sch71] E. Schröder. Elimination of granulation in laser beam projections by means of moving diffusers. *Optics Communications*, 3(1):68–72, 1971.

[Sch94] U. Schnars. Direct phase determination in hologram interferometry with the use of digitally recorded holograms. *J. Opt. Soc. Am. A*, 11:2011–2015, 1994.

[SDF+07] F. Soulez, L. Denis, C. Fournier, É. Thiébaut, and C. Goepfert. Inverse-problem approach for particle digital holography: accurate location based on local optimization. *J. Opt. Soc. Am. A*, 24(4):1164–1171, 2007.

[SFSL97] F. Sattar, L. Floreby, G. Salomonsson, and B. Lovstrom. Image enhancement based on a nonlinear multiscale method. *IEEE Transcations on Image Processing*, 6:888–895, 1997.

[SJ94] U. Schnars and W. P. O. Jüptner. Direct recording of holograms by a ccd target and numerical reconstruction. *Applied Optics*, 33:179–181, 1994.

[SJ04a] A. Stern and B. Javidi. Generalized sampling theorem and application to digital holography. *Optical Information Systems II, B. Javidi and D. Psaltis, eds., Proc. SPIE*, 5557, 2004.

[SJ04b] A. Stern and B. Javidi. Sampling in the light of Wigner distribution. *J. Opt. Soc. Am. A*, 21:2038–2038, 2004.

[SJ04c] A. Stern and B. Javidi. Sampling in the light of Wigner distribution: eratta. *J. Opt. Soc. Am. A*, 21:360–366, 2004.

[SKM90] C. Saloma, S. Kawata, and S. Minami. Speckle reduction by wavelength and space diversity using a semiconductor laser. *Applied Optics*, 29(6):741–742, 1990.

[SNJ06a] A. E. Shortt, T. J. Naughton, and B. Javidi. A companding approach for nonuniform quantization of digital holograms of three-dimensional objects. *Optics Express*, 14(12):5129–5134, 2006.

[SNJ06b] A. E. Shortt, T. J. Naughton, and B. Javidi. Compression of digital holograms of three-dimensional objects using wavelets. *Optics Express*, 14(7):2625–2630, 2006.

[SNJ06c] A. E. Shortt, T. J. Naughton, and B. Javidi. Compression of optically encrypted digital holograms using artificial neural networks. *Journal of Display Technology*, 2(4):401–410, 2006.

[SP65] K. A. Stetson and R. L. Powell. Interferometric hologram evaluation of real-time vibration analysis of diffuse objects. *J. Opt. Soc. Amer.*, 55:1694–1695, 1965.

[SSJM08] A. Sharma, G. Sheoran, Z.A. Jaffery, and Moinuddin. Improvement of signal-to-noise ratio in digital holography using wavelet transform. *Optics and Lasers in Engineering*, 46(1):42–47, 2008.

[SV73] D. W. Sweeney and C. M. Vest. Reconstructions of three-dimensional refractive index fields from multidirectional interferometric data. *Applied Optics*, 12, 1973.

[SX04] P. Sun and J.-H. Xie. Method for reduction of background artifacts of images in scanning holography with a Fresnel-zone-plate coded aperture. *Applied Optics*, 43(21):4214–4218, 2004.

[TBPN00] J. B. Tiller, A. Barty, D. Paganin, and K. A. Nugent. The holographic twin image problem: a deterministic phase solution. *Optics Communications*, 183(1), 2000.

[Tho65] B. J. Thompson. A new method of measuring particle size by diffraction techniques. *Japanese Journal of Applied Physics*, 4:302–307, 1965.

[TIA81] N. Takai T. Iwai and T. Asakura. The autocorrelation function of the speckle intensity fluctuation integrated spatially by a detecting auerture of finite size. *Optica Acta*, 28(10):1425–1437, 1981.

[TJ00] E. Tajahuerce and B. Javidi. Encrypting three-dimensional information with digital holography. *Applied Optics*, 39:6595–6601, 2000.

[TKO99] Y. Takaki, H. Kawai, and H. Ohzu. Hybrid holographic microscopy free of conjugate and zero-order images. *Applied Optics*, 38(23):4990–4996, 1999.

[TLH91] S. Y. Tong, H. Hua Li, and H. Huang. Energy extension in three-dimensional atomic imaging by electron emission holography. *Phys. Rev. Lett.*, 67(22):3102–3105, 1991.

[Tri02] J. I. Trisnadi. Speckle contrast reduction in laser projection displays. *Proc. SPIE*, 4657:131–137, 2002.

[TT76] G. A. Tyler and B. T. Thompson. Fraunhofer holography applied to particle size analysis: a reassessment. *Optica Acta*, 23:685–700, 1976.

[TWZ67] B. J. Thompson, J. H. Ward, and W. R. Zinky. Application of hologram techniques for particle size analysis. *Applied Optics*, 6:519–526, 1967.

[Ull93] J. R. Ullmann. Edge replacement in the recognition of occluded objects. *Pattern Recognition*, 26:1771–1784, 1993.

[USB03] M. O. Ulfarsson, J. R. Sveinsson, and J. A. Benediktsson. Wavelet footprints for speckle reduction of SAR images. *IEEE*, pages 4092–4094, 2003.

[vL73] R. F. van Ligten. Speckle reduction by simulation of partially coherent object illumination in holography. *Applied Optics*, 12(2):255–265, 1973.

[VZW+05] A. C. Völker, P. Zakharov, B. Weber, F. Buck, and F. Scheffold. Laser speckle imaging with an active noise reduction scheme. *Optics Express*, 13(24):9782–9787, 2005.

[WBL02] Z. Wang, A. C. Bovik, and L. Lu. Why is image quality assessment so difficult. *Proc. IEEE Int. Conf. Acoustics, Speech, and Signal Processing*, 4:3313–3316, 2002.

[Wie49] N. Wiener. *Extrapolation, Interpolation, and Smoothing of Stationary Time Series with Engineering Applications*. Wiley and Sons, New York, 1949.

[Wig32] E. Wigner. On the quantum correction for thermodynamic equilibrium. *Phys. Rev.*, 40:749–759, 1932.

[XMA00] L. Xu, J. Miao, and A. Asundi. Properties of digital holography based on in-line configuration. *Optical Engineering*, 39(12):3214–3219, 2000.

[XPMA01] L. Xu, X. Peng, J. Miao, and A. Asundi. Studies of digital microscopic holography with applications to microstructure testing. *Applied Optics*, 40:5046–5051, 2001.

[XXZ+98] T. Xiao, H. Xu, Y. Zhang, J. Chen, and Z. Xu. Digital image decoding for in-line x-ray holography using two holograms. *Journal of Modern Optics*, 45(2):343–353, 1998.

[XZR+11] W. Xiao, J. Zhang, L. Rong, F. Pan, S. Liu, F. Wang, and A. He. Improvement of speckle noise suppression in digital holography by rotating linear polarization state. *Chinese Optics Letters*, 9(6):060901–060903, 2011.

[Yam03] I. Yamaguchi. Fundamentals and applications of speckle. *Proc. SPIE*, 4933:1, 2003.

[YAW96] R. Yu, A. R. Allen, and J. Watson. An optimal wavelet thresholding method for speckle noise reduction. *In Summer School on Wavelets: Papers, Publ:Silesian Technical University*, pages 77–81, 1996.

[YKA82] N. Takai Y. Kawagoe and T. Asakura. Speckle reduction by a rotating aperture at the fourier transform plane. *Optics and Lasers in Engineering*, 3(1):197–218, 1982.

[YM80a] L. P. Yaroslavskii and N. S. Merzlyakov. *Methods of Digital Holography*. Consultants Bureau, New York, 1980. Translated from Russian by Dave Parsons.

[YM80b] L. P. Yaroslavskii and N. S. Merzlyakov. *Methods of Digital Holography*. Consultants Bureau, New York, 1980.

[YW73] F. T. S. Yu and E. Y. Wang. Speckle reduction in holography by means of random spatial sampling. *Applied Optics*, 12(7):1656–1659, 1973.

[YXLH06] W. Yan, C. Xu, J. Li, and J. Huang. The use of discrete wavelets for signal denoising in microchip capillary electrophoresis. *Intelligent Control and Automation, 2006. WCICA 2006.*, 2:5254–5258, 2006.

[YXZJ99] S. Yang, X. Xie, Y. Zhao, and C. Jia. Reconstruction of near-field in-line hologram. *Optics Communications*, 159(1):29–31, 1999.

[YYMY06] I. Yamaguchi, K. Yamamoto, G. A. Mills, and M. Yokota. Image reconstruction only by phase in phase-shifting digital holography. *Applied Optics*, 45:975–983, 2006.

[YZ97] I. Yamaguchi and T. Zhang. Phase-shifting digital holography. *Optics Letters*, 22(16):1268–1270, 1997.

[ZLG04] Y. Zhang, Q. Lü, and B. Ge. Elimination of zero-order diffraction in digital off-axis holography. *Optics Communications*, 240(4-6), 2004.

[ZPOT03] Y. Zhang, G. Pedrini, W. Osten, and H. Tiziani. Whole optical wave field reconstruction from double or multi in-line holograms by phase retrieval algorithm. *Optics Express*, 11(24):3234–3241, 2003.

[ZT02] D. A. Zimnyakov and V. V. Tuchin. Optical tomography of tissue. *Quan. Elec.*, 32:849–867, 2002.

[ZY98] T. Zhang and I. Yamaguchi. Three-dimensional microscopy with phase-shifting digital holography. *Optics Letters*, 23:1221–1223, 1998.

[ZZ03] Y. Zhang and X. Zhang. Reconstruction of a complex object from two in-line holograms. *Optics Express*, 11(6):572–578, 2003.